Metal-oxide integrated Calcium Hydroxyapatite as a Potential Nano-antibiotic for Biomedical Applications

A

Thesis *submitted*

in Partial Fulfillment of the Requirements

for the *degree of*

DOCTOR OF PHILOSOPHY

by

VARUN SAXENA

Under supervision of

Dr. Lalit M. Pandey

February 2021

Department of Biosciences and Bioengineering

Indian Institute of Technology Guwahati

Guwahati 781 039, Assam, India

DECLARATION

This is to certify that the thesis entitled **"Metal-oxide integrated Calcium Hydroxyapatite as a Potential Nano-antibiotic for Biomedical Applications"**, submitted by me to the *Indian Institute of Technology Guwahati*, for the award of the Doctor of Philosophy, is a bonafide work carried out by me under the supervision of Dr. Lalit M. Pandey. The content of this thesis, in full or in parts, has not been submitted to any other University or Institute for the award of any degree or diploma. I also wish to state that to the best of my knowledge and understanding nothing in this report amounts to plagiarism.

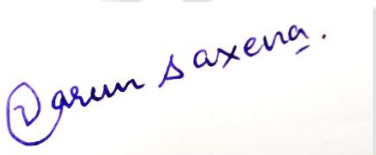

Varun Saxena
Department of Biosciences and Bioengineering,
Indian Institute of Technology Guwahati,
Guwahati-781039, Assam, India.
Date: 29-09-2021

CERTIFICATE

This is to certify that the thesis entitled **"Metal-oxide integrated Calcium Hydroxyapatite as a Potential Nano-antibiotic for Biomedical Applications"**, submitted by VARUN SAXENA (156106030), a PhD student in the *Department of Biosciences and Bioengineering*, *Indian Institute of Technology Guwahati*, for the award of the degree of Doctor of Philosophy, is a record of an original research work carried out by him under my supervision and guidance. The thesis has fulfilled all requirements as per the regulations of the institute and in my opinion has reached the standard needed for submission. The results embodied in this thesis have not been submitted to any other University or Institute for the award of any degree or diploma.

Supervisor: Dr. Lalit M. Pandey
Department of Biosciences and Bioengineering,
Indian Institute of Technology Guwahati,
Guwahati-781039, Assam, India.
Date: 29-09-2021

ACKNOWLEDGEMENTS

First and foremost, I am extremely thankful to my PhD supervisor, Dr. Lalit M. Pandey, for being an avid supporter, believing in my credentials and providing me with this opportunity. It is under his undue guidance, that I understood the importance of hard work and patience. Being his second PhD student will always be an honour to me. I appreciate all his contributions of time, ideas and suggestions, to make my research extremely productive. His passion and enthusiasm for research has always motivated me to keep moving forward, even during the difficult times.

Besides my advisor, I would like to thank the rest of my doctoral committee Dr. Ajai B. Kunnumakkara (committee chairman), Dr. Soumen Maiti, and Dr. Vimal Katiyar, not only for their insightful comments, suggestions and encouragement, but also for the critical questions which pushed me to dive further into my research. I also extend my sincere gratitude to Dr. Ishani Shukla for her generous support, suggestions and contributions, which have helped me in nurturing this thesis in the current form.

I convey my special thanks to the Department of Biosciences and Bioengineering (BSBE), Indian Institute of Technology Guwahati, for giving me this golden opportunity to be a part of this prestigious institute. I also thank all the faculty members and staff of BSBE department for their constant help and support. I am highly thankful to the Central Instrument Facility (CIF), IIT Guwahati for allowing me to use the sophisticated instruments, which significantly improved the quality of my work.

Furthermore, Commonwealth Commission, UK is highly acknowledged for selecting me as a suitable candidate for the Commonwealth Split-site fellowship and providing me with the opportunity of carrying out research for 12 months at University of Strathclyde, UK. I would like to convey my gratitude to my UK supervisor, Dr. King Hang Aaron Lau, for his constant involvement and support, which encouraged me to grow as a researcher.

I sincerely thank Dr. Abshar Hasan for always being a supporter and providing me with a homely environment throughout my PhD. I am also thankful to my friends Suraj, Dr. Faheem, Dr. Rasmi, Apurba, Dr. Reshmi, Richa and Srirupa for always being friends-cum-family here at IIT Guwahati, and making this part of my life enjoyable.

I am also thankful to my fellow-mates Sakshi, Poulami, Swati, Aquib, Gayatri, Aman, Rushikesh, Rahul, Vivek, Ravi and Samvidha for the thought-provoking discussions, motivating words, and every supporting nature. I am thankful to my fellow colleagues at Strathclyde University,

especially Martyn and Iqra for not letting me feel like an outsider, and making that place a home away from home. A special thanks to Master Mridul Pandey for keeping the homely environment alive throughout my journey in Guwahati.

Last but not the least, I thank my family members, Dr. Yogesh Chandra, Smt. Sandhya Saxena, Tarun Saxena, Arun Saxena, and Mrs. Ila Saxena, who are the most important part of my life. I thank them for always believing in me and my different working methods.

I thank the Almighty God, for providing me with courage, determination and support during all these years of doctoral studies.

Sincerely,

Varun Saxena

ABSTRACT

Hydroxyapatite (HAp) is a widely studied material for bone tissue engineering applications, but it has no intrinsic antibacterial properties to prevent infection. Further, target deficiency is also an obstacle in its commercialization. Various nanoparticles (NPs) such as ZnO, Fe_3O_4, Ag, peptides, and peptoids, a new class of bio-organic nanomaterials, have been found to possess antibacterial activity. The objective of this thesis was to explore the effect of metal ion integration with the HAp lattice to incorporate the self-antibacterial activity as well as the target efficacy for biomedical applications. The entire thesis is divided into five sections explaining the step-wise extension of the thesis. The first section deals with the synthesis and characterization of the ZnO nanoparticles and the evaluation of their antibacterial activity. The antibacterial activity of ZnO remains dependent on its size and morphology. The size and morphology can be tuned by using various sophisticated techniques. Our idea was to obtain the required antibacterial activity by simple co-precipitation method via metal ion doping. In this section, we have scrutinized the effect of doping of trivalent Al^{3+} ions into the ZnO lattice to enhance its antibacterial action. The minimum inhibitory concentration (MIC) value was decreased by ~19 times at 15 % doping, and the major antibacterial activity was found due to the intracellular accumulation of the Zn^{2+} ions and reactive oxygen species (ROS) independent. However, rupturing in the bacterial cell wall could not be achieved. Hence, in the second section, we doped another trivalent ion, $Fe^{3+,}$ into the ZnO lattice and explored its antibacterial activity and mechanism. In the case of Fe doping, the release of the Zn^{2+} ions was linear as compared to Al doping (exponential), leading to the rupturing into the bacterial cell wall. These two sections explained the tuning of the Physico-chemical properties of ZnO based on the dopant type. Following the rupturing of the bacterial cell wall and enhanced antibacterial activity, in the third section, Zn and Fe were co-integrated with the HAp lattice. A biphasic ferric-HAp-zincite nanoassembly was designed and was explored for its antibacterial, biocompatibility, and bone cell proliferation ability. The designed ferric-HAp-zincite nanoassembly possessed excellent antibacterial activity, which was ROS independent, and due to the linear release of the Zn and Fe ions, causing the rupturing of the bacterial cell wall. Additionally, the designed ferric-HAp-zincite nanoassembly possessed a cell viability ~300 times higher than that of control cells and reflected no inflammatory response studied via TNF-α activity. Furthermore, the designed ferric-HAp-zincite nanoassembly possessed excellent bone cell

proliferation ability (alkaline phosphatase activity) based on the concentration of the Zn within the designed HAp based nanoassembly. Moreover, this ferric-HAp-zincite nanoassembly possessed paramagnetic behavior, which is ideal for the target efficiency. This section explained the role of metal ion doping into the HAp lattice and tuning of its biological responses via altering the lattice parameters and phases. The fourth section of this thesis explains the bone tissue engineering application of the designed ferric-HAp-zincite nanoassembly. In this section, we fabricated the Chitosan-CMC-ferric-HAp-zincite scaffold and scrutinized its biochemical properties. The biochemical properties such as porosity, swelling behavior, and enzymatic degradation were found to be dependent on the concentration of the ferric-HAp-zincite nanoassembly. The designed scaffolds possessed excellent bone cell proliferation and bio-mineralization ability. Hence, the scaffolds are plausible for bone tissue engineering applications. This thesis's fifth and final section comprises the design, characterization, and antibacterial activity of the novel peptidomimetics "peptoid" (Ampetoids) micelles. These micelles may be suitable to fabricate the ferric-HAp-zincite-Ampetoids organic-inorganic hybrid nanomedicine systems.

Contents

List of Figures

List of Tables

Abbreviations

HAp	Calcium Hydroxyapatite
β-TCP	β-Tricalcium phosphate
FTIR-ATR	Fourier-transform infrared spectroscopy-attenuated total reflectance
ITC	Isothermal titration calorimetry
EDX	Energy-dispersive X-ray spectroscopy
FESEM	Field emission scanning electron microscopy
AFM	Atomic force microscopy
NPs	Nanoparticles
AZO	Aluminum doped Zinc oxide nanoassembly
ROS	Reactive Oxygen Species
MIC	Minimal Inhibitory Concentration
MTT	3-(4,5-dimethylthiazol-2-yl)-2,5-diphenyltetrazolium bromide
DSC/TGA	Differential scanning calorimetry/ Thermogravimetric Analysis
DMEM	Dulbecco's Modified Eagle's Medium
FBS	Fetal Bovine Serum
PBS	Phosphate Buffer Saline
DMSO	Dimethyl sulfoxide
DCFH-DA	Dichloro-dihydro-fluorescein Diacetate

CFDA	Carboxyfluorescein Diacetate Succinimidyl Ester
FWHM	Full-Width Half Maxima
LO	Longitudinal Optical
TO	Transverse Optical
FSC	Forward Scattering Counts
CF	Fluorescent carboxyfluorescein
FZO	Fe(III) doped Zinc oxide nanoparticles
ZOI	zone of Inhibition
PI	Propidium Iodide
HAp	Hydroxyapatite
ZFHAp	Zinc and Iron co-integrated HAp Nanoparticles / ferric-HAp-ZnO
ALP	Alkaline phosphatase
MG-63 cells	Human osteosarcoma cell lines
VSM	Vibrating Sample Magnetometer
CMC	Carboxymethylcellulose
SBF	Simulated Body Fluid
UTM	Electromechanical Universal Testing Machine
HMDS	Hexamethyldisilazane

CCNWs-AgNP	Chitosan/Carboxymethyl cellulose/Silver nanoparticles modified Cellulose nanoWhiskers
RP-HPLC	Reverse-Phase High-Pressure Liquid Chromatography
LCMS	Liquid Chromatography-Mass Spectroscopy
AMPs	Antimicrobial peptides
Ampetoids	Antimicrobial peptoids
DIC	N,N′-diisopropyl carbodiimide
EG_2	ethylene glycol
DMF	Dimethylformamide
DCM	Dichloromethane
NMP	N-Methyl-2-pyrrolidone
TFA	Trifluoroacetic acid
DIEA	N,N-Diisopropylethylamine
BAA	Bromoacetic acid
HBTU	2-(1H-benzotriazol-1-yl)-1,1,3,3-tetramethyluronium hexafluorophosphate
NLys	Tert-butyl N-(4-aminobutyl) carbamate
NSpe	(1S)-1-Phenylethylamine
LC-ESI-MS	Liquid Chromatography-Electrospray Ionisation-Mass Spectrometry

Chapter 1
Introduction

Calcium Hydroxyapatite (HAp, $Ca_{10}(PO_4)_6(OH)_2$) is the major mineral component of bone. It is one of the most studied bone bio-mimic, which possesses substantial properties for bone tissue engineering applications [1-4]. These properties include and are not limited to good bioactivity, biodegradability, osteoconductivity, biological stability, and affinity at biological pH values [5]. In the human body, it is found in carbonated apatite form with small calcium deficiency. HAp is insoluble at physiological pH (7.4) but is slightly soluble at acidic pH, *i.e.,* below 6.5 [6]. Depending upon the Ca/P ratios, calcium phosphate encompasses variable phases, such as Monocalcium phosphate, Dicalcium phosphate, Tricalcium phosphate, and Hydroxyapatite for 0.5, 1.0, 1.5, and 1.67, Ca/P ratios, respectively.

However, HAp possesses various above-discussed properties, yet it lacks in its commercialization due to three major lags, *i.e.,* lack of self-antimicrobial activity, target deficiency, and generation of other phases of calcium phosphate, *e.g.,* β-TCP along with HAp. Various approaches have been endeavored to change the crystal structure of the HAp lattice to enhance the existing properties of HAp and to acquire the self-antimicrobial activity, target efficiency with various degrees of success [5, 7-11], yet no study has been successful in achieving them together. These studies have also confirmed the generation of other phases along with HAp at elevated dopant concentrations. The doping of metal ions causes various imbalances as well as the deformation in the crystal lattice and alters the properties of the material. In this context, the nano-HAp and its composites have also been attempted to explore the generation of self-antimicrobial activity and target efficiency [8, 12-14]; yet did not report the simultaneous incorporation of these two highly demandable properties for biomedical applications.

In addition to the metal ion doping, several metal oxides have been tested to be integrated with the HAp lattice to acquire antimicrobial activity, anticancer activity [15] as well as target efficiency. Yet, no reports are available to acquire them together without harming the HAp phase or the required bioactivity as well as the mechanical properties [16-18]. For example, the chemical charge imbalance due to the monovalent and trivalent-doped ions causes changes in the chemical

properties of HAp. Although doping of divalent ions does not cause the charge imbalance, yet the size of the metal ion plays an important role.

The selection and concentration of metal ion/metal oxide play a crucial role in delivering the desired phase as well as the biological responses of the HAp lattice and hence, provides an opportunity to tune the biological properties of the HAp to a biomaterial researcher [19]. Hence, the need to understand the selection of metal ion/metal oxide is crucial. Metal ions/metal oxides with self-antimicrobial activity could incorporate the desired properties to HAp. For example, the ionic radii of zinc (0.074 nm) is smaller than that of calcium (0.099 nm). Hence, incorporation of zinc into the HAp lattice declined the 'c' lattice parameter and enhanced the 'a' lattice parameter, which decreased the crystallinity of HAp with an increase in the zinc concentration [20, 21]. Similarly, metal ion/metal oxide with target efficiency could generate target efficiency in the HAp lattice [3, 22]. As HAp does not possess any self-antibacterial activity, the incorporation of metal ions as well as the separate metal oxide phase generation without hampering the HAp phase is one of the major challenges for a biomaterial researcher [23, 24].

Hence, to achieve the antibacterial and target efficacy together, we planned to modify the HAp lattice by integrating it with the metal oxides. For this purpose, various metal/metal oxides were scrutinized based on the available literature. Primarily, Chitosan, Ag, Cu, Zn, and peptoids "bio-mimic of peptides" were scrutinized [25-30], and ZnO was selected to be integrated with the HAp lattice because of its abundance in nature, ease of synthesis, and detailed antibacterial mechanisms. Zn doped HAp shows different mechanical behavior due to two reasons: first, the difference in the size of Zn and Ca, and second, the different melting temperatures of Ca and Zn, *i.e.*, 842 °C and 419.5 °C, respectively. In addition, it has been observed that the major antibacterial mechanism by ZnO is given in three ways. 1) by membrane damaging through Zn ions, 2) by rupturing in the cell wall of bacteria through the generation of Reactive Oxygen Species (ROS), and 3) via entering into the bacterial cell and damaging the cellular components [19]. Among all these mechanisms, ROS dependent antibacterial mechanism is not preferable for the human cells, as the major toxicity to the human cells by the nanoparticles (NPs) is due to the ROS production.

Similarly, doping of Fe not only provides target efficiencies but also functions for various therapeutic applications [31, 32], yet suffers the lack of desired antibacterial activity. Iron-based nanocomposite has been proven for its antibacterial properties [33, 34] and hyperthermia

applications [35, 36]. Furthermore, it has been observed that nano-iron oxide increases the osteoblast density but suffers in its direct application due to its biofouling in blood plasma [37]. The integration of Zn and Fe has been proven to play a pivotal role in incorporating the desired properties to the HAp lattice, yet the co-integration of them has not been processed yet. The major challenge in incorporating the Zn and Fe into the HAp lattice remains in managing the HAp phase of calcium phosphate for bone integrity, low Minimum Inhibitory Concentrations (MIC) values, as well as the paramagnetic behavior for target efficiency altogether.

In this thesis work, we first analyzed ZnO's antibacterial activity and modified its structure via doping with trivalent ions (Al^{3+} and Fe^{3+}) to enhance the antibacterial efficacy. Additionally, the antibacterial mechanism of the modified ZnO lattice was also studied. Parallelly, we synthesized the antibacterial peptoids and scrutinized their antibacterial activity over a wide range of bacteria, along with their cytocompatibility to integrate it with HAp. Finally, the Zn and Fe integrated HAp nanoassembly was designed with the desired self-antibacterial activity and target efficiency. Following the successful synthesis of ferric-HAp-zincite nanoassembly, we examined its biomedical application, *e.g.,* by designing Chitosan, Carboxymethyl cellulose (CMC), and ferric-HAp-zincite nanoassembly scaffolds for bone tissue engineering applications. Chitosan and HAp are the major constituents of bone. Human bone mineral is a non-stoichiometric nanocrystalline apatite with impurities in the form of co-substituted trace elements of Na^{+}, Mg^{2+}, Zn^{2+}, Sr^{2+}, K^{+}, F^{-}, Cl^{-}, CO_3^{2-}, Si, etc. Chitosan possesses many properties desired for biomedical applications like biodegradability, biocompatibility, bioactivity, and antimicrobial properties. CMC, an anionic polymer with chemical similarity with chitosan, provides a strong ionic cross-linking to enhance the biochemical feature. Hence, chitosan, cellulose, and ferric-zincite in HAp were blended to mimic the bone microenvironment for bone tissue engineering applications. To control the porosity and its dependant biochemical properties, the concentration of ZFHAp-2 was varied.

1.1 Objectives

The overall aim of this study was to incorporate and elaborate the two most desired properties of the HAp system required for efficient bone tissue engineering applications, *i.e.*, self-antibacterial activity and target efficacy. For this purpose, the ZnO was first synthesized and were modulated to reduce the MIC values via doping Al and Fe ions. The antibacterial activity and mechanism were evaluated by calculating the release of metal ions and ROS generation. After successfully incorporating these properties into the HAp lattice, the designed material was scrutinized for bone tissue engineering application in powder and scaffold forms. The point wise objectives are as follows:

1. Formulation, characterization, and antibacterial mechanism analysis of Al-doped ZnO
2. Design and characterization of Fe(III) doped ZnO nanoparticles (NPs) and evaluation of its antibacterial mechanism
3. Selection and formulation of Al or Fe and ZnO co-integrated HAp NPs and evaluation of its antibacterial activity, cytocompatibility, and target efficacy
4. *In-vitro* osteogenic activity analysis via synthesizing scaffold of the designed material
5. Synthesis and characterization of the antimicrobial peptoids micelles

1.2 Thesis outlines

Based on the above objectives, the present thesis is divided into 8 chapters. The detailed outline for this thesis is as follows:

In Chapter 2, we have critically reviewed the studies over HAp, its existing properties, and the shortcomings for its commercialization. Additionally, the addition of various metal ions/oxides has been reviewed to finalize the selection of antimicrobial nanomaterials to be integrated with the HAp. Furthermore, metal ions have been explored with inherent antibacterial activity as well as the target efficiency. Following the review, in Chapter 3, we discussed the synthesis characterization and antibacterial activity of ZnO NPs. Further, the doping of Al^{3+} ions into the ZnO lattice was studied. The effect of metal ion doping on the physical and chemical properties of ZnO lattice was explored. In brief, the crystal structure of AZO (Al-doped ZnO) nanoassembly was explored and was evaluated for its antibacterial activity and mechanism. The cytocompatibility of the AZO nanoassembly was also examined. Summarily, the physical and chemical properties of AZO nanoassembly were co-related with its biological responses. However, the inactivation of the bacterial cells was achieved successfully, the rupturing in the cell wall could not be acquired. Hence, in Chapter 4, we examined the doping of another trivalent metal ion Fe(III), into the ZnO lattice (FZO). Similar to that of Chapter 3, the effect of Fe^{3+} ion doping over its physical, chemical, and biological responses was evaluated. In brief, the difference in the antibacterial activity and mechanism of metal ion doping into the ZnO lattice was explored. Summarily, the selection of metal ion doping with respect to its biological interactions and responses was explored and detailed.

After successfully achieving the lower MIC values of FZO and rupturing in the bacterial cell wall, we intended to incorporate the FZO into the HAp lattice. Hence, Chapter 5 is dedicated to the design and characterization of the self-antibacterial ferric-HAp-zincite bimetallic nanoassembly. Briefly, this chapter explains the design of the said nanoassembly for incorporating the simultaneous self-antibacterial activity as well as the target efficacy to the HAp lattice. The designed nanoassembly was examined for its physicochemical properties, and these were co-related with its biological interactions. The designed nanoassembly was evaluated for its antibacterial activity, antibacterial mechanism, target efficiency, cytocompatibility, anti-inflammatory responses, and bone cell proliferation ability for biomedical applications.

Chapter 6 is focused on the biomedical application of the designed ferric-HAp-zincite nanoassembly, particularly for bone tissue engineering applications. In this regard, a scaffold of Chitosan-CMC-ferric-HAp-zincite was fabricated and was evaluated for its physicochemical properties. The required scaffold properties such as swelling behavior, porosity, and enzymatic degradation were evaluated and were co-related with the concentration of the ferric-HAp-zincite nanoassembly. Additionally, the fabricated scaffolds were examined for their self-antibacterial utility as well the bone cell proliferation efficacy. In Chapter 7, we designed the micelles of the antibacterial peptoids "Ampetoids" and assessed them for their physical and chemical characterizations. The micelles were also evaluated for their antibacterial activity as well as their cytocompatibility. Additionally, various peptoid sequences were also evaluated to calculate their MIC values for biomedical applications. Finally, Chapter 8 summarizes the conclusions and findings of the thesis work. Additionally, suggestions for future work are also listed.

Chapter 2

Literature Survey

Calcium hydroxyapatite, commonly known as Hydroxyapatite (HAp), is a metal bioceramic typically made up of calcium phosphate. HAp is one of the most abundant bioceramics in nature and is found in all vertebrates in the form of bones and shells. In a typical chemical structure, HAp carries the molar ratio of Ca:P as 1.67, which possesses physical, chemical, and biological similarities with the hard tissues such as bone, dentine, enamel, and tendons [5]. The major mineral component of the bone is found in the form of hydroxyapatite, and this similarity with bone provides HAp various properties suitable for bone tissue engineering applications. These properties include and are not limited to biogenic activity, osteoconductivity, required bio-stability, and degradability [19]. In general, HAp is considered the most studied bioceramic for bone tissue engineering applications, with and without modifications.

In general, Apatites are known as metal phosphate with chloro, fluoro, or hydroxyl substitutes. Apatites reflect various colors based on their metallic composition. The basic formula of an apatite remains in the form of $M_{10}(PO_4)_6X_2$, where M represents a variety of minerals such as Ca, Mg, Fe, Cd, etc., and Z represents P, As, V, S, C, S, etc. X represents F, Cl, Br, OH, etc. [38]. The HAp being "Calcium" and "Hydroxy" substitutes carries the chemical formula of $Ca_{10}(PO_4)_6(OH)_2$. As discussed earlier, HAp possesses physical and chemical similarities with bone. However, calcium phosphate possesses various forms based on its Ca: P ratio, which are listed in Table 2.1. All these forms of calcium phosphate have their respective bioactivity, mechanical behavior as well as biodegradability. However, the chemical similarity is maximum matched with its HAp phase. Hence, obtaining a pure HAp phase has been a great challenge for biomedical researchers. Various researchers have tried to modify the crystal lattice of the HAp depending on the required applications with varying degrees of success. However, in-depth information about the crystal lattice of the HAp is highly required for an efficient modification for site-specific applications.

To enhance to biochemical properties of the HAp lattice, researchers have also tested to modulate the size as well as the morphology of the HAp. The major work has been applied over the nano-ranged HAp. Nanotechnology has been proven to play a pivotal role in enhancing the surface properties of various materials for a wide range of applications. High surface-to-volume ratios and

the confined directional properties help researchers to tune the material properties based on their required applications [39]. Nanomaterials being in the nano-ranged or sub-atomic range provide an opportunity for the researcher to modulate the specific surface, interfacial as well physical, and mechanical properties of the biomaterials. Hence, nano-HAp was considered to be a proven strong candidate than that of micro or bulk HAp for various biomedical applications. Nano-HAp pristine or doped nano-HAp has also been investigated for various biomedical applications, majorly for hard tissue engineering applications such as Bone Tissue Engineering (BTE) and dental applications.

Table 2.1. Variable phases of HAp

S. No.	Ca/P Ratio	General Name	Formula
1	0.5	Monocalcium phosphate	$Ca(H_2PO_4)_2$
2	1.0	Dicalcium phosphate	$CaHPO_4$
3	1.33	Octacalcium phosphate	$Ca_8(HPO_4)_2(PO_4)_4$
4	1.5	Tricalcium phosphate	$Ca_3(PO_4)_2$
5	1.67	Hydroxyapatite	$Ca_{10}(PO_4)_6(OH)_2$

Musculoskeletal diseases have become more frequent these days due to the increased number of accidents, fatigue in a rush, and old age. In developing countries like India, it's expected that the cases of osteoarthritis may reach up to 60 million by 2025 [40]. Hence, designing bio-material with frequent synthesis routes and treatments is the necessity of the current scenario. Nano-HAp is one of the most studied materials in BTE and has been utilized for various biological applications at the laboratory or *in-vivo* level. These applications include and are not limited to bone tissue engineering [41-43], drug delivery [44-46], treatment of osteomyelitis [47-49], and osteoporosis [14, 50, 51], *etc*.

One of the major advantages of the HAp remains its abundance in nature to be extracted from the natural waste and resources as well the tunability of its size and morphology, resulting in the site-specific design of HAp for various BTE. Various synthesis routes provide a variety of control over its properties, which in turn results in the altered biological response of the HAp, such as bioactivity, biodegradability as well as bio-compatibility. In general, the size and the morphology of the HAp NPs can be controlled by varying the changing the concentration of the dispersions

such as surfactant and the reducing agent's concentration. The detailed information about these synthesis routes is discussed after defining the crystal structure of the HAp lattice.

2.1 Chemical structure of HAp

The crystal structure of a biomaterial plays a crucial role in its biomedical applications. The first interaction with proteins and cells and the biological responses, such as the selection and/or rejection of a biomaterial, is guided by the crystal structure of the biomaterial. One can tailor the biological fate of material by altering the crystal symmetry or by modulating the crystal grains by creating deforms and doping various metallic ions. HAp has substantial biological properties such as solubility, bioactivity, and biocompatibility. All these properties can be tailored by substituting the Ca/P of the OH group from the HAp crystal structure, and the biological responses will be altered. For example, carbonate substituted HAp is more bioactive than stoichiometric HAp [52]. In brief, the HAp crystal possesses the hexagonal structure with space group $P6_3/m$. The lattice parameter are as follows; a = b = 9.432 Å and c = 6.881 Å and $\gamma = 120°$ [53]. However, the stoichiometric HAp carries the space groups monoclinic $P2_1/b$ form [54]. HAp does not carry a high crystallite structure in both natural and synthetic powder, which results in the identical symmetry between the hexagonal and monoclinic structure when analyzed through the XRD data. Both hexagonal and monoclinic structure carries the similar chemical and biological properties in terms of bioactivity and biodegradation, however, $P6_3/m$ hexagonal structure is not favorable [55]. The comparison between the hexagonal and monoclinic HAp lattice is given in Table 2.2. It has been reported that HAp crystal may also be found as a mixture of hexagonal and monoclinic symmetries, and this can cause crystal deforms in the lattice. Hence, designing a pure phase HAp with a hexagonal structure has been a challenge for biomaterial researchers [56]. In addition, the hexagonal structure carries the nonstoichiometric HAp, which results in the co-existence of the impurities in the HAp lattice, such as Cl^- and F^- ions. Figure 2.1 illustrates the crystal structure of the hexagonal HAp. As shown in Figure 1, Ca occupies two different sites, Ca1 (columnar Ca, four sites) and Ca2 (axial Ca, six sites). Six PO_4 groups occupy the Ca1 site, and five PO_4 groups occupy the Ca2 site, and one OH group. Substitution at any of the Ca sites alters the lattice parameters of the pristine HAp, which ultimately alters the biochemical responses of the formulated HAp. These very small differences between the hexagonal and the monoclinic

geometry and lattice parameters of the HAp particles effectively impact the physicochemical properties of the HAp such as compressive strength and porosity [57].

Table 2.2. Hexagonal and Monoclinic crystal structure of HAp

Properties	Hexagonal	Monoclinic
Space group Symmetry	$P6_3/m$	$P2_1/b$
Lattice Parameter	a = b = 9.432 Å c = 6.881 Å γ = 120°	a = 9.4214 Å b = 2a c = 6.8814 Å γ = 120°
Sintering Temperature	25-100 °C	Elevated temperature, 850 °C
Details	Array of PO_4 tetrahedra held together by Ca ion. Ca ions occurs at axes and in accurately aligned columns	Same as hexagon, only direction of OH group changes

However, the replacement of calcium ions from either of the Ca sites changes the biological properties; the replacement of the OH group surrounding the Ca ion at the Ca2 site also plays a crucial role in tuning the crustal properties and the interfacial responses pf the HAp lattice. The human bone is an organic-inorganic hybrid of HAp-collagen. Typically in structure, the human bone remains in the form of Ca substituted HAp matrix with collagen fibers. The metal ion which replaces Ca in HAp is Na^+, Mg^{2+}, Zn^{2+}, Sr^{2+}, K^+, F^-, Cl^-, CO_3^{2-}, Si, etc. [38]. These impurities cause the inversion in the centers for the OH directions, resulting in the alteration in the HAp lattice parameters and thus forms a stable and mechanically strong bone. Hence, to maintain the charge stoichiometry, the Ca^{2+} ion is replaced by the cations, SiO_4^{4-} replaces the PO_4 tetrahedra and fluoride and the chloride ion replaces the hydroxyl group in the basic crystal lattice [58]. Another difference between the hexagonal and monoclinic symmetry remains the arrangement of the metal ions. In detail, the hexagonal structure is centrosymmetric, whereas the monoclinic geometry of HAp is non-centrosymmetric, which results in the piezoelectric properties of HAp.

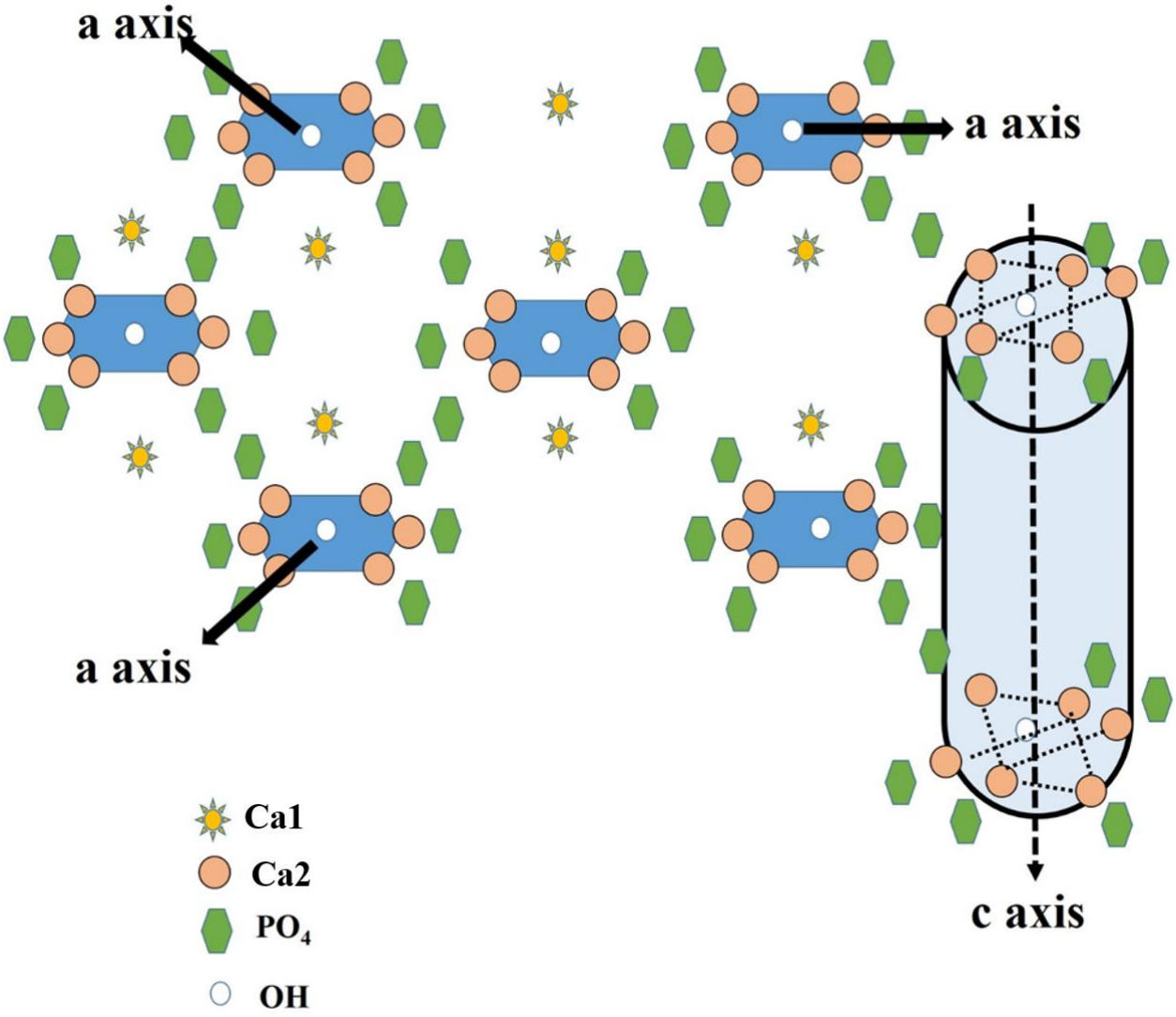

Figure 2.1. Crystal structure of HAp, the three a-axis at 120° angle, and the perpendicular c-axis

To design an effective HAp lattice based on site-specific applications, the in-depth knowledge of HAp lattice, the metal ion replacing site, and thermodynamics plays an important role. For example, the synthesis route (discussed later) and sintering temperature play the deciding role in defining the phase as well as the crystal structure of the HAp lattice. It has been observed that the sintering at a higher temperature usually generates the β-Tri calcium phosphate (β-TCP) of calcium phosphate along with the HAp phase of the calcium phosphate [19]. The pristine HAp is usually obtained while sintering at low temperatures. Hence, researchers are under investigation to acquire

the pure HAp phase in pristine and doped HAp lattice as the integration of metal ions generates β-TCP phase as a secondary phase in the calcium phosphate lattice [59-61]. Hence, obtaining a pure HAp phase after transition metal ion doping still remains a challenge for biomaterial researchers.

2.2 Synthesis routes of HAp

The synthesis procedure of the biomaterial is the most important and primitive step towards the selection/rejection of a biomaterial. Plenty of researches have been optimized in order to obtain the desired phase as well as the size and morphology of the HAp. As discussed earlier, various reaction procedures for designing a nano-HAp have been tested. Various factors during the synthesis of HAp have been observed to result in different sizes and morphologies, and these factors majorly include aging time, chemical solutions, temperature, pH, and the sintering temperature. These factors were found to play a decisive role in deciding the size as well as the morphology of the HAp lattice. These synthesis parameters, as well as the reactions, play a crucial role in the commercialization of the HAp based materials based on their respective chemical solutions and the inputs of energies while synthesis by governing the end cost of the material. In general, the synthesis of the HAp can be divided into two major methods, *i.e.,* Biological or from natural resources, and chemical methods. The details are as follows:

2.2.1 Nano-HAp from natural resources

As discussed earlier, HAp is found in abundance in nature in the form of shells and bones. In the extraction from the natural resources, the HAp is extracted from the natural resources such as fish scale, fishbone, eggshells, and seashells. The biological wastes are harvested to produce HAp, leading to high environmental cleanup as well as a low-cost synthesis of HAp. However, these techniques do not provide the control to tune the size and morphology of the HAp, for example, granular, rod-shaped, flower-shaped, and particulate structure, etc. However, because of being extracted from the natural resources, the Ca/P ratio remains constant at 1.67, resulting in the pure HAp phase. Furthermore, few metals ions are found to be integrated with the HAp as a mineral supplement, depending on the source of the HAp. Similarly, the mechanical strength of samples remains close to that of bone, as they are extracted from similar resources. The advantage of such a method is that these methods do not require the usage of toxic chemical solvents in synthesis and

do not produce toxic waste end materials. Conversely, few solvents are used to clean the shells prior to the synthesis. There are majorly two methods in extracting HAp from natural resources;

2.2.1.1 Solid-state method

In this method, the waste biosamples are washed with MilliQ water to remove the dirt and impurities. The washed powders are then dried at temperatures ranging from 60-80 ºC. The dried samples are then physically processed to produce the HAp. In few studies, the biosamples have been smashed into small pieces followed by the sintering at a higher temperature, *i.e.*, 900 ºC. The samples were then grounded through various ways, such as grinding by the mortar pestle before applications [62]. Similarly, samples were the first ball milled until 10 h to obtain the nano-HAp prior to the calcination at a higher temperature, *i.e.*, 800 ºC [63]. In addition, an ultrasonic technique has also been used to produce the nano-sized HAp from biowastes [64].

2.2.1.2 Wet technique

In this method, the biosamples are first washed and cleaned by MilliQ water followed by heating at high temperatures to remove the organics wastes. The samples are then dried, and after drying, the samples are placed in a hydrothermal chamber at 280 °C for 3 h prior to the calcination [65]. In another approach, *Tilapia* scales were treated with 5 % NaOH solution to remove the organic waste, followed by the heat treatment at 70 ºC. The samples were again treated with 50 % NaOH, followed by heating at 100 ºC. Finally, the samples were filtered, and the 7 pH of the solution was achieved by the addition of H_3PO_4 solution followed by drying the samples at 100 ºC [66]. In wet techniques, washing with solvents as well as sintering at high temperatures removes most of the organic waste from the biowastes, and a pure form of HAp is achieved.

2.2.2 Chemical methods

The synthesis through the natural resources is an efficient technique with a high yield, yet it does not provide control over the tuning of size and the morphology of the HAp. Hence, chemical methods are used as an alternative to natural processes. In this process, the chemical precursors of the Ca and P are processed in various ways. The HAp produced is typically known as synthetic HAp. The reaction parameters which govern the size and the morphology of the HAp are reaction solvents' concentration, temperature, pH, and the reaction conditions such as stirring speed and

titration speed. However, the inputs of energy and the cost of precursors make them costlier processes as compared to the natural HAp synthesis routes. A few of the most used methods are discussed below;

2.2.2.1 Chemical precipitation method

The chemical precipitation method is one of the simple most methods to produce the HAp. In brief, the Ca and PO_4 precursors are mixed with the MilliQ water with a predefined molar ratio of 1.67 and are heated at elevated temperatures, *i.e.*, > 65 ºC temperature. Separate solutions for both the precursors are prepared, and the PO_4 solution is titrated dropwise with the Ca solution. The rate of titration plays a crucial role in defining the size and the morphology of the produced HAp. After the titration is completed, the pH of the solution is increased to > 9 using liquid ammonia. The respective chemical reaction is as follows;

$$10\ Ca(NO_3)_2.4H_2O + 6\ (NH_4)_2.HPO_4 + 8\ NH_4OH = Ca_{10}(PO_4)_6(OH)_2 + 20\ NH_4NO_3 + 46\ H_2O$$

In this process, the HAp gets reduced or precipitated at elevated pH values, as it remains unsoluble at those pH values. In addition to the titration speed, the reaction temperature, as well as the pH of the solution, plays a crucial role in governing the particle size, morphology as well as surface charge over the HAp crystals. After precipitation, the pH of the solution is reduced to 7 by washing multiple times with MilliQ water followed by drying. The calcination at high temperatures provides the HAp phase with nano-sized crystals [67-69]. It is to be noted that the calcination temperature also plays a crucial role in defining the phase of the material. Usually, elevated temperatures > 850 °C are considered to provide secondary phases such as β-TCP.

2.2.2.2 Sol-gel method

This is the second most used protocol for producing HAp, and produce HAp by converting the precursor solution into the gel form. In a typical process, the Ca and PO_4 precursors are first mixed dropwise, similar to that of the chemical precipitation method, followed by elevating the pH of the solution > 9. After increasing the pH, the reaction temperature is increased to > 90 ºC for few hours ranging from 9-12 h. As a result, a thick gel of calcium phosphate is produced. The gel is then dried at high temperature without stirring, and the produced HAp is washed to reduce the pH down

to neutral. The advantage of this method lies in its mechanism of mixing the metal precursors at the atomic level due to elevated temperatures, leading to the synthesis of nano-sized HAp lattice. Similar to that of the chemical precipitation method, calcination at high temperatures provides the HAp phase with size ranging in the nano range. In a typical reaction, the solution temperature for gel formation, pH, and gel formation time plays a crucial role and provides control over the size and the morphology of the HAp NPs [69-73].

2.2.2.3 Hydrothermal/Solvothermal method

As the name suggests, these methods use the thermal incubation of the chemical precursors underwater in the solution environment. A water solvent-based reaction is known as Hydrothermal Reaction, and solvents other than water (such as organic solvents) assisted synthesis is known as the Solvothermal Method. In a typical process similar to that of the precipitation method, the Ca:P precursors in 1.67 Ca/P ratios are first mixed and stirred for few hours until precipitation; after mixing, the solution is transferred into a Teflon coated stainless steel autoclave with controlled temperature and pressure. The autoclave is then placed into a heat chamber, and the temperature is raised ranging from 200-500 ºC for 3-4 h. The solution is then washed and dried at high temperatures, followed by calcination at elevated temperatures. The control over the size and the morphology is majorly governed by the type of solvent and the pressure and temperature of the autoclave chamber. This method is majorly utilized to produce the doped and co-doped HAp crystals. In addition, various researchers have also utilized hydrothermal coating of HAp over metallic implants [12, 74] for various biomedical applications [75-79].

2.2.2.4 Surfactant Assisted technique

Surfactants are used to produce the HAp for majorly two reasons. First, to direct the morphology of the material, and second to prevent the aggregation of the nanomaterials. In this process, the concentration of surfactants at their respective Critical Micellar Concentrations (CMC) values governs the morphology of the HAp NPs. At CMC, surfactant forms micelles, and spherical nanoparticles (NPs) are produced as the precipitated particles are entrapped within the surfactant micelles. The concentration below and above CMC provides rod-shaped and elongated morphologies than that of spherical morphology. In brief, first, the precursors are mixed with the desired surfactant concentration to form the micelles. This process can be followed by either a

similar process to that of the chemical precipitation process or by other wet methods. The selection of the surfactant is majorly dependant on its stability at high pH values and the melting point of the surfactant. Another benefit of surfactant-based synthesis is to obtain mesoporous and nanoporous materials. Surfactants usually get evaporated while calcinating the HAp samples at elevated temperatures, resulting in the formation of pores within the samples. The homogenous mixing of surfactant results in the mesoporous HAp NPs [80-83].

Among all these chemical methods, the chemical precipitation method is preferred to produce the HAp, as this method requires the least amount of precursors, input of energies, and solvents. In addition, the yield remains higher than that of other methods. Furthermore, the tuning of size and morphology, as per the application, can be governed by simply changing the reaction temperature, titration speed, and aging time.

2.3 Role of elemental doping in HAp

As discussed earlier, the human bone mineral is a non-stoichiometric nanocrystalline apatite with impurities in the form of co-substituted trace elements of Na, Mg, Zn, Sr, K, F, Cl, Si, etc. Hence, the various substitution of ions into the HAp lattice has been attempted, which deviates the lattice parameters, crystal arrangement, and biological responses of the HAp. A few of the examples are listed below;

2.3.1 Lithium doped HAp

Few researchers have used the doping of lithium-ion into the HAp lattice. It was expected that a higher concentration of Li increases the mechanical strength HAp. Li substituted HAp also altered the dielectric properties of HAp cement and hence is majorly recommended for bone and dental implants. However, due to gamma irradiation, a lower concentration of lithium doped HAp is suggested for the patient who undergoes radiation examinations with gamma rays [84, 85].

2.3.2 Selenium doped HAp

Selenium deficiency can cause various ill conditions, majorly cancer [86]. The doping of Se into the HAp matrix alters the charge distribution at the material surface and thus enhances the loading efficiency of the HAp for its usage as a drug delivery vehicle. An increase in loading efficiency from 34.1 % to 41.7 % was obtained after Se doping. Se doped HAp has been utilized as a potential

lysozyme delivery vehicle [87]. Besides this, the excellent antitumor activity of the Se doped HAp was also examined [88]. The study revealed that 10 % doping of Se into the Hap matrix was sufficient to degrade the osteosarcoma cells. The synthesized material was presumed to be the pH-responsive material for anticancerous activity.

2.3.3 Aluminum doped HAp

Aluminum is the trace elements found in hard tissues and has been reported to be a disease inducer at elevated concentrations [89]. Doping of Al into HAp decreases the size as well as crystallinity of HAp. It distorts the vicinity and integrity of the crystal at the site of doping [90], which consequently increases the calcium deficiency in the HAp crystal, and thus, the Ca/P ratio alters. However, low cytotoxicity can be implemented at Al doping. It was reported that a lower concentration of Al, *i.e.,* 1 mg mL^{-1} of HAp crystal, did not cause any cytotoxicity [91].

2.3.4 Zirconium doped HAp

Zirconium is generally utilized for its mechanical strength. Although the intrinsic doping of Zr into the HAp matrix enhances the mechanical property, osteogenicity remains very low. Various researchers have tried to co-dope Zr with other elements such as Ca, Mg, Sr, Zn, etc. Ca-Zr doped HAp showed enhanced osteogenic activity [92]. Other elements, when co-doped with Zr, showed enhanced mechanical and biological properties and did not alter the basic phase configuration of HAp crystal. An increment in compressive strength of Zr doped HAp was found to be 850 MPa which was higher than that of pure HAp, *i.e.,* 300-600 MPa. [93].

2.3.5 Silver doped HAp

Silver nanoparticles are a well-known antimicrobial agent. Ag NPs are found in trace concentration in the human body and are utilized as a nutrient element in hard and some soft tissues. In addition, silver is used to stimulate the immune system in the body. Silver readily reacts with the body's protein, amino acids, and free anions [94]. Silver composites have shown excellent antimicrobial activity [95], and hence doping of Ag NPs generally results in the antimicrobial HAp matrix. Various authors have reported doping of Ag into HAp matrix with various applications [23, 96-98]. Doping of Ag into the HAp matrix also enhances the mechanical strength of HAp ceramic without altering the phase behavior of HAp. Hence, HAp doped with Ag is considered as a best-

fit scaffold material for orthopedic applications [97]. Also, Ag-doped HAp has shown better corrosion resistance in the presence of Seminal Body Fluid (SBF) [99].

2.3.6 Magnesium doped HAp

Magnesium is also found as the trace element in the bone as well as other hard tissues and hence is very useful for bone tissue engineering. In addition, Mg is also utilized in more than 300 metabolic reactions in the human body. Mg also serves for normal neural function and supports the maintenance of the immune system. Mg also serves in maintaining the blood glucose level and helps in the production of protein. Similar to that of Zr, doping of Mg into the HAp matrix enhances the crystallinity as well as the mechanical strength of HAp. A lower concentration of Mg doping has shown no toxicity with enhanced mechanical strength from 38 MPa to 72 MPa [100]. In addition, Mg doping enhances the osteoblast activity with optimized degradability and thus enhances bone growth [101].

2.3.7 Iron doped HAp

Iron is an important trace material found in the human body. It serves in the formation of red blood cells. In addition, it is a major part of Hemoglobin. It serves in the transportation of oxygen from the lungs to the rest of the parts of the body. Iron also helps in the conversion of energy from blood sugar. Besides this, iron serves in the normal functionality of the nervous as well as the immune system and takes part in the formation of various metabolic enzymes. Iron-based nanocomposite has been proven for its antibacterial properties [33, 34] and hyperthermia applications [35, 36]. The doping of iron into HAp serves various functions and helps in the vast applications of HAp. Because of its natural magnetic properties, iron serves to magnetically target the HAp at the site of action and hence is very useful in targeted drug delivery through HAp [102]. In addition, doping of iron also serves in making HAp suitable for hyperthermia application for cancer treatment [103]. Fe doped HAp has also been utilized for bone tissue engineering as it enhances the stability of HAp and also provides the dielectric properties to HAp, which is the native property of bones [13].

2.3.8 Zinc doped HAp

Zinc is the native element found in the body. It is found in the bone as well as other hard tissues. It plays a major role in the immune system and serves in cell division and cell growth. Zinc servers various metabolic as well as defense reactions of the human body and precisely works in wound healing and energy conversion. A zinc deficiency has been noticed in Alzheimer's and Parkinson's disease [104]. In addition, zinc also acts as an antidepressant [105]. The incorporation of zinc into the HAp matrix takes place by removing Ca ions from the lattice. An ion-exchange method takes place during this process. ZnO NPs are considered antimicrobial agents, and hence doping of ZnO NPs into HAp serves in the utilization of HAp as an antimicrobial agent with enhanced mechanical properties [19, 106, 107].

2.3.9 Anion doped HAp

Doping of anions in the HAp matrix stabilizes the HAp structure. Generally, fluoride, chloride, and carbonate are substituted in the HAp matrix for various biomedical applications. Unlike cation, anionic doping takes place by the removal of the OH group present in HAp [108]. Carbonated HAp is considered the second most abundant element found in bone apatite after calcium phosphate. In addition, carbonated HAp is considered more bioactive in terms of osteogenesis than pure and synthetic HAp [52]. Similarly, fluoridated HAp has shown better osteogenic activity than that of pure HAp. Fluorine is present in a trace amount in bone and is considered as the promotor for osteogenesis [4]. Chloride substitution provides thermal and electrical stability to the HAp [109].

Various approaches have been tried to change the crystal structure of the HAp lattice to acquire the antibacterial as well as target efficacy with various degrees of success [5], yet no study has been successful in achieving them together. In addition to the metal ion doping, several metal oxides have been tested to be integrated with the HAp lattice to acquire the antibacterial activity, anticancer activity [15] as well as target efficiency, yet no reports are available to acquire them together without harming the HAp phase or the required bioactivity as well as the mechanical properties [16-18]. The selection and concentration of metal ion/metal oxide play a crucial role in delivering the desired phase as well, and the biological responses of the HAp lattice and hence provides an opportunity to tune the biological properties of the HAp to a biomaterial researcher [19]. For example, the ionic radius of zinc (0.074 nm) is smaller than that of calcium (0.099 nm).

Hence, incorporation of zinc into the HAp lattice declined the 'c' lattice parameter and enhanced the 'a' lattice parameter, which decreased the crystallinity of HAp with an increase in the zinc concentration [20, 21]. As HAp does not possess any self-antibacterial activity, the incorporation of metal ions as well as the separate metal oxide phase generation without hampering the HAp phase is one of the major challenges for a biomaterial researcher [23, 24]. Similarly, to achieve target efficiency, HAp has been modified with various metals and biological substances. However, these modifications remain very specific in terms of their applications [3, 22]. Hence, various nanomedicines were scrutinized for their integration with HAp. The detailed discussion is as follows;

2.4 Types of Nanomedicines and their antibacterial mechanism

Various kinds of metals, metal oxides, and organic moieties have been utilized as nanomedicines. Before integrating the nanomedicines with HAp, detailed information about their antibiotic action is required.

2.4.1 Silver Nanoparticles

Silver NPs have been widely utilized for their antibacterial activity. Ag NPs and their composites have been synthesized via various synthesis methods; these methods include the chemical precipitation method [110], a sol-gel technique [111], sonochemical synthesis [112], and microwave-assisted synthesis [113]. However, these methods are widely used for the synthesis of Ag and its composites, but the chemical reaction remains toxic to the environment. Hence, various researchers are working in the direction of the green synthesis of Ag NPs [114, 115]. Ag NPs typically possesses a Faced-Centered-Cubic (FCC) structure [116] with XRD diffraction planes at 38.28 °, 44.40 °, 64.57 °, and 77.48 ° 2θ values [117]. Ag NPs exhibit UV-visible spectral values between 300-400 nm as one of its most characteristic confirmations [117]. It has been proposed that due to their high specific surface area, and surficial electrons, Ag NPs showed higher antibacterial action than that of bulk Ag [118]. The antibacterial activity of Ag NPs depends on their size, size distribution, synthetic methods, and reducing agents and stabilizers [119]. Ag NPs have shown excellent antibacterial properties over a wide range of bacterial strains, including both gram-positive and gram-negative bacteria.

2.4.1.1 Antibacterial mechanism and of Ag NPs

Ag NPs possesses various kinds of antibacterial mechanism to kill the pathogens. These mechanisms include ROS generation through surficial electrons [120] and through the penetration of released Ag ions. However, the antibacterial mechanism varies from one strain to another. The contact-based killing (through Ag ions), and Non-contact killing (ROS), depends on the surface charge over the bacterial strain as well as the Ag NPs. Higher electrostatic interaction leads to the contact-based killing of the bacterial strain, which remains non-specific as compared to the ROS-based mechanism [121]. It has been proposed that Ag NPs can interact with thiol groups of the l-cysteine to inactivate the enzymatic function of various proteins [122]. The Ag NPs majorly create permeable bacterial cell walls, deactivate cellular enzymes, and disrupt the membrane to cause the cell disruption toxic effect to bacteria.

2.4.1.2 Problems associated with Ag NPs

Few of the researchers have reported that few of the bacterial strains have evolved genes to counteract the toxic effect of Ag ions and have shown their resistance towards it [123]. Recently, Panacek *et al.* reported that *Escherichia coli* 013, *Pseudomonas aeruginosa* CCM 3955, and *E. coli* CCM 3954 generated resistance towards Ag NPs via producing flagellin, an adhesive flagellum protein, which causes the aggregation in Ag NPs, which could eliminate the antibacterial activity of Ag NPs [124]. The situation is highly critical, as this resistance was generated without any genetic modification, and only physical changes could be able to surpass the antibiotic activity. The aggregation of Ag NPs can act against all antibacterial mechanisms, including contact inhibition as well as ROS generation, as all these activities depend on surficial properties and bio-interfacial interactions. Hence, researchers should focus on more precise synthesis techniques to synthesize Ag NPs, which could produce non-aggregated NPs to fight against superbugs. In addition, Ag NPs have also shown cyto-toxic effect over human cells as well. These cytotoxic effects remain dose and size dependent. Hence, researchers are working towards controlling the specificity of the Ag NPs for their effective clinical actions.

2.4.2 Zinc Oxide (ZnO) NPs

Various researchers have explained the use of ZnO NPs as a potential nanoantibiotic. ZnO is an (II-VI) type of semiconductor, which is being utilized in various semi-conducting applications. ZnO NPs are believed to be stable under harsh processing conditions and show selective antibacterial activity due to their positive surface charge at physiological pH. Our group has discussed the structural as well as the physical properties of ZnO previously [19]. ZnO NPs are believed to carry high antibacterial activity with a minimal toxic effect on human and animal cells. In addition, Zn is cheaper than Ag, Au, and Ti. A typical ZnO possesses a hexagonal wurtzite structure and P63/m symmetry with the diffraction at 31.9°. 34.7°, 36.2°, 47.6°, 56.6°, 63.1°, 67.9°, and 69.0° '2θ' values. A typical ZnO structure reflects characteristic peaks at 436cm^{-1} in the Raman spectra and FTIR spectra for the Zn-O bond. ZnO NPs can be synthesized via any chemical or physical route. The most widely used methods are co-precipitation [125], sol-gel method [126], ultrasonication [127], microwave-assisted synthesis [128], and polyol method [129]. However, for commercialized applications of ZnO NPs, various researchers are working towards the biogenic synthesis of ZnO NPs [130]. In addition to its antibacterial activity, ZnO has also been utilized for its antifungal [131] as well as anti-cancerous activity [132]. It is believed that the antibacterial activity of ZnO NPs remains dependent on their size and morphology [133].

2.4.2.1 Antibacterial mechanism of ZnO NPs

Various researchers have explained three different antibacterial mechanisms of ZnO NPs. Few of the literature indicates that ZnO NPs possess high specific surface area and discrete bandgap. Such a small surface area enhances the contact between NPs and the bacterial cell. As described previously, ZnO NPs carry a positive surface charge at physiological pH, which helps in the electrostatic contact between bacteria and ZnO NPs. Higher surface area enhances the contact points between them, resulting in the accumulation of higher NPs at the bacterial surface. Interfacial interaction between the bacterial cell and ZnO NPs plays a crucial role in the antibacterial activity of ZnO NPs. This interaction also causes the selectivity of ZnO NPs. After accumulation at the bacterial surface, ZnO NPs show majorly three distinct ways to kill the bacterial cells. 1) ROS generation; ZnO NPs, due to their discrete bandgap, carry a higher number of electrons at their surface, which reacts with the intermediates of the metabolic pathways and the surrounding environment and gives rise to the hydrogen peroxide, hydroxyl radicals, and

superoxide anions. Radical causes the disruption and changes in the bacterial cell wall to kill the bacterial cell. Various reports have suggested the altered permeability as well as the morphology of the bacterial cell wall after incubating with ZnO NPs [134]. 2) Cell wall rupturing: Electrostatic interaction between ZnO NPs and the bacterial cell also causes damage in the bacterial cell wall due to the crystal defects of ZnO NPs [19]. 3) Internalization of ZnO NPs: after accumulating at the surface of the bacteria, ZnO NPs, due to their small size, get accumulated inside the bacterial cell, which in turn release more amount of Zn^{2+} ions. These Zn^{2+} ions disrupt the bacterial DNA as well as the protein to inactivate the bacterial cells [125]. The antibacterial mechanism of the ZnO NPs is given in Figure 2.2. In addition to all the above-stated mechanisms, ZnO NPs may cause death to bacterial cells via oxidative stress and Zn toxicity as well. After the internalization of Zn^{2+} ions, more amount of ROS is generated, which causes oxidative stress inside the bacterial cell. Also, a high amount of accumulated ZnO NPs at bacterial surfaces releases more Zn^{2+} ions. Higher concentrations of Zn^{2+} ions cause malfunctioning of the metalloproteins of the bacterial cell wall, which in turn allows the accumulation of more Zn^{2+} ions, which causes toxicity to bacterial cells.

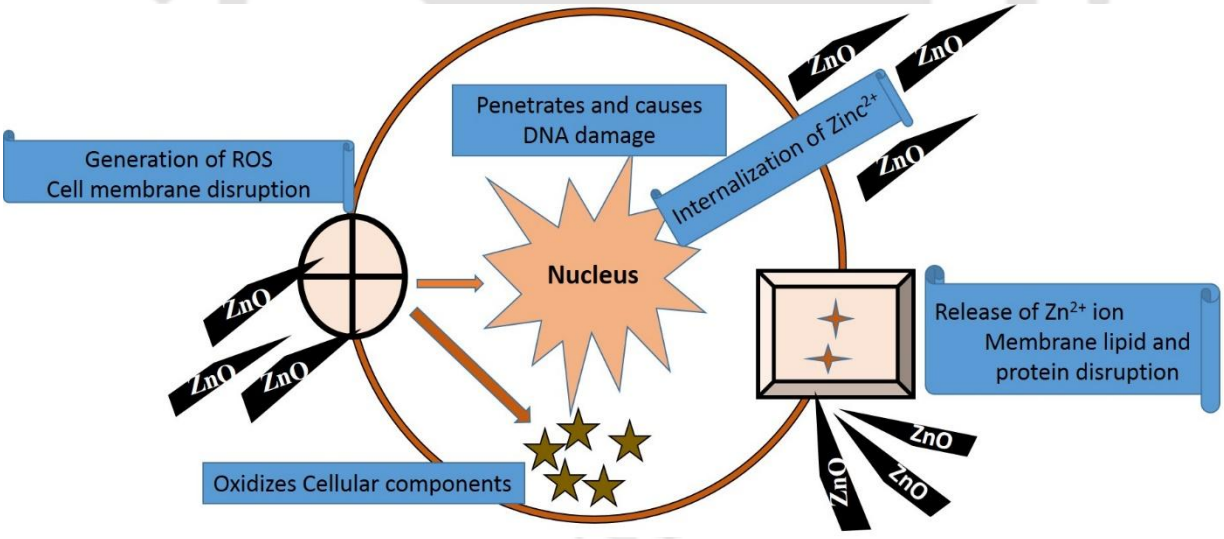

Figure 2.2. Antibacterial mechanisms of ZnO NPs

2.4.2.2 Problems associated with ZnO NPs

ZnO NPs are believed to carry effective antibacterial applications. However, their main antibacterial mechanism is due to their photocatalytic activity. The photocatalytic activity requires

the addition of sunlight/UV light to excite the electron from the valance band to the conduction band for ROS production. It is difficult to obtain photocatalytic activity of ZnO NPs during *in-vivo* applications as well as for clinical applications. Such kinds of applications can only be utilized for clinical applications for the sterilization of medical equipment. Another drawback of ZnO NPs is the solubility of these NPs. ZnO NPs are poorly soluble in water, which interrupts the direct use of ZnO as a nanoantibiotic. In addition, the cytotoxic behavior of ZnO is still unknown. A recent study explained that the toxic behavior of ZnO is not only because of the Zn^{2+} ions [135]. Hence, it can be concluded that the toxic behavior of ZnO NPs is majorly due to their ROS generation ability at the nanoscale. However, the lower surface area produces a high amount of ROS at the site of action, which consequently may cause a detrimental effect on the human cells as well. Hence, nano-cytotoxicity of ZnO is still required to be studied for its long-term applications. Additionally, Zn^{2+} ions are also believed to cause aggregation in globular proteins [136], which eventually may cause other side effects to the animal body, leading to questionable medical applications.

However, ZnO NPs possesses a broad spectrum of antibacterial activity as well as all the required antibacterial mechanism. Various researches are under investigation to enhance the antibacterial efficacy as well as the removal of the discussed lags of the ZnO lattice. A few of the recent advances of ZnO NPs are discussed in Table 2.3.

Table 2.3. Recent advances in ZnO NPs as nanomedicine

S. No	Metal	Synthesis method (temp)	Morphology	Size	Organism and MIC		Ref.
1	ZnO	Precipitation method using *Monsonia burkeana* plant extract	hexagonal wurtzite	5 to 15 nm	*Escherichia coli*, *Pseudomonas aeruginosa*, *Staphylococcus aureus* and *Enterococcus faecalis*	NA	[137]
2	ZnO	Precipitation method using	Hexagonal	16 nm (callus), 22	*Staphylococcus aureus*,	NA	[138]

		Verbascum thapsus extract (leaf, aerial and callus)		nm (leaf), 24 nm (aerial part)	*Streptococcus pneumoniae, Klebsiella pneumonia* and *E. coli*		
3	ZnO	Precipitation method using *Penicillium chrysogenum* MF318506 strain	Hexagonal	9 to 35 nm	*Staphylococcus aureus*	2 mg/mL	[139]
					Bacillus subtilis	3 mg/mL	
					Pseudomonas aeruginosa	2 mg/mL	
					Escherichia coli	2 mg/mL	
					Salmonella typhimurium	3 mg/mL	
4	ZnO	Precipitation method using *Tecoma stans* leaf extract (60°C)	Triangular	20.42 nm	*Achromobacter spanius*	NA	[140]
					Acinetobacter johnsonii		
					Achromobacter xylosoxidans		
					Chromobacterium pseudoviolaceum		
					Bacillus cereus		
5	ZnO	Precipitation method using *Saponaria officinalis* leaves extract (35°C)	Spherical	20 to 80 nm	*P. aeruginosa*	206.1 μg/mL	[141]
					Escherichia coli	61.30 μg/mL	
					B. subtilis	14.50 μg/mL	

					S. aureus	14.46 *μ*g/mL	
					A. baumannii	86.21 *μ*g/mL	
					C. albicans	0.098 *μ*g/mL	
6	ZnO	Biogenic synthesis using *Artemisia pallens* plant extract	Crystalline and Hexagonal	50 to 100 nm	*Bacillus subtilis,*	62.5 µg/ml	[142]
					Staphylococcus aureus	31.25 µg/ml	
					Eschercia coli	62.5 µg/ml	
7	ZnO	Precipitation method using zinc acetate dihydrate to form ZnO/Chitosan nanocomposites (90 °C)	Nanorods	200 to 300 nm diameter and 2 to 3 µm length	*Brevibacterium lactofermentum*	NA	[143]
					Escherichia coli		
					Corynobacterium glutamicum		
8	Ag-doped ZnO	Biogenic synthesis using *Moringa oleifera* plant extract	Crystalline	54.1 nm (Scherrer method) and 36.187 nm (Williamson-Hall method)	*Staphylococcus aureus*	NA	[144]
					Escherichia coli		
					Pseudomonas aeruginosa		
					Salmonella typhi		
					Klebsiella pneumonia		

9	A-Bismuth ZnO	Ultrasound assisted chemical precipitation	Monoclinic and hexagonal	4 to 5 µm breadth and 10 to 11 µm length	*S. aureus.*	0.05 mg/L	[145]
10	Fe-Cu-ZnO	Chemical precipitation	Hexagons and spheres	100 nm to 2 mm and 0.4 to 0.5 nm	*Xanthomonas campestris* *Pseudomonas aeruginosa* *Pseudomonas fluorescens*	NA	[146]
11	Pb substituted ZnO	Co-precipitation method	Hexagonal and Spindle	5- to 110 nm	*Salmonella typhi* *Klebsiella pneumonia* *Vibrio cholera*		[147]
12	Hybrid g-C_3N_4/ Cr-ZnO	Co-precipitation method	Heterostructures (Cr-ZnO hexagonal and g- C_3N_4 nanosheets)	10 to 12 nm Cr-ZnO	*Escherichia coli* *Bacillus subtilis* *Staphylococcus aureus* *Streptococcus salivarius*	NA	[148]
13	Nd(OH)3-ZnO	Co-precipitation method	Hexagonal	32 nm	*Escherichia coli* *S. aureus*	NA	[149]
14	ZnO	Biogenic synthesis using *Justicia procumbense* plant extract	Hexagonal	5 to 15 nm	*Escherichia coli* *Staphylococcus aureus* *Pseudomonas auriginosa*	NA	[150]
15	N-succinyl	Co-precipitation	Spherical	40 nm	*Staphylococcus aureus*	10 µg/ml	[151]

	chitosan-ZnO	and chemical modification			*Escherichia coli*	5 µg/ml	
16	ZnO	*Periconium sp.* extract mediated sol-gel synthesis	hexagonal wurtzite	40 nm	*Staphylococcus aureus*	50 µg/ml	[152]
					Escherichia coli	50 µg/ml	
17	ZnO	Sol-gel method	hexagonal wurtzite	10 to 20 nm	*Escherichia coli*		[153]
					Staphylococcus aureus		
					Bacillus subtilis		
18	Cr doped ZnO	Co-precipitation method	hexagonal wurtzite	22.15 nm	*K. pneumoniae*	100 µg/ml	[154]
					Pseudomonas aeruginosa	100 µg/ml	
19	ZnO	Biogenic synthesis and sol-gel method using *Azadirachta Indica* leaf extract	hexagonal wurtzite	25.97 nm (biosynthesis) and 33.20 nm (sol-gel)	*Escherichia coli*	NA	[155]
20	Cu_2O-ZnO	Sol-gel method (calcination at 500°C)	Spherical	10 to 60 nm	*Staphylococcus aureus*	0.16 ng/mL	[156]
					Escherichia coli	1.25 mg/mL	

2.4.2.2 Effect of Zinc integration to HAp over Mechanical properties and microstructure

As mentioned earlier, HAp possesses high brittleness and lower fracture toughness. The bio-apatites have better biological and indentation properties than HAp under physiological conditions. This prompts various researchers to focus on the substitution of HAp with various metal ions, which subsequently can improve these lags for biomedical applications. The incorporation of Zn enhanced the mechanical properties of HAp [157]. These substitutions revised the lattice parameters, which altered the crystallinity as well as the physical properties of HAp [158]. Incorporation of zinc into the HAp lattice declined the c lattice parameter and enhanced the lattice parameter, which decreased the crystallinity of HAp with an increase in the zinc concentration [20, 21]. Zn doped HAp shows different mechanical behavior due to two reasons: first, the difference in the size of Zn and Ca, and second the different melting temperatures of Ca and Zn, *i.e.*, 842 °C and 419.5 °C, respectively. Various studies are ongoing to reduce the formation of β-TCP in the HAp doped with zinc. In this contrast, Huang *et al.* (2016) co-doped Zn^{2+} ions with F^{-} ions, and co-doping inhibited the formation of β-TCP phases at 200 ºC. It was concluded that the mechanical and chemical stability of co-doped HAp is higher than that of pure HAp at physiological conditions [159]. However, doping of Zn^{2+} ions and integration of ZnO with the HAp have different effects on the crystal structure of HAp, which imparts different physical, chemical, mechanical and biological responses to the HAp.

Summarily, we can conclude that the doping of zinc alone does not play a role in the generation of other phases such as β-TCP. Zn doped HAp, when sintered at a higher temperature such as 900 ºC, showed the other phases. Iconaru *et al.* 2017 sintered the Zn doped HAp at 500 ºC, and Ran *et al.* 2017 did not sinter the composite. The major phase as HAp along with the dopant phase was observed in both the studies, with a reduction in 'c' lattice parameter, indicating that only zinc doping does not disperse the HAp into other phases. However, sintering temperature also plays an important role in the HAp phase generation during synthesis.

2.4.3 Copper (Cu), and CuO NPs

Cu NPs are another widely studied and utilized NPs for antibacterial actions. Cu^{2+} ions-based toxic effects towards bacterial cells have been utilized in various laboratories. In general, CuSO4 solution is utilized in a CO_2 incubator and water bath to check bacterial contaminations. CuO is one of the most promising nanoantibiotic and is being utilized in various other applications such

as magnetic storage, solar cells, electronics, and catalytic activities [160]. Like other metals and metal oxides, CuO and Cu NPs can also be synthesized through various above-given synthesis methods, including precipitation [161], sol-gel method [162], ultra-sonication [160], and microwave-assisted synthesis [163]. However, recently, the green synthesis of these NPs has been under investigation due to the harsh effect and more input of the energy for the synthesis. The biosynthesis of CuO and Cu NPs has been proven to be the best fit method for commercial synthesis due to their non-toxic effect as well as less waste production [164]. Cu NPs generally carry an FCC structure, with diffraction peaks at 43.2°, 50.3°, and 73.9° 2θ values. Similarly, CuO reflects a monoclinic crystalline phase [165].

2.4.3.1 Antibacterial mechanism of Cu and CuO NPs

Various researchers investigated the antibacterial action of Cu and Cu-based nanocomposites for their clinical applications. Majorly, Cu and CuO possess two bactericidal actions. These methods include oxidative stress caused by the generation of ROS [160], which attributes to its higher surface area and lowered bandgap. A small bandgap causes the requirement of less energy to excite an electron from the valance band to the conduction band of NPs; these electrons react with the metabolic oxygen to generate the ROS, leaving a hole (positive charge) in the valance band. The process continues to stabilize the crystal by attaining a zero-valent structure. This continuous process causes a high amount of ROS generation, which surpasses the enzymatic activity of the bacteria to fight against ROS, resulting in the death of the bacteria. Another antibacterial activity of Cu and CuO-based alloys include the release of the toxic Cu ion, which causes structural changes in the bacterial cell wall, resulting in false permeability. This malfunctioned permeability of the bacterial cell wall causes the outflow of the cytoplasm, which in turn causes cell disruption [166]. Another study reported that Cu and CuO-based nanocomposites, due to their smaller size, can get internalized to the bacterial cell and release higher amounts of Cu ions. These Cu ions interact and disrupt plasmid pUC19 DNA to cause bacterial cell disruption [167].

2.4.3.2 Problems associated with Cu and CuO NPs

Copper and copper-based nanocomposites and alloys are very prone to corrosion. The disability of Cu to fight against corrosion is one of the major drawbacks of Cu to be utilized in biomedical applications. Liu *et al.* found that Cu-bearing stainless steel was worse resistant to corrosion in the

presence of sulfate-reducing bacteria [168], which indicates that the addition of Cu may also not only introduce the antibacterial activity but also ca reduce the corrosion resistance. This indicates the low-spectrum antibacterial activity of Cu. Furthermore, metal-contaminated soils are considered as one of the major sources of metal-resistant bacteria, which can cause damage to the fertility of the soil, as well as the contamination to the crop as well. In early 2005, Berg *et al.* isolated twenty-five gram-negative bacteria from Cu enriched soil. However, the number of gram-positive Cu-resistant bacteria was lower. In addition, the Cu resistant bacteria were also found to be resistant to chloramphenicol and other two antibiotics, which hints that Cu resistance may give rise to bacterial resistance to other antibiotics as well [169]. The situation remains highly critical, as this may cause severe harmful effects if Cu is being used for prolonged treatment. Another study revealed that modified bacteria are already have existing protein structures to generate resistance against Cu [170]. Hence, Cu-based nanoantibiotics cannot be utilized for prolonged action, for example, in the case of osteomyelitis, where regular incubation of antibiotics is required. Another drawback of Cu and Cu-based composites is their toxic effect on human cells as well. A study explained that Cu could catalyze a Fenton-like reaction that causes lipid peroxidation as well as lead to protein damage [170]. Hence, elevated Cu concentrations may damage human cells as well as protein. All these studies together question the clinical application of Cu as a potential nanoantibiotic.

2.4.4 Titanium dioxide (TiO_2) NPs

TiO_2 is also one of the most studied nanoantibiotic because of its well-known photocatalytic activity. TiO_2 is majorly used as a semiconductor and a photocatalyst. TiO_2 NPs exhibit strong bactericidal activity with near-UV light and UVA. The MIC of TiO_2 varies from 100 to 1000 ppm, depending on its size as well as the light source. The major property, which makes TiO_2 a strong candidate to be utilized as a nanoantibiotic, is its antibacterial activity under visible light itself. TiO_2, like other NPs, can also be synthesized through various chemical and physical methods. Major routes include the precipitation method [171], sol-gel technique ultrasonic [172], microwave [173], hydrothermal, and ionothermal methods. However, various researchers have also utilized green routes for the synthesis of TiO_2 NPs. TiO_2 NPs possess anatase phase with a space group of I41/and) or rutile phase with space group P42/mnm). Although TiO_2 NPs possess a wide bandgap,

which restricts their usage under UV light only, researchers are focusing on metal-doped TiO_2 NPs for their usage under visible light [174].

2.4.4.1 Antibacterial mechanism of TiO_2 NPs

As demonstrated earlier, TiO_2 NPs majorly reflect its antibacterial mechanism via photocatalytic activity due to the wide-bandgap. Various researchers have explained the photo-gradation of bacterial species under different conditions. Yadav *et al.* 2016, reviewed the photocatalytic mechanism of TiO_2 NPs. It was explained that, under UV light, the TiO_2 semiconductor gets excited and generates a positively charged hole in the valance band and a negatively charged electron in the conduction band. The UV light brings the excitation because of carrying higher energy than that of the bandgap energy. These holes are then filled by the adjacent molecule, and the free electron moves out. This free electron remains mobile and carries high reducing ability, which in turn generates the ROS species, which is responsible for rupturing the bacterial cell wall, causing cell disruption [175]. Long *et al.* 2014, explained the antibacterial action of TiO_2 NPs under the influence of UV light. Two bacterial species *Salmonella* and *Listeria*, were tested. The study explained a sequential killing of the bacterial species starting from the bacterial cell wall. It was observed that TiO_2 NPs ruptured the bacterial cell by disrupting the outer cell wall, followed by rupturing the inner membrane and peptidoglycan. Ultimately, the cell lost its integrity, and cellular substances were moved out, causing the complete removal of the bacterial cell [176]. In a similar way, Ma *et al.* 2015 explained the photo-degradation of *E.coli* and *S. aureus* using Fe_3O_4-TiO_2 nanosheets under solar light. It was explained that the nanosheets exhibited an excellent antibacterial action via different mechanisms over gram-positive and gram-negative bacterial cells. The Fe_3O_4-TiO_2 nanosheets possessed more separation of the electron-hole pair, which in turn enhanced the generation of ROS. The mechanism proposed by the authors elucidated that the rupturing in the cell wall and the cell bodies of *E.coli* was the main antibacterial mechanism, whereas adsorption of bacterial clusters over Fe_3O_4-TiO_2 nanosheets caused the malfunctioning in the permeability of the bacterial cell wall, which ultimately destroyed *S. aureus* [177]. These studies revealed that TiO_2 possesses different antibacterial actions against a wide variety of bacteria. The band-gap, which is solely responsible for the disruption of the cell wall, can be tuned by modulating the crystal structure of the TiO_2, thus, providing the choice of designing target-specific nanoantibiotics.

2.4.4.2 Problems associated with TiO_2 NPs

As previously explained in section 5B(ii), it is difficult to obtain the antibacterial activity of an NP based on photo-catalysis for its practical applications. TiO_2 has shown excellent antibacterial activity under the influence of UV/visible light, which remains a major drawback of these NPs to be utilized in biomedical industries. Moreover, these NPs produce excessive amounts of ROS, which is found to be lethal for human cells as well as after a certain concentration. In this regard, Zhang *et al.* 2019, explained the toxicity of the TiO_2 NPs due to excessive ROS production through dermal exposure and its relation with cardiac malfunctions. It was revealed that exposure to TiO_2 enhanced the increase in the ROS as well as the 8-hydroxy-2'-deoxyguanosine, thus indicating excessive oxidative stress in the dermal cells. In addition, the inflammatory biomarkers were also enhanced under increased ROS concentrations. These biomarkers include IgE, intercellular adhesion molecule-1, interleukin-8, and hypersensitive C-reactive protein. These results indicated that a higher ROS concentration might bring cell apoptosis as well. It was also studied that via oxidative stress-induced inflammation and cytotoxicity; dermal exposure brought the cardiac dysfunction s well in the Balb/c mice. However, it was found that antioxidants, such as Vitamin E, may reduce the side effects of TiO_2 NPs [178]. Various studies revealed the accumulation of nano-TiO_2 in macrophages. Hence, it is necessary to study the effect of TiO_2 NPs over macrophages. Recently, Brzicova *et al.* 2019 explained various factors, which affect the toxicity of the TiO_2 NPs over macrophages. It was perceived that exposure for a long duration, stable dispersion, and particle size 20-60 nm have more toxic effects as compared to the nonstable dispersion and smaller particle size. It was also explained that the toxicity of the TiO_2 NPs remains unchanged with respect to their shape and morphology. However, these results indicate the toxic effect of TiO_2 but also provide the criteria for selection of the TiO_2 NPs, based on its size and the exposure time to reduce its cytotoxic effect [179]. Similarly, Andreoli *et al*. 2018, explained the significant increase in 8-oxo-7,8-dihydro-2′-deoxyguanosine (a product of DNA oxidation) and the breakage of the DNA strands by the exposure of the TiO_2 NPs in the peripheral blood mononuclear cells. The probable reason for the cytotoxicity as well as the genotoxicity of the TiO_2 NPs was found to be caused by excessive ROS generation at the surface of the cells, which was covered by NPs after exposure [180]. All these cytotoxic effects over different cell types restrict the potent usage of TiO_2 NPs at a commercial scale.

2.4.5 Antimicrobial peptoids

Poly-(*N*-substituted glycine) "peptoids" are structural isomers of peptides, with the only difference between them being the attachment position of the functional sidechain for *e.g.,* poly(N-(2-methoxyethyl) glycine). These are located on the backbone α-carbon in peptides while they are instead located at the α-nitrogen in peptoids. This rearrangement is not recognized in nature and accounts for the protease resistance of the peptoids [181]. Functional group attachment at the amide group also removes chirality and hydrogen-bond (H-bond) donors from the peptoid backbone, promoting increased backbone conformation flexibility while enabling a versatile synthetic route (the "submonomer" method) to install a diverse array of commercially available sidechains [182]. The conformational flexibility and lack of intra- and inter-backbone H-bonding also increase thermal processability and solubility in common solvents [181, 183]. Overall, the combination of biomimetic properties, resistance to enzymatic degradation, and material processability make peptoids a potential candidate for various biomedical as well as technological applications [181, 182, 184].

2.4.5.1 Antimicrobial mechanism of peptoids

The exact antibacterial mechanism of the peptoids is still unclear. However, it is believed that peptoids mimic the peptides in their antibacterial action [185], hence can cause the rupturing in the cell wall of the bacteria by interacting with it [186]. However, the mode of interaction is debatable. In broad terms, it can be concluded that the antibacterial action of the peptoids remains dependent on their peptoid length, orientation charge, and cationic/hydrophobic ratios [187]. Hence, further studies are required to explore the possible antimicrobial mechanism of the peptoids.

2.4.5.2 Problems associated with antimicrobial peptoids

A plethora of antimicrobial peptides occurs in nature, but their susceptibility to enzymatic degradation has hindered their application. Hence, peptoids, which are resistant to proteolysis, are considered a plausible molecular platform for the development of novel antimicrobial agents [188-193]. However, the cytotoxic effects of current antimicrobial peptoids, as well as the general problem of rising antimicrobial resistance with the environmental release of antimicrobials, remain

untouched. The application routes, methods to integrate with inorganic moieties, as well as the synergistic effect over the material properties are still understudies

Based on the given nanomedicines, ZnO NPs were selected because of their non-resistance for bacteria, a broad spectrum of antibacterial activity and mechanism, abundance in nature as well as the ease of synthesis to be integrated with the HAp lattice to incorporate the antibacterial activity to the HAp lattice. Along with the ZnO NPs, Fe was selected to co-integrate the magnetic targeting to the HAp lattice for various biomedical applications.

2.5 Biomedical applications of HAp

As discussed earlier, HAp possesses chemical and biological similarities with bone, has higher mechanical strength, and is the most studied bioceramic for hard tissue treatments and regenerations. Hence, HAp is majorly utilized for BTE applications. In addition, due to its high mechanical strength, bioactivity, and stability, HAp has also been utilized for dental applications [194, 195]. Nevertheless, the required bioactivity, biodegradation, and mimicking of exact mechanical strength to that of bone have been the major challenges for biomaterial researchers. Hence, diverse studies have been performed to alter the crystal lattice of the HAp by doping the transition metal ions or by compositing the HAp lattice with other metal oxides and polymers. Each substitution has provided different add-on properties to HAp for a diverse range of applications. A few of the alterations of the HAp lattice are listed in Table 2.4. Based on these alterations, miscellaneous applications of HAp have been scrutinized. Typically, HAp has been produced as doped HAp, inorganic-organic hybrid, and biphasic HAp for various applications. In order to obtain the desired property, metal ions with ionic radii less than Ca are selected, as it decreases the particle size of HAp and results in reduced lattice properties for biomedical applications. In addition, the integration of lanthanides and actinides into the HAp matrix provides the dual functionality of diagnosing and treatment via incorporating the bio-imaging properties to the HAp NPs.

Table 2.4. Recent advances in Hydroxyapatite and its composites for biomedical applications

S.No	Hydroxyapatite and other metals	Size (nm)	Morphology	Applications	References
1.	HAp and Chitosan	49.79 ± 20.90	Round shape	Scaffold for bone tissue engineering	[41]
2.	Yttrium and strontium co-substituted nano-hydroxyapatite	60 to 84 And 64-120 for agglomerates	Spherical	Biomedical Applications (Load Bearing Applications)	[70]
3.	HAp	At pH 7- 44 At pH 11- 10	At pH 7 rectangular shaped At pH 11 infantile particles	Tailoring of particle size and morphology	[73]
4.	HAp	55-69	Rod-shaped to stubby shaped	Tailoring of particle size and morphology	[75]
5.	Gd^{3+}, Eu^{3+} doped HAp	Pure HAp 42.7 ± 6.3 nm, Gd doped HAp 40.22 ± 4.7 nm, and Eu doped Hap 38.14 ± 8.5 nm	Spherical	Biomedical imaging and therapeutic applications	[196]
6.	Ag/Zn doped HAp	18 ± 2 for powder	NA	Antimicrobial surfaces	[197]

		15± 2 for coatings			
7.	Ag-doped HAp	22-23 nm	Rod-shaped	Antimicrobial surfaces	[198]
8.	Graphene doped HAp	25-115 nm	Particulate shaped	Dielectric and ferroelectric Biomedical applications	[199]
9.	Lanthanum-doped hydroxyapatite	50-150 nm	Plate-shaped	Bone Regeneration	[200]
10.	Ce doped HAp	40–60 nm	Rod-shaped	Biomedical application	[201]
11.	Cu/Ag-doped HAp	20-57 nm	Rod-shaped	Nanomedicine	[202]
12.	Co-doped Hyaluronan-directed HAp	diameter: 32 ± 11 nm length: 138 ± 26 nm	Rod-shaped	Tumor specific bio-imaging	[203]
13.	Se doped HAp	<200 nm	Multi-walled sphere	Bone scaffold	[204]
14.	Sm doped HAp	17-19 nm	Rod-shaped	Antibacterial and antifungal	[205]
15.	Er-doped HAp	<100 nm	Spherical and near elongated	Diagnosis and Bio-imaging	[2]
16.	Cu doped HAp	Length 73 ± 8 nm; Width 25 ± 6 nm	Rod-shaped	Drug delivery	[206]

17.	Pt-loaded, Se doped HAp	156-256 nm	Particulate shaped	Treatment of breast and prostate cancer	[207]
18.	Ce doped HAp	Length ~100 nm; Width ~20 nm	Needle-like	As bright phosphor	[208]
19.	Ce doped HAp	12 nm	Needle-like	Biomedical Applications	[209]
20.	Fe (III) doped HAp	< 100 nm	Round shaped	Triple-negative breast cancer monitoring	[210]

2.5.1 Hydroxyapatite in bone tissue engineering

HAp and its composites have widely been used for bone tissue engineering in their direct powdered form. HAp is used either as a matrix for bone tissue engineering or as a filler for the treatment of osteoporosis. In recent studies, various composites of HAp are being tested for bone repair or obtaining the required osteogenesis by enhancing its bioactivity. As discussed before, the size and the morphology of material play a pivotal role in the biological responses of that material. The size of NPs remains a tunable property, depending on the route of synthesis and its parameters. Hence, several studies have been performed to observe the size-based biological responses as well as the physical and mechanical behavior of the nano-HAp lattice. Recently, Indra *et al.* studied the effect of size over the physical and mechanical behavior of the HAp bioceramic. For this purpose, the authors mixed the 2.5 µm size of HAp with the 200 nm of HAp itself, ranging up to 20 wt %. The pallets were designed using a uniaxial pressing method by applying a pressure of 200 MPa. The pallets were then sintered at higher temperatures, *i.e.*, 1200 ºC for 2 h. The mechano-testing indicated that the addition of nano-HAp enhanced the mechanical strength of the HAp bioceramic by multiple folds. In detail, at the addition of 20 wt% of nano-sized HAp, the compressive strength was increased from 132.2 MPa to 208.6 MPa without altering the HAp phase. The increase in the compressive strength is believed due to the filling of the micron-sized pores of the macro-HAp by the addition of the nano-sized HAp fillers [211]. This indicates that the doping and/or co-doping

of other transition metal ions may alter the mechanical strength of the HAp bioceramic up to the required level without altering the HAp phase. Similarly, various metal ions have been scrutinized to understand the effect of doping on the mechanical behavior of the HAp matrix. In a recent study, it was seen that the addition of Si, Mg, Zn, Sr alters the mechanical behavior of the chitosan/HAp matrix. The elastic modulus was found to be in the range of Si-CS/HAp > Zn-CS/HAp >Mg-CS/HAp >Sr-CS/HAp >CS/HAp and fracture stress and toughness was found to be in the order of Si-CS/HAp >Sr-CS/HAp>Mg-CS/HAp>Zn-CS/HAp>CS/HAp and Mg-CS/HAp>Sr-CS/HAp>CS/HAp >Si-CS/HAp >Zn-CS/HAp order [212]. The metal ions either replaces the Ca ion from the HAp lattice incorporating the crystal defects or alters the mechanical behavior by working as a strong filler in the mesoporous HAp matrix. This results in the enhanced and tunable physical, chemical and mechanical properties of the HAp matrix.

In addition, the incorporation of various transition metal ions is expected to enhance the other biological responses of HAp due to their native properties and biological characters. For example, Karunakaran *et al.* studied the polyvinylpyrrolidone (PVP)-assisted microwave synthesis of Mg-doped HAp NPs from seashell bio-wastes. The $CaCl_2$ was harvested using HCl-based washing and grinding. Finally, the Mg precursor was mixed with the obtained Ca precursor and was titrated against K_2HPO_4 followed by PVP-based microwave-assisted synthesis to produce the Mg-doped HAp samples. It was found that doping of Mg incorporated a rod-shaped morphology for HAp lattice with a width of 5-20 nm and length of 50-80 nm. The surface area of the NPs was found to be increased with the increase in the Mg concentration from 47.2 to 113 until 1.7 M of Mg concentration. Similarly, the zeta potential was also found to be increased with an increase in Mg concentrations. In terms of biological responses, the cells were viable > 80 % until 250 µg/ml concentration with decent antibacterial activity. However, the cell mortality rate was increased from 2.9 % to 4.1 %, with an increase in Mg concentration from 2.9 % to 7.3 %. Hence, the incorporation of Mg not only governed the size and morphology but also incorporated the antibacterial activity to the HAp lattice [213]. In another approach, Abutalib *et al.* designed Mo-doped hydroxyapatite nanorods via microwave-assisted synthesis. They reported the rod-shaped morphology of 25–70 nm diameter and 25 nm to 200 nm of length. With an increase in the Mo concentration from 0.05-0.5 wt %, the crystallite size was found to be increased from 16 to 30 nm, with an increase in the crystallinity from 0.5 to 0.7 %. The addition of Mo also incorporated the antibacterial activity to the HAp matrix [214]. In addition, multi-elements, *i.e.,* Mg, Zn, Sr, Si-

doped HAp, have also been synthesized. Authors varied the concentration of Sr by 5 % and 10 %. Similar to the previous results, the surface area and the pore size of the HAp were found to be increased with an increase in the dopant concentrations. In addition, the increased dopant concentration inhibits the faster degradation of the HAp matrix via controlling the release of the ions [215]. It can be seen that the transition metals with lower ionic radii than Ca incorporated the lowering in size and resulted in a rod-shaped morphology. In addition, it has also incorporated antibacterial activity into the HAp matrix at elevated concentrations.

2.5.2 Hydroxyapatite in scaffolds

Various polymers have been studied to explore their effect on the native properties of the HAp matrix. Various polymer/HAp composites have been studied with enhanced composite properties for bone tissue engineering and for the differentiation of stem cells to bone cells [216]. Diverse applications of polymer-HAp composites have been studied for bone tissue engineering applications. For example, nano-hydroxyapatite/graphene oxide/chitosan was studied for the treatment of osteosarcoma treatment. The composite achieved 48ºC under 808-nm NIR irradiation and killed the human osteosarcoma cells. It was also observed that hBMSC was promoted for osteogenesis at 42 ± 0.5 ºC, and the post-operative bone volume/tissue volume ratio was found to be 20.36 % within 8 weeks [217]. It is also believed that the addition of polymeric matric to the HAp lattice and vice-versa enhances the biological responses of HAp to the required level. For example, Mobika *et al.* studied the effect of the addition of silk fibroin to the HAp ceramic and studied its biological responses. Authors reported that addition of silk fibroin not only governed the size of the HAp NPs, but also regulated its morphology, with no organic-inorganic phase separation. It was reported that the swelling ratios and the biodegradation was found to be increased with the addition of silk fibroin protein to the HAp matrix. Similarly, bioactivity of the sample was also found to be increased [218]. Another report by Luz *et al.* suggested that the oxidation of bacterial cellulose and its composite with HAp is more bioactive and biodegradable. In brief, bioactivity and biodegradation were found to be the function of the degree of oxidation of bacterial cellulose [219]. Hence, nanocomposites of HAp and natural polymers are of great potential for bone regeneration application. Modification in polymers or in HAp lattice alters the bioactivity, bio-responsivity as well as bio-interfacial interactions of the composite scaffolds.

Various studies have confirmed that after the incorporation of HAp bioceramic, the biological properties enhance with an increase in the HAp concentrations. For example, Kandasamy *et al.* designed a nanocomposite made up of Zn and Mn substituted HAp with Carboxymethyl cellulose (CMC) and (Polyvinyl pyrrolidone (PVP) for bone repair via electrospinning. A random fiber arrangement was obtained with rough surfaces and interconnected pores. The addition of Zn/Mn/HAp introduced more roughness to the obtained fibers at 60 % of its contribution to the whole system. Similarly, polymer solution possessed the viscosity value of 186 ± 3.0 cP, and with increase in ceramic concentration, (60 wt %) (PC60 (Zn-Mn-0.5M) and PC1-60 (Zn=Mn=1M)) obtained higher viscosity 311 ± 2.81 cP and 327 ± 2.45 cP values, respectively. Indicating the role of HAp ceramic in controlling the roughness as well as the viscosity of the fiber solution required for the biological responses of the nanocomposite. In a similar way, an increase in the bioceramic also enhances the porosity of the samples. In brief, the sample containing higher ceramic concentration, *i.e.,* 60 wt %, possessed a higher porosity value of 97.8091 ± 1.19 for PC60 and 98.6870 ± 1.14 for PC1-60. Another advantage of adding Zn/Mn/HAp ceramic to the polymeric matrix was to obtain higher mechanical strengths. The mechanical strength was increased with an increase in the ceramic concentration and was found to be maximum for PC60 and PC1-60 samples. The maximum values obtained were 63.35 ± 2.06 and 65.86 ± 1.81 MPa tensile strength, 1015.73 ± 2.05 and 1149.03 ± 4.15 MPa Young's modulus and 137.35 ± 1.36 and 139.94 ± 1.65 % of elongation at break for PC60 and PC1-60 samples. In addition, for samples PC60 and PC1-60 the biocompatibility was also found to be increased. In detail, within the 15th day, the mineral crystals cover the whole surface after incubating in SBF. In addition, the hemolytic rate was found to be decreased to 2.6 and 2.23 % for PC60 and PC1-60 from 4.4 % of the pure polymeric solution. In addition, the antibacterial activity was also found to be increased with an increase in Zn/Mn/HAp concentration, probably due to the increased Zn and Mn concentration. The study shows that by altering the ceramic concentration, various properties of the nanocomposites can be governed required for bone repair applications [220].

Similarly, *Gan et al.* reported that the addition of the HAp enhances the mechanical strength of the double-crossed network of the physically cross-linked poly (vinyl alcohol)-(nanohydroxyapatite)/(2-hydroxypropyltrimethyl ammonium chloride chitosan) (PVA-HA/HACC-Cit) hydrogels. It was reported that the nano-composite hydrogels possessed excellent mechanical properties, *i.e.,* a fracture tensile stress of 2.70 ± 0.24 MPa, toughness 14.09 ± 2.06

MJ/$m^{3,}$ and compressive modulus of 0.88 ± 0.09 MPa. It was observed that the cytocompatibility of the nano-composite was increased with an increase in the HAp concentration. In addition, a low friction coefficient of 20 mm/s and excellent ear resistance of the nano-composite postulates the designed nanocomposite hydrogels for cartilage repair [221]. The addition of HAp or modified HAp alters the size, morphology, and mechanical behavior of the composite materials to be utilized for bone tissue engineering applications. Studies suggested that the addition of carbonated-HAp to the PVA/Chitosan decreased the diameter of the fiber from 160 nm to 139 nm at 15 wt % of its addition. In addition, Young's modulus and ultimate strength were also found to be increased from 56.01 ± 16.48 to 103.86 ± 37.30 MPa and 5.44 ± 1.89 to 7.49 ± 4.04 MPa, respectively. However, the Elongation of break (%) was decreased from 22.00 ± 8.71 to 12.73 ± 3.77 % at 15 % addition of carbonated-HAp. The swelling ratio and the protein adsorption was also found to be increased from 125.5 ± 17.8 to 208.3 ± 41.7 % and 0.7 ± 0.1 to 1.8 ± 0.1 % respectively [41]. However, the addition of 20 % carbonated-HAp affected these biological properties adversely. Hence, the bioactivity and the biochemical properties of the polymeric-HAp composites can be tuned based on the HAp concentration, and application-specific scaffolds can be designed.

Although majorly HAp based scaffolds have been studied for bone tissue engineering. Nevertheless, researchers have also utilized these scaffolds for various other environmental applications as well. In a study, the HAp matrix was first functionalized with the 3-aminopropyltrimethoxysilane to produce the amino-HAp and was then further cross-linked with the chitosan by using glutaraldehyde as the linker. The nanocomposite was found to achieve the adsorption capacity of 125 mg g^{-1} at 15 min for diclofenac sodium [222]. Scaffolds carrying higher surface area can be utilized for various other environmental cleanup applications such as heavy metal removal, dye degradation, and dye adsorption.

2.5.3 Hydroxyapatite in drug delivery

Increased number of bacterial infection and cancer cases have raised the concern to design the effective drug delivery vehicle. For a long, it has been a challenge for biomedical/ biomaterial researchers to design a cost-effective, biocompatible and biodegradable drug delivery based on site-specific applications. The traditional antibiotics are effective over a range of concentrations and least effective at lesser concentrations and may be toxic at elevated levels [223]. However, these drugs being non-soluble in aqueous media, require a cartridge for their effective delivery at

the site of action. Hence, the delivery of medicine at a particular concentration is essential for its effect or biological responses. In bone infections such as osteomyelitis, a regular dosage of antibiotics is required at the site of infection for a long duration. Hence, it is essential to design such a drug delivery vehicle, which can release the drug in a sustained and controlled manner for its effectiveness. Nanomaterials carry high surface area than their bulk materials and are of great interest in designing the drug delivery vehicle. Nano-HAp being bioceramic possesses two major and essential properties for being applicable as a drug delivery vehicle for various biomedical applications. Firstly, nano-HAp is a bioactive material, its controlled biodegradation rate helps in loading more amount of drug, and the release of the drug can be achieved in controlled kinetics, suitable for the treatment of osteomyelitis. Secondly, HAp is an inorganic bioceramic and hence is stable for the aqueous environment, pH, and temperature variations within the human body. Various types of medicines have been studied to load over nano-HAp for their potential applications. A few of them are discussed herewith.

Chen *et al.* designed a multi-responsive drug delivery system based on mesoporous HAp, Au nanorods, and poly(N-isopropylacrylamide- co-acrylic acid) (PNA). The composite material was found to be pH-responsive due to the presence of mesoporous HAp, and the thermal responsiveness and NIR responsiveness were achieved by the addition of PNA and Au nanorods, respectively. The doxorubicin (DOX) loading capacity was found to be 77.05 ± 11.11 %, with a drug content was 0.18 ± 0.02/10 mg sample. A high DOX loading is expected due to the electrostatic interactions between the HAp and the drug. The nano-composite carried a drug release of 18.15 % within 36 h at a HAp concentration of 46.09 % at room temperature and pH 7.4. In addition, at the cumulative response, *i.e.*, pH 4.5 and NIR irritation, a high drug release rate was observed, and 67.89 % of the drug was released within 6 h [46]. Hence, depending upon the requirement/application, the drug release rate and concentration could be tuned. Such multi-responsive drug release systems are of great applications for the treatment of osteomyelitis. Similarly, Yang *et al.* prepared a Rhein-PEG-nano-HAp composite material for the sustained release of the doxorubicin. A spherical morphology for both nano-HAp (with smooth surfaces) and Rhein-PEG-nano-HAp was achieved with a size less than 100 nm. A 19.68 % of drug loading capacity was observed. At pH 7.4, a total of 50.42 % drug was released as compared to pH 6.8 and 5, as the release was found to be 60.37 % and 85.85 %, respectively. Under different pH intervals, the sustained release of the drug was observed within 360 h [224]. The results showed the long-

term release of the drug, indicating the high potential of its application in the treatment of the bone diseases such as osteosarcoma and osteomyelitis.

In another study, the DOX was loaded over the PLGA NPs followed by their incorporation in the formulated bone cement for a highly localized drug release proficiency. The study elaborates that the loading of DOX also changes the pore size of the bone cement. In brief, the bone cement without DOX carried the largest pore area (0.56 μm^2) as compared to the 40 μM (0.0195 μm^2) and 100 μM (0.0198 μm^2), respectively. In both conditions, around 80 % of the DOX was released within 7 days. However, < 20 % of DOX was released without NPs attaining a plateau within 2–3 days of the incubation. Hence, the study suggests that effective drug delivery can be achieved by loading the drug over polymer and then embedding it within bone cement as compared to the bone cement loaded with the drug [225]. Similarly, Zha *et al.* prepared the Zein/HAp NPs and explored their applications as a drug delivery system. A pH-based drug release was observed with IC_{50} of HAp/Zein-DOX NPs and DOX to be 17.89 and 133.10 μg/ml. This indicates that the efficacy of the DOX is increased by the seven folds after incorporating them into the Zein/HAp nanocomposite than that of pristine DOX solution. After injecting intravenously, the C_{max} value of HAp/Zein-DOX NPs and DOX solution was found to be 8.82 ± 0.53 and 12.66 ± 0.91 mg/ml, respectively, indicating a sustained release of DOX through HAp/Zein-DOX NPs [226].

However, these studies have shown potential application in the treatment of osteosarcoma, yet their commercial applications are still hindered due to the application sustained at the laboratory scales only. Further clinical trials are under investigation for their commercial applicability. However, until the effective delivery of antibiotics is achieved, researchers are working to enhance the drug loading efficiency of the HAp NPs for the better incubation and treatment of osteomyelitis and osteosarcoma. In continuation, Souza *et al*. explored the loading and the release profile of Doxycycline antibiotics from the mesoporous HAp bioceramic as a bone targeting drug delivery system. The loading capacity was found to be 28.2 ± 4.5 mg doxycycline/mg HAp. It was observed that the loading of the drug affected the porosity of the HAp bioceramic. In detail, the pristine HAp retained 26 % ± 5.0) of pores, whereas at 1.5 mg/mL drug loading concentration of drug-enhanced it to 52.0 % ± 2.5. A release of around 20 % was observed within the initial 24 h, followed by a slow and steady drug release. After nine days, 40 % of the total drug concentration was released from the HAp microspheres [44]. These studies revealed that the loading of the drug over the bioceramic enhances their porosity. Similar kind of results can be observed when bioceramics are

composited with the polymeric matrix. Hence, it can be concluded that the mixing of bioceramics with organic/aromatic moieties enhances their porosity, required for various purposes in biomedical applications.

2.5.4 Hydroxyapatite as surface coatings

Metallic implants are entrenched at the site of injury, where the damage is non-self-curable, or the bone has been damaged completely. However, various metallic implants are under study and are being used for various commercial applications; they are usually bio-inert. This bio-inert nature affects the biological responses and the corrosion behavior of metallic implants under hydrophobic/biological environments. In addition, metallic implants are also liable to the infection during and after the implantation and may cause severe detrimental effects on the host health, sometimes may lead to the death of the host body. Hence, the bio researchers are focusing on the modification of the metallic surfaces via various Self Assembled Monolayers (SEMS) [227] or via bioceramics [228] to enhance their bioactivity and biocompatibility. Various techniques have been optimized for the coating of HAp over metallic implants, sorted based on the stability, bioactivity, and biological responses of the bioceramic coatings.

Coating of HAp modifies the mechanical and tribological behavior of the metallic surface, which in turn alters the biological behavior of the metallic alloy. Various studies are under investigation for the coating of biphasic calcium phosphate (BCP) over metallic implants. It was found that 4 h, 6 h, and 8 h of Radio Frequency Sputtering (RF Sputtering) provided the 400 nm, 700 nm, and 1000 nm of the thickness of the BCP coatings over the Ti-6Al-4V surfaces. The thickness of the BCP coatings altered the surface roughness and contact angles from 112–153 nm and 89.6 ± 2° to 61.2º ± 2, respectively. In 1000 nm surface thickness, no cracks were observed at 2.3 N, and no delamination up to the load of 7.8 N could be observed as reflecting the maximum strength of the film coating. The biomineralization was also found to be increased from 44.87 % to 86.7 % after 14 days in the 1000 nm thickening, which is expected to alter the biological responses positively [63].

Alteration in mechanical behavior should positively affect biological responses. Hence, biological characterization is one of the most important studies for these metallic implants. In this regard, Behera *et al.* deposited the BCP over Nd-YAG laser textured Ti-6Al-4V surfaces to enhance the biocompatibility of the metallic surface. It was observed that the simultaneous effect of laser

texturing and BCP coating directly altered the surface wettability. The contact angle of Ti-6Al-4V surfaces was found to be 89º, which was reduced to the range of 71º-77º and was further reduced to the range of 17º-21º after coating with BCP. Similarly, the surface roughness of the bare Ti-6Al-4V was found to be incease4d from 0.94 nm to 0.98-1.84 µm after laser texturing, which was not further affected by the BCP coating. Because of the change in the hydrophobicity and the surface roughness, the protein adsorption was found to be increased from 5.3 to 7.11 µg/cm^2. Additionally, the MG63 cell size was found to be in the range of 50-200 µm, indicating a more number of cells than that of textured surfaces only. Hence, the laser texturing enhanced the surface properties of the Ti-6Al-4V metal, which was further enhanced by the BCP coating [229]. In a similar way, Ti-6Al-4V surfaces were modified with the laser cladding using 100 % HAp and functionally graded TiO_2-HAp material (FGM) to enhance the cytocompatibility as well as the bioactivity of the surfaces. The hydrophobicity of the samples was changed from 91.9° (±1°), 71.3° (±2 °), and 60.6 ° (±2 °) for non-cladded Ti–6Al–4 V, 100 % HA, and FGM cladding surfaces, respectively. Similarly, the surface roughness was found to be 0.99 ± 0.1 µm, 5.16 ± 0.5 µm, and 3.57 ± 0.4 µm for non-cladded Ti–6Al–4 V, 100 % HA, and FGM cladding surfaces, respectively. These changes in the surface roughness resulted in the altered protein adsorption of 1.31 µg/cm^2, 2.94 µg/cm^{2,} and 4.14 µg/cm^2 for non-cladded Ti–6Al–4 V, 100 % HA, and FGM cladding surfaces, respectively. As a result of protein adsorption, the maximum to minimum cell density was found to be 85 ± 8 %, 71 ± 11 %, and 60 ± 2 % for FGM cladding, 100 % HA, and non-cladded Ti-6Al-4V, respectively [228]. In another study, TiO_2 was mixed with the BCP, and the changes in the surficial and biological responses were studied. It was detected that the wettability was decreased from 95°(±3°) to 73°(±2°) and 35°(±1°), for 100 % BCP, for 25 % TiO_2-75 % BCP, and for 50 % TiO_2-50 % BCP coated surfaces respectively. The critical load-bearing capacity was enhanced from 8.7 N to 14.8 N to >19 N for 100 % BCP, for 25 % TiO_2-75 % BCP and for 50 % TiO_2-50 % BCP. The adsorption of fetal bovine serum (FBS) was enhanced from 7.11 ± 0.25 to 4.42 ± 0.17 µg/cm^2 with an increase in TiO_2 percentage, and globular apatite formation was observed at a higher rate in 50 % TiO_2 concentration. As a result of apatite formation and protein adsorption, 210.1 ± 6.5 % of cell proliferation was counted in the 50 % TiO_2-50 % BCP coatings [230]. Hence, it can be seen that the mechanical treatment simultaneously with the HAp coating enhances the surface properties of the metallic implants, and as a result, biological activity and other responses also get altered positively.

2.6 Disadvantages of nanoantibiotics

Many NPs are already being utilized in many pharmaceuticals as well as cosmetics products; however, their toxic effect is still an untouched challenge for their commercialization. It is noteworthy that nano-medicine appears to be a promising alternative to traditional antibiotics, yet many of the aspects of these nanomedicines are still untouched.

2.6.1 Synthesis route and mode of action

The synthesis of NPs is a tedious process governing most of the responses of the material inside the host body. Various researchers have shown the size and morphology-dependent antimicrobial mechanism of these NPs. However, controlling the morphology as well as the morphology requires more input of energy, which in turn causes hindrance in the commercialization of these nano-medicines. Various researchers have explored a vast level of synthesis routes for the synthesis of NPs, yet none of the approaches has been focused on the scaled-up production of NPs. Besides this, the purity of an NP is the key factor for their application in the medical industry. Unfortunately, none of the techniques provide a pure form of NPs, which is the main factor of the non-commercialization of nanomedicine. Another drawback in this section comes from the target deficiency. Except, magnetic NPs, no other nanomedicine carries target efficiency. Moreover, no synthesis route provides target efficiency to nanomedicine. This encumbers the performance of the nanomedicines to be utilized at a commercial level. An ideal drug contains a self and non-self-recognition ability to specifically treat a disease. However, the interaction between the cells and NPs majorly depends on the surface properties of NPs, which is majorly contributed by the electronic interaction and conjugate bonding at the interface of cell-material [231]. This leads to another drawback of the nanomedicines, which backs in non-commercialization of the nanoantibiotics.

2.6.2 Antibacterial mechanism

Majorly, nanomedicines are considered for their antimicrobial action. Various studies have revealed different kinds of antibacterial activity of the designed NPs. However, none of the studies precisely explains the antibacterial mechanism of nanomedicines. The major antibacterial mechanism is considered through ROS generation, which will be discussed in the next section. Conversely, effective metal oxide NPs show ROS generation under the influence of light, which

is not suitable for the *in-vivo* application of NPs. Although at the nano-level, the band-gap of the metal oxide NPs gets reduced, which in turn causes the generation of ROS, still many questions are still untouched in the nano-medicine industry. These include a) selectivity of NPs; how does an NP selectively kill the bacterial cell? b) cell-dependent mechanism- why are there different mechanisms for different bacterial cells if there are no surface markers? c) Fate of NPs after internalization- after being internalized to the bacterial cell, how do they cause the disruption in the cell body, and why not to the human/healthy cells? These studies are still untouched by the research community. However, few of the studies have explained the significance of NPs to be utilized as direct medicine, yet their commercialization requires a full proof mechanism of action that must not harm the host body. All these together are major factors for the non-commercialization of nanomedicines.

2.6.3 ROS generation and cytotoxicity

As discussed above, the generation of ROS is one of the major antibacterial mechanisms of most nanomedicine. Nevertheless, various researchers have reported the ROS-dependent toxicity of NPs to human cells [232, 233]. Table 2.5 summarizes the production of ROS by various NPs at different surface areas.

Table 2.5. ROS production by different NPS

S.no.	Nanoparticles	Morphology and size	ROS production	Cytotoxic Concentration	Reference
1.	Ag/TiO_2 and Ag/N-TiO_2 NPs	Spherical, 3-5 nm	At >300 µg/ml	>500 µg/ml	[234]
2.	Ag-Fe NPs	Spherical, ~35 nm	At >500 mg/L	>1000 mg/L in sludge	[235]
3.	Phycocyanin-ZnO	Rod shaped, ~35 nm	At >100µg/ml	At >200 µg/ml	[236]
4.	Cu doped ZnO	Particulate, ~20 nm	At >50 µg/ml	At >200 µg/ml	[237]

5.	Surface coated CuO	Particulate, ~12 nm	At <25 µg/ml	No effect of ROS	[238]
6.	Cu NPs	Particulate, ~29.5 nm	At 0.2-1mg Cu/L	At >5 mg Cu/L	[239]
7.	TiO_2 NPs	Spherical ~12-48 nm	At, 25 mg/ml	At, 25 mg/ml	[240]
8.	Fe_3O_4-TiO_2	Particulate, 20-25 nm	At, 25 µg/cm^2 surface area	At, 15.625 µg/cm^2 surface area	[241]

The oxidative stress caused by NPs has shown various adverse effects on the host body. As discussed previously, the side effect of ROS generated through NPs, which explained the various adverse effects of NPs while being utilized as a nanomedicine. In addition to the ROS generation, NPs have also shown the dose defendant cytotoxicity to the human cells [242, 243]. The providence of NPs inside the human body is undescribed fully. Researchers have disputed over the excretion of NPs from the body, as well as their effect at an elevated concentration over the normal cells have been a question for their clinical applications. Moreover, the effect of NPs over the cell bodies, including DNA, RNA, and protein, has been intact for research. No study comprehensively demonstrates the impact of NPs over the cell bodies; however, few researchers have claimed the mutations caused by NPs [244]. Hence, these studies are essential prior to the commercialization of NPs.

2.6.4 Complement activation

An idyllic drug should not induce any adverse effect on the host cell. Precisely, they should not provoke any immune response after coming in contact with the immune cells. Few of the researchers claimed that the macrophage could interact with the polymeric as well as the inorganic NP. Wysokinska *et al.* 2019, studied the low dosage effect of NaGdF4:Yb^{3+}, Er^{3+} over macrophage. Authors reported an interaction and internalization of NPs by the macrophage, which subsequently increased the lysosomal compartment with a decrease in mitochondrial potential, indicating the impairment of mitochondrial homeostasis [245]. In a similar way, Liang *et al.* 2018,

studied the effect of ZnO NPs over BSA (Bovine Serum Albumin; a model protein) and macrophage cells. The result indicated that ZnO NPs significantly encouraged cytotoxicity and lysosomal subversion. In addition, long exposure of ZnO NPs enhanced the intracellular concentration of Zn^{2+} ions, which in turn enhanced the expression of Endoplasmic Reticulum (ER) stress markers (DDIT3 and XBP-1s) and apoptosis genes (CASP9 and CASP12) [246]. Moghimi *et al.* 2011 explained that various chemical properties of NPs, including chain length and architecture for polymeric NPs, size, morphology, and surface chemistry are the main factors that can provoke the complement systems, which might consequently result in the rejection of NPs via host body and toxicity [247]. Quach *et al.* 2017, explored the complement activation via Au NPs and reported that non-specific protein adsorption over the Au NPs significantly provoked complement activation leading to its toxic and inflammatory effects [248]. Hence, designing NPs with precise size, morphology and architecture are the key aspects that govern the commercialization of nanomedicines. In addition, the choice of metal ion/oxide doping in HAp, its concentration as well as the final composition are the major factors governing the selection/rejection of HAp based nanomedicine. As indicated by the literature, HAp lacks in self-antibacterial activity and target efficacy. Although, doping of metal ions incorporates antibacterial activity to the HAp, but also generates undesirable secondary phases. In addition, the MIC values remain very high, which hinders its practical applications. Furthermore, the size and morphology-based dependency of NPs for their antibacterial action require sophisticated techniques leading to the commercial incompatibility of these NPs. Hence, based on the given literature review, the chemical precipitation method along with the integration of Zn and Fe with HAp were selected for designing the HAp based nano-antibiotic for biomedical applications. Parallelly, antimicrobial peptoids' micelles were also synthesized, and scrutinized for their antibacterial activity and cytocompatibility.

Chapter 3

Design and characterization of Al-doped ZnO (AZO) nanoassembly

This chapter discusses the synthesis and characterization of ZnO and Al-doped ZnO (AZO) NPs. ZnO and AZO NPs were synthesized via a simple co-precipitation method. The synthesized NPs were analyzed using various characterization techniques. The XRD data, together with EDX and Raman analysis, confirmed a hexagonal wurtzite structure of AZO. A rod-shaped morphology up to 15 % doping of Al was obtained. The antibacterial activity enhanced to ~19 times in terms of MIC values, which were decreased to 14.33 ± 0.20 and 14.68 ± 0.20 µg/ml for AZO_{15} (15 % doping) as compared to 254.88 ± 3.0 and 338.14 ± 9.0 µg/ml for ZnO against *E. coli* and *E. hirae,* respectively. An electrostatic interaction between the negatively charged bacterial cells and positively charged AZO nanorods, followed by the intracellular accumulation of the Zn^{2+} ions released under a kinetic controlled (diffusion-limited) manner, caused the bacterial inactivation.

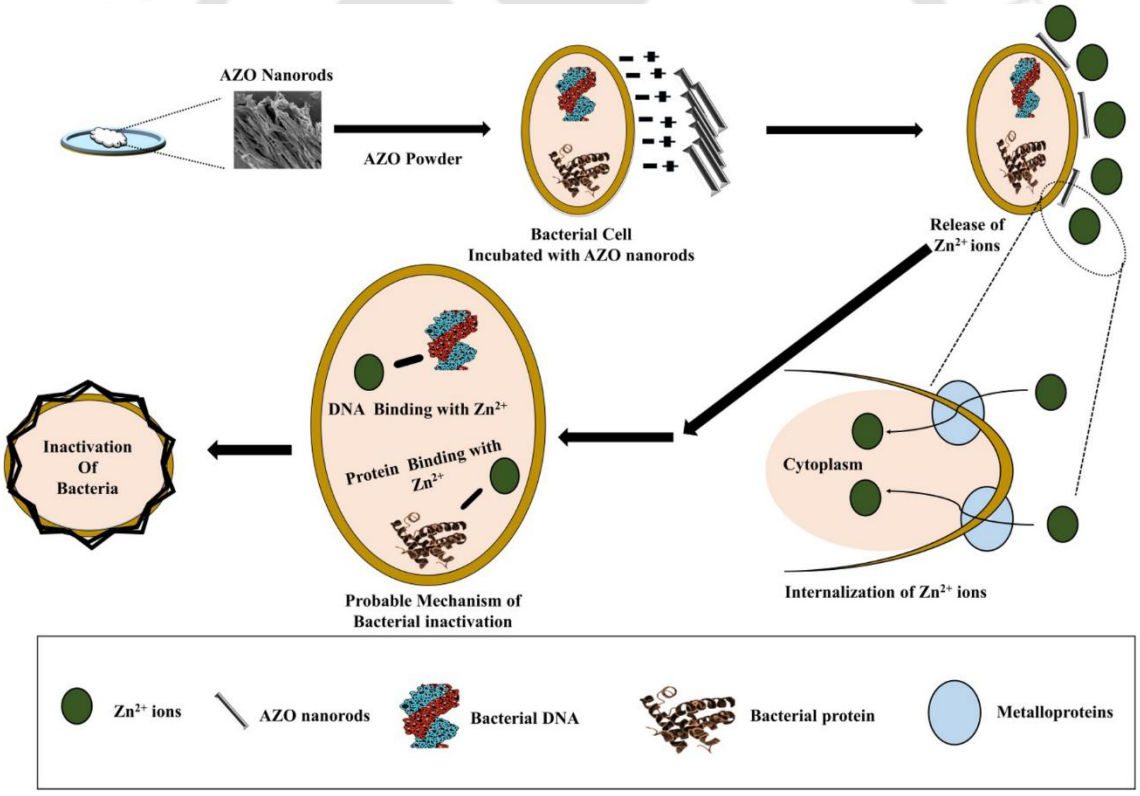

Schematic 3.1. Antibacterial mechanism of the synthesized AZO NPs; Figure indicates the electrostatic interaction between the AZO NPs and Bacterial cells, followed by the internalization of the Zn^{2+} ions and inactivation of cells by the interaction between the DNA and Protein binding to Zn ions (Applied Nanoscience 8 (8), 1925-1941, 2018)

3.1 Introduction

As discussed in Chapter 2, various NPs have been scrutinized for their antibacterial activity. Among all the NPs, ZnO NPs were selected because of their broad spectrum of antibacterial activity, ease of synthesis, and possession of all the three possible antibacterial mechanisms, *i.e.*, intracellular accumulation of Zn^{2+} ions, ROS generation and rupturing into the cell wall, and cell wall rupturing by the crystal defects. The advantage of using ZnO as an antimicrobial agent also includes Zn as a mineral, essential to humans, non-toxicity, long-term stability (controlled degradation), and strong activity (bio-interactions) even at lower concentrations [249, 250].

It has been reported that the antimicrobial effect of ZnO depends on its size and morphology [251, 252]. Various researchers have hypothesized that the production of Reactive Oxygen Species (ROS) and the accumulation of Zn^{2+} ions in the cytoplasm or the outer plasma membrane of the bacterial cell are the main factors governing the antimicrobial activity of ZnO [251, 253]. However, the release of Zn^{2+} ions from ZnO and production of ROS at physiological conditions remain very slow, which affects its antibacterial efficacy. Hence, based on the size and the morphology of the ZnO NPs, the Minimum Inhibitory Concentration (MIC) values vary in the range of 512 µg/ml to 25 µg/ml [254-256].

As the antibacterial activity of the ZnO NPs depends on their size and morphology, tuning of the lattice parameters of the ZnO plays a crucial role in its antibacterial activity and mechanism. To control the antibacterial activity of the ZnO NPs, researchers have tried various synthesis techniques to alter the lattice parameters and the morphology of the ZnO NPs. Although, these techniques such as hydrothermal synthesis, ultrasonic methods, ball-milling, *etc.*, were found to be successful in reducing the size and controlling the morphology of the ZnO NPs, however they require sophisticated instruments and input of higher energies during synthesis. Elemental doping into the ZnO lattice can be an efficient way to control the size and morphology of the NPs by creating the charge imbalance and altering the bond length [257, 258]. Here, the selection of dopant ions can be crucial for the reduction and control over the morphology. Hence, a simple precipitation method for doping transition metal ions into the ZnO lattice may be feasible for the bulk production of the ZnO NPs.

In this chapter, we synthesized the ZnO NPs via a simple precipitation method and examined their antibacterial activity. The MIC value of ZnO NPs was found to be ~250 µg/mL. Hence, to reduce the antibacterial activity of the ZnO NPs, first, trivalent ions Al^{3+} ions were incorporated to reduce

the lattice parameters. Al doping has been proven to induce the upregulation of apoptotic genes in breast cancer cell lines (MCF-7) [259]. Furthermore, Al^{3+} ions were selected to be doped into the ZnO lattice because of their smaller size and higher reduction potential than Zn^{2+} ions.

3.1 Material and methods

3.1.1 Materials

The precursors for Zn, Al, and O were selected as Zinc nitrate hexahydrate, $Zn(NO_3)_2.6H_2O$ (EMPLURA Merck, India, 1.93703.0521), Sodium hydroxide, NaOH (Himedia, India, MB095), and Aluminum Nitrate nonahydrate, $Al(NO_3)_3.9(H_2O)$ (Himedia India, GRM 3880). For biological characterization, fluorescent dyes such as MTT [3-(4,5-dimethylthiazol-2-yl)-2,5-diphenyltetrazolium bromide, TC191] were purchased from Himedia India. Other fluorescent dyes such as CFDA (Carboxyfluorescein diacetate succinimidyl ester, C4915), PI (propidium iodide, P4170), and DCFH-DA (dichloro-dihydro-fluorescein diacetate, D6883) were procured from Sigma Aldrich. Phosphate Buffer Saline (PBS) was synthesized by mixing NaCl (EMPARTA Merck, India 1.93206.0521, 137 mM), KCl (EMPARTA Merck, India, 1.93238.0521, 2.7 mM), $Na_2HPO_4.2H_2O$ (EMPARTA Merck, India 1.93209.0521, 10 mM), KH_2PO_4 (EMPARTA Merck, India, 1.93205.0521, 1.8 mM) in appropriate concentrations. Luria Bertani Broth Media, (LB Media), (Himedia India, M 1245)) was used for bacterial culture. Double distilled water (MiliQ, 18 mΩ, Millipore systems) was used throughout the experiments.

3.1.2 Methods

A simple one-step precipitation method was utilized for the production of ZnO and AZO NPs. The detailed process is as follows;

3.1.2.1 Preparation of ZnO and AZO

The ZnO NPs were synthesized via a co-precipitation method as described previously with slight modifications [260]. In brief, 25 ml of 1M $Zn(NO_3)_2.6H_2O$ solution was prepared, which was transferred to an oil bath at a reaction temperature of 65 ºC. 25ml of 2M NaOH preheated solution was then titrated to the above solution under vigorous stirring. Then, the mixture was heated at 65 ºC and stirred continuously for three h, followed by washing with deionized water (18mΩ, Milli-

Q, Millipore systems) several times until neutral pH was obtained. After washing, the samples were air-dried at 80ºC in a hot air oven and were sintered at 450 ºC.

AZO was synthesized by using a similar synthesis process to that of ZnO, as given in scheme 1. The Aluminum precursor was mixed in four different concentrations in the solution containing (1-N) molar concentrations of $Zn(NO_3)_3.9H_2O$, where N= 0, 0.05, 0.1, 0.15, 0.20. The precursor molar concentrations and their sample codes are listed in Table 3.1. The samples are represented as AZO_M, where M is the dopant (metal; Al), percentage (M=0, 5, 10, 15, and 20 % Al). The same codes are referred throughout the thesis.

Table 3.1. Molar concentrations of Zn and Al in AZO samples

S. No.	Sample code	Doping Percentage (w/v)	Concentration of Zinc (Moles/Liter)	Concentration of Al (Moles/Liter)
1	AZO_0	0	1	0
2	AZO_5	5	0.95	0.05
3	AZ_{10}	10	0.90	0.1
4	AZO_{15}	15	0.85	0.15
5	AZO_{20}	20	0.80	0.20

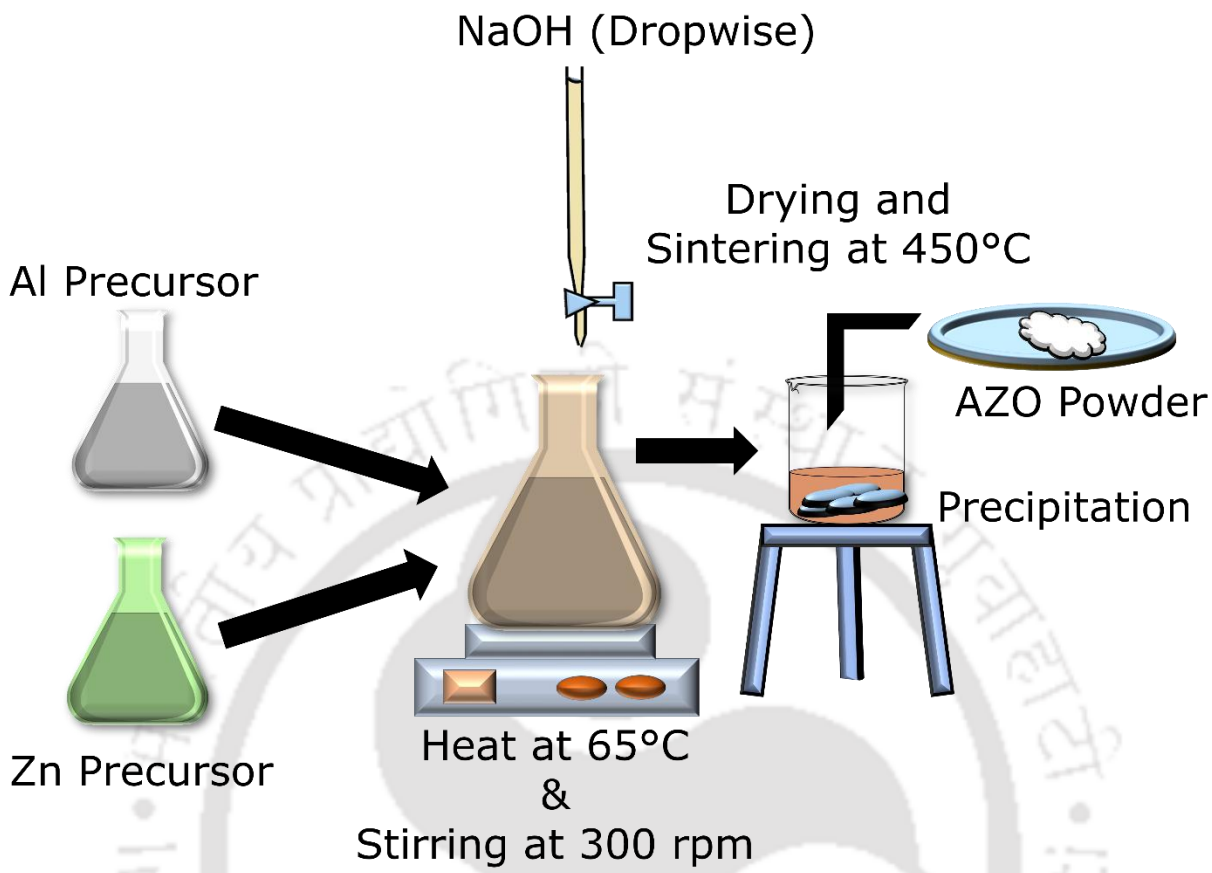

Schematic 3.2. Schematic representation of AZO synthesis from its precursors

3.1.3 Characterizations of the synthesized materials

As synthesized AZO NPs were characterized using various techniques. The crystal characterization was done using a high-resolution X-ray powder diffraction (XRD) (RIGAKU, ULTIMA IV, JAPAN). The XRD data were recorded by placing the samples over a silicon zero-background sample holder with Cu Kα radiation (λ= 1.5406 Å) at slow step size (of 0.03° 2θ). The synthesis was further confirmed by recording Raman spectra using a LabRam HR laser micro Raman system from Horiba with 514 nm wavelength incident laser light. Field Emission Scanning Electron Microscope (FESEM) (Zeiss, Model: Sigma) was used for size and morphology analysis of AZO NPs. The elemental analysis of the designed NPs was confirmed by using Energy-dispersive X-ray spectroscopy (EDX) analysis using the same FESEM instrument. The samples' thermal analysis with the lowest and highest concentrations of dopant Al (5 % and 20 %) was analyzed using a high-temperature Differential scanning calorimetry/ Thermogravimetric Analysis

(DSC/TGA) system (Netzsch, Model: STA449F3A00) at a rate of 10K/min under an argon environment.

3.1.4 *In vitro* experiments

Two *in vitro* experiments were performed with the synthesized NPS. Firstly, the cytocompatibility analysis of the designed NPs was analyzed, followed by the antibacterial activity as well as the mechanism analysis of the designed NPs. The details of these procedures are as follows.

3.1.4.1 *In vitro* cytocompatibility analysis

The *in-vitro* cytocompatibility was analyzed using MTT [3-(4,5-dimethylthiazol-2-yl)-2,5-diphenyltetrazolium bromide] assay using procedures described previously [261-263]. For this purpose, mouse fibroblast (L929, NCCS India) cell line was grown in Dulbecco's Modified Eagle's Medium (DMEM, Invitrogen) augmented with 10 % fetal bovine serum (FBS, Invitrogen) and 1 % antibiotic (Pen Strep, Invitrogen) at 37 ºC, 5 % CO_2 and 85 % humidity in a CO_2 incubator. 5×10^3 cells per well in 100 µl of DMEM were added to 96 well plates, carrying lower 20×10^3 µg/ml concentration to the higher 40×10^3, 80×10^3, 160×10^3, and 320×10^3 µg/ml concentrations of the minimum and maximum Al-doped samples, *i.e.*, AZO_5 and AZO_{20}. Cells were incubated for 1, 3, and 6 days to assure the long-term applicability of the designed nano-assembly. Cells without any material incubation were considered as a positive control. The media was replaced with 20 µl of MTT solution (5000 µg/ml, PBS pH 7.4) and fresh media. The cells were further incubated, as mentioned above for 4 h. After incubation, 150 µL of Dimethyl sulfoxide (DMSO) was supplemented for 10 minutes, and the optical density (OD) was measured at 570 nm using an Infinite M200 PRO Tecan plate reader. The viability of the cells was calculated using the following equation:

$$\%\ Cell\ viability = \frac{A_s}{A_c} * 100 \qquad (3.1)$$

Where, A_s is the optical density in the presence of designed material, A_c is the optical density of the positive control.

3.1.4.2 Antibacterial activity and determination of MIC values

The bacterial inactivation studies were carried out using a serial broth dilution method. The antimicrobial activity of synthesized material was analyzed over *Escherichia coli* (*E. coli*, Gram-

negative, MTCC 1610) and *Enterococcus hirae* (*E. hirae*, Gram-positive, MTCC 3612) bacteria. In brief, the bacterial culture was first inoculated in the fresh LB media (Himedia, India). The optical density at 600 nm (OD_{600}) of the suspensions was adjusted to 0.025, corresponding to an approximate concentration of 1×10^7 CFU/ml. The OD-adjusted cultures were incubated at 37 °C and 120 rpm for 12 hrs in a 96-well plate, and the OD_{600} values were recorded in the presence of various concentrations of the synthesized NPs. The MIC value for AZO samples was defined as the lowest concentration of NPs at which it inhibited bacterial growth.

3.1.4.3 Assessment of antibacterial mechanism

In order to elucidate the antimicrobial action of AZO, three major mechanisms discussed in Chapter 2 were discussed.

3.1.4.3.1 Cells staining and ROS production

Bacterial cells were grown in LB medium up to log phase and were washed twice with freshly synthesized and autoclaved PBS (pH 7.0). The cells (OD_{600}=0.025) were grown in 500 µg/ml of samples at 37 °C and 120 rpm for 6 h. A higher concentration (500 µg/ml) of AZO was chosen instead of MIC values in order to minimize the experimental error while measuring Zn^{2+} concentrations. The cells were separately stained with 10 µL of 2 mM CFDA (green fluorescent dye, λ_E = 515 nm, λ_{ex} = 495 nm) for live cells staining [264], and 15 µL of 1.5 mM of PI (red fluorescent nucleic acid staining dye, λ_E = 617 nm, λ_{ex} = 535 nm) for dead cells staining [265]. Cells were also stained with 10 µM of DCFH-DA (λ_E = 530 nm, λ_{ex} = 480 nm) for ROS detection [266]. Live cells stained with CFDA, dead cells stained with PI, and H_2O_2 treated cells stained with DCFH-DA were used as a positive control, and dead cells stained with CFDA, live cells stained with PI were used as the negative control. Finally, flow cytometric analysis was accomplished on a BD FACS flow cytometer, and data were analyzed using the FCS Express 5 Flow software. The ROS production was also confirmed through the measurement of fluorescence intensities of DCFH-DA staining after treating the bacterial cells with and without AZO samples for 6 h. LB media, 0.9% saline solution, and bacterial cells in LB media without any AZO incubation were considered positive controls. The fluorescent intensities were recorded using Infinite M200 PRO Tecan plate reader at 495 nm and 529 nm excitation and emission wavelength of the DCFH-DA dye, respectively.

3.1.4.3.2 Release of Zn^{2+} ions

500 µg/ml of the as-prepared samples (AZO_0, AZO_5, AZO_{10}, AZO_{15}, and AZO_{20}) were incubated with the bacterial cells as well as in 0.9 % saline solution for 6, 24, and 48 hrs. After incubation, the cells were isolated via centrifugation, and the supernatant was collected separately. The cells were then sonicated for 5 minutes at 35 % amplitude and 750 Watt power and were washed with 1 X PBS. The intracellular and extracellular concentration of Zn^{2+} ions was calculated using Atomic Absorption Spectroscopy (AAS) analysis of re-suspended ruptured cells and supernatant, respectively, using spectra 55B Varian atomic absorption spectrometer. The intra and extracellular Zn^{2+} ion concentrations were compared with the Zn^{2+} ion concentration in saline solution.

3.1.4.3.3 Analysis of cell membrane rupturing

The rupturing of the cell membrane was analyzed via FESEM analysis of bacterial cells grown after the treatment of samples (AZO_0, AZO_5, AZO_{10}, AZO_{15}) and the PI staining. In brief, the cells were first grown in LB medium incubated with the synthesized NPs, followed by centrifugation at 10000 rpm for 5 minutes. The cellular pellet was then dissolved in sterile PBS and was washed thrice with the same buffer. The cells were then fixed with 2.5 % glutaraldehyde for 2-4 hrs. Finally, the dehydration with various concentrations of alcohol was performed before drop-casting it onto the carbon tape. The gold coating was performed prior to the imaging.

3.1.4.3.4 Measurement of zeta potential

The specificity of the antibiotic is the main factor for its effectiveness. Presuming the electrostatic interaction between the bacterial cells and the synthesized material (AZO_0, AZO_5, AZO_{10}, AZO_{15}, and AZO_{20}), the zeta potential of the samples was measured using Zetasizer Nano ZS90 (Malvern, ZEN3690) to measure the surface charge, at 50 µg/mL concentration. The samples were first taken in 500 µg/ml concentrations and were sonicated for 30 minutes. The samples were further diluted ten times for the final measurement. Water (refractive index 1.333) was taken as a diluent. The pH of the samples was measured and adjusted to 7.4.

3.2 Results and discussion

The synthesized AZO NPs were characterized to evaluate the various physical and chemical properties.

3.2.1 Physical characterization of AZO

All the samples were analyzed via XRD, and the patterns are shown in Figure 3.1. The XRD pattern represented the classical polycrystalline hexagonal wurtzite structure of ZnO (JCPDS 36-1451) [267, 268]. Various peaks corresponding to the different planes of zinc wurtzite structure are listed in Table 3.2.

Table 3.2. XRD peaks of ZnO hexagonal wurtzite structure (JCPDS 36-1451)

S. No.	*h*	*k*	*l*	d [A°]	2θ[°]	I [%]
1	0	1	0	2.81	31.79	52.7
2	0	0	2	2.60	34.45	41.3
3	0	1	1	2.47	36.28	100.0
4	0	1	2	1.90	47.57	22.3
5	1	1	0	1.62	56.65	36.0
6	0	1	3	1.47	62.91	31.5
7	0	2	0	1.40	66.44	4.8
8	1	1	2	1.37	68.01	26.7
9	0	2	1	1.35	69.15	13.5

Figure 3.1 confirmed that the doping of Al did not alter the wurtzite structure of ZnO as no separate peaks of Al were identified. From this result, it was anticipated that the Al^{3+} ions replaced the Zn^{2+} ion in the lattice. The critical analysis of the XRD patterns of the designed samples reflected a shift of major peaks (2θ =31.79, 34.4 and 36.28) at higher dopant concentrations (*i.e.*, >5 %) of the synthesized nanoparticles (Figure 3.1B), presumably due to the smaller ionic radii of Al^{3+} ions (0.053nm) than that of Zn^{2+} ions (0.074nm) [269, 270]. The smaller atomic radius of Al remains helpful in replacing the Zn^{2+} ion. In addition, the reduction potential of Al (-1.68 mV) [271] is higher than that of Zn (-0.763 mV) [272], which indicates that they underwent the displacement reaction in the ZnO lattice. The averaged spacing of the AZO lattice was found to be 2.47 nm. The crystallite size of the synthesized material was also calculated according to the full-width half maxima (FWHM) of the strongest (011) diffraction peak by Scherrer equation as follows.

$$d = \frac{K\lambda}{\beta Cos\theta} \tag{3.2}$$

Where d is the mean size of the crystallite domain, K is a non-dimensional shape factor (0.94), λ is the wavelength of incident X-ray (1.54A°), β is the FWHM of maximum intensity, and θ is the Bragg's angle. The calculated values are given in Table 3.4, where sharp peaks with respect to different planes confirmed the high crystallinity of AZO samples [273]. The crystallinity analysis revealed the minimum crystallite size (36.98 nm) for AZO_{15}. Similarly, no significant difference could be observed for lattice parameters 'a' and 'b', but the values for 'c' constant was found to be decreased with an increase in the Al concentration (Table 3.4; Figure 3.2, linear co-relation; R^2= 0.99). As per Vegard's rule, the lattice constant of the alloy (made of two metals A and B) remains in the weighed proportions of a and b from A and B, *i.e.*, a(1-x)bx. Hence, the decrement in the lattice parameter with respect to Al concentration affirms the successful doping of Al into the ZnO lattice.

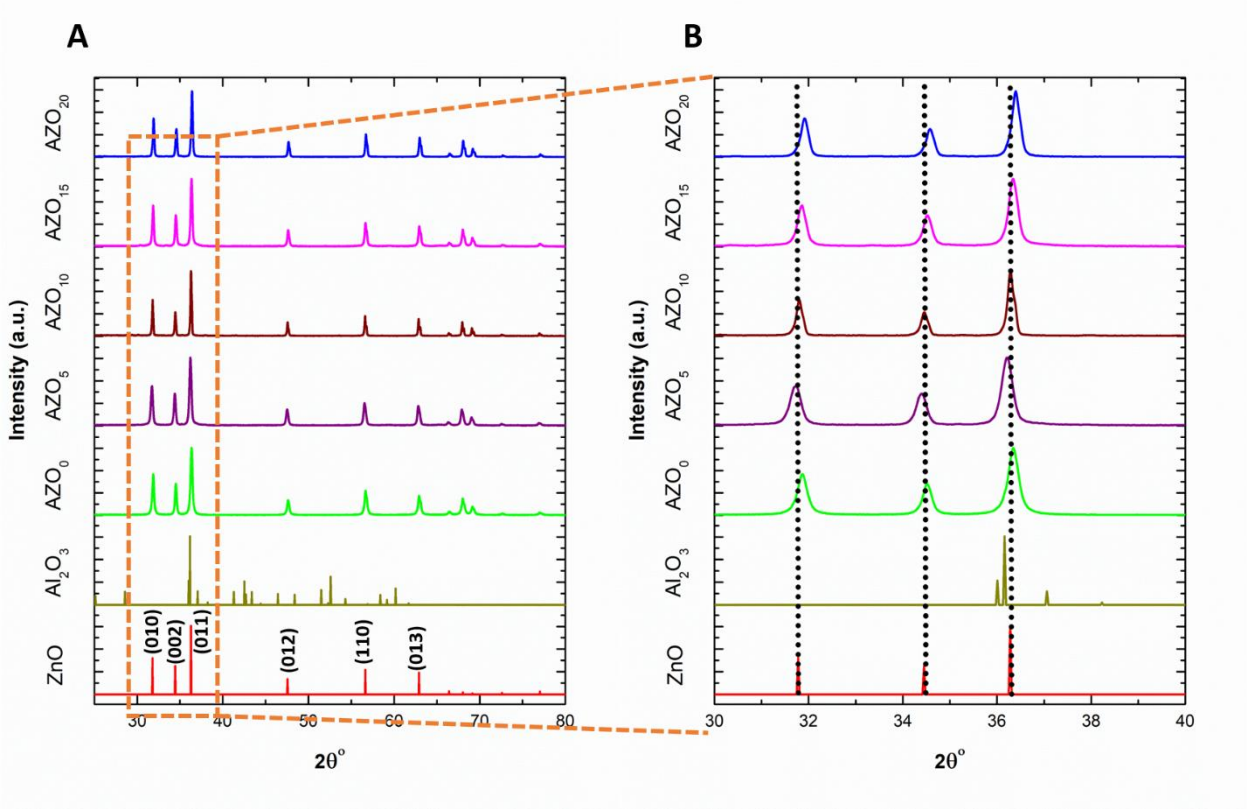

Figure 3.1. XRD data of (A) various AZO samples along with references ZnO (JCPDS 36-1451) and Al_2O_3 (JCPDS 98-011-3790), **(B)** Change in the peak position with respect to doping

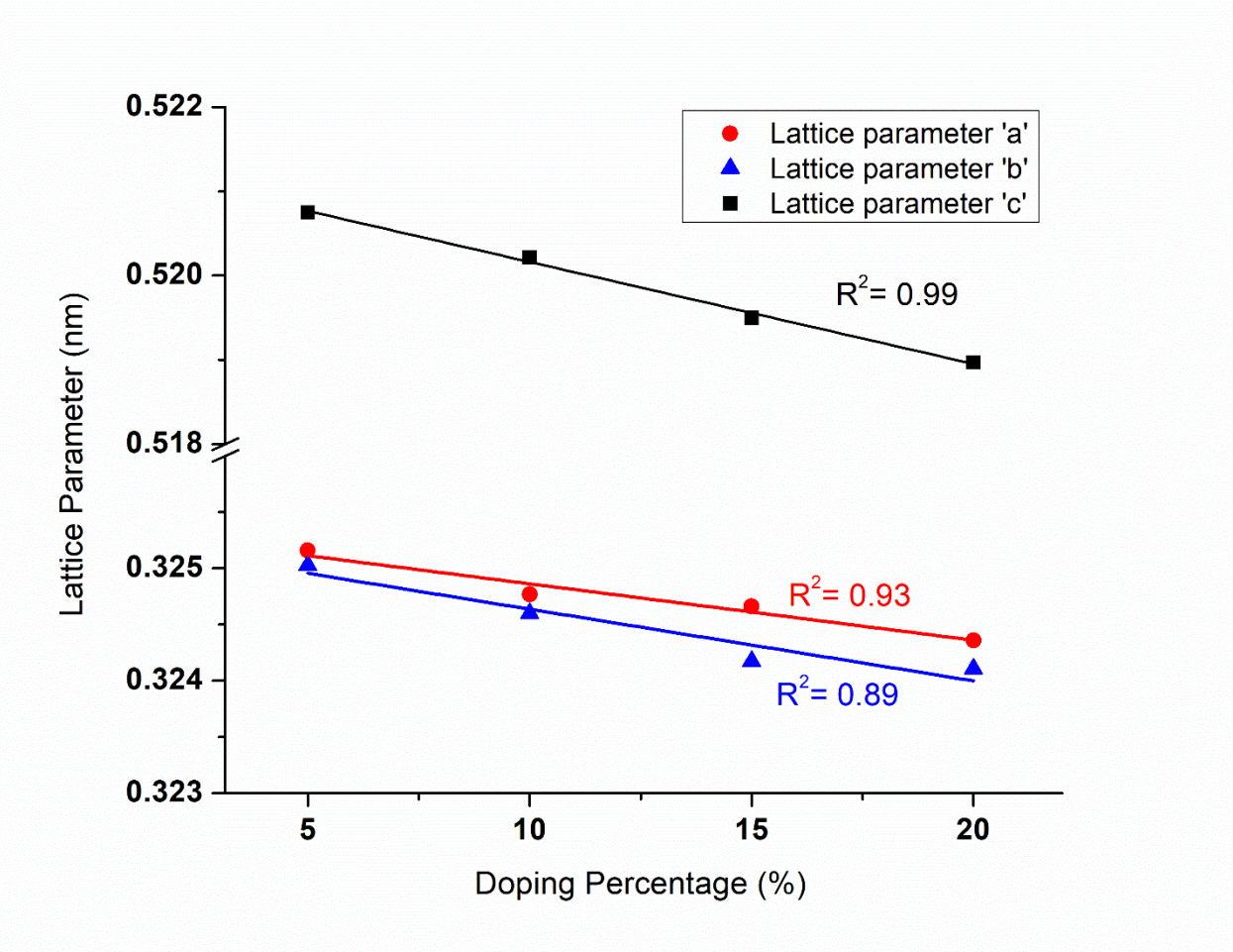

Figure 3.2. Decrease in the Lattice parameter a, b and c with respect to doping percentage

Table 3.4. The crystallite sizes of AZO samples

S. No	Sample Name	FWHM (°)	2θ (°)	Crystallite size (nm)	Lattice Parameter (nm)		
					a	b	c
1	AZO_5	0.17712	36.27	49	0.3252	0.3250	0.5205
2	AZO_{10}	0.17712	36.31	49	0.3248	0.3246	0.5207
3	AZO_{15}	0.23616	36.20	37	0.3247	0.3246	0.5202
4	AZO_{20}	0.20664	36.33	42	0.3244	0.3242	0.5195
5	AZO_0	0.20664	36.34	42	0.3244	0.3242	0.5190

A typical wurtzite ZnO structure reflects Raman active symmetries A1 and E1, which split into two components LO (Longitudinal optical) and TO (transverse optical), due to the induced macroscopic electric field coupled with LO [274]. The characteristic vibrational peaks of ZnO in the Raman spectrum corresponding to 2E2 (M), A1 (TO), and E2 (high) vibration modes were found at 331, 382, and 438 cm^{-1}, respectively [275]. The doping of Al causes structural alteration in the ZnO lattice as the mean size of the lattice is reduced. Hence, the vibrational signal of the $P6_3mc$ symmetry is budged and weaken. Figure 3.3 shows the vibrational signals corresponding to 2E2 and A1 vibration modes, which got diminished and shifted at every Al doping concentration [276]. The vibrational peak corresponding to 2E2 vibration at 438 cm^{-1} presents in all the samples complimented the result obtained from XRD analysis. Based on the concept given by Wang *et al.* and Sahni *et al.*, the AZO samples' synthesis mechanism can also be explained in a systematic process. First, the Zn-O bond was formed, followed by the replacement of Zn^{2+} ions by Al^{3+} ions forming small degrees of Al-O bonds at the molecular level, resulting in the peak shifts in the XRD pattern and budged the signals in Raman spectra [277, 278]. As the doping concentration was kept up to 20%, not all the Zn^{2+} ions were replaced, which assisted in retaining the hexagonal wurtzite structure.

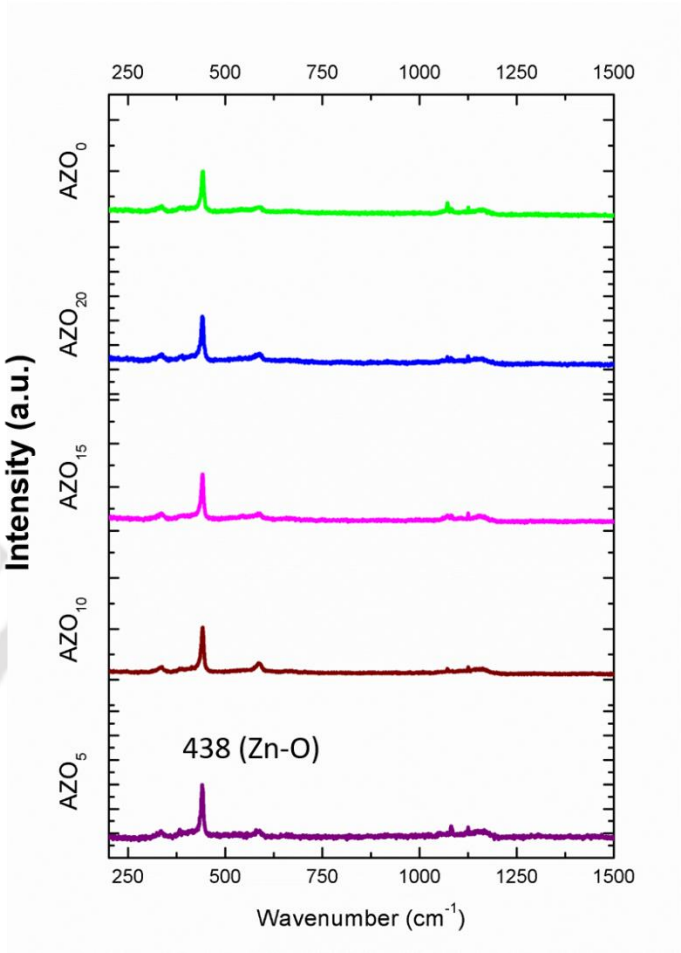

Figure 3.3. Raman analysis of AZO_5, AZO_{10}, AZO_{15}, AZO_{20}, AZO_0; Result shows that classical 2E2 vibration of ZnO at 438 cm^{-1} is present in all the samples

Various morphologies of as-prepared AZO NPs were observed depending upon the concentration of dopant, as displayed in Figure 3.4. The particle size was analyzed using Image J software. Different concentrations of Al had a divergent effect on the morphology of the synthesized nanorods. With an increase in Al concentration (up to 15 %), one dimension of the designed nanomaterials was reduced. Hence, AZO_0 obtained spike-like structure, and AZO_0 obtained spike-like structure, and AZO_5, $AZO_{10,}$ $AZO_{15,}$ and AZO_{20} were mixed morphology, *i.e.*, rod-shaped, fibrous, globular, and irregular shaped in morphology. The average diameter of the samples was found to be 126 ± 38 nm, 65 ± 15 nm, 59 ± 16 nm, 46 ± 12 nm, and 115 ± 32 nm, respectively for AZO_0, AZO_5, $AZO_{10,}$ $AZO_{15,}$ and AZO_{20} samples. The AZO_5 and AZO_{10} samples reflected a mixed morphology with rod-shaped and globular morphology, and AZO_{15} samples obtained a thin

fibrous structure. Further AZO_{20} samples were found to be irregular in shape. One dimension of the AZO samples was found to be larger than another, and hence the samples were termed nanorods. At 20 % doping of Al, the second dimension (length) of the designed material was also reduced, and irregularly shaped morphology of AZO_{20} with an average diameter of 115 ± 32 nm was obtained. We re-examined the samples using FESEM, and similar morphologies were obtained as given in Figure 3A-5 of Annexure 3A. Additionally, a size distribution histogram based on the shortest diameter to the area covered by the particle is also added as Figure 3A-6.

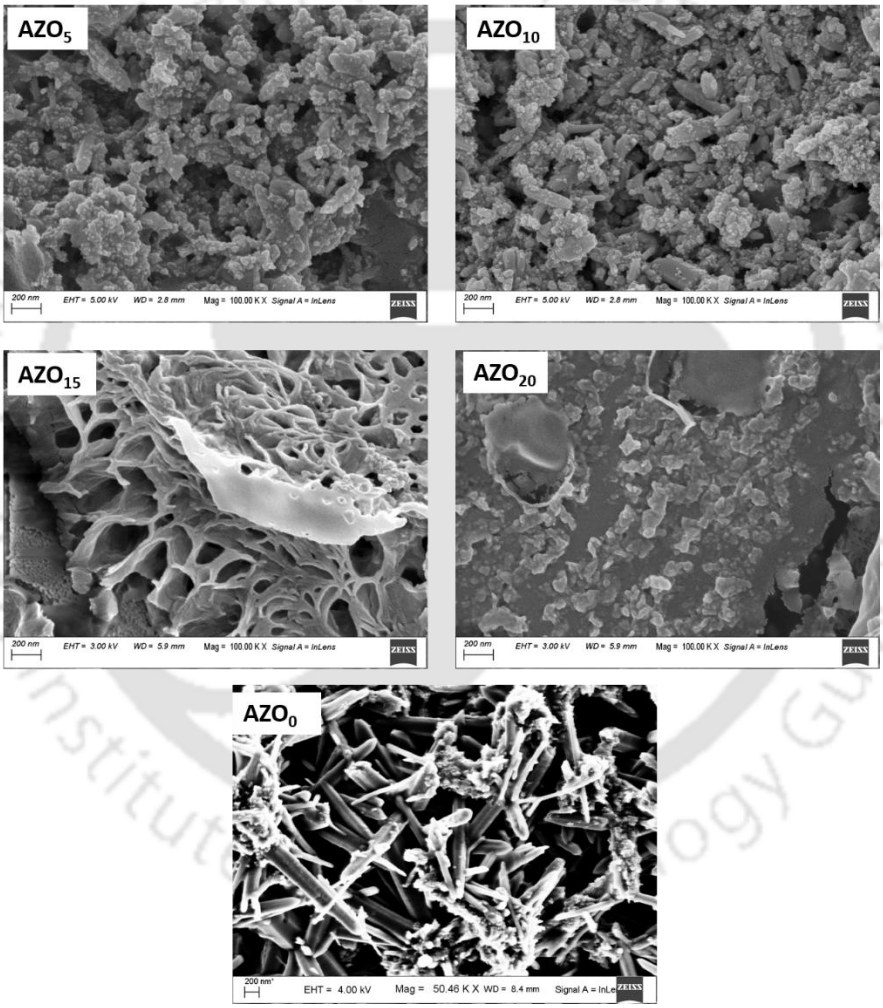

Figure 3.4. Various morphologies attained by **A)** AZO_5, **B)** AZO_{10}, **C)** AZO_{15}, **D)** AZO_{20}, **E)** AZO_0; The result shows that increase in Al concentration decreased the width up to 15 % doping of Al, however at 20 % doping of Al, the second dimension also decreased resulting into particulate morphology

The morphology of the designed AZO nanorods was found to be dependent on the dopant concentration. For example, at 5 % doping of Al, *i.e.*, AZO_5, the NPs started acquiring the rod-shaped structure. The rods became more developed at 10 % doping of Al (AZO_{10}), and further narrowing in the width of the nanorods at 15 % doping of Al (AZO_{15}) was observed. However, at 20 % doping, the rod-shaped morphology became diminished, and the reduction in the second dimension took place, and the AZO_{20} acquired spherical morphology [279]. Hence, the morphology of the as-prepared nanomaterial became dependent on the dopant concentration.

The elemental composition of these materials was analyzed by recording the EDX data. As shown in Figure 3.5A, the principal elements of the samples are Zn and O, with varying concentrations of Al, confirming the successful doping of Al into the ZnO matrix. The Al wt % increased with an increase in the doping concentrations as follows: AZO_5 (0.6) < AZO_{10} (3.4) < AZO_{15} (5.3) < AZO_{20} (7.7), indicating the bimetallic composition of the nanoassembly. The theoretical Al wt % was calculated using a molecular formula $Zn_xAl_{(1-x)}O$ for all the samples. The value of x was taken as the molar concentration of Zn listed in Table 3.1. The Al wt % obtained from EDX analysis was found to be linearly correlated with the theoretical wt % of Al (R^2=0.98) as given in Figure 3.5B. These results clearly show the successful doping of Al into the ZnO matrix without affecting the basic wurtzite structure of the ZnO.

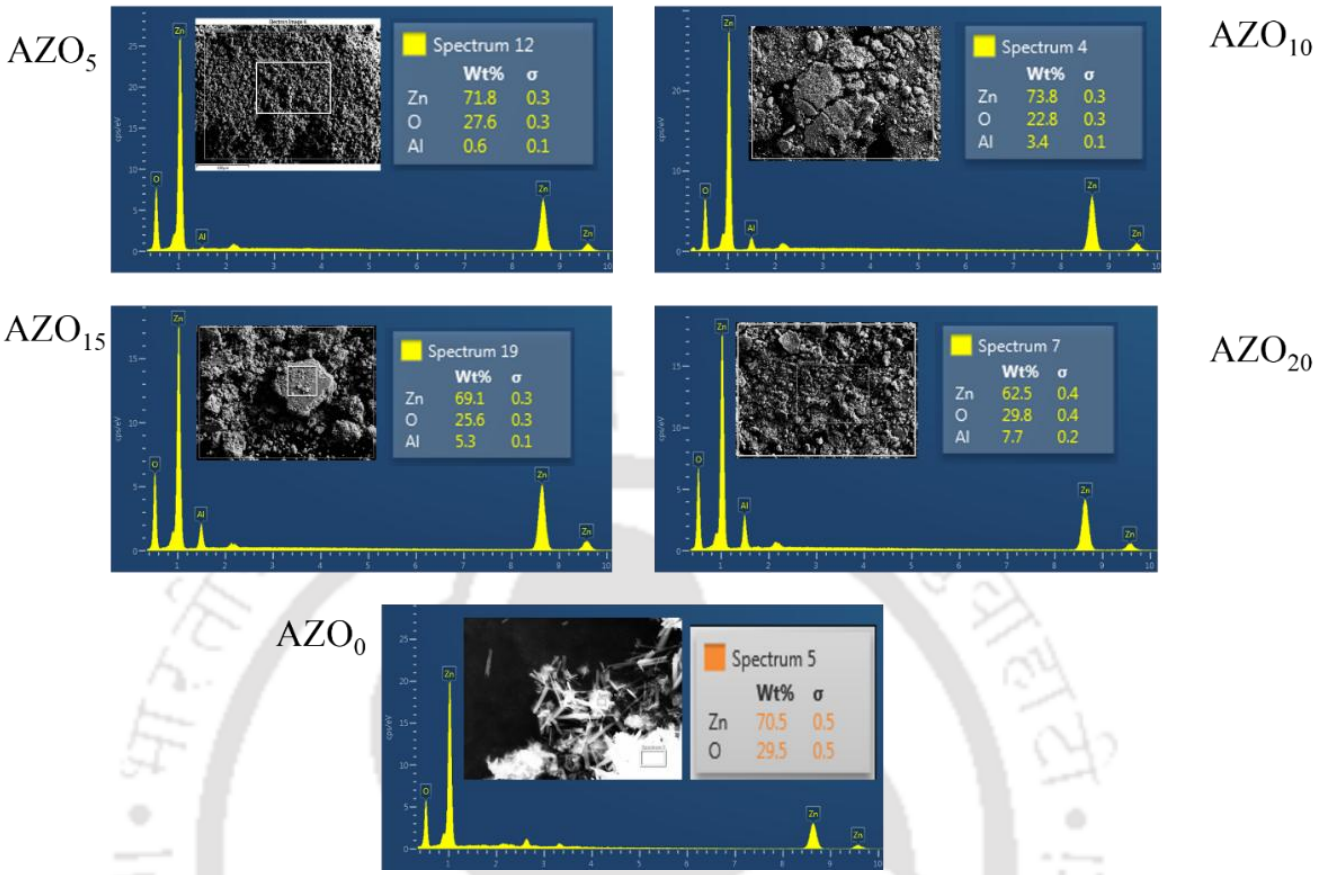

Figure 3.5A. EDX spectrum of AZO_5, AZO_{10}, AZO_{15}, AZO_{20}, AZO_0; the result confirms the presence of Zn, Al, and O, with an increase in the Al concentration, with respective doping percentage

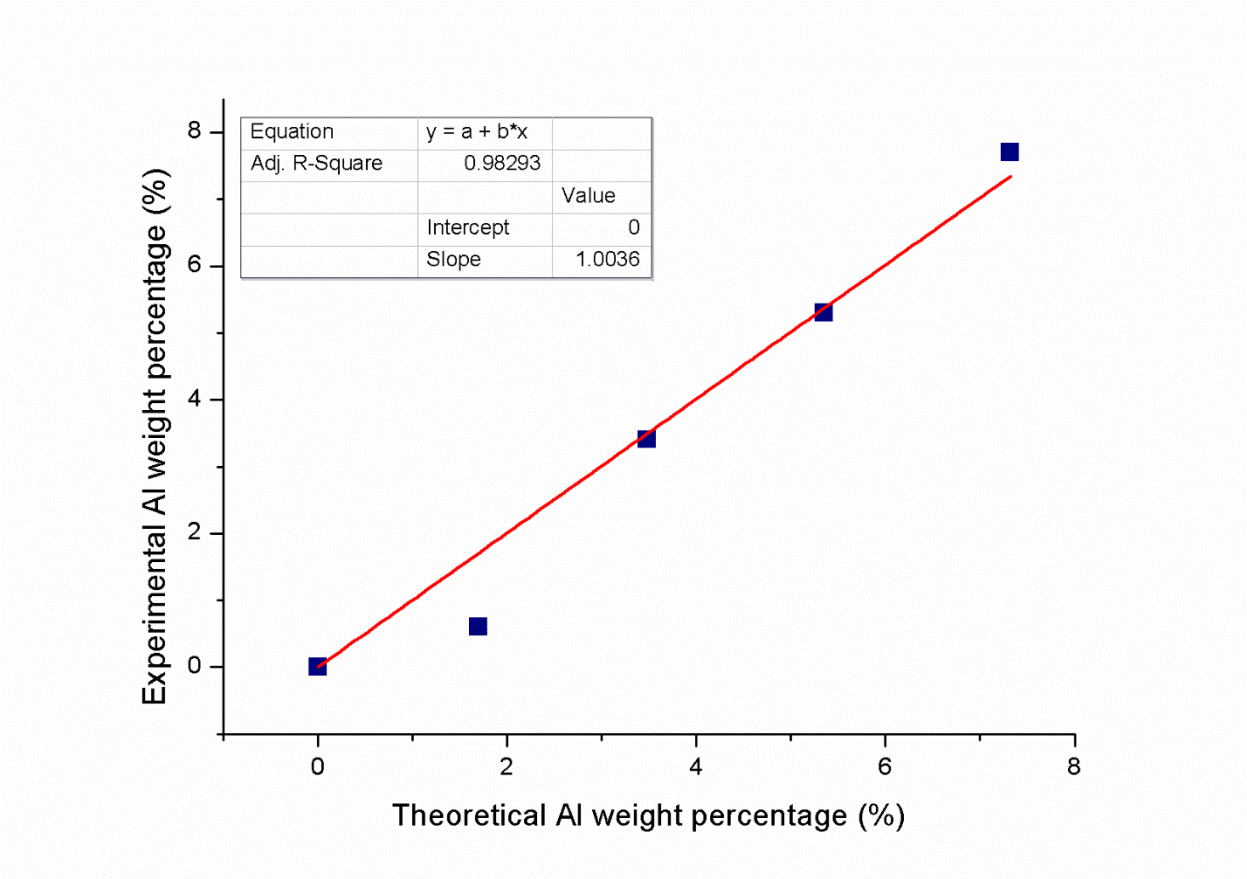

Figure 3.5B. The correlation between the theoretical and experimental Al wt% values; Al (R^2=0.98)

The materials' thermal stability was further analyzed using DSC/TGA, which showed the crystallinity temperature of 390 ºC, 410 °C, and 440 °C for AZO_0, AZO_5, and AZO_{20}, respectively (Figure 3.6). In a similar way, the melting point for AZO_0, AZO_5, and AZO_{20} was found to be 610 °C, 800 °C, and 900 °C, respectively. TGA data showed good thermal stability of synthesized nanorods. Hence, the doping of Al to the ZnO lattice enhanced the thermal stability of ZnO at increasing concentrations of Al. This high thermal stability of AZO samples can be further utilized for thermoelectric applications.

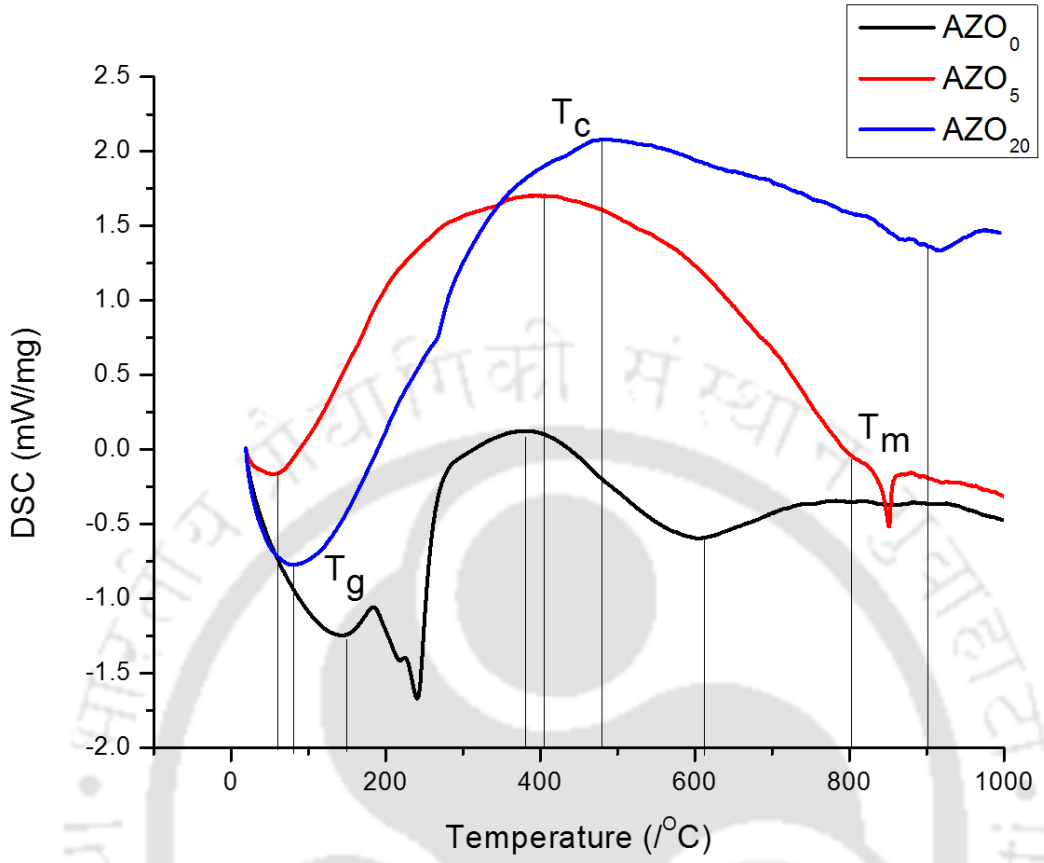

Figure 3.6. DSC curve of AZO_0, AZO_5, and AZO_{20}

The zeta potential of the AZO samples was measured to examine their respective surface charges to identify the electrostatic interaction between the bacterial cell surface and the synthesized nanorods. The zeta potential was found to be the maximum for AZO_{15} (22.7 ± 0.3 mV) and the minimum for AZO_0 (6.17 ± 0.5 mV). The zeta potential of AZO_5 (13.8 ± 0.9 mV), AZO_{10} (16.1 ± 0.9 mV), and AZO_{20} (18.2 ± 1 mV) ranged in between the two. The measured zeta potential was found to increase with an increase in Al doping up to 15 %, presumably due to the replacement of Zn^{2+} by Al^{3+} (Figure 3.7). The evaluation would correspond to the antibacterial potency of the AZO samples. AZO_{15} possesses the maximum positive surface charge at physiological pH, which enhances the electrostatic interaction with the bacterial cell surface (negatively charged, owing to polyphosphate anions). This electrostatic interaction contributed to the antibacterial activity of AZO samples, as discussed in the following section.

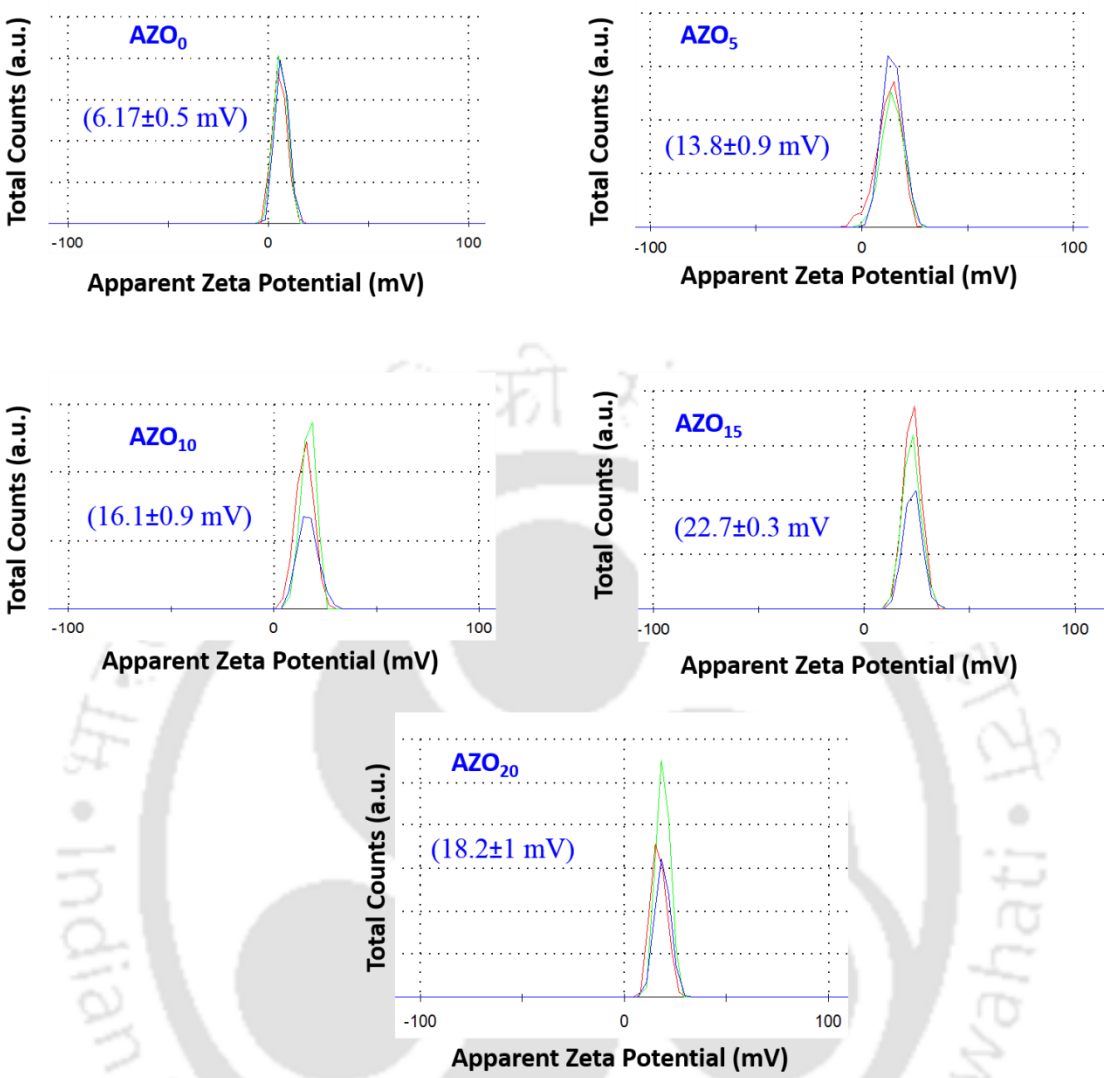

Figure 3.7. Zeta potential of various samples, AZO_5, AZO_{10}, AZO_{15}, AZO_{20}, AZO_0; measured in water at pH 7.4; the result shows that the zeta potential of ZnO increases with an increase in dopant: Al concentration up to 15 % doping

3.2.2 *In vitro* cytocompatibility analysis

In order to explore the biocompatibility of the prepared materials, minimum and maximum Al-doped nano-assembly (AZO_5 and AZO_{20}) samples were examined using L929 (mouse fibroblast, P-38) cells. Various concentrations of the samples, *i.e.*, 20×10^3 µg/m, 40×10^3 µg/ml, 60×10^3 µg/ml, 800×10^3 µg/ml, 160×10^3 µg/ml, and 320×10^3 µg/ml concentrations of both samples were examined for their cytotoxicity. The MTT assay was performed as discussed above, and the results

were validated by performing a positive control experiment, as shown in Figure 3.7. The cell viability was found to be > 97 ± 4% in the presence of both AZO_5 and AZO_{20} (Figure 3.7) after three days. The excellent cell viability > 9 2 ± 2% was observed for both the samples (Figure 3.7), even at a very higher concentration of the samples, *i.e.*, 320×10^3 µg/ml. The statistical analysis revealed that there was no significant difference (*p value* ≥ 0.05) in the cell growth as compared to the control samples. After long-term incubations, the cell viability was found to be > 93 ± 3% even after six days of incubation, as shown in Figure 3.8. Similarly, the spreading of the MG63 cells was performed by replacing the Pen-strep with AZO samples. The cell circularity and fraction area covered by the cells were measured using ImageJ software. The cells with Pen-strep showed a circularity index of 0.58 ± 0.2 with 26 ± 3 % fraction area covered. Similarly, the circularity index of the cells incubated with AZO samples was found to be 0.60 ± 0.1, 0.54 ± 0.2, 0.52 ± 0.1, and 0.56 ± 0.2, respectively for AZO_5, AZO_{10}, AZO_{15}, and AZO_{20} samples. The fraction area covered by the cells was found to be 24 ± 1 %, 26 ± 2 %, 28 ± 1 %, and 27 ± 2 %, respectively for AZO_5, AZO_{10}, AZO_{15}, and AZO_{20} samples (Figure 1A-3). Hence, no differences as compared to the control cells could be observed, indicating them as cytocompatible. These results clearly indicate that the biocompatibility of ZnO was not altered after doping of Al^{3+} ion at various concentrations into ZnO lattice. This designates the material best fit for various other biomedical applications *in vivo*.

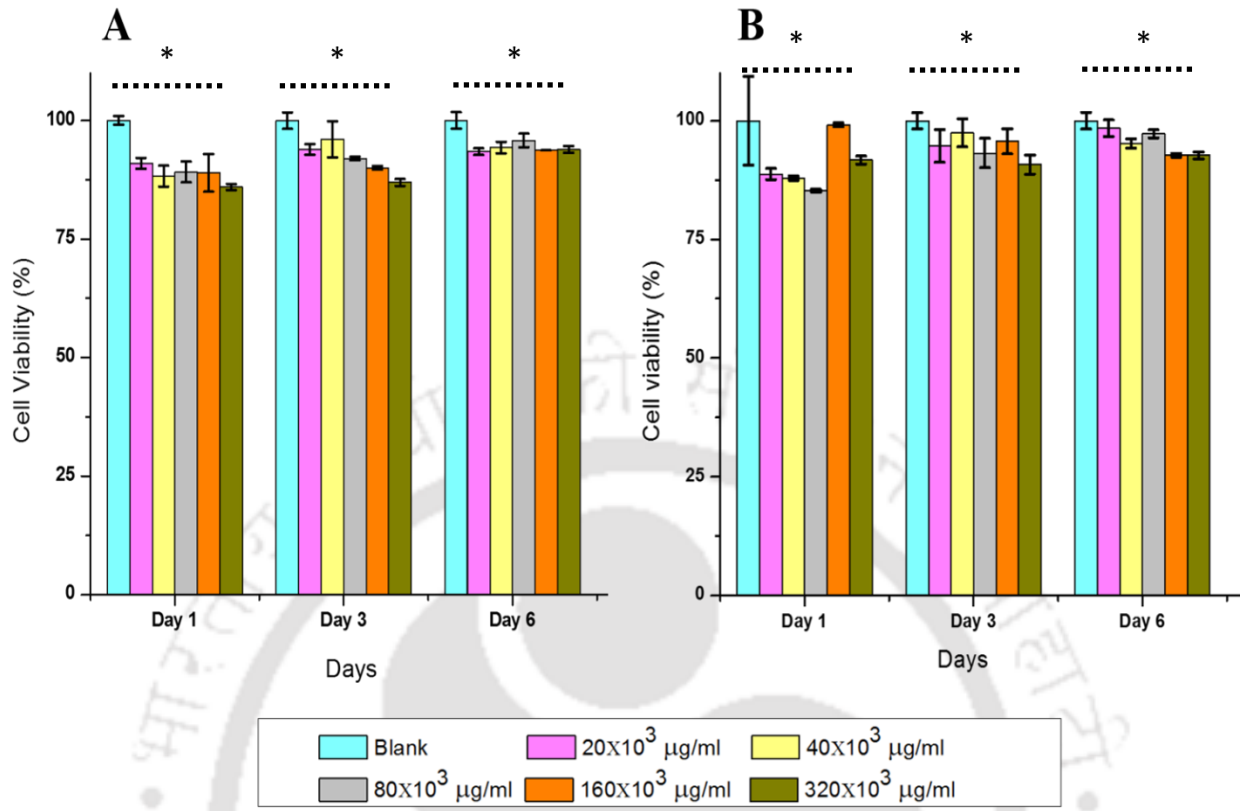

Figure 3.8. *In vitro* cytotoxicity analysis of A) AZO_5, B) AZO_{20}; the results show the cell viability > 93 ± 3 % up to prolonged 6 days of AZO incubation; × *p value* > 0.05; n = 3.

3.2.2.1 Antibacterial assay

The growth for both *E. coli* and *E. hirae* bacteria was hindered in the presence of AZO nanorods. The MIC values were determined against both the bacteria by incubating them at various concentrations of AZO at 1000, 500, 250, 125, 62.5, 31.25, 15.625, and 7.81 µg/ml. The OD_{600} vs. concentration graphs are shown in Figures 3.9A and 3.9B. There is an initial sharp decrease in OD_{600} values followed by a slighter decrease and finally a plateau with an increase in the dosages. The MIC values were chosen as the lowest concentration of AZO, which obstructed bacterial growth. A tangent was drawn to the initial OD_{600} drop, and its intersection point at the lowest OD value was referred to as MIC. Table 3.5 summarizes the regression value, initial slope, and MIC values for AZO nanorods against both bacteria.

Table 3.5. Regression and slope value of the antibacterial activity

S. No.	Sample code	Bacteria					
		E.coli			*E. hirae*		
		R^2 Value	Initial slope	MIC (µg/ml)	R^2 Value	Initial slope	MIC (µg/ml)
1	AZO_0	0.93	-3.22 ± 0.04	254.88 ± 3.18	0.93	-1.64 ± 0.03	338.14 ± 9.34
2	AZO_5	0.79	-24.95 ± 0.24	33.08 ± 0.32	0.77	-7.50 ± 0.01	62.67 ± 0.35
3	AZO_{10}	0.78	-27.79 ± 0.20	29.25 ± 0.14	0.88	-14.81 ± 0.46	35.16 ± 0.84
4	AZO_{15}	0.76	-58.66 ± 1.01	14.33 ± 0.20	0.75	-34.58 ± 0.38	14.68 ± 0.20
5	AZO_{20}	0.80	-19.05 ± 0.68	45.67 ± 1.53	0.95	-9.85 ± 0.21	47.42 ± 0.73

The antibacterial activity of the ZnO was enhanced up to 15 % of Al doping, which was interestingly reduced at 20 % doping. The slope of the AZO_{15} sample against both the bacteria was steepest (-58.66 ± 1.01 for *E.coli* and -34.58 ± 0.38 for *E. hirae*), confirming the more effective antibacterial activity of AZO_{15}. These results are also in correlation to the maximum positive charge of AZO_{15}. The statistical significance of experimental OD_{600} values corresponding to the bacterial growth in the presence of AZO was analyzed, which showed the p-value < 0.001 (n = 6) for all the samples against both bacteria (Figure 3.9C and 3.9D). To further confirm the effectiveness of the MIC values, the *E. coli* cells were treated at MIC of AZO_0 and AZO_{15}. Cells without AZO were taken as positive control and resulted in a typical sigmoidal growth profile, with a specific growth rate of 0.73 h, which is consistent with previous reports [280]. There were no growths of bacterial cells at the MIC of both the samples, confirming that the MICs are effective enough to control the bacterial growth (Figure 3.10).

The enhanced antibacterial activity of the synthesized AZO nanorods can be attributed to their reduced sizes and elevated positive surface charges. AZO_{15} showed the maximum inhibitory action against both the bacteria indorsed to its smallest crystallite size, rod-shaped morphology, and the maximum surface charge. Additionally, AZO_{15} samples were found to be fibrous in their morphology, with maximum homogenous size distribution ranging between 50-100 nm as compared to the other AZO samples. This homogeneity was gradually enhanced with an increase in the Al concentration up to 15 %, and AZO_{20} was found to possess the most heterogeneous size

distribution resulting in the decrease in the antibacterial action. The electrostatic interaction between AZO nanorods (positively change) and bacterial cell surface (negatively charged) attributes to its functional specificity. The reduced antibacterial activity (higher MIC) at 20 % doping of Al can be explained through its spherical-shaped morphology and particle aggregation. Researchers have also explained the morphology-based antibacterial activity of ZnO [252]. Interestingly, we obtained the desired morphology, depending upon the dopant concentration, which resulted in enhanced antibacterial activity.

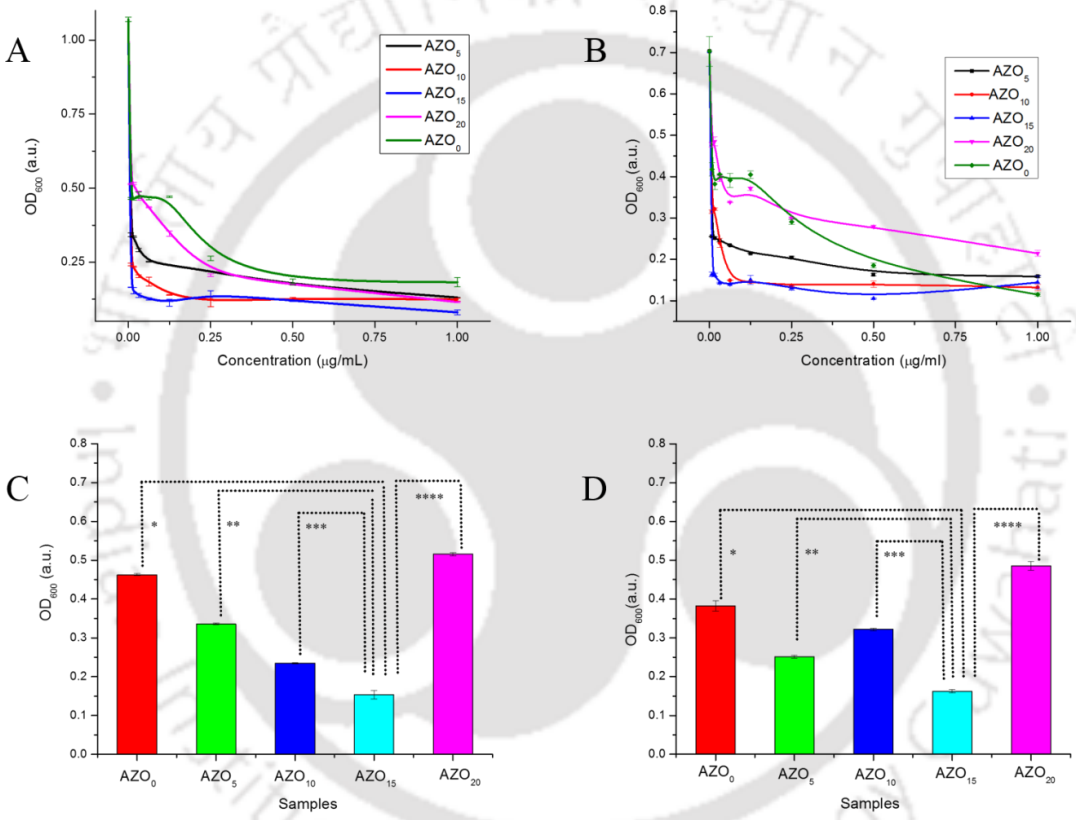

Figure 3.9A, B, C & D. Antimicrobial Activity of AZO_5, AZO_{10}, AZO_{15}, AZO_{20}, AZO_0; against *E. coli* **(A)**; against *E. hirae* **(B);** Statistical dependency of AZO_{15} with *AZO_0, **AZO_5, ***AZO_{10} and **** AZO_{20} (p-value <0.001; *n*=6) at 15.625µg/ml concentration; against *E. coli* **(C)**, against *E. hirae* **(D);** The results shows the effective most antibacterial activity of AZO_{15} against both Gram-positive and Gram-negative bacteria with statistical significance

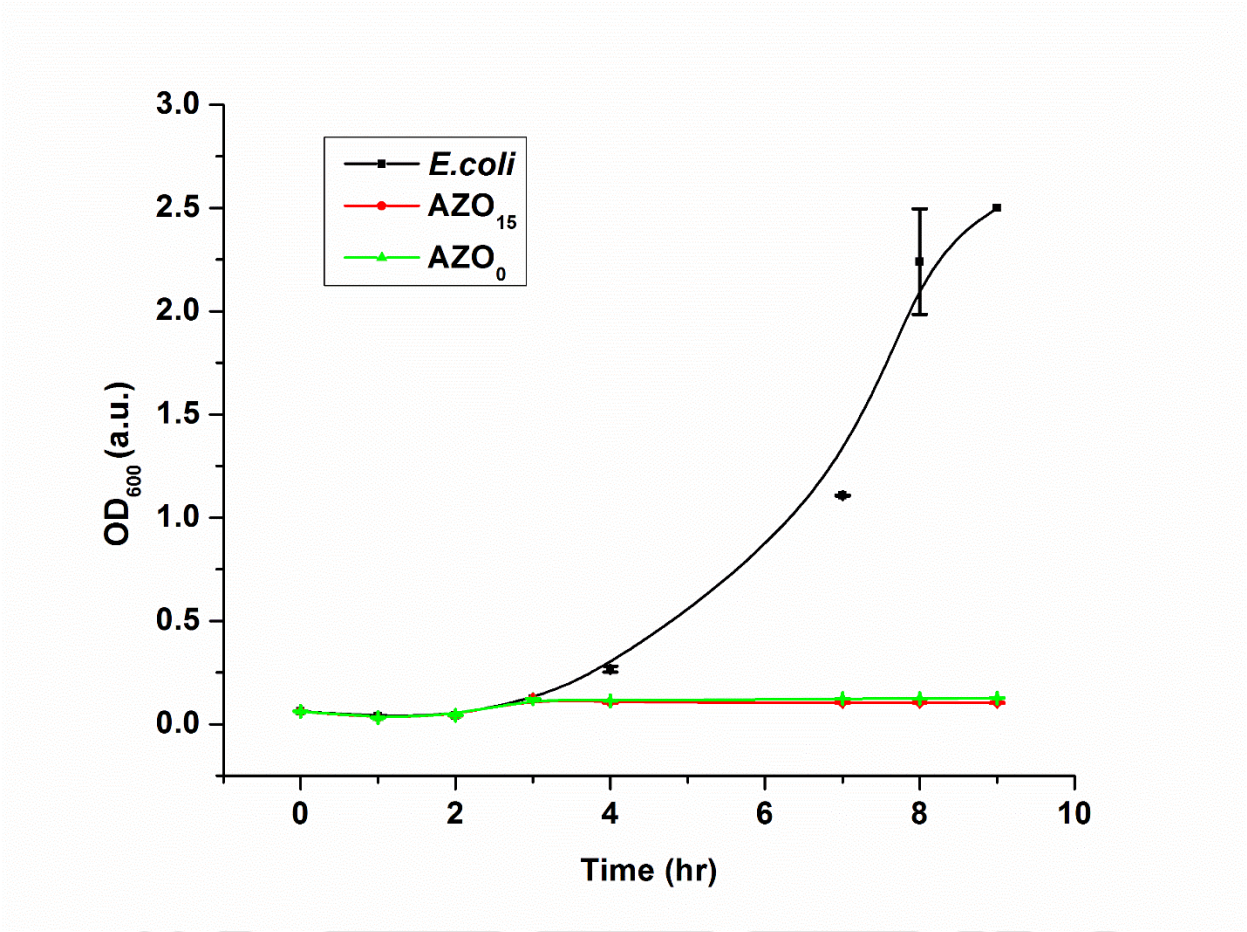

Figure 3.10. Growth kinetics *of E. coli* at MIC of AZO_{15} and AZO_0

3.2.2.2 Antibacterial mechanism of AZO

To analyze the main antibacterial mechanisms of AZO NPs, the bacterial cells were incubated with 500 µg/ml solution of AZO samples for various time intervals (6, 24, and 48 hrs).

3.2.2.2.1 Cells staining and ROS production

The live/dead analysis of the cells was carried out by first staining the cells with CFDA. Figure 3.10A shows the flow cytometry profile for live cells (positive control) density above 10^2 Forward Scattering Counts (FSC) (Figure 3.11A (1)), while dead cells (negative control) density below 10^2 FSC (Figure 3.11A (2)). The flow cytometry profile for CFDA staining revealed a very dense population much lower than the 10^2 events indicating the least number of viable cells after

incubation with AZO samples (Figure 3.11A(3-7)). These observations also confirm no bacterial growth at and above respective MIC values, as shown in Figure 3.9.

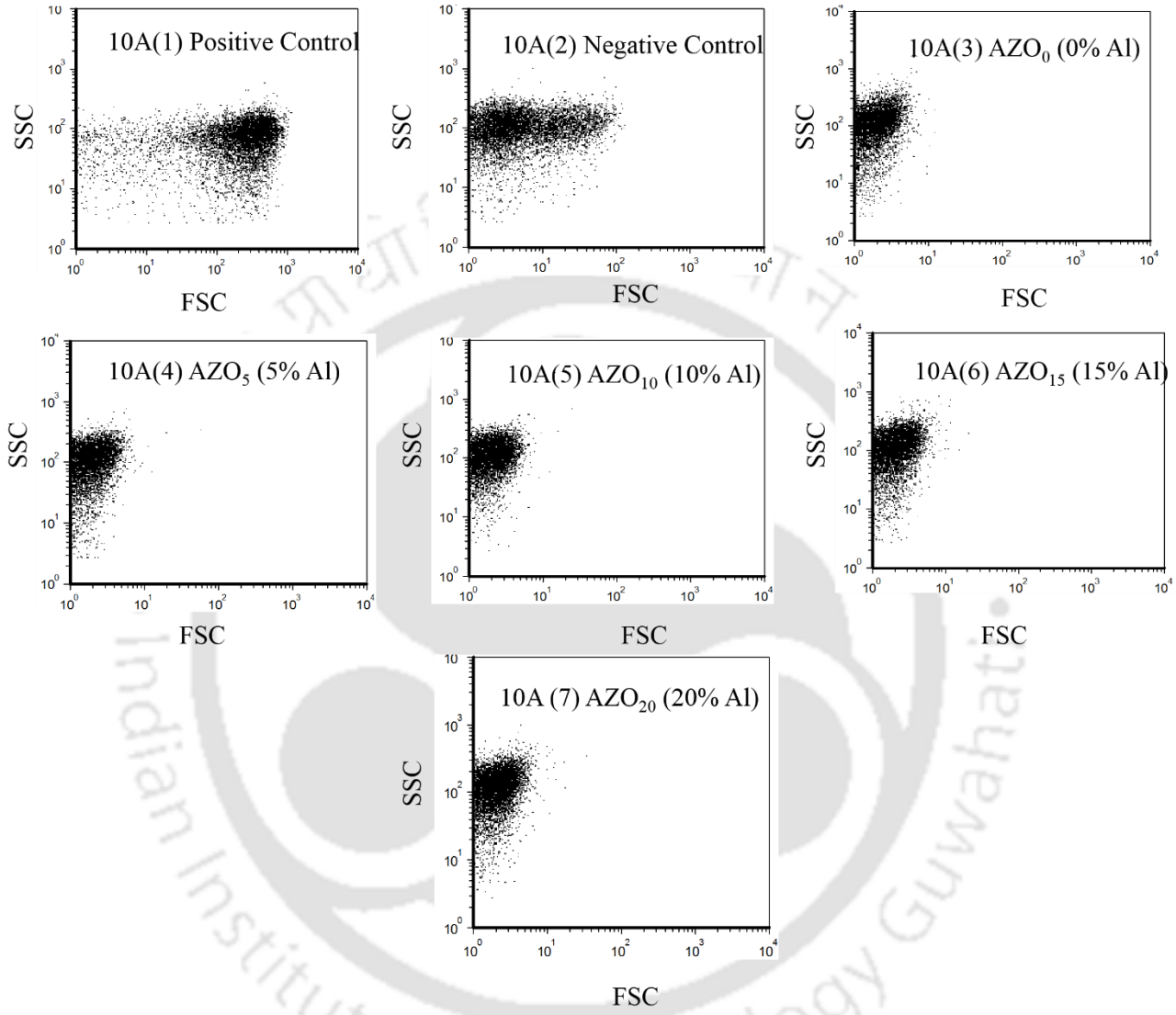

Figure 3.11 A. CFDA staining of samples, (1) Positive control, (2) Negative control, (3) AZO_0, (4) AZO_5, (5) AZO_{10}, (6) AZO_{15}, (7) AZO_{20}

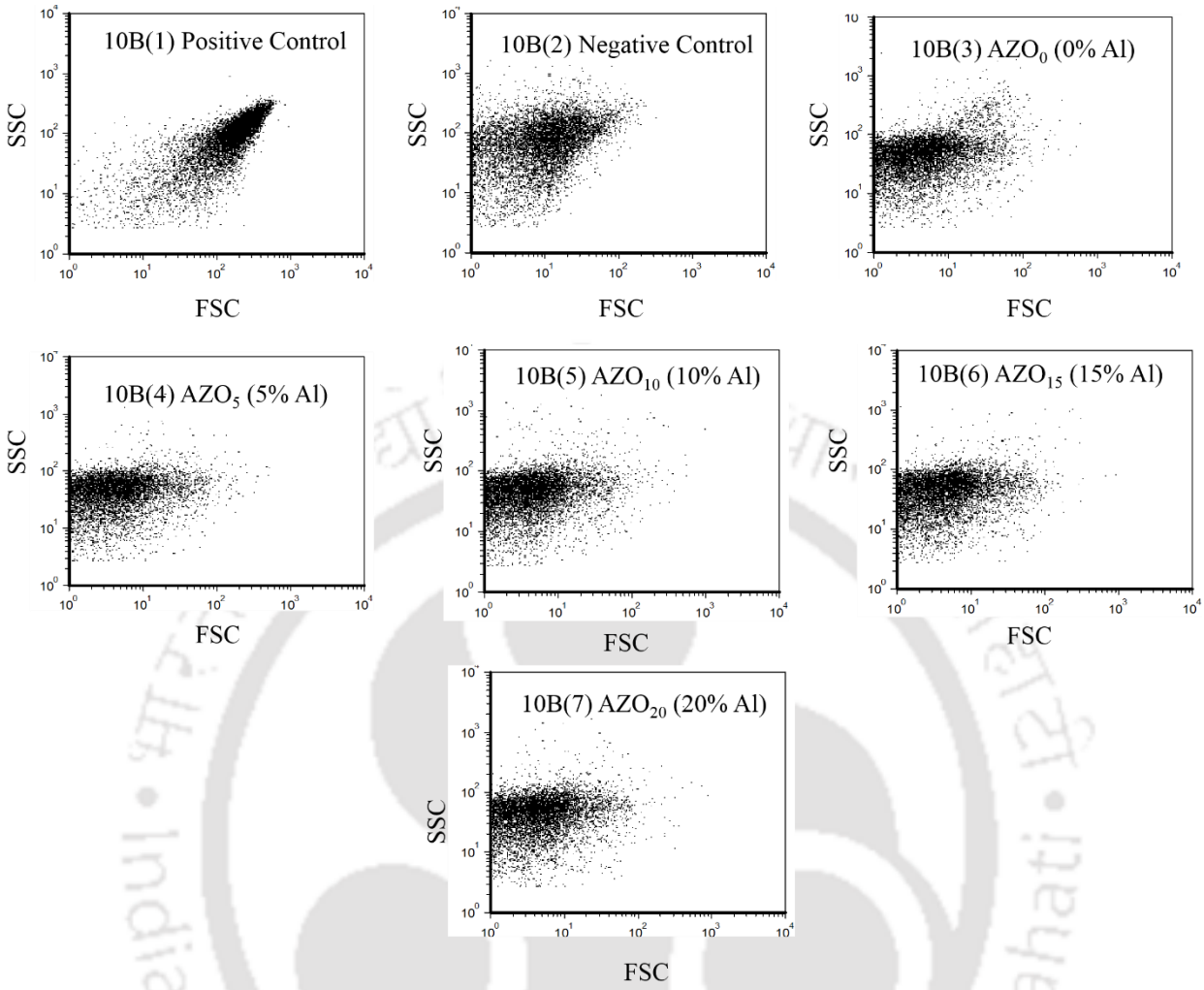

Figure 3.11 B. PI staining of samples, (1) Positive control, (2) Negative control, (3) AZO_0, (4) AZO_5, (5) AZO_{10}, (6) AZO_{15}, (7) AZO_{20}

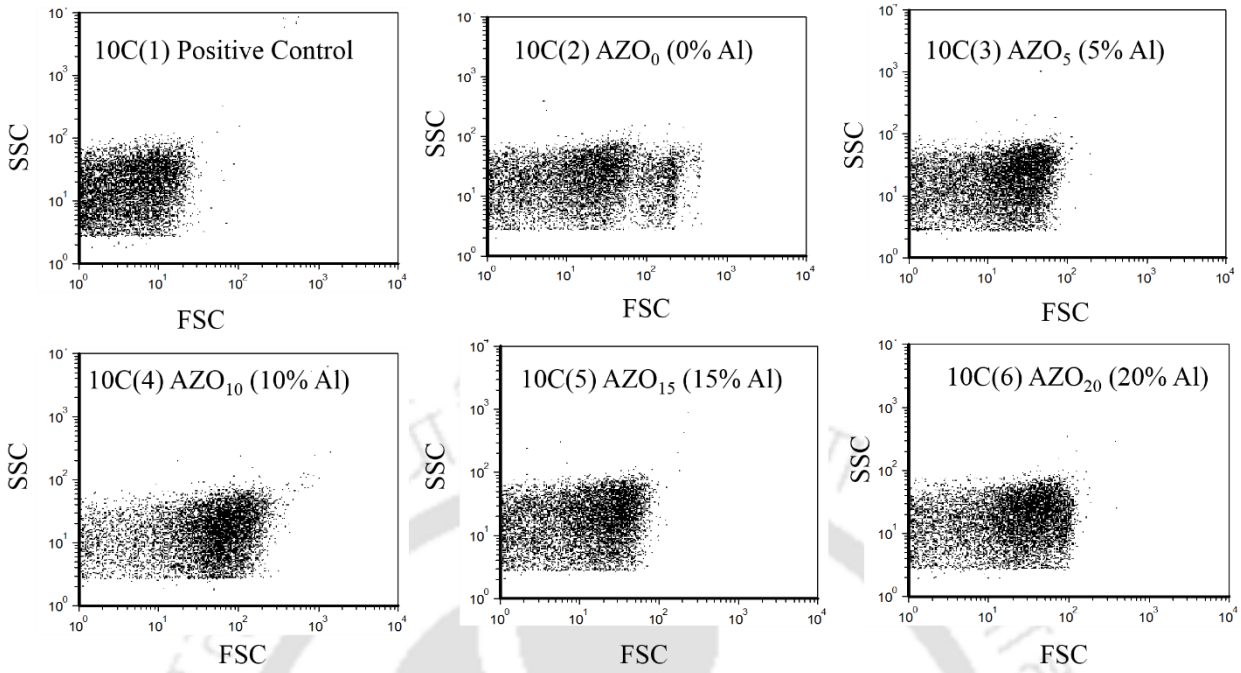

Figure 3.11 C. DCFH-DA staining of samples, (1) Positive control, (2) AZO_0, (3) AZO_5, (4) AZO_{10}, (5) AZO_{15}, (6) AZO_{20}

In a similar way, The PI staining was performed to analyze the cell rupturing / membrane damage in bacterial cells, if any. PI stained dead cells showed population density above 10^2 FSC (Figure 3.11B (1)), while live PI stained cells showed population density below 10^2 FSC (Figure 3.11B(2)). Surprisingly, a lower cell density below 10^2 FSC values was observed after incubation with all the AZO samples (Figure 3.11B (3-7)), indicating no damage to the cell membrane.

The reduction in the OD600 values, as shown in Figures 3.7A and 3.7B, reflects the decrease in the number of viable cells. This can be explained through the fluorescence mechanism of the dyes. CFDA is a lipophilic diacetate dye, which binds with the plasma membrane and is cleaved by intracellular non-specific esterases. Fluorescent carboxyfluorescein (CF) is produced after this cleavage, which remains intact with plasma membrane indicating the live cells' integrity [281]. As no significant CFDA signals were recorded with the incubated cells, the cells can be termed metabolically inactive. Similarly, the nucleic acid staining is achieved using PI only if the cell membrane is damaged [282]. Significant PI signals were not observed for cells treated with AZO samples, indicating no rupturing of the bacterial cell membrane. The CFDA and PI staining together indicated the inactivation of cells rather than the lysis of the cell membrane. This was further confirmed through the FESEM analysis of AZO-treated cells. No apparent cell membrane damage or cell lysis was detected, as shown in Figure 3.12.

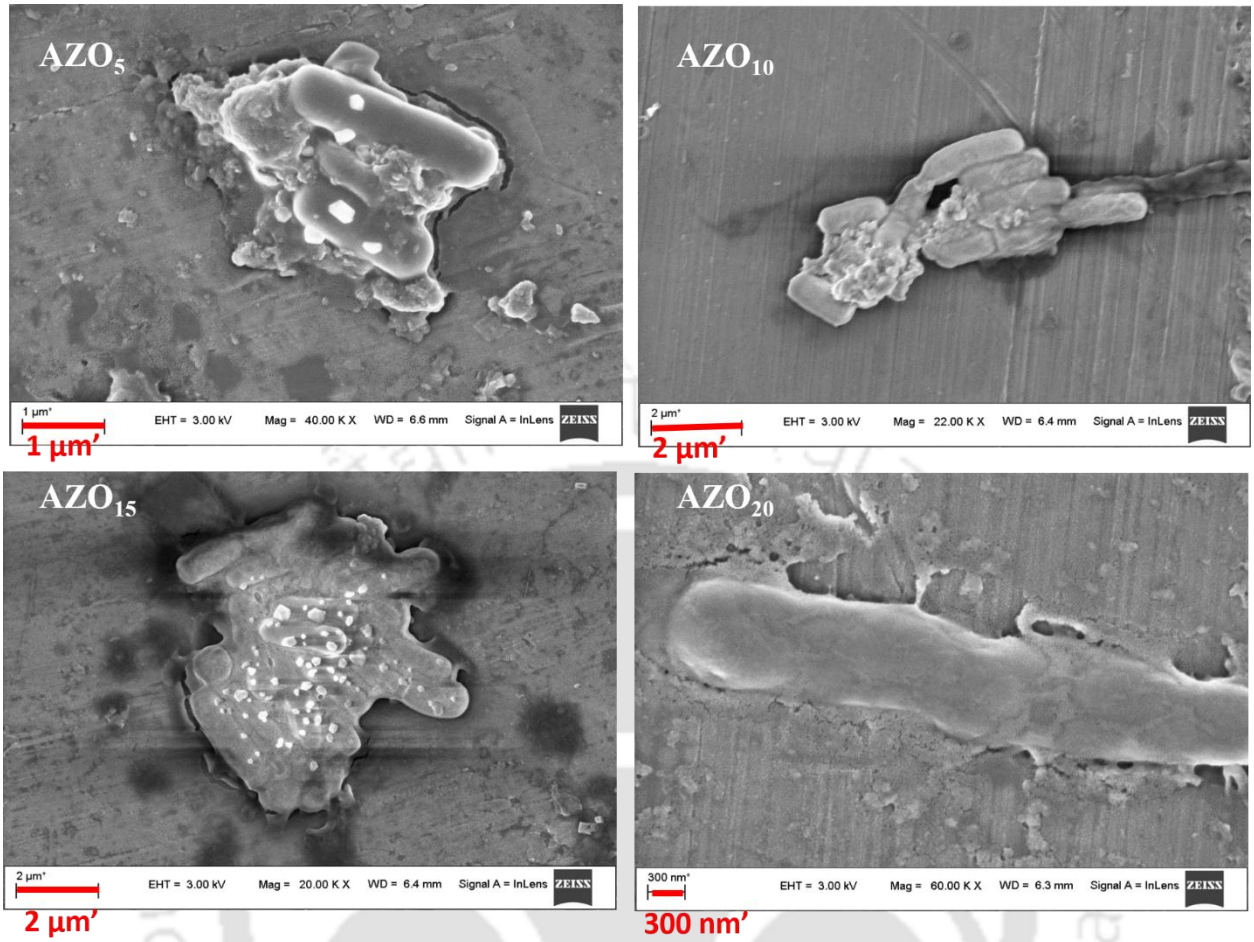

Figure 3.12. FESEM imaging of bacterial cells treated with AZO_5, AZO_{10}, AZO_{15}, AZO_{20}, AZO_0; the figure shows no cell membrane rupturing in the presence of AZO

ROS generation was analyzed using DCFH-DA dye. The staining profile of positive control was not dense, with a low FSC value of 10^1 (Figure 3.11C(1)). However, the DCFH-DA signals could be obtained after incubating the cells with AZO in between 10^1 and 10^2 FSC values, which can be attributed to the auto-fluorescence of the dye (Figure 3.11C(2-6)). There were no significant increases in the ROS production in the presence of AZO samples in saline, LB media, and cells compared to all three controls (*p* values > 0.05) (Figure 3.13). Hence, it can be concluded that ROS production did not attribute to the antibacterial mechanism.

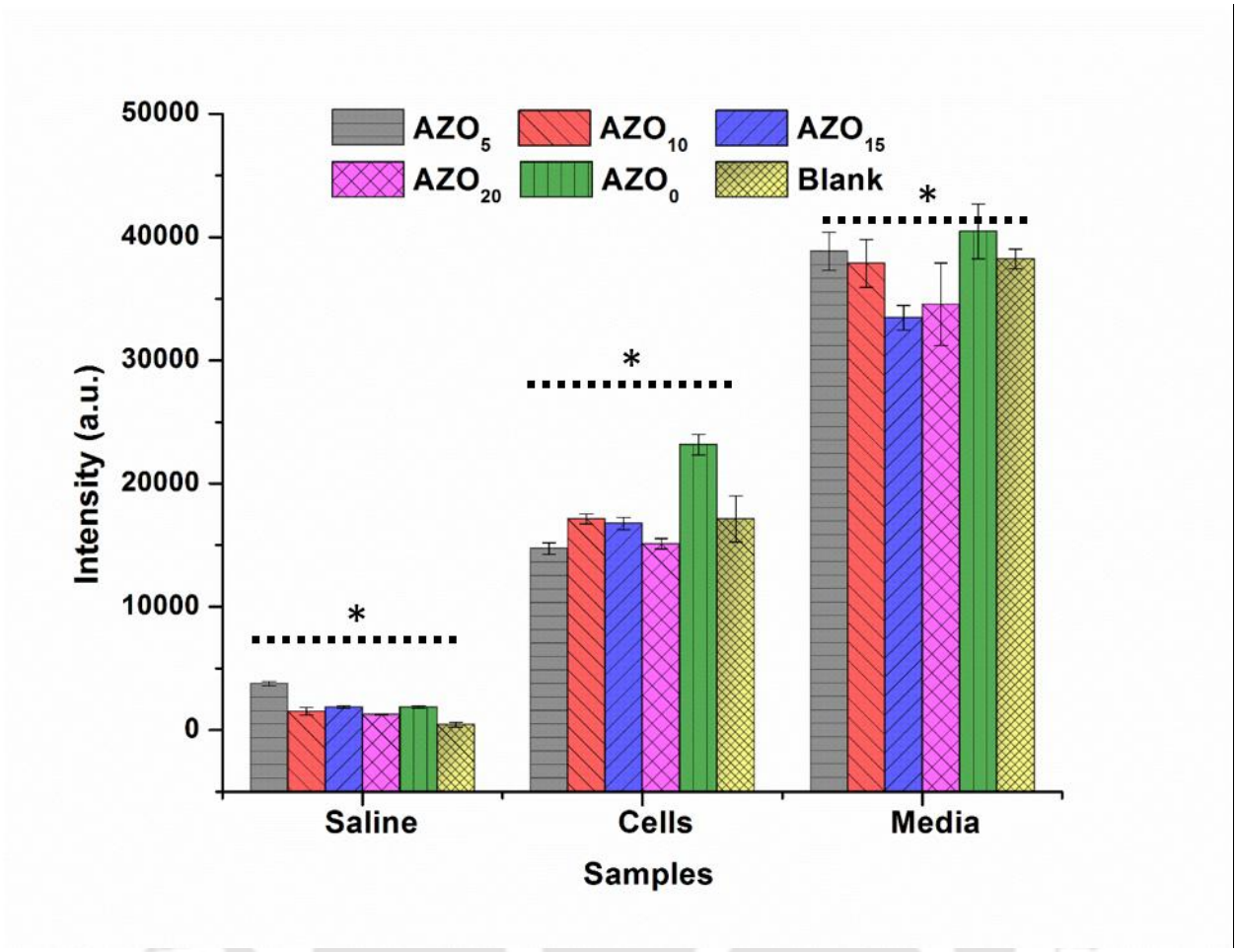

Figure 3.13. ROS production by AZO_5, AZO_{10}, AZO_{15}, AZO_{20}, AZO_0; the result shows no significant ROS production by AZO samples; Statistical analysis as compared to control resulted in *p *value* > 0.05 ; n=2.

3.2.2.2.2 Intracellular accumulation of Zn^{2+} ions

As no noteworthy ROS production could be obtained, the ROS-independent antibacterial mechanism of AZO nanorods was confirmed. To proceed further, the release of Zn^{2+} ions from AZO samples in the presence and absence of cells was calculated. The release of Zn^{2+} ions from AZO samples was examined using AAS in 0.9 % saline solution, LB media, and LB media with bacterial cells. The concentration of released Zn^{2+} ions was found to increase with an increase in incubation time, as shown in Figure 3.14. The release amounts of Zn^{2+} ions from AZO in media and supernatant as well as in saline (0.9 %) and intercellular were found to be comparable, respectively, owing to their similar salinity. Experimental release data for all the samples in various

above solutions were fitted by combining a diffusion-controlled (Higuchi model) and a kinetic controlled (1st order kinetics) models [262, 263, 283], as follows:

$$f_t = A(1 - e^{-k_1 t}) + B(K_H \times t^{0.5}) \quad (3.3)$$

Where f_t is the concentration of Zn^{2+}release (ppm) in time t, A and B are constants, K_H is the Higuchi diffusion constant, and k_1 is the first-order rate constant.

Table 3.6 summarizes the fitted parameters A, B, k_1 and K_H and the fitted data are plotted in Figure 3.14. The release of the Zn^{2+} ions from AZO_0 was majorly diffusion-controlled (kinetic limited) under all the local environments such as intracellular, supernatant, media, and saline, as the K_H. Values were found to be higher for AZO_0 samples, which were decreased with the Al doping. Whereas the release of Zn^{2+} ions from other AZO samples was majorly 1st order kinetic controlled (diffusion-limited), as the k_1 values were higher than that of the K_H values in all the doped samples. Hence, the doped samples reflected first-order release kinetics for its antibacterial action. The kinetics of Zn^{2+} release can be correlated with a change in lattice structure due to the replacement of Zn^{2+} ions with Al^{3+} ions. It is reported that the c/a ratio of ZnO decreases with an increase in Al doping [284]. Smaller atomic radii of Al (R_{aAl} =1.18 Å) as compare to Zn (R_{aZn}=1.42 Å) presumably eliminated the diffusion-controlled release of Zn^{2+} ions. Therefore, all AZO samples except AZO_0 resulted in a kinetically controlled release of Zn^{2+} ions. The release of the Zn^{2+} ions was increased with an increase in the Al doping up to 15 % with the maximum release for AZO_{15} and further decreased at 20 % Al doping. The rate constant k_1 values were found to be the maximum for the release of Zn^{2+} ions from AZO_{15} samples in various solutions. The highest release of Zn^{2+} ions in the presence of AZO_{15} is attributed to its lowest MIC value.

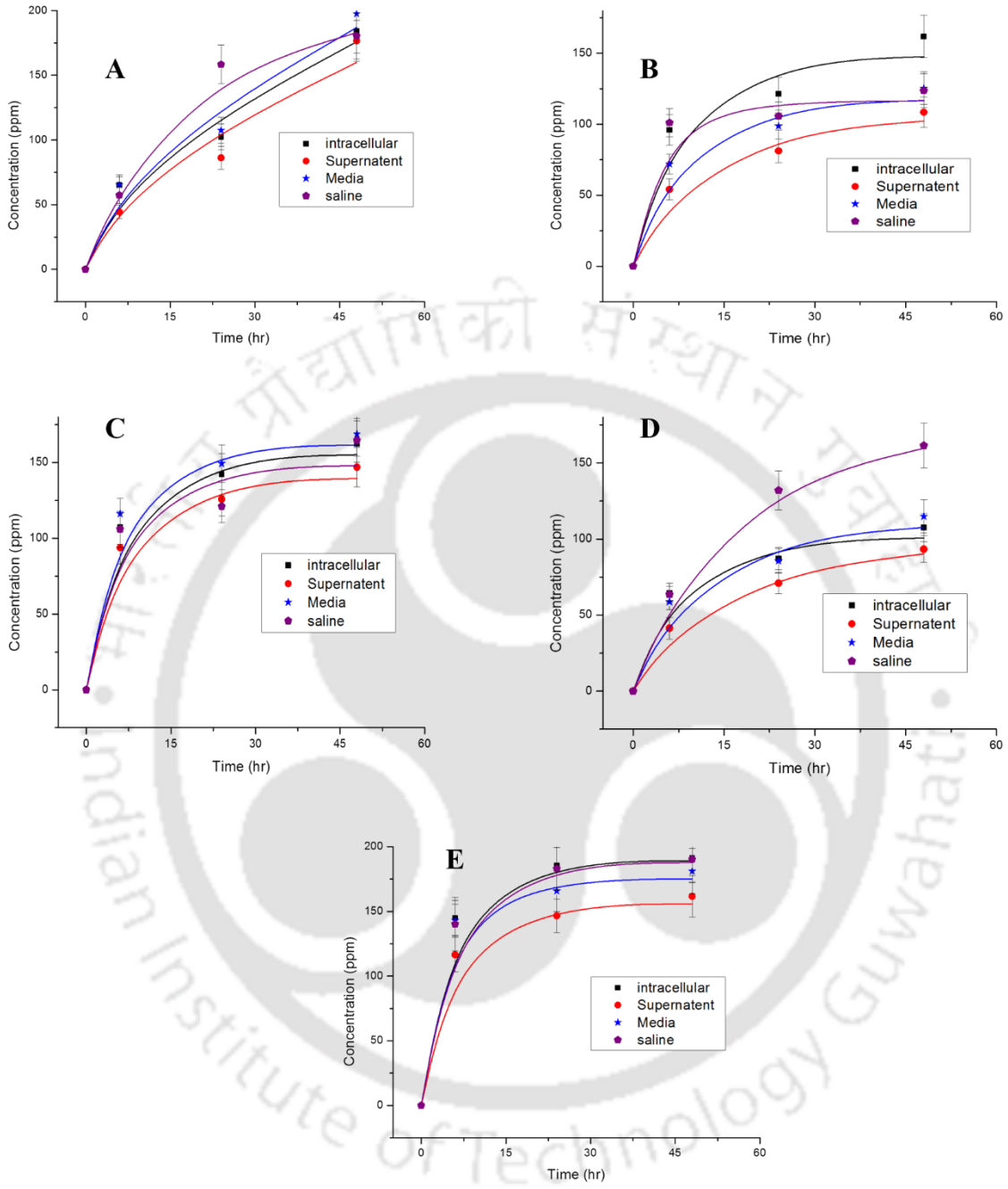

Figure 3.14. The release profile of Zn^{2+} ions from A) AZO_5, B) AZO_{10}, C) AZO_{15}, D) AZO_{20}, E) AZO_0 in various local environments; scattered data are experimental values and fitted data are plotted as line graph.

Table 3.6. Kinetic parameters for the release of the Zinc ions in saline, media, supernatant and intracellular for various AZO samples

Sample code	Intracellular Zinc (ppm)				Zinc released in cell supernatant (ppm)				Zinc released in LB Media (ppm)				Zinc released in 0.9% Saline (ppm)			
	A (ppm)	B (ppm)	K_1 (h^{-1})	K_H ($h^{-0.5}$)	A (ppm)	B (ppm)	K_1 (h^{-1})	K_H ($h^{-0.5}$)	A (ppm)	B (ppm)	K_1 (h^{-1})	K_H ($h^{-0.5}$)	A (ppm)	B (ppm)	K_1 (h^{-1})	K_H ($h^{-0.5}$)
AZO_0	102	82.35	0.007	0.251	86	90.67	0.015	0.182	107	90.46	0.010	0.231	169.99	10.47	0.069	0.264
AZO_5	98	9.53	0.162	0.040	85.15	8.12	0.082	0.118	106.56	8.3	0.107	0.027	160.78	0.62	0.075	0.745
AZO_{10}	144.22	17.51	0.163	0.027	101.77	6.67	0.101	0.027	114.75	10.60	0.147	0.027	114.73	8.86	0.345	0.027
AZO_{15}	188.74	2.55	0.242	0.027	154.61	6.99	0.229	0.027	173.58	7.53	0.286	0.027	187.17	3.20	0.228	0.027
AZO_{20}	153.19	9.22	0.193	0.031	137.76	9.18	0.181	0.027	159.86	8.95	0.210	0.027	144.05	20.55	0.206	0.027

3.3 Antibacterial mechanism of AZO

From section 3.7.1, it is confirmed that a very small amount of ROS is being produced, which cannot be much effective for the inactivation of the bacterium. The intracellular accumulation of the Zn^{2+} ions may be one of the major causes of the bacterial cells' inactivation. Doping of Al enhances the electrical conductivity [285] and surface charge (positive) over the ZnO lattice as suggested by zeta potential, which helps in enhanced electrostatic interactions between the bacterial cells and AZO nanorods [286]. The zinc release study indicated the internalization (transport) of Zn^{2+} ions into the cytoplasm of the bacterial cells after the electrostatic binding of AZO with cells caused bacterial inactivation.

The intracellular Zn^{2+} ions cause damage to the DNA and proteins of the bacterial cells, which consequently turns bacteria into an inactive form. Ara joe *et al.* 2017, explained the role of membrane metalloproteins such as the ATP-binding cassette (ABC) family and Natural resistance-associated Macrophage Protein (NRAMP) in the transportation of transition metal ions into the cytoplasm. The exporter metalloproteins maintain the homeostasis of competitive metals in the Irving–Williams series (*i.e.,* Zn^{2+} and Cu^{2+}). However, at higher concentrations of Zn^{2+} ions, the critical selectivity of these metalloproteins loses, which consequently results in the transport of more Zn^{2+} ions intracellularly instead of other noncompetitive metal ions (*i.e.,* Ca^{2+} and Mg^{2+}) [287]. We have also observed a higher concentration of Zn^{2+} ions intracellular than in supernatant. Various researchers have also confirmed the antibacterial activity of ZnO by cellular internalization of Zn^{2+} ions under dark conditions [288, 289]. The exponential release of the ions caused the excessive Zn^{2+} concentrations at the bacteria-nanorods interface, leading to the internalization of the Zn^{2+} ions, causing damages to the genomic or protein material of the bacteria. This leads to the metabolic inactivation of the bacterial cells. Hence, the major mechanism of bacterial inactivation through AZO remains the electrostatic interaction between AZO and cells followed by the Zn2+ ions' internalization. The burst release of the Zn^{2+} ions in the first 6 h inhibited the cellular growth in the log phase, followed by a slower release of Zn2+ ions, which may help in prolonged antibacterial activity of the synthesized AZO.

3.4 Conclusions

In this chapter, we successfully synthesized different Al-doped ZnO (AZO) nanorods and characterized their physical and chemical properties. AZO samples possessed the hexagonal

wurtzite structure and nanorods assembly. The size and morphology of the AZO nanorods were found to be governed by the dopant concentration. Hence, the morphology and the size of the ZnO NPs could be altered by synthesizing the NPs through a simple precipitation method, depending on the choice and concentration of the dopant. The positive surface charge was found to increase with the increase in Al doping and was found to be the maximum for AZO_{15}, which in turn significantly enhanced the antibacterial activity. As expected from the surface charge and particle size values, the MIC values were found to be decreased with an increase in the Al concentration. AZO_{15} resulted in the least MIC values of 14.33 ± 0.20 and 14.68 ± 0.20 µg/ml against both *E. coli* and *E. hirae*, bacteria, respectively. The pristine ZnO reflected the MIC value of 254.88 ± 3.0 and 338.14 ± 9.0 µg/ml against *E. coli* and *E. hirae*, respectively. Hence, the MIC values were decreased by ten folds as compared to ZnO nanorods at Al doping.

The present findings explained the electrostatic interaction between the bacterial cell and the AZO, followed by the internalization of the Zn^{2+} ions as the main antibacterial mechanism of the AZO. The release of the Zn^{2+} ions from the AZO lattice was found to be kinetic controlled and diffusion-limited, which will aid in the prolonged antibacterial activity of the AZO. The AZO nanorods did not rupture the bacterial cells, but the bacterial cells were inactivated. No rupturing in the bacterial cell wall could be obtained while staining the cells with PI or while the FESEM analysis of the treated bacterial cells. However, at MIC value, the bacterial cells did not show any growth, indicating the metabolic inactivation of the bacteria. Exponential release of the Zn^{2+} ions due to the presence of crystal defects caused by the presence of Al reasons the charge imbalance at the bacteria-nanorods interface leading to the internalization of the Zn^{2+} ions. Hence, the antibacterial mechanism of the ZnO nanorods was controlled by the dopant choice and concentration.

This chapter correlated the physical and chemical properties of synthesized AZO nanorods with their antibacterial mechanism, which will help design efficient nanoantibiotics for sustained uses. The study provides in-depth knowledge to develop more efficient nanoantibiotics against resistant bacteria and reduce traditional antibiotics' harmful side effects.

Chapter 4

Design and characterization of Fe(III) doped ZnO nanoparticles (NPs) and evaluation of its antibacterial mechanism

This chapter explains the design of Fe doped ZnO (FZO) NPs. Similar to that of Chapter 3, the FZO NPs were synthesized via a simple co-precipitation method. Identical to that of AZO NPs, FZO NPs also acquired the typical hexagonal wurtzite structure of ZnO with an increase in the lattice parameters with increasing dopant concentration. The FZO NPs possessed dual morphology of rod-shaped and particulate shaped with < 100 nm of one dimension and a lower surface area (2.301 m^2/g). Additionally, the FZO NPs reflected the soft ferromagnetism and positive surface charge. FZO NPs possessed enhanced antibacterial activity than ZnO and AZO at 15% doping of Fe(III). FZO_{15} resulted in the least IC_{50} value of 0.20 µg/ml. Here, the rupturing in the bacterial cell wall through the release of Zn^{2+} and Fe^{3+} ions was found to be the main bactericidal mechanism. Furthermore, high cytocompatibility at 20 times higher concentration than MIC value was obtained.

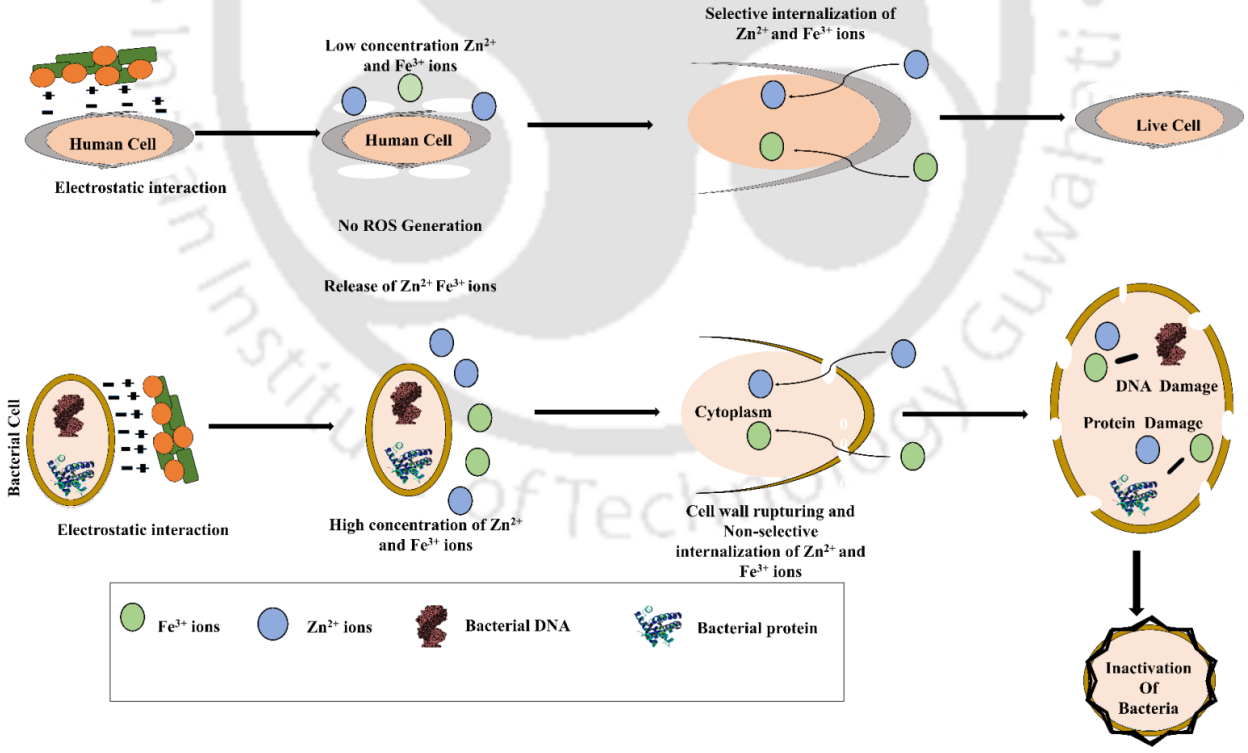

Schematic 4.1. Proposed cytotoxicity mechanism of FZO NPs (J. Trace Elem. Med. Biol. 57: 126416, 2020)

4.1 Introduction

As discussed in Chapters 2 and 3, ZnO NPs are one of the most studied nano-systems for biomedical applications [126, 290, 291] and have been proven to offer a broad spectrum of antibiotic activities. However, the ZnO NPs synthesized by the co-precipitation method possessed higher MIC values due to larger particle size than that of ZnO NPs produced through sophisticated techniques. The AZO NPs reflected their main antibacterial mechanism by the release of Zn^{2+} ions, followed by internalization. However, no rupturing in the bacterial cell wall could be obtained [292].

Majorly, ZnO NPs cause genotoxicity and damage in the cell wall through the generation of ROS [293, 294] or by photocatalytic activity [295, 296]. The ROS are undesirable for clinical applications, as it is found to cause cytotoxicity for human cells as well at elevated concentrations [297, 298]. However, ZnO has been conflicted for its cytotoxicity to the human cells [299], yet it has also been effective against various superbugs [300]. Henceforth, the medical implementation of ZnO NPs is still under extensive research. It is essential to reduce the MIC values of ZnO nanoantibiotic, as well as to achieve the ROS-independent antibacterial mechanism for the effective clinical applications of ZnO. Various reports affirmed that ZnO's antibacterial activity is size and morphology-dependent [13]; hence, altering the dimensions of ZnO crystal is expected to lower MIC values. The antibacterial mechanisms are reported to differ based on the dopant types and their concentrations. [125, 301, 302]. Fe-based complexes have been proven to produce enhanced antibacterial activities against various pathogens [33, 303]. Also, due to their magnetic properties, Fe-based nanomaterials provide target efficiency for the localized antibacterial action, and its degradation has been found to be faster, *i.e.*, within 28 days [304]. Hence, Fe^{3+} ions were doped into the ZnO lattice due to their ionic radii of Fe^{3+} (0.06 nm) lesser than that of Zn^{2+} (0.074 nm), which is expected to amend the crystal defects in the ZnO lattice to enhance its antibacterial activity without implying any cytotoxicity. Additionally, doping of Fe(III) may introduce rupturing of bacterial cells as an antibacterial mechanism via quick release of metal ions, owing to the smaller size than Zn and Al.

4.1 Materials and methods

4.2 Materials

All the chemicals were utilized to prepare FZO as that of AZO, except Ferric chloride anhydrous $FeCl_3$ (Merck India, 6178905001730). Similar chemicals were used for the detection of the antibacterial mechanism, as given in section 3.1.1.

4.2.1 Preparation of FZO NPs

The FZO NPs were synthesized through a similar co-precipitation method. In brief, 50 ml of (1-M) molar concentrations of $Zn(NO_3)_3.6H_2O$, (where M=0, 0.05, 0.1, 0.15, 0.20) solution was mixed with M molar anhydrous $FeCl_3$ solution at 65 °C. To this solution, 2 M and 50 ml NaOH (preheated at 65 °C) solution was added dropwise. After titration, the synthesis reaction mixture was kept at continuous stirring for 3 h. The precipitate was then separated out and was washed with deionized water (18mΩ, Milli-Q, Millipore systems) until neutral pH, followed by drying at 80ºC. The samples were then sintered at 650 ºC.

4.2.2 Characterizations of the synthesized materials

The synthesized FZO NPs were characterized over various physical techniques as given in section 3.1.3.

4.2.3 Biological Characterizations

The synthesized NPs were tested for their cytotoxicity against both bacterial and human cells. The detailed procedure is as follows:

4.2.3.1 Antibacterial activity and determination of MIC/Minimum Bactericidal Concentration (MBC) values

The antibacterial activity of the synthesized NPs was carried out using a broth dilution method. Four clinically significant bacteria (Two gram-positive and negative each) were chosen to analyze the broad spectrum of the synthesized nanoantibiotic. These bacteria include *Escherichia coli* (*E. coli*, Gram-negative, MTCC 1610; *S paratyphi* Gram-Negative, MTCC 735) and *Enterococcus hirae* (*E. hirae*, Gram-positive, MTCC 3612; *S. aureus*, MTCC 6538). The MIC values were calculated using the same protocol as that of AZO nanorods. Additionally, the concentration at

which FZO NPs completely killed the bacterial cells was considered as the MBC. The effectiveness of the MIC concentration was tested using a disc diffusion method. In detail, the bacterial cells at OD_{600}=0.025 were spread over the agar plate, and small discs carrying FZO NPs, and Kanamycin (30 µg disc concentration) were placed at respective sites. The corresponding Zone of Inhibition (ZOI) was then measured and compared to Kanamycin's ZOI.

4.2.3.2 Nano-cytotoxicity analysis for Human cells

The nano-cytotoxicity of the FZO NPs was analyzed using tetrazolium dye MTT [3-(4,5-dimethylthiazol-2-yl)-2,5-diphenyltetrazolium bromide assay, same as that of AZO (Section 3.1.4.1) using Human osteosarcoma cell lines (MG-63, NCCS, India).

4.2.3.3 Analysis of the antibacterial mechanism

Similar to that of AZO, as given in section 3.1.3, the antibacterial mechanism were identified using flow cytometry and Atomic Absorption Microscopy (AAS).

4.2.3.3.1 The release of Zn^{2+} ions

The release of FZO NPs was examined using the same protocol as given in section 3.1.4.3.2.

4.3 Results and discussion

Four different concentrations of Fe(III) were doped into the ZnO lattice. The molar concentrations of the precursor ions and the respective sample codes are listed in Table 4.1. Same sample codes are referred throughout the chapter.

Table 4.1. Sample codes and the molar percentages of the respective ions

S.No	Sample Code	$Zn(NO_3)_2.6H_2O$ (M)	$FeCl_3$ (M)	NaOH (M)
1	FZO_5	0.95	0.05	2
2	FZO_{10}	0.90	0.10	2
3	FZO_{15}	0.85	0.15	2
4	FZO_{20}	0.80	0.20	2

4.3.1 Physical characterizations of the synthesized FZO NPs

The successful synthesis of FZO NPs was confirmed using XRD, Raman, and FTIR analyses. The XRD data, as shown in Figure 4.1A, revealed the classical hexagonal wurtzite structure of FZO NPs (2θ=31.84 (010), 34.55(002), and 36.35 (011)), corresponding to the JCPDS ID (98-002-8858). As shown in Figure 4.1A, the XRD result imitated a smaller peak corresponding to the Fe_3O_4 at 2θ values of 35.45º and 62.61º (JCPDS 98-001-7122). Nevertheless, no other significant peak corresponding to the Fe_3O_4 could be observed. Hence, Rietveld refinement of the XRD data was performed to confirm the presence of Fe^{3+} ions in the ZnO lattice, either as an impurity or replaced ions in the ZnO lattice. The XRD patterns were refined using FullProf software for hexagonal P63/m space group symmetry, as described elsewhere [305, 306]. The refined pattern (solid line, Figure 4.1B) and the recorded pattern (open circle) are represented in Figure 4.1B. The reliability parameters and lattice parameters are listed in Table 4.2. The refinement data revealed that Fe^{3+} ions were present in the form of Fe-O impurity in the ZnO lattice. The impurity level was increased with an increase in the concentrations of the Fe^{3+} ions (High R_{Bragg} values as listed in Table 4.2). FZO_{20} sample was found to possess the maximum impurity, and FZO_{15} sample was found to carry the minimum impurity, resulting in a very low-intensity peak corresponding to the Fe_3O_4 at 2θ values of 35.45º. As shown in Table 4.2, the refinement values reflected that lattice parameter a, b, and c of the hexagonal wurtzite structure were increased with an increase in the Fe^{3+} ion concentrations. The crystal size was found to be increased up to 15 % doping of Fe^{3+} (Table 4.2), which was reduced at higher (20 %) dopant concentration indicating the maximum crystallinity up to 15 % doping, which resulted in the reduction in the crystal size by 50 % in increasing the dopant concentration from 15% to 20 %. At intermediate zinc concentrations (15 % < x < 65 %), the material transforms into a nano-composite rather than doping [307]. Similarly, in this study, FZO_{20} was found to be with maximum impurity and the least crystallinity. Therefore, further doping concentrations were not tested. The crystallinity and orientation uniformity is important for various biomedical applications such as cytocompatibility and surface coated materials [308, 309].

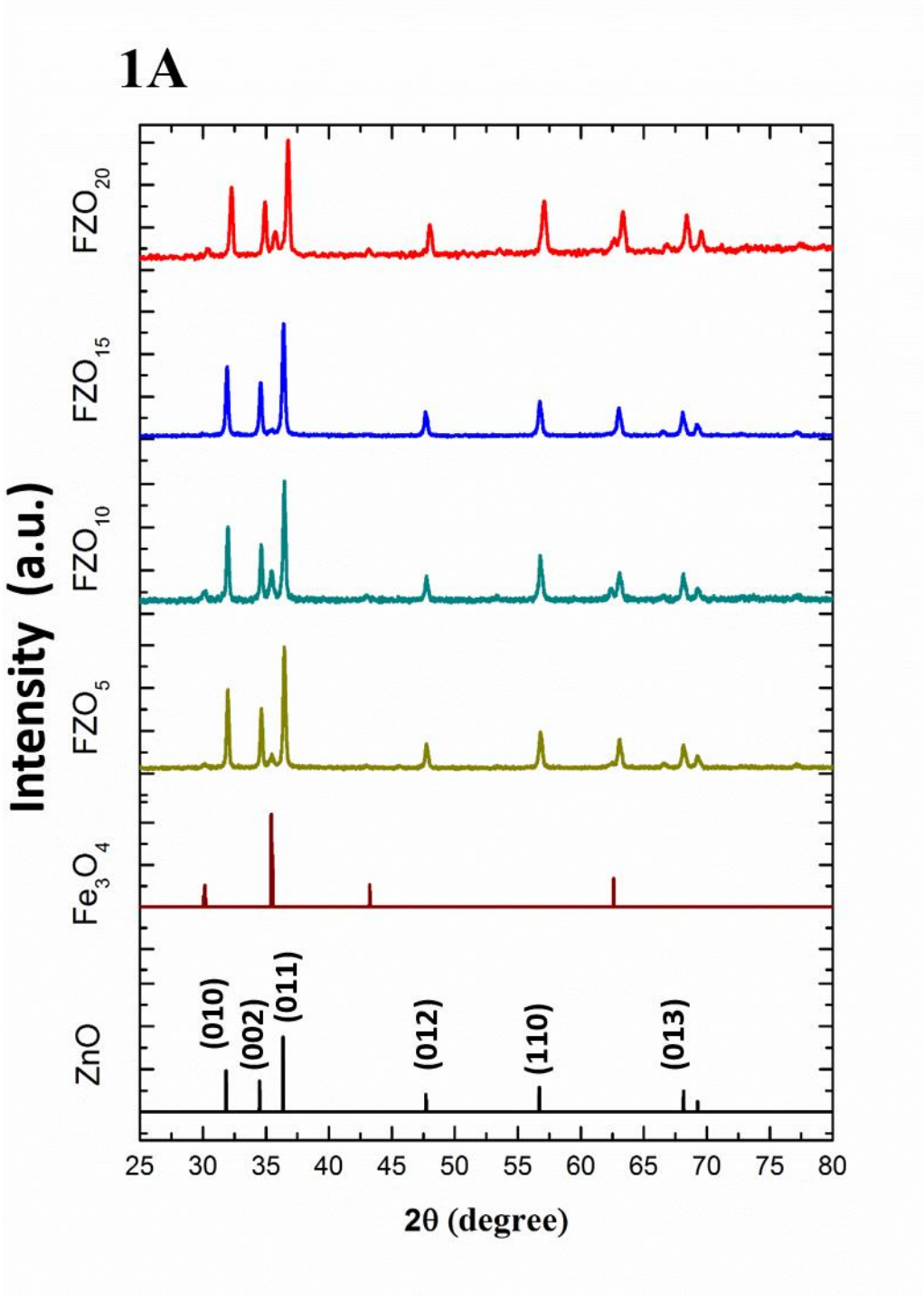

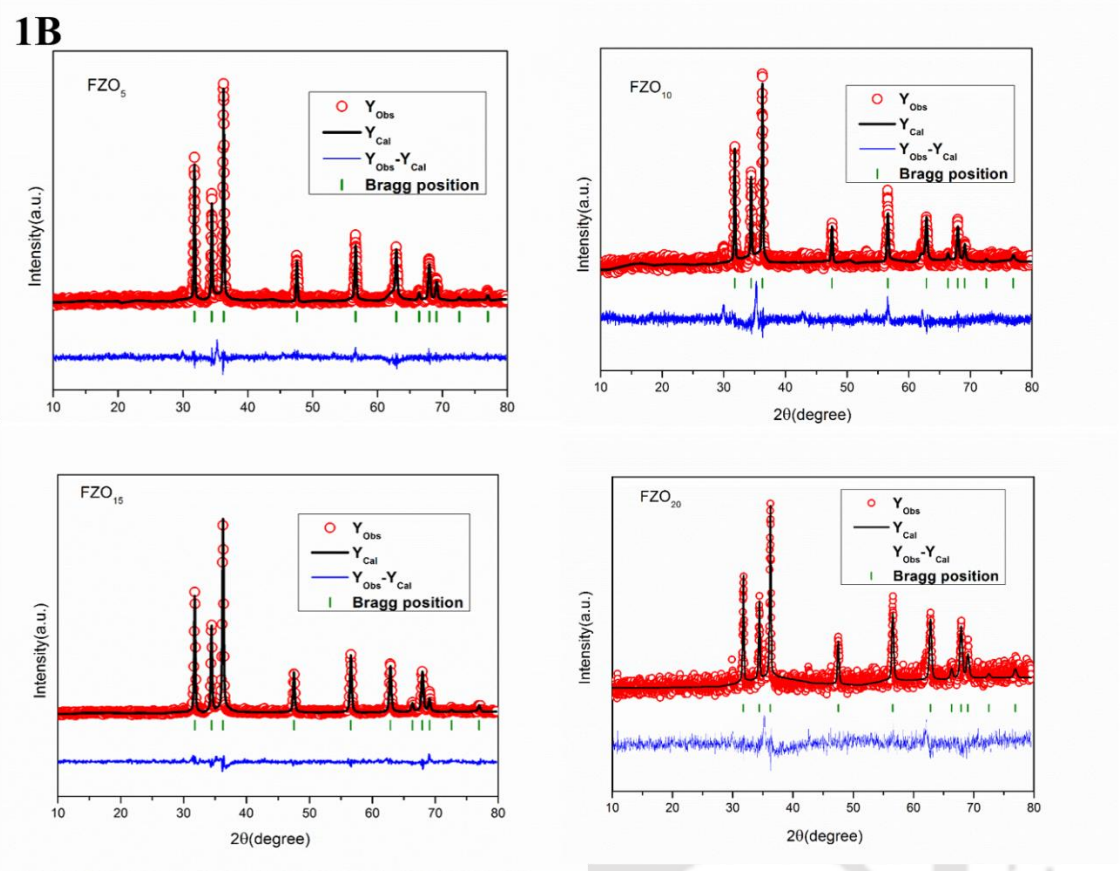

Figure 4.1. XRD data of FZO_5, FZO_{10}, FZO_{15}, and FZO_{20} along with standard ZnO JCPDS ID (98-002-8858), and Fe_3O_4 (JCPDS 98-001-7122) **(A),** Rietveld refinement of FZO_5, FZO_{10}, FZO_{15} and FZO_{20} NPs **(B)**

Table 4.2. Rietveld refinement parameters and crystal sizes of various FZO NPs

S.No.	Sample	R_{bragg}	R_f	χ^2	Lattice Parameters (nm)			Occupancy			Crystal Size (nm)
					a	b	c	Zn	Fe	O	
1	FZO_5	12.3	13.4	1.75	0.3239	0.3239	0.5187	0.958	0.05	1	55.14
2	FZO_{10}	14.95	22.09	2.06	0.3233	0.3232	0.5187	0.938	0.10	1	62.49
3	FZO_{15}	3.44	4.89	1.96	0.3230	0.3230	0.5186	0.848	0.145	1	72.77
4	FZO_{20}	23.5	21.2	1.58	0.3219	0.3217	0.5186	0.800	0.22	1	37.85

Where R_{Bragg} is the Bragg factor, R_f is the crystallographic factor, and χ^2 refers to the goodness of fit.

As can be obtained from Table 4.2, the Fe/Zn (0.05, 0.10, 0.17, and 0.27 for FZO_5, FZO_{10}, $FZO_{15,}$ and FZO_{20}, respectively) ratios were found to be equivalent with the Fe/O (0.05, 0.10, 0.145, and 0.22 for FZO_5, FZO_{10}, $FZO_{15,}$ and FZO_{20}, respectively) ratios indicating the homogenous distribution of Fe into the ZnO lattice. However, for FZO_{20} samples, these ratios were differed, resulting in the heterogeneous size distribution. However, the Fe+Zn/O ratios were 1.008, 1.038, 0.993, 1.02, respectively, for FZO_5, FZO_{10}, $FZO_{15,}$ and FZO_{20} samples. A slight decrement in Fe+Zn/O ratio indicates an anion-rich FZO lattice as compared to other cation-rich FZO samples. Raman and FTIR spectra of the synthesized NPs were recorded to confirm the successful synthesis of FZO NPs. After doping of Fe^{3+} ions into the ZnO lattice, the vibrational peaks at 341 and 436 cm^{-1} were obtained (Figure 4.2A). The shift in the classical E2 (high) vibration mode from 438 cm^{-1} wavenumber reflected the successful doping of F0.10, e^{3+} ions into the ZnO lattice. Similarly, the classical hexagonal wurtzite lattice reflected the stretching of Zn-O at 436 cm^{-1} in FTIR spectra [310]. We also observed a blue shift from 431 cm^{-1}, which indicated the replacement of Zn^{2+} ions with Fe^{3+} ions.

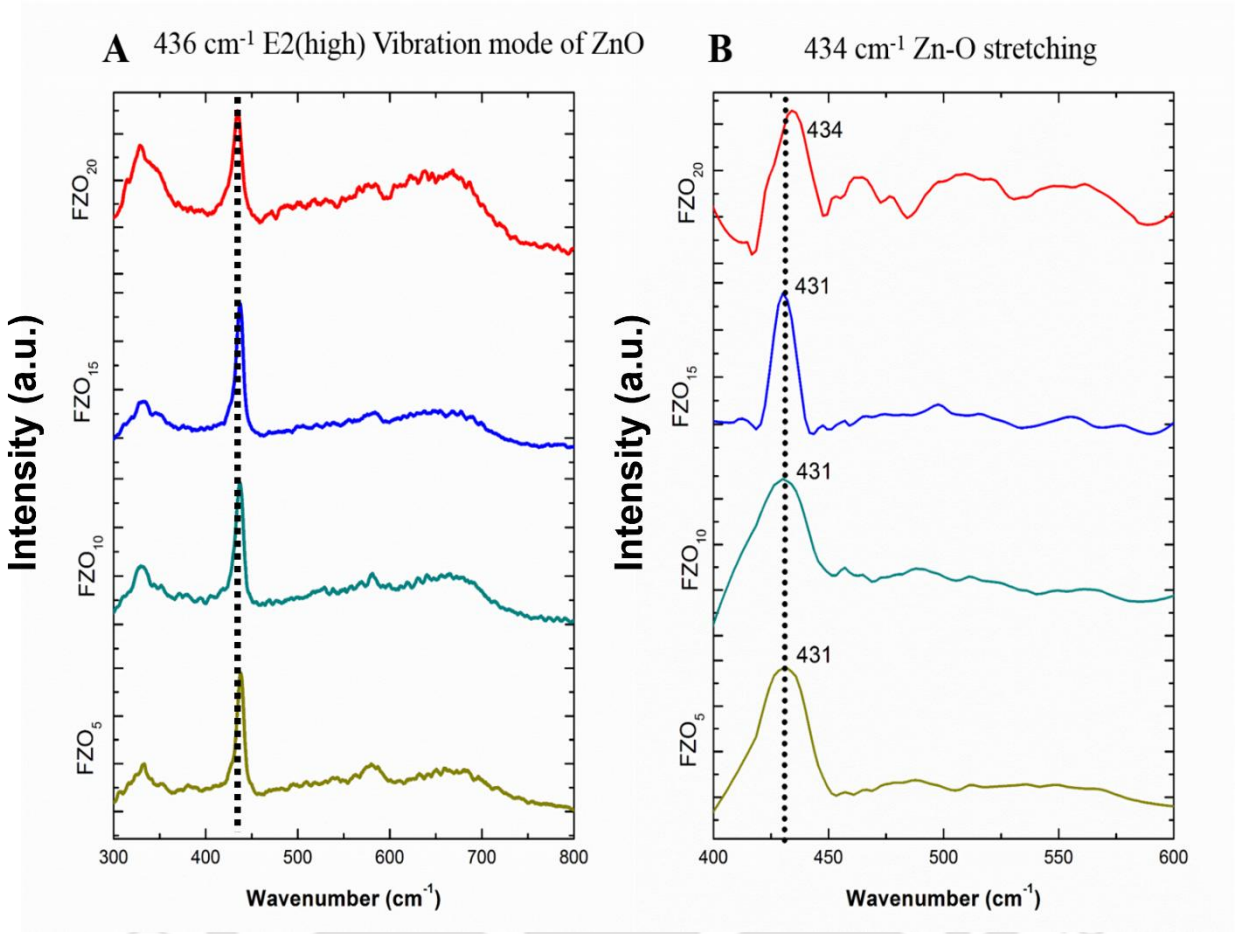

Figure 4.2. Spectroscopic analyses of FZO_5, FZO_{10}, FZO_{15}, and FZO_{20} samples, A) Raman Spectra, B) FTIR Spectra

The elemental composition of the FZO NPs was confirmed using EDX (Figure 4.3B). The EDX spectra reflected that Zn and O were the major constituents of the FZO lattice, and Fe was present as a minor element. The weight percentages of Fe are listed in Table 4.3, which was found to be in a linear co-relation ($R^2 = 0.99$) with the theoretical values calculated using the empirical formula $Zn_xFe_{(1-x)}O$ (Figure 4.3C). The EDX analysis was also confirmed by the occupancy obtained by the Zn and Fe ions calculated using Rietveld refinement as given in Table 4.2. The occupancy calculated was found to be in good correlation with the theoretical and experimental fraction of the Zn and Fe ions, affirming the successful doping of the desired Fe concentration into the ZnO lattice. Hence, Raman spectra together with FTIR and EDX endorsed the result obtained from the XRD refinement and confirmed the successful synthesis of FZO NPs. The morphology and the particle size of the synthesized NPs were calculated using FESEM. The FZO samples contained

mixed morphology, particulate and rod-shaped (perfect crystals with a hexagonal shape and no perfect ones (between amorphous state and crystallographic one)) as shown in Figure 4.3A. The mixed morphology confirmed the results obtained from the refinement of XRD data and indicated that Fe^{3+} ions were present in the form of impurity in the ZnO lattice. From the FESEM image, the average particle size was determined using ImageJ software and found to be 79 ± 8, 100 ± 12, 110 ± 14 and 160 ± 61 nm for rod-shaped morphology (width only), and 33 ± 9, 54 ± 6, 53 ± 5 and 54 ± 12 nm for particulate morphology, for FZO_5, FZO_{10}, FZO_{15}, and FZO_{20}, respectively. However, due to this large deviation in sizes, the size distribution histogram based on the shortest diameter to the area covered by the particles was plotted for an average of 50 particles of each sample, as given in Figure 4.3B. Similar to that of AZO samples, the homogenous size distribution was found to be in FZO_{15} samples as compared to the other FZO samples, resulting in their least MIC values. It has been observed that the nano-size and rod-shaped morphology of the ZnO-based NPs can be obtained by regulating the calcination (> 500 ºC) as well as the reaction temperature (> 50 ºC) [311, 312]. In this study, the FZO samples were synthesized at a constant temperature of 65 ºC throughout the reaction, and the calcination temperature was kept constant at 650 ºC for four h based on the DSC analysis of the highest dopant concentration (Figure 4.3E), which was presumed to provide low dimensioned rod-shaped morphology. In addition, studies have revealed that the rod-shaped morphology with a high surface-to-volume ratio can be obtained by optimizing the Zn^{2+}/OH^- ratio [312]. In the current work, the Zn^{2+} concentration was reduced with an increase in the Fe^{3+} ions, which presumably provided a dual morphology with reduced surface area, which facilitated no ROS production.

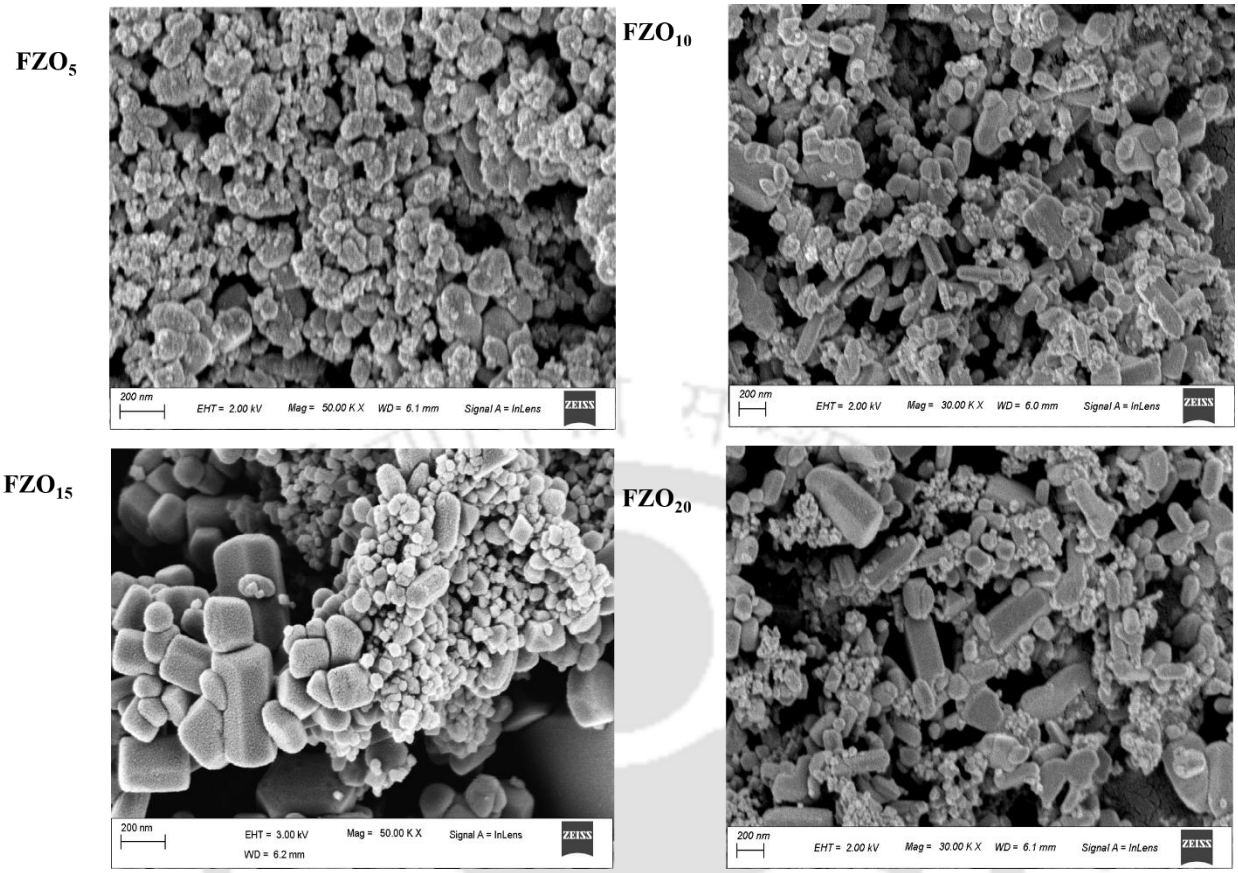

Figure 4.3. A) FESEM images of the synthesized FZO NPs

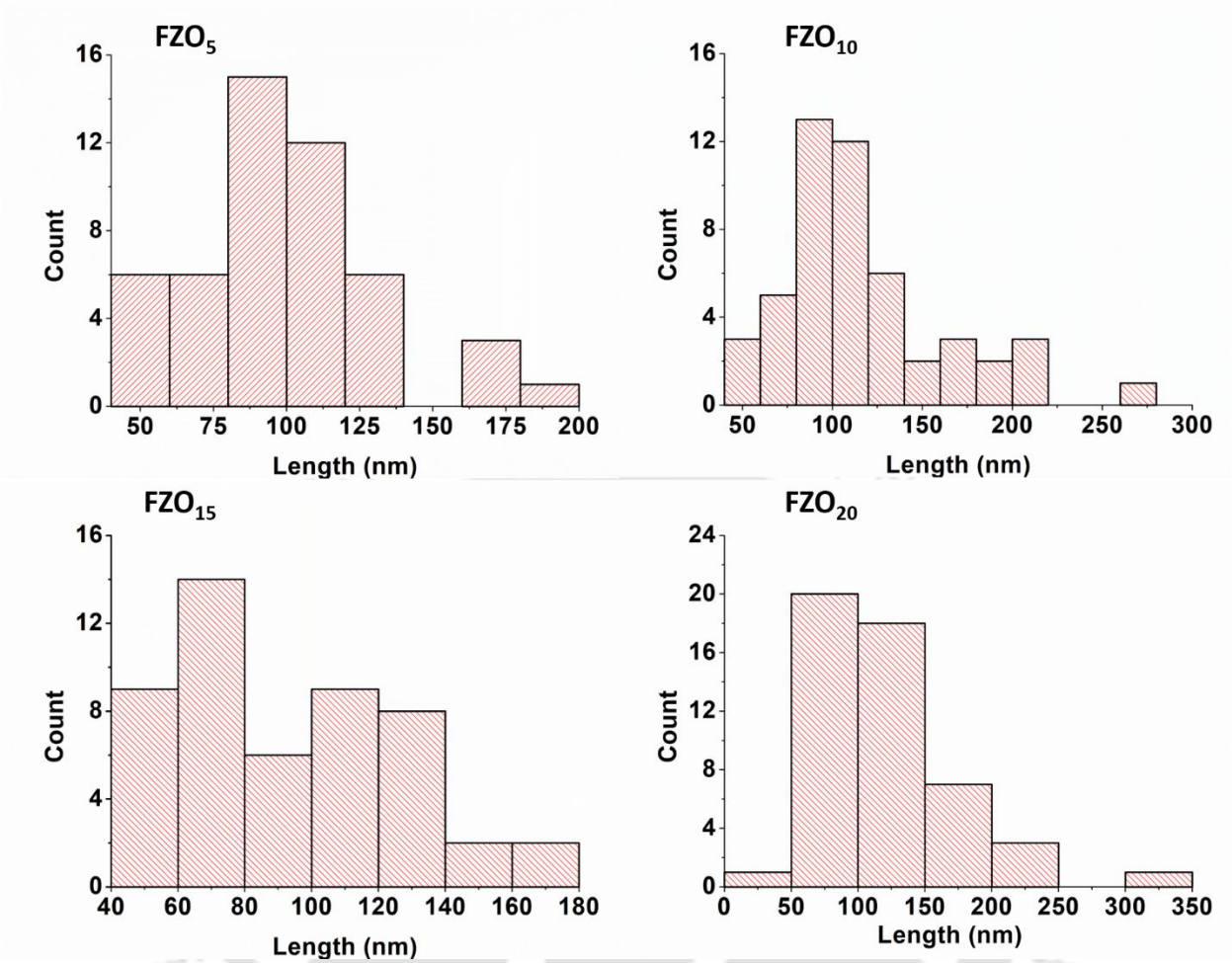

Figure 4.3. B) Particle size distribution histogram of FZO samples

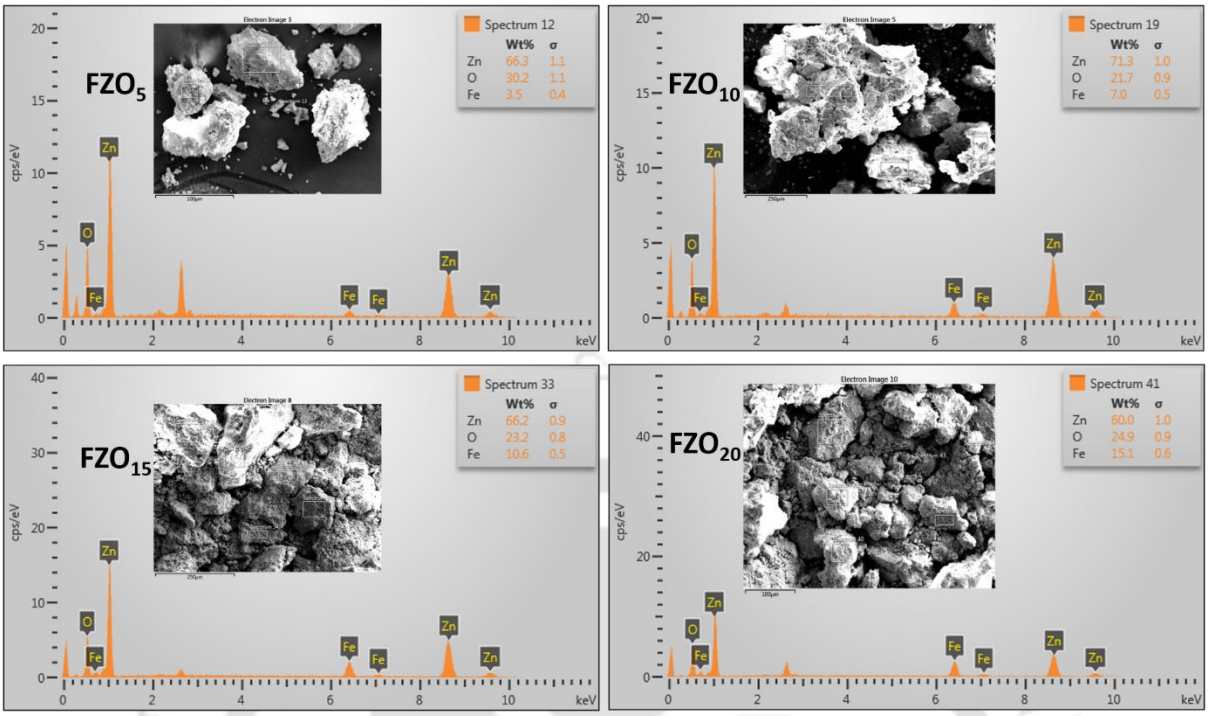

Figure 4.3. C) EDX spectra of the FZO NPs

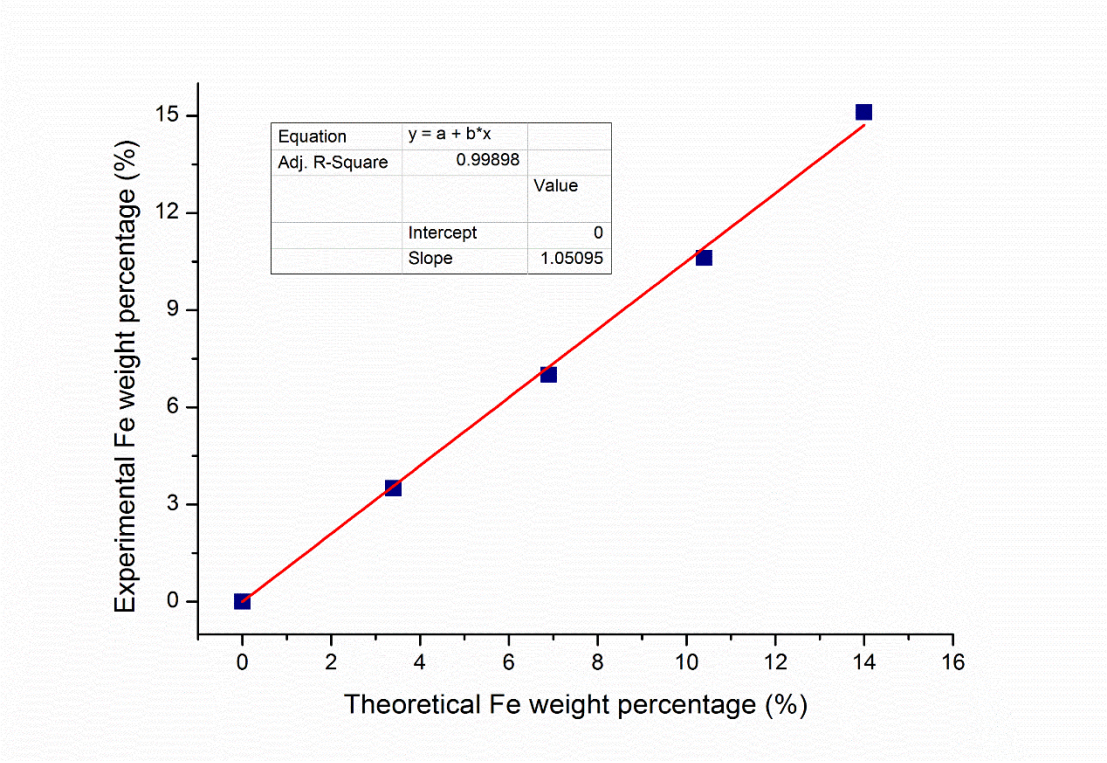

Figure 4.3 D) Co-relation between the theoretical and experimental wt % of Fe

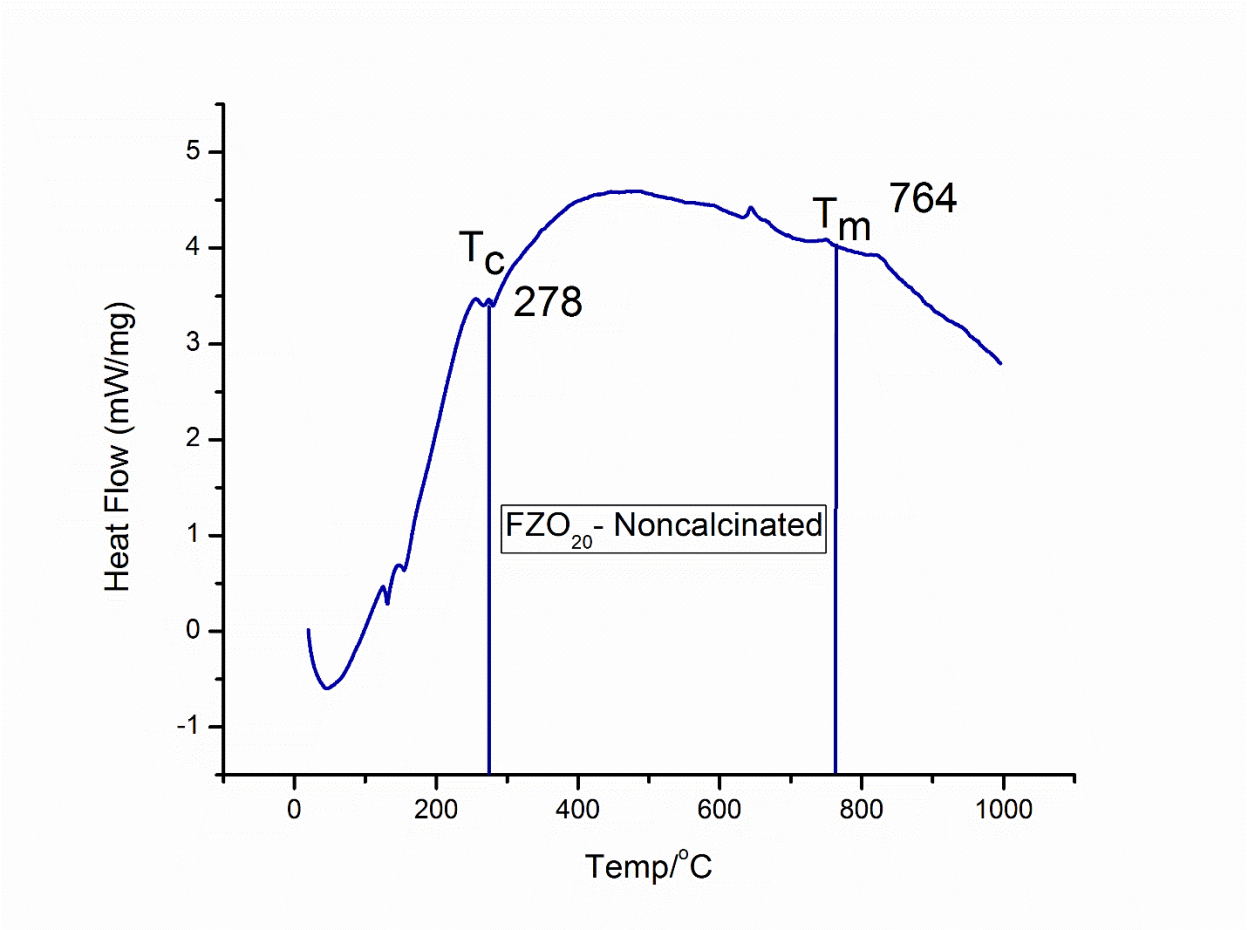

Figure 4.3. E) DSC curve of non-calcinated FZO_{20} NPs

Zeta potential of all the samples was measured at pH 7.4 to examine respective surface charges. The corresponding zeta potentials of the synthesized bimetallic FZO NPs are listed in Table 4.3 (Figure 4.3A). The positive zeta potential of the synthesized NPs was enhanced up to 15 % doping of the Fe(III) and was reduced at further doping, *i.e.*, at 20 %. The reduced zeta potential at 20 % doping of Fe^{3+} ions was presumably due to the decreased lattice parameters and lower crystallinity of the FZO_{20} samples. The data obtained from XRD refinement revealed that, as the impurity level of FZO NPs was significantly enhanced, the crystallinity was reduced, which consequently reduced the zeta potential. Target deficiency is one of the major drawbacks of traditional as well as nanomedicines. Doping of Fe^{3+} ions helps in originating the magnetic target efficiency in NPs and nanomedicines. Hence, FZO samples were analyzed for their magnetic properties. All the samples exhibited soft ferromagnetic properties. The retentivity and coercivity values of the synthesized NPs were found to be increased up to 15 % doping and were decreased at higher

Fe(III) (20%) concentration (Figure 4.3C, Table 4.3), presumably due to the decreased lattice parameters. An apparent increase in the magnetization values of the FZO NPs with an increase in dopant concentration was observed. The magnetization values were linearly (slightly) increased with an increase in the Fe^{3+} ions concentration with a slope value of 0.0015. Hence, the magnetic properties of the synthesized material can be tuned based on its variable applications via altering the concentration of Fe^{3+} ions (Figure 4.3D).

Table 4.3. Surface charge and magnetic behavior of FZO NPs

S.No.	Sample	Fe (wt %)	Surface Charge (mV)	Magnetization (emu)	Retentivity (emu)	Coercivity (Oe)
1	FZO_5	3.5	13.1 ± 0.7	4.4938E-3	46.505E-6	19.118
2	FZO_{10}	7.0	17.9 ± 0.4	6.4594E-3	100.71E-6	27.929
3	FZO_{15}	10.6	32.6 ± 1.4	13.794E-3	230.30E-6	45.676
4	FZO_{20}	15.1	27.5 ± 2.6	22.101E-3	229.74E-6	42.992

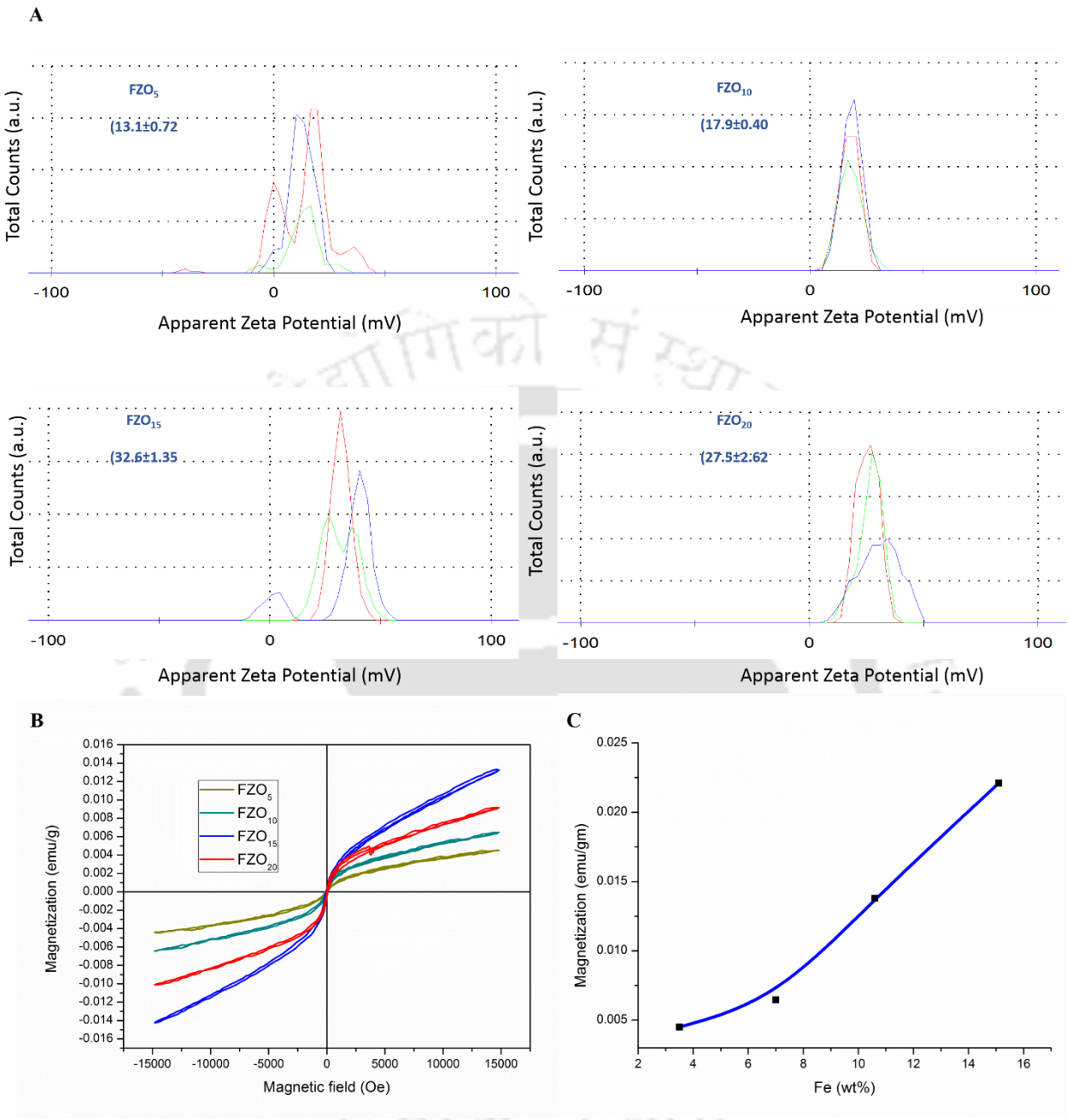

Figure 4.4. A) Zeta potential of FZO NPs; indicating the positive surface charge, with the maximum surface charge on FZO_{15}**, B)** VSM curve of FZO NPs; showing an increase in magnetization with an increase in Fe^{3+} concentration **C)** Relation between the Fe wt % and magnetization; A linear relation R^2= 0.94

4.3.2 Biological characterizations

The synthesized NPs were tested for their cytocompatibility, as well as their antimicrobial activity and mechanism of action. The detailed results are as follows:

4.3.2.1 Antibacterial Activity

As discussed before, the Fe^{3+} ions were chosen as a dopant, majorly because of the three reasons (a) smaller atomic ((Fe (0.126 nm), Zn (0.138 nm)) and ionic radii, ((Fe^{3+} (0.06 nm), Zn^{2+} (0.074 nm)), (b) more reduction potential, (c) self-antibacterial activity. Hence, it was presumed that Fe^{3+} ions would replace the Zn^{2+} ions in the ZnO lattice and may produce synergistic antibacterial activity.

The MIC and MBC values were determined as the concentration at which no visible growth was observed. However, IC_{50} and IC_{90} values were theoretically calculated using a simple double exponential equation [59] as follows:

$$OD\ (Cells) = A_1\ (1 - e^{-k_1 x}) + A_2\ (1 - e^{-k_2 x}) \quad (4.1)$$

Where, and refer to the rates of rapid killing and slow killing, respectively. A_1, k_1, k_2, and A_2 are constants, and x refers to the concentration of NPs. IC_{50} and IC_{90} concentrations were determined at OD values as 50 % and 10 % of the initial OD, respectively. MIC, MBC and the IC_{50} and IC_{90} values, and the respective Zone of Inhibition are listed in Table 4.4 (Figure 4.5). FZO_{15} exhibited the lowest IC_{50} and IC_{90} value (Figure 4.5; Lower OD_{600} curve; blue line), presumably due to the least Fe impurity and maximum positive surface charge. Additionally, the Fe+Zn/O ratio for FZO_{15} was found to be 0.993, indicating anion-rich ZnO lattice, which presumably reduced the MIC values of the FZO_{15} samples by elevating the release of Zn^{2+} and Fe^{3+} ions.

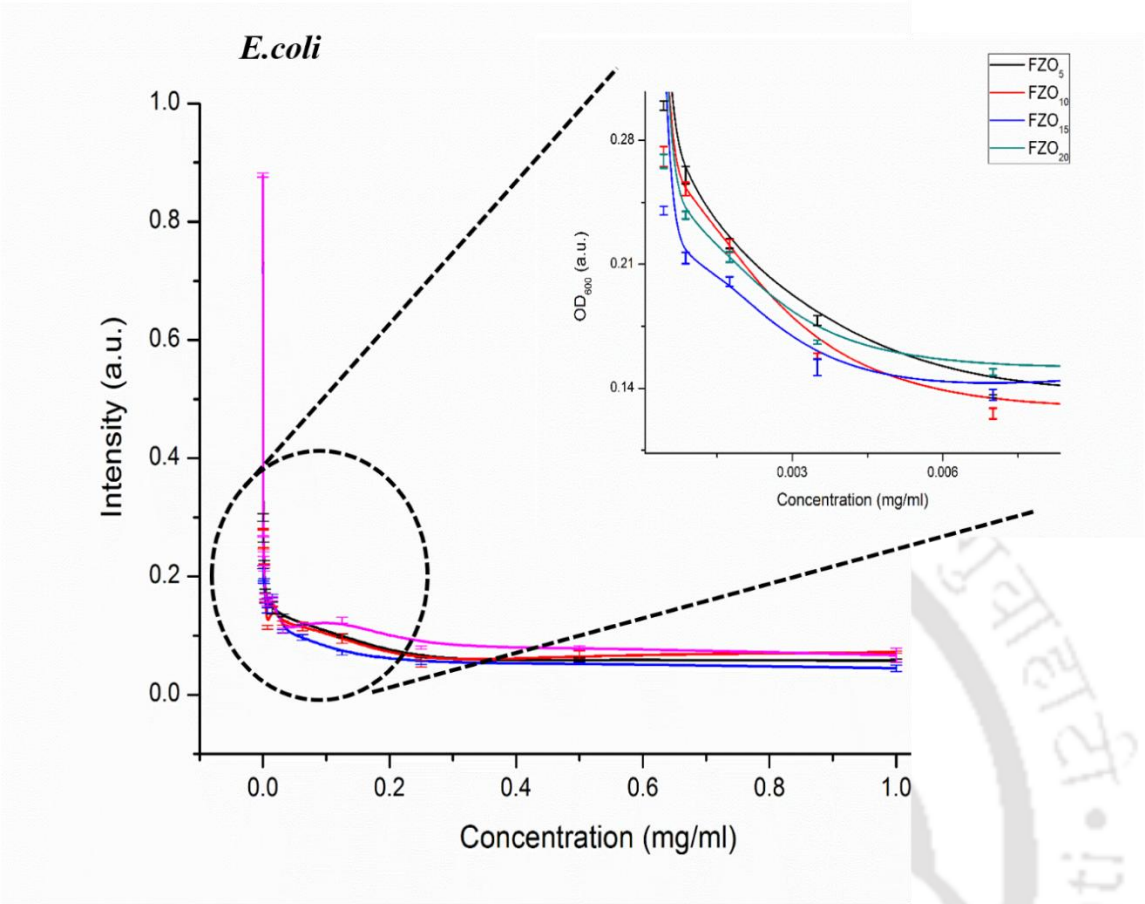

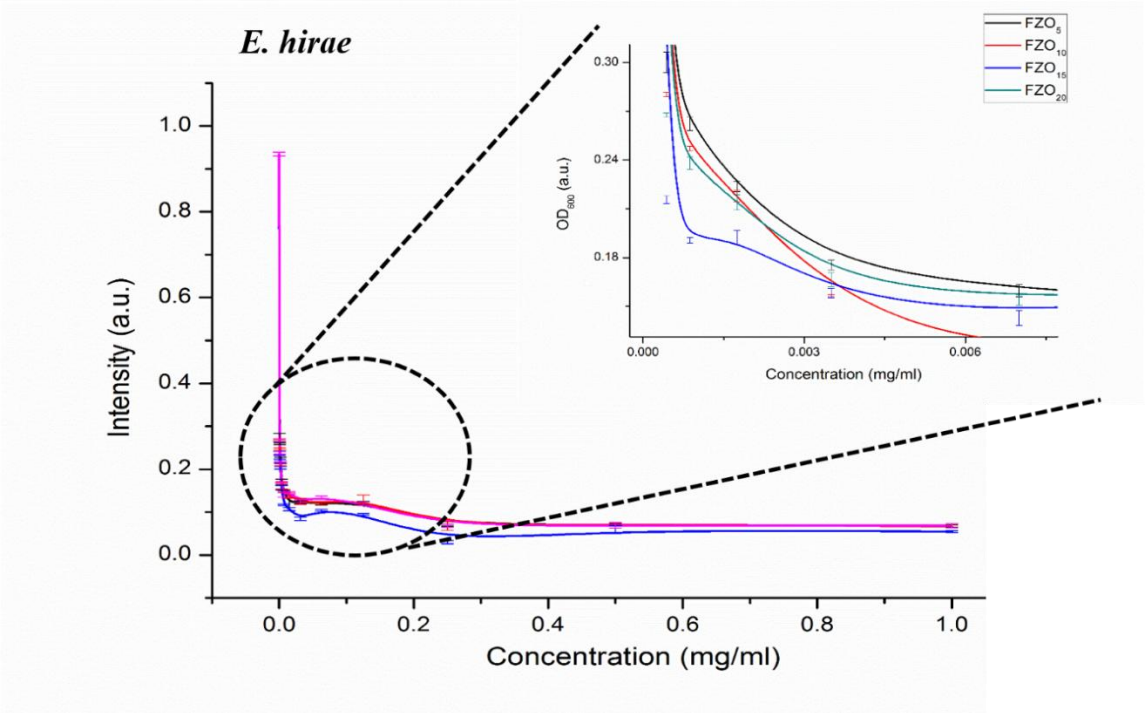

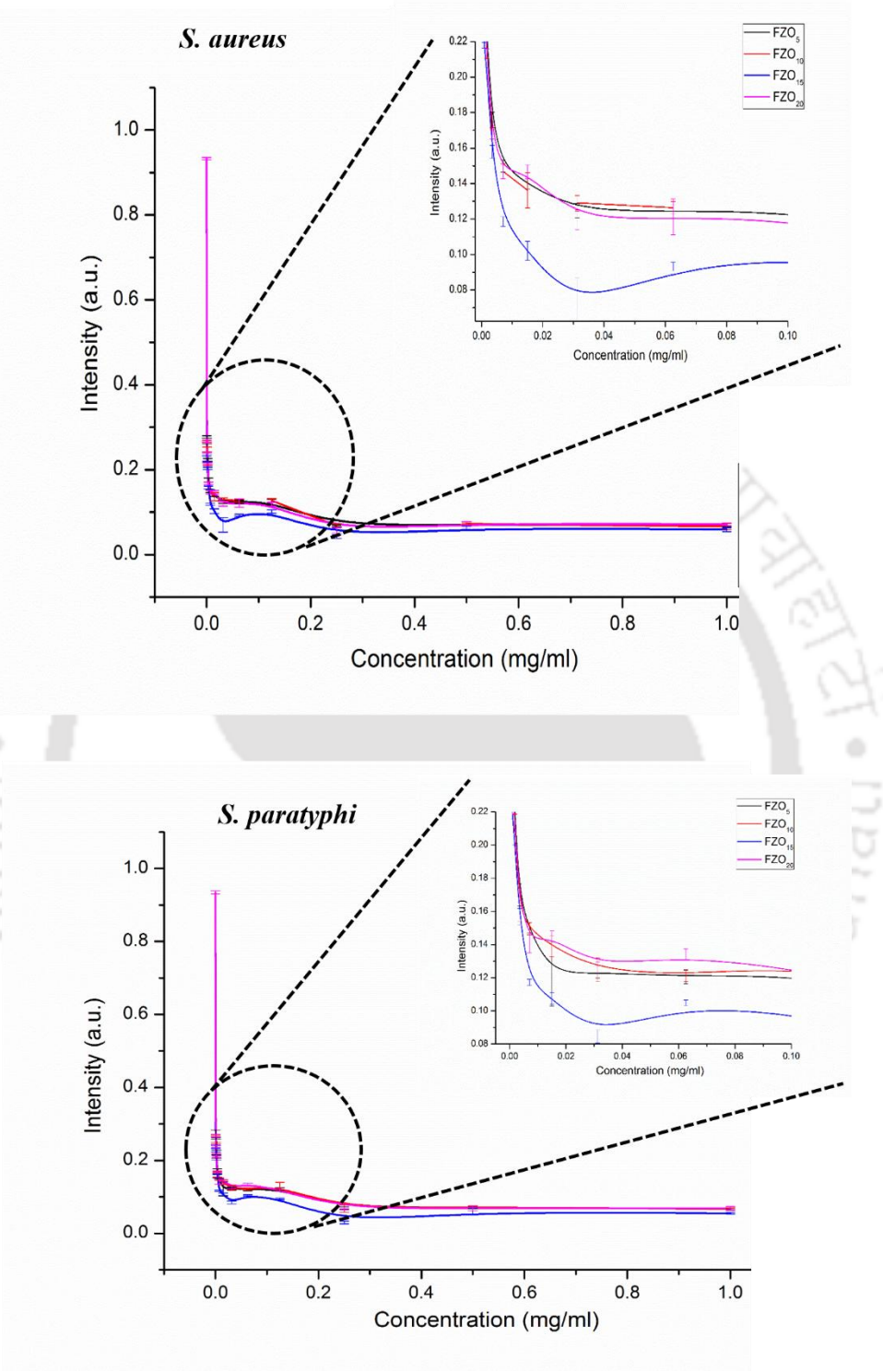

Figure 4.5. Antibacterial activity of FZO samples against different bacterial species; indication the least OD_{600} values for FZO_{15}, corresponding to its highest antibacterial affinity

Similarly, the bacterial species were incubated with the synthesized NPs at the 0.25 mg/ml concentration, which resulted in zero or no growth of the bacteria. The MBC visualized was found to be 0.25 mg/ml for all the samples against all the bacteria inspected (Figure 4.6A). The effectiveness of the MIC value was examined via the disc diffusion method (Figure 4.6B). The Zone of Inhibition (ZOI) was calculated and was validated against the standard Kanamycin (K-disc; concentration 30 µg/mg) [313]. The ZOI for the respective nanoantibiotics is given in Table 4.4. The synthesized NPs were found to be comparable with Kanamycin. These results indicated that the FZO NPs are practically effective against all the clinically applicable bacteria.

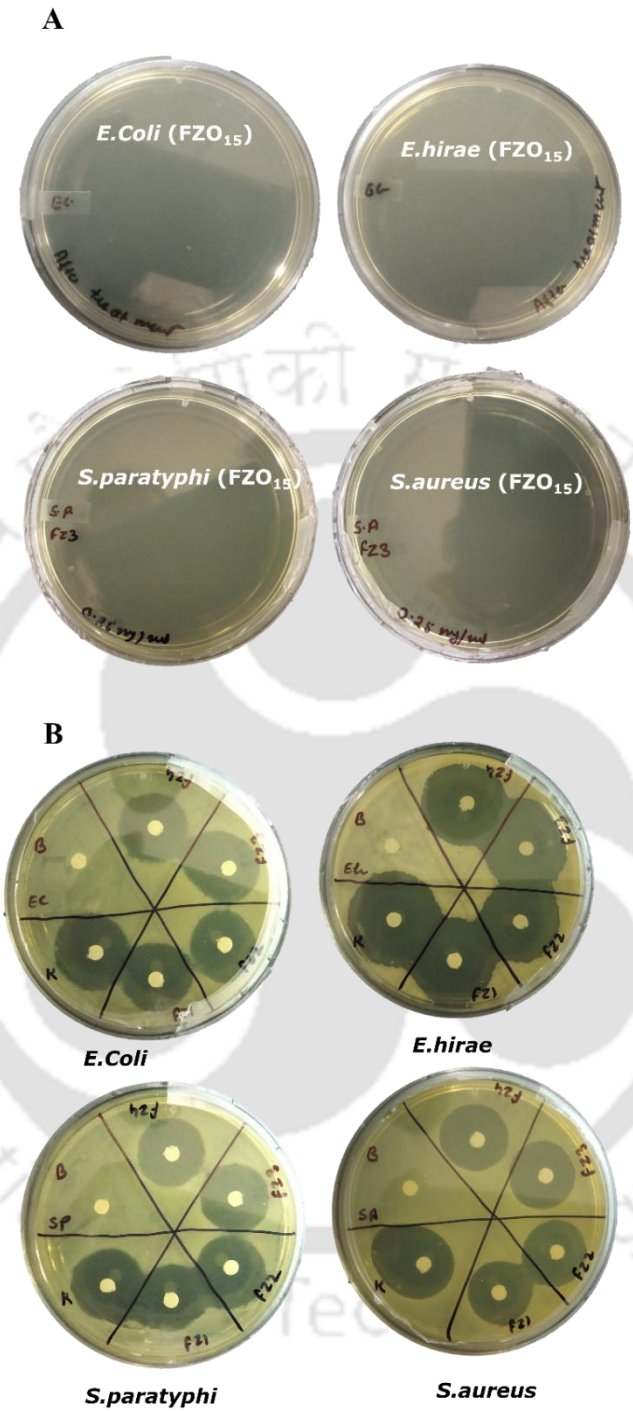

Figure 4.6A). Effect of MBC over bacterial growth; No bacterial growth after treatment at MBC **B)** Antibacterial effect of FZO NPs, at their respective MIC values, where K-Kanamycin 30 µg disc concentration, B-30 % DMF (FZ1-FZO_5, FZ2- FZO_{10}, FZ3-FZO_{15}, and FZ4-$FZO_{20;}$ ZOI consistent to the Kanamycin

Table 4.4. MIC values of FZO NPs against various bacterial species and their respective ZOI

S.No.	Sample ID	*E. Coli*		*S. paratyphi*		*E. hirae*		*S. aureus*	
		MIC /IC_{90} (mg/ml)	ZOI (mm)	MIC /IC_{90} (mg/ml)	ZOI (mm)	MIC /IC_{90} (mg/ml)	ZOI (mm)	MIC /IC_{90} (mg/ml)	ZOI (mm)
		IC_{50} (µg/ml)		IC_{50} (µg/ml)		IC_{50} (µg/ml)		IC_{50} (µg/ml)	
1	FZO_5	0.25/0.33	18.32± 1.24	0.25/0.29	20.00± 1.37	0.25/0.18	22.84 ±1.14	0.25/0.29	17.75 ±0.81
		0.28		0.24		0.27		0.24	
2	FZO_{10}	0.25/0.38	18.72± 1.97	0.25/0.30	29.69± 0.94	0.25/0.25	23.04 ±1.29	0.25/0.30	18.09 ±0.67
		0.25		0.22		0.26		0.22	
3	FZO_{15}	0.125/0.31	19.95± 0.70	0.125/0.10	21.72± 0.84	0.125/0.11	23.99 ±2.06	0.25/0.15	18.83 ±1.55
		0.20		0.19		0.16		0.20	
4	FZO_{20}	0.25/0.53	17.35± 0.52	0.25/0.29	19.39± 1.66	0.25/0.38	21.72 ±0.84	0.25/0.27	17.72 ±0.98
		0.24		0.22		0.24		0.22	
5	Kanamycin	0.5 (Standard)	20.82± 0.70	0.5 (Standard)	21.84± 0.40	0.5 (Standard)	26.01 ±0.96	0.5 (Standard)	19.72 ±0.85

In addition, the designed bimetallic FZO was found to be more effective in terms of MIC with recently reported ZnO-based NPs, as listed in Table 4.5. After doping of Fe^{3+} ions into the ZnO lattice (as indicated by XRD data), the lattice parameters were decreased, and the impurity level was enhanced, which enhanced the antibacterial activity of the FZO NPs. The enhanced antibacterial activity might also be the result of the reduced size as well as the rod-shaped morphology of the synthesized NPs. As presumed, FZO_{15} was found to be the most effective (Least MIC values and Higher ZOI) against all the bacterial species due to their higher crystallinity, least impurity, higher zeta potential, lowest width, and higher colloidal stability. The visible MIC values (Table 4.4) were found to be effective against all the bacterial species.

Table 4.5. Recent advances in ZnO nanomedicine

S.No.	Sample	Surface area (m^2/g)	ROS production	Bacteria	MIC (mg/ml)	MBC (mg/ml)	Reference
1	ZnO nanorods	14.1	Yes	*B. subtilis*	*0.128*	0.512	[314]
				S. aureus	0.512	0.512	
2	Li doped ZnO	NA	Yes	*E. Coli*	0.400	NA	[315]
				S. typhimurium	0.300	NA	
				E. faecalis	0.600	NA	
3	Ag/ZnO	NA	Yes	*S. mutans*	0.256	0.512	[316]
4	ZnO/GQD	NA	Yes	*E.coli*	3.2	NA	[317]
5	Ni/ZnO	NA	NA	*P. aeriginosa*	0.125	0.125	[318]
				B. subtilis	0.015	2.0	
				C. albicans	0.5	2.0	
6	GPTMS modified ZnO-Annealed at 600ºC	NA	NA	*E.coli*	1.25	Bacteriostatic only	[319]
				S. aureus	0.4167	Bacteriostatic only	
7	Ag nanoparticles supported on ZnO flowers	NA	NA	*E.coli*	0.25	0.5	[320]
				S. aureus	0.25	1.0	
8	ZnO NPs	6.2	Yes	*E.coli*	0.125	4.0	[321]

4.3.2.2 Cytotoxicity analysis for Human cells

To analyze the cytotoxic effect of FZO, the NPs were incubated with Human osteosarcoma MG63 cell lines [322, 323] at various concentrations, *i.e.,* from 20-80 mg/ml, and MTT assay was

performed as mentioned above. Cells without material were treated as the positive control. Cells were found to be more than 90 % viable at a higher concentration (80 mg/ml) of FZO_{15} sample up to three days of incubation. However, at the same concentration, the cell viability was decreased slightly to 87.67 % after six days of incubation. The cells were more than 90 % viable after six days of incubation at 20 mg/ml concentration of the FZO (Figure 4.7A), which is around ten times higher concentration than that of the MIC values. Hence, no negative effect of material concentration could be observed (p values ≥ 0.05). Various researches claimed that metal-doped ZnO or surface-modified ZnO NPs produced ROS at around > 200 µg/ml concentration, which was toxic to human cells [236, 324]. However, bare ZnO has been proven to produce ROS after entering into the cells and causing around 50% cell death at a concentration of 10 µg/ml [325]. To verify the antibiotic action as well as the cytocompatibility of bimetallic FZO, MG63 cells were incubated with DMEM media in three different batches for 48 h; (i) DMEM with Penstrep antibiotic, (ii) DMEM with FZO NPs, and (iii) DMEM without any antibiotic. As shown in figure 4.4C, FZO NPs effectively functioned as an antibiotic (Penstrep) and hindered the bacterial infection possibilities to MG63 cells, same as Penstrep incubated cells (Figure 4.7B). The confluency level was quantified using ImageJ software, which was found to be the highest (85 ±3 %) in the presence of FZO_{15} followed by Penstrep (80 ± 5 %) and without antibiotic (60 ± 2 %). These observations indicated that the synthesized NPs are highly cytocompatible to be utilized as nanoantibiotic for their clinical applications.

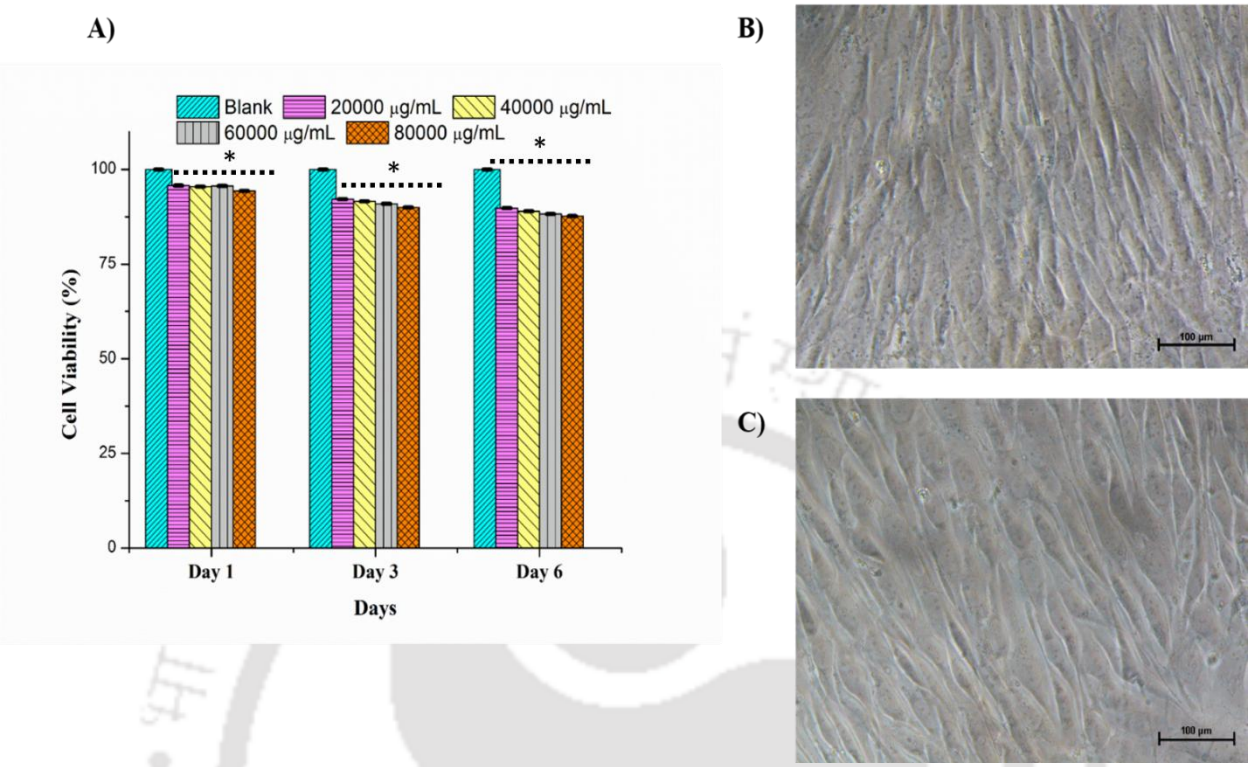

Figure 4.7. A) Cytocompatibility of FZO NPs against MG-63 cells in the range of 20 mg/ml to 80 mg/ml, **B)** MG63 cells incubated for 48 hrs in DEMEM with Penstrep antibiotic, and **C)** MG63 cells incubated for 48 hrs in DEMEM with FZO NPs; *p *value* > 0.05 ; n=3.

NPs possess specific properties such as high surface area, distinct morphology, and nano-ranged size, which contributes critically to their antibacterial and toxic behavior to human cells. However, the toxicity majorly depends on their size, solubility, surface coating, UV induction, and metal release [326-328]. These properties play a crucial role in the bio-interface to enhance the biological activities of the NPs. Hence, it is essential to evaluate the nano-leveled properties of these materials, which include size, morphology, and surface charge. In this study, the FESEM image as shown in Figure 4.3A, indicated dual morphology; rod-shaped morphology with size ~100 nm and particulate shaped morphology with average size ~55 nm. The particle size was increased with dopant concentration FZO_{15} samples were found to carry the least dual morphology (Minimum R_{Bragg} value, Table 4.1). Figure 4.3A corresponded to the result obtained after refinement that the Fe^{3+} ions enhanced the impurity of the ZnO lattice leading to the dual morphology of the FZO

samples. This, in turn, helped in the enhancement of its antibacterial activity, as well as the lowered ROS production, which was presumed to help in obtaining high cytocompatibility to human cells. Similarly, the surface charges of the synthesized NPs were evaluated by calculating the zeta potential of the NPs. All the samples showed positive zeta potential; the highest zeta potential was found to be of FZO_{15} NPs, which complemented the antibacterial analysis of FZO samples. The high positive zeta potential values indicated, the higher the colloidal stability of the synthesized NPs. In addition, a positive surface charge helps in the interaction and selectivity of the NPs for their antibacterial activity, as shown in Figure 4.8.

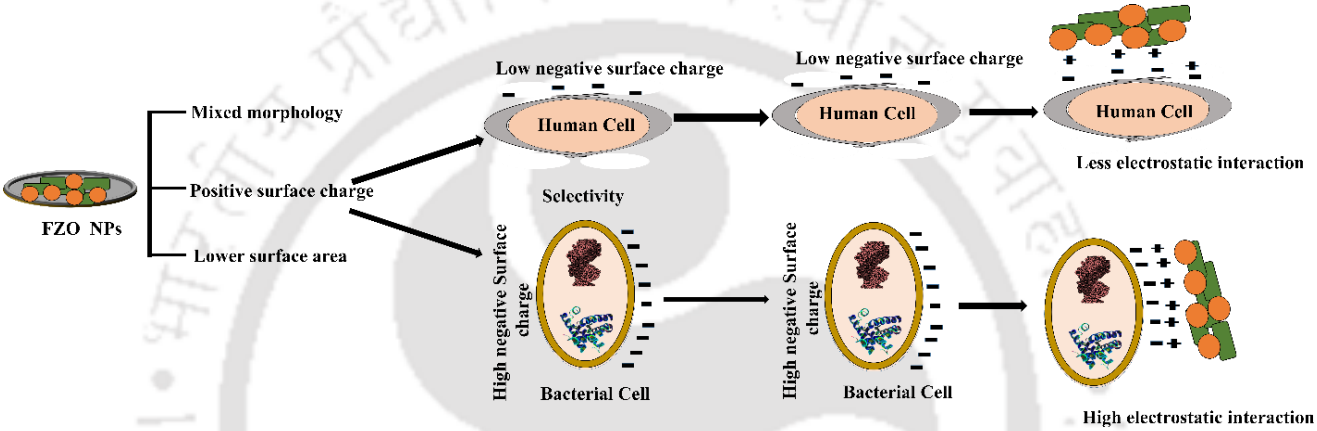

Figure 4.8. Selective electrostatic interaction of FZO NPs with bacterial cells

4.3.2.3 Analysis of the Antibacterial mechanism

To analyze the antibacterial mechanism of FZO, we investigated three major mechanisms as previously performed for AZO. Cells were stained with CFDA and PI dyes to analyze the live and dead cells, respectively. The flow cytometric analysis, as shown in Figure 4.9A, displayed the CFDA staining lesser than 10^2 FSC values (negative control), indicating the auto-fluorescence and the presence of dead cells. Similarly, as shown in Figure 4.9B, the PI stain was found to contain more than 10^2 FSC values (comparable to positive control), which complemented the CFDA data. Hence, fluorescence studies confirmed the killing of bacterial cells. Additionally, PI staining confirmed the rupturing of the bacterial cell wall after incubation with the FZO samples. This rupturing in the bacterial cell wall can be because of two obvious factors; ROS generation by released toxic ions. To analyze the ROS production, we stained the cells with DCFH-DA dye and analyzed using an Infinite M200 PRO Tecan plate reader at 495nm/529nm excitation and emission wavelengths, respectively. The fluorescence intensities obtained from various cells incubated with

FZO were found to be lesser than that of media. These observations revealed that there was no ROS production in the presence of FZO samples under dark conditions (p values ≥ 0.05) (Figure 4.9C).

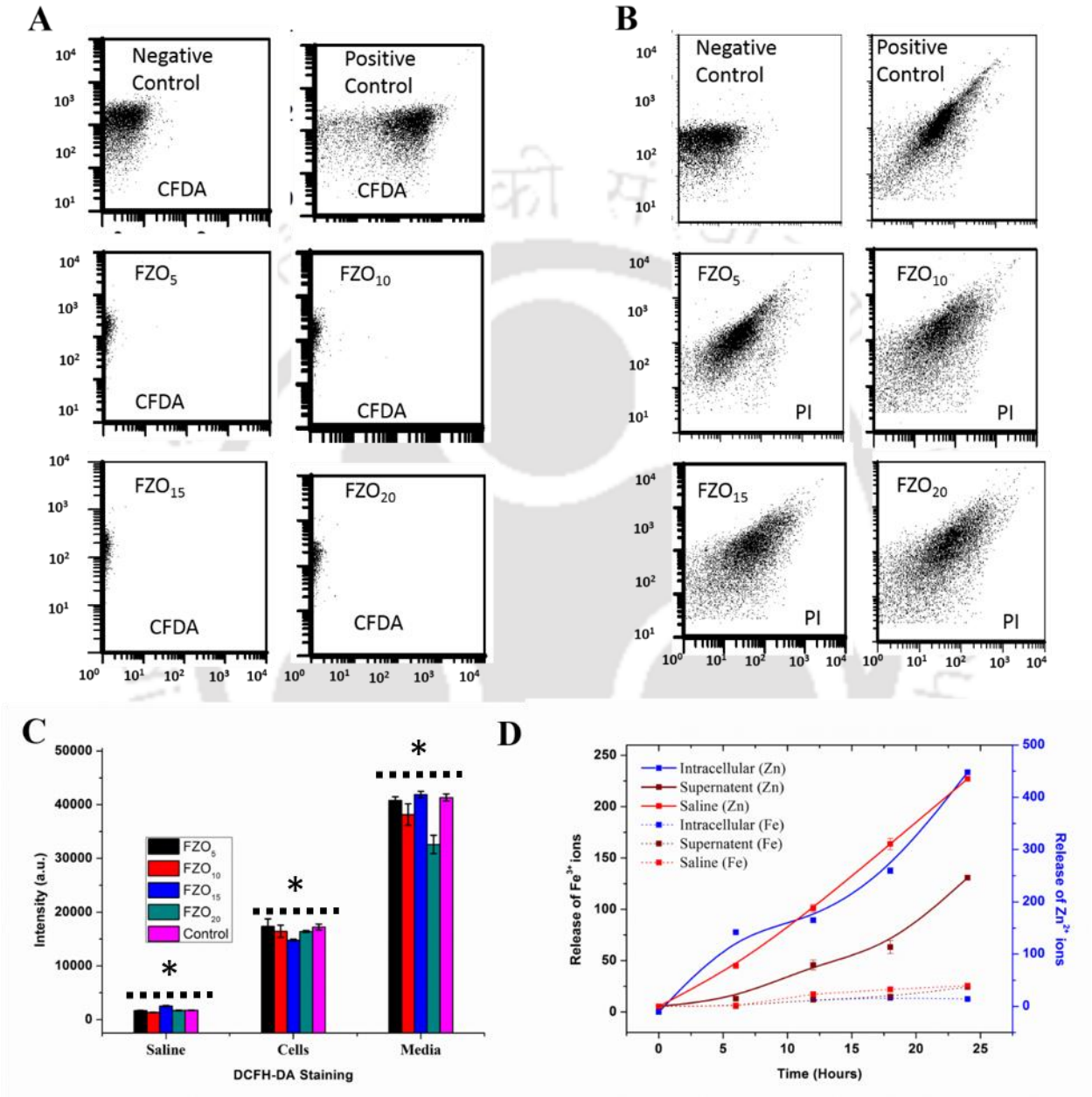

Figure 4.9. A) CFDA, B) PI, and C) DCFH-DA stain profile after incubating cells with FZO NPs D) Release profile of Zn^{2+} and Fe^{3+} ions in ppm from FZO_{15}, under various environments; Solid line Zn^{2+} and dotted line Fe^{3+}; **p value* > 0.05 ; *n*=2.

This can be explained by the previous studies through various research groups. ZnO NPs are known for their photocatalytic activity through ROS generation [329]; as all the experiments were performed under dark conditions, FZO NPs did not result in ROS production. Also, nano-sized ZnO has been proven to exhibit nano-cytotoxicity through its higher reactive surface area, which consequently results in the production of ROS [330]. In this study, the effective surface area calculated through BET isotherm was found to be smaller, *i.e.*, 1.014, 5.134, 2.301, and 0.387 m^2/g (Figure 4.10 for FZO_{15}), which is presumably not sufficient to produce ROS. This reduced surface area was due to the dual morphology of FZO because of the reduction in the Zn^{2+}/OH^- ratio. These observations were also supported by the MTT assay, as ten times higher concentrations than MIC values did not show any cytotoxicity.

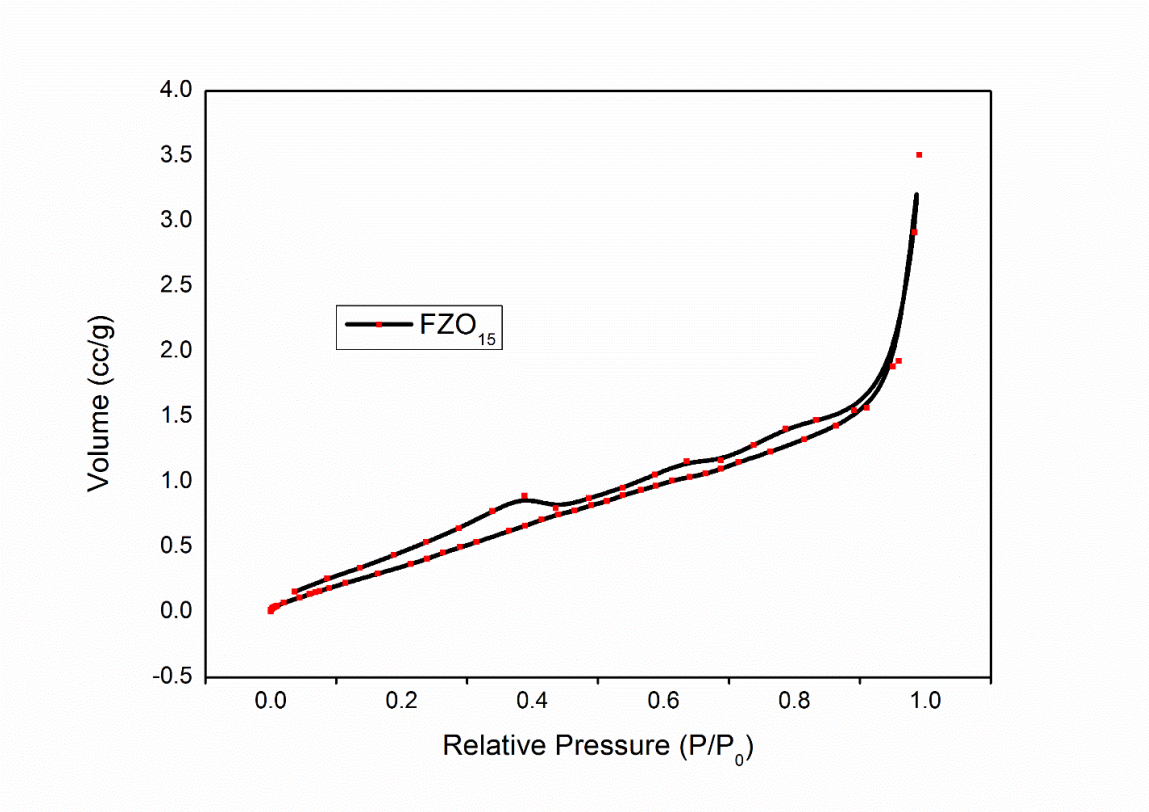

Figure 4.10. Nitrogen adsorption-desorption isotherm of the FZO_{15} NP; a lowered surface area resulting in no ROS production

As no ROS production could be obtained, the release of Zn^{2+} and Fe^{3+} ions from the FZO lattice was analyzed to establish antimicrobial action. The release of Zn^{2+} ions was enhanced with an increase in time. The intracellular accumulation of the released Zn^{2+} ions was found to be the

maximum, with a linear release profile, indicating the slower degradation of FZO than that of AZO under various local environments, *i.e.*, saline solution and physiological pH. The release profile of Zn^{2+} ions was found to be almost similar for intracellular as well as the other saline environments (Figure 4.9D, solid line). However, the concentrations of the Zn^{2+} ions (intracellular) were around 50 % higher than that of extracellular Zn^{2+} ions concentrations within 24 h.

Similarly, the release of Fe^{3+} ions was higher for PBS solution and was an almost similar profile for supernatant and 0.9 % saline environment. However, after 24 h, an almost equal concentration of Fe^{3+} ions was found in the supernatant than that of the saline environment (Figure 4.9D, dotted line). The release rate of Zn^{2+} ions and Fe^{3+} ions and their maximum concentration released are listed in Table 4.6A and B, which corresponded to the lowest MIC values of FZO_{15} among all FZO samples.

Table 4.6A. The release rate of Zn^{2+} and Fe^{3+} ions under various environments

S.No	Environment	Ions	Release rate (ppm/hr)			
			FZO_5	FZO_{10}	FZO_{15}	FZO_{20}
1	Intracellular	Zn	17.54 ± 0.44	16.8 ± 0.14	17.89 ± 0.30	17.35 ±0.36
		Fe	2.06 ± 0.02	1.96 ± 0.02	1.96 ± 0.02	1.92 ± 0.03
2	Supernatant	Zn	8.47 ± 0.17	8.97 ± 0.15	8.96 ± 0.21	8.38 ± 0.18
		Fe	0.95 ± 0.07	0.88 ± 0.01	0.94 ± 0.02	0.98 ± 0.01
3	Saline	Zn	16.95 ± 0.04	17.23 ± 0.53	17.64 ± 0.48	17.45 ± 0.44
		Fe	2.03 ± 0.07	1.95 ± 0.04	2.08 ± 0.10	1.95 ± 0.08
4	PBS	Zn	17.00 ± 0.10	17.32 ± 0.08	17.67 ± 0.36	17.88 ± 0.35
		Fe	2.13 ± 0.02	2.14 ± 0.07	2.30 ± 0.06	2.17 ± 0.02

Table 4.6B. Maximum amount of the released Zn^{2+} and Fe^{3+} ions under various environments

S.No	Environment	Ions	Maximum amount of ion released (ppm)			
			FZO_5	FZO_{10}	FZO_{15}	FZO_{20}
1	Intracellular	Zn	432 ± 10	426 ± 7	458 ± 8	432 ± 10
		Fe	52 ± 1	49 ± 1	48 ± 1	48 ± 1
2	Supernatant	Zn	208 ± 4	228 ± 3	218 ± 5	207 ± 4
		Fe	25 ± 1	21 ± 1	23 ± 1	25 ± 1
3	Saline	Zn	432 ± 12	440 ± 12	447 ± 10	448 ± 10
		Fe	52 ± 1	48 ± 1	50 ± 1	49 ± 1
4	PBS	Zn	432 ± 7	441 ± 10	441 ± 9	450 ± 10
		Fe	51 ± 1	51 ± 1	52 ± 1	49 ± 1

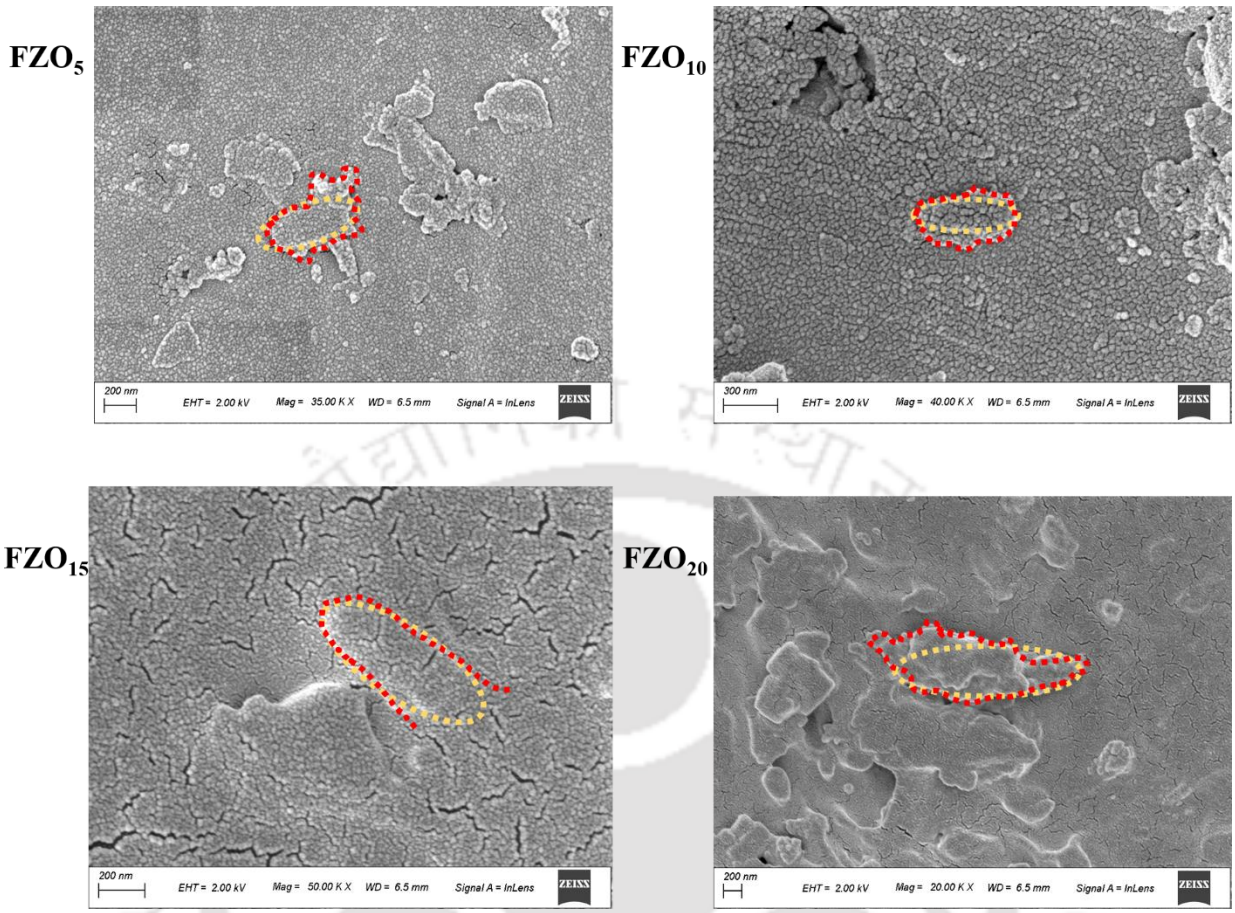

Figure 4.11. Antibacterial mechanism identification using FESEM imaging (Light Brown line- Normal cell lineage; Redline- Ruptured cell wall after treatment)

As shown in Figure 4.11, the bacterial cell was found to be ruptured and shrunk. These outcomes are consistent with previously observed results, which states that the untreated cells do not exhibit any injury to the cell wall, whereas the treated cells undergo cell shrinkage and disruption and disorganization of the cell membrane [331]. The release of more Zn^{2+} and Fe^{3+} ions at the interface resulted in electrostatic interaction (Scheme 4.1), which triggered the damage of the cell wall of the bacteria as well the internalization of ions, and consequently caused the bacterial cell death [125]. The fluorescence and FESEM imaging, as shown in Figures 4A-1 and 4.11, also confirmed the rupturing of the cell wall of the bacteria and their genetic material. Hence, the main antibacterial mechanism of FZO was found to have occurred through the release of Zn^{2+} and Fe^{3+} ions. A similar mechanism has been reported recently for the anti-tumor activity of the ZnO NPs [332].

The ROS independent mechanism of action resulted in excellent cytocompatibility up to a very high concentration of 80 mg/ml. In addition, FZO NPs not only effectively hindered the bacterial infection to the MG63 cells but also helped in its proliferation, as indicated by the highest confluency level. Hence, FZO can be effectively utilized for various biomedical applications.

4.4 Conclusions

In this chapter, the bimetallic FZO nano-assemblies were successfully synthesized and characterized. The physical properties of the synthesized NPs were correlated to their bio-interfacial properties. FZO NPs exhibited a classical hexagonal wurtzite structure and were found to carry dual morphology with an average size < 100 nm and positive surface charge. However, their effective surface area was found to be lower (2.301 m^2/g), which resulted in no ROS generation and excellent cytocompatibility to human cells (87.67 % after six days of incubation at 80 mg/ml concentration). The magnetization values of the FZO NPs were found to increase linearly with dopant concentrations. The MIC values were found to be comparable to the MIC value of Kanamycin, and MBC values showed the complete inhibition of bacterial cells. FZO_{15} resulted in the least IC_{50} value of 0.20 µg/ml due to its highest surface charge. Rupturing of the cell wall as well as the genetic material of bacteria through the release of Zn^{2+} and Fe^{3+} ions synergistically was found to be the main antibacterial mechanism of FZO.

In chapter 2, it was found that the doping of the Al^{3+} ions causes a decrement into the ZnO lattice, which consequently results in the inactivation of the bacteria. Similarly, in this chapter, the doping of the Fe^{3+} ions into the ZnO lattice caused the antibacterial action by the release of the Zn^{2+} and Fe^{3+} ions. Doping of both the transition metal ions into the ZnO lattice caused the crystal distortion in different ways due to the difference in their respective ionic sizes and the reduction potential. In the case of AZO, no separate peak corresponding to the Al_2O_3 could be obtained in the XRD data, but a shift into the ZnO peaks was observed. In FZO NPs, peaks corresponding to the Fe_3O_4 were observed, and the refined XRD data expressed a distorted ZnO lattice with increased Fe^{3+} ion concentration. Fe_3O_4 is cubic in nature, which creates more crystal imbalance as compared to the Al doping, causing different release patterns and kinetics for Zn^{2+} ions. This change in the lattice parameters not only altered the crystal sizes but also affected the antibacterial activity as well as the mechanism of the ZnO NPs. The MIC values were found to be ~ 16 µg/mL for AZO, and an IC90 value for FZO was found to be ~ 33 µg/mL. In addition, in the case of AZO nanorods, the

major antibacterial mechanism was found to be the release of Zn^{2+} ions, followed by internalization, causing the inactivation of the bacterial cell. However, in the case of the FZO NPs, the major antibacterial activity was due to the release of Zn^{2+} ions, causing the rupturing in the cell wall of the bacteria. The variance in the different modes of bacterial killing can be explained by the rate of release of Zn^{2+} ions. In AZO, the Zn^{2+} ions were released at a higher rate (exponential release) than that of the Zn^{2+} ions released from the FZO NPs (linear release). As discussed in Chapter 2, more release of Zn^{2+} ions caused the charge imbalance at the material-cell wall interface, leading to the altered permeability of the cell membrane and internalization of the Zn^{2+} ions**.** However, the slow release of the Zn^{2+} ions in FZO did not cause the charge imbalance, and the interactions of the Zn^{2+} ions with the cell wall caused the rupturing into the bacterial cell wall. Hence, the selection of the dopant plays a crucial role in the antibacterial mechanism of the ZnO lattice. By the selection of the dopant ion and controlling the release of the Zn^{2+} ions**,** the antibacterial mechanism of the nanoantibiotics can be tuned. As rupturing into the bacterial cell wall was caused by the FZO NPs, the Zn^{2+} and Fe^{3+} ions were selected for their co-integration with the HAp, as given in Chapter 3.

Chapter 5

Selection and formulation of Al or Fe and ZnO co-integrated HAp NPs and evaluation of its antibacterial activity, cytocompatibility, and target efficacy

This chapter explains the design of Zn and Fe co-integrated HAp (ZFHAp) NPs. Similar to that of Chapters 3 and 4, the ZFHAp NPs were prepared via a simple one-step co-precipitation method. The designed nanoassembly acquired a bi-phasic nanosystem, *i.e.*, ferric-HAp and zincite phases. Ferric-HAp obtained $Ca_{9.333}Fe_{1.167}(PO_4)_7$ phase, and a separate zincite phase was present in all the samples. The Fe dopant concentration governed secondary phases such as $Ca_9Fe(PO_4)_7$ and $Ca_{28.8}Fe_{3.2}(PO_4)_{21}O_{0.5}$. A dual morphology, *i.e.*, rod-shaped (77.8 ± 10 nm; major corresponding to HAp) and particulate shaped (30.9 ± 5 nm; minor due to zincite), was obtained for all the samples. The ZFHAp samples were paramagnetic, resulting in the magnetic target efficiency. ZFHAp samples showed lower MIC values (60-80 µg/ml) and no cytotoxicity to bone cells up to 5 mg/mL concentration. The ZFHAp samples did not show any TNF-α activity and exhibited excellent ALP activity, which was found to be increased with an increase in Zn concentration within the HAp matrix.

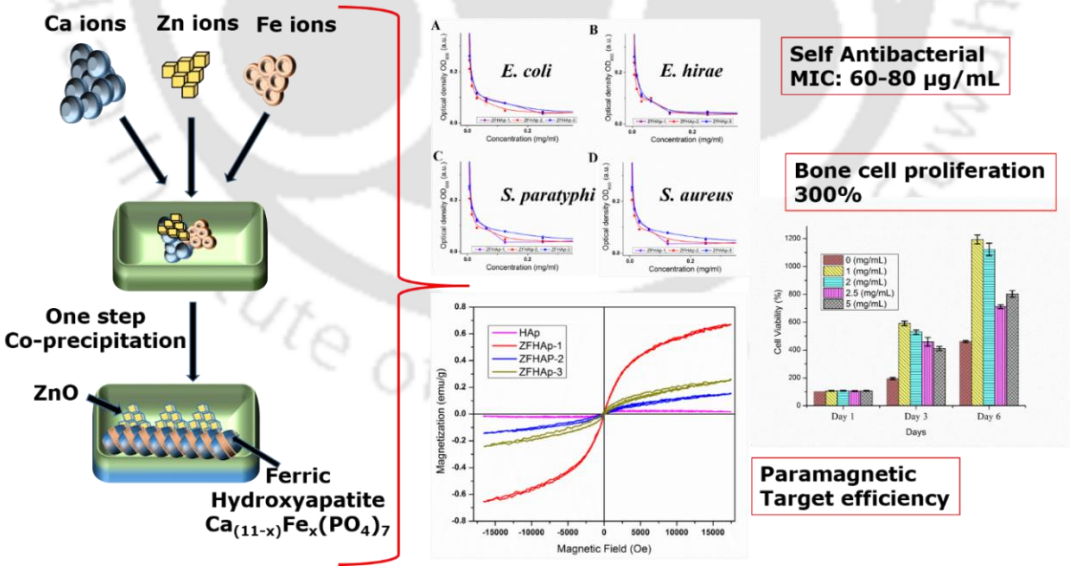

Schematic 5.1. Bi-phasic Ferric-HAp-zincite nanoassembly; Self-antibacterial, Paramagnetic target efficiency, higher bone cell proliferation (Ceramic International; 47 (20); 28274-28287; 2021)

5.1 Introduction

Various biomaterials have been investigated for orthopedic and dental applications, including HAp, ZnO, Zr, and Ag-based materials. HAp is the most extensively studied material for orthopedic applications. However, the clinch of non-commercialization of the HAp relics its target deficiency and non-antimicrobial properties [333, 334]. Hence, it is clinically significant to focus on upgrading the HAp metrics for its commercial biomedical applications. As explained in Chapters 2 and 3, via doping of transition metals into the ZnO matrix, the antibacterial activity, as well as the mechanism of the ZnO, could be altered. The ROS independent antibacterial mechanism, along with the rupturing into the bacterial cell membrane, was obtained via doping of Fe^{3+} ions into the ZnO matrix. Hence, Fe was selected along with Zn to integrate with the HAp matrix to obtain the two most desirable properties of the biomaterials, *i.e.*, antibacterial activity and the target efficiency. Doping of Zn^{2+} ion into HAp has been proven to provide the desired antibacterial properties [19] and a suitable environment for bone regeneration [335]. Also, it has been a challenge for the researchers to obtain the HAp phase after doping the desired concentration of Zn^{2+} to obtain antimicrobial activity into the HAp lattice [336-339] or to avoid β-TCP (Ca/P= 1.5). β-TCP is less stable and higher degradable than that of HAp [340] and hence is not suitable for prolonged applications such as the treatment of osteomyelitis.

Similarly, doping of Fe not only provides target efficiencies but also functions for various therapeutic applications [31], yet suffers the lack of desired antibacterial activity. Furthermore, it has been observed that nano-iron oxide increases the osteoblast density but suffers in its direct application due to its biofouling in blood plasma [37]. In this context, we designed a biphasic ferric-HAp-ZnO (ZFHAp) nanomaterial to incorporate the essential anti-bacterial and target efficiency properties to the HAp. The Zn and Fe co-integrated HAp (ZFHAp) was synthesized via a simple co-precipitation method and explored its antibacterial activity, mechanism, and biocompatibility.

5.2 Materials

All the precursors for the synthesis of ZFHAp were used as procured without any further modification. Calcium nitrate tetrahydrate $Ca(NO_3)_2.4H_2O$ (HiMedia India) and diammonium hydrogen phosphate $(NH_4)_2.HPO_4$ (HiMedia India), were used for HAp's synthesis. Similar precursors for Zn and Fe were used as given in section 3.1. Cell proliferation analysis was done

using MTT dye as given in section 3.1.1. Alkaline phosphatase (ALP) activity was analyzed using the ALP kit (CCK035, Himedia India), and the TNF-α activity was analyzed using the TNF-α analysis kit (Sigma, RAb0476). Double distilled water (MiliQ, 18 mΩ, Millipore systems) was used throughout this research study.

5.3 Synthesis of Zn and Fe co-integrated HAp nano-assembly

The ZFHAp samples were prepared via a simple one-step co-precipitation method using the previous process reported by our group [292]. As discussed in Chapter 3 and 4, a 15 % doping of metal ions into ZnO was found to improve its antibacterial activity [292, 341]; hence the molarity of Zn and Fe was varied within 0.15 M. At the same time, the molar concentration of Ca was kept constant at 0.85 M. In brief, 0.85 M of $Ca(NO_3)_2.4H_2O$ aqueous solution (50 ml) and 0.6 M of $(NH_4)_2.HPO_4$ aqueous solution (50 ml) was prepared separately. Varying concentrations of $Zn(NO_3)_2.6H_2O$ and Ferric chloride anhydrous $FeCl_3$ were premixed with Ca precursor as per Table 5.1. The precursor molar concentrations and their sample codes are listed in Table 5.1, and the same codes are followed throughout the thesis. The final molar ratio was kept constant with (Ca+Zn+Fe)/P= 1.67. The mixture was transferred to an oil bath at the reaction temperature of 65 °C. Once the temperature was stabilized, 50 mL of 0.6 M $(NH_4)_2.HPO_4$ preheated at 65 °C was added in a dropwise manner to the mixture under vigorous stirring. Afterward, NH_4OH solution was further added dropwise until the pH of the mixture reached 11. The mixture was continuously heated at 65 °C, with vigorous stirring for 3 h, and then was aged for 24 h. Further, the solution was washed several times with deionized water until pH reached neutral. The samples were air-dried at 80 °C in a hot air oven followed by sintering at a temperature evaluated using differential scanning calorimetry (DSC) analysis (Netzsch, Model: STA449F3A00) at a rate of 10 K/min under Ar environment. The DSC analysis revealed that the crystallization temperature of the as-prepared HAp sample was 447.5 °C. Hence, all the samples were calcinated at 650 °C for further evaluation and applications.

Table 5.1. The precursor molar concentrations used for the synthesis of ZFHAp samples and their sample codes

S.No.	Sample code	Conc. of Ca (M)	Conc. of Zn (M)	Conc. of Fe (M)	Conc. of P (M)
1	ZFHAp-0 or "HAp"	1.0	0	0	0.6
2	ZFHAp-1	0.85	0.075	0.075	0.6
3	ZFHAp-2	0.85	0.10	0.05	0.6
4	ZFHAp-3	0.85	0.05	0.10	0.6

5.4 Characterizations of synthesized ZFHAp

Similar to that of AZO and FZO nanomaterials, the ZFHAp samples were evaluated as given in sections 3.1.3 and 4.2.2.

5.5 Biological characterizations

The synthesized ZFHAp samples were assessed for their suitability for biomedical applications. Two biological characterizations were carried out. First, the synthesized ZFHAp samples were evaluated for their incorporated antibacterial activity, and the mechanism of the antibacterial activity was deciphered. Second, the cytocompatibility, as well as the cell proliferation analyses, were conducted. The detailed procedures are as follows:

5.5.1 Antibacterial activity analysis

The broad-spectrum antibacterial activity of the designed ZFHAp samples was evaluated as given in section 4.2.3.1. Further, the OD_{600} values were recorded at different concentrations (c) and fitted with an exponential decay expression to determine the MIC value.

$$OD_{600} = y_0 + Ae^{-kc} \quad (5.1)$$

Where A is a constant, y_0 refers to the MIC value, and k is the decay constant.

5.5.2 Cytotoxicity and Cell proliferation analysis

The cytotoxicity and the cell proliferation analysis of ZFHAp samples were carried out following the previously reported protocols [292] using the MTT assay a given in section 4.2.3.2.

5.5.2.1 Anti-inflammatory assay

In addition to cytocompatibility, the TNF-α activity (inflammatory response) of the prepared material was evaluated by using the protocol provided by the manufacturer of the TNF-α kit from Sigma Aldrich. In detail, the MG-63 cells were first grown in the presence 1 mg/mL concentration of the ZFHAp samples. The cell media was then analyzed for its TNF-α activity using the TNF-α ELISA kit.

5.5.2.2 Bone cell proliferation assays

The practical applicability of the designed material was evaluated as nano-antibiotic in place of Pen-strep antibiotic in DMEM media. The MG63 cells (5×10^4 cells/mL) were incubated in a 24-well plate for 24 h using ZFHAp samples (0.25 mg/mL) in DMEM without Pen-strep antibiotic at 37 ºC, 5 % CO_2, and 85 % humidity in a CO_2 incubator. In this analysis, DMEM with Pen-strep was taken as control. After the incubation, cell viability was analyzed using an MTT assay, and cell proliferation (growth) was examined using an optical microscope. Similarly, to analyze the bone proliferation efficiency of the ZFHAp samples, the ALP activity of the ZFHAp samples was investigated. In brief, the cells were first incubated at two concentrations of material, *i.e.*, 1 and 0.1 mg/mL. After incubation, the cell lysate was collected, and the ALP activity was analyzed using the manufacturer's protocol on the 7^{th}, $14^{th,}$ and 21^{st} days, respectively.

All the experiments were performed in triplicates. The results are presented as the average values ± standard deviations.

5.6 Results and discussion

5.6.1 Phase structures of prepared ZFHAp samples

The phase analysis of the designed ZFHAp samples was carried out using XRD analysis. The diffractograms of the prepared samples, along with standard JCPDS patterns, are shown in Figure 5.1A. The XRD data elucidated that ZFHAp samples contained the major peaks corresponding to

the hexagonal HAp (JCPDS 98-010-3652) but blue-shifted from 28.90°, 31.85°, 39.99°, and 49.59° (Figure 5.1B). The presence of a peak corresponding to 77.33° of Fe_3O_4 (JCPDS 98-001-7122) indicated the successful synthesis of Fe^{3+} doped HAp by replacing a few of the Ca^{2+} ions from the hexagonal HAp matrix. In addition, different peaks corresponding to the hexagonal wurtzite structure of ZnO (JCPDS 98-001-5464) were coincided in ZFHAp samples, along with two distinct peaks at 33.43° and 44.24° (Figure 5.1C and D), confirming the successful synthesis of Zn and Fe co-integrated HAp. Ca^{2+} ions of the HAp matrix were preferentially displaced by Fe^{3+} ions because of the highest reduction potential (+0.77 V) and the lowest ionic radii of 0.06 nm than Zn (0.074 nm) and Ca (0.099 nm). The crystallite sizes of the samples were calculated using the Scherrer equation as previously described [341]. The crystallite size of the samples was found to be 22.70, 46.07, 51.08, and 68.04 nm for HAp, ZFAHp-1, ZFHAp-2, and ZFHAp-3 samples, respectively. It is reported that the doping of ions alters the crystalline structure and size of HAp [19].

The phase analysis was performed by comparing the obtained XRD patterns with various JCPDS data. It was observed that $Ca_{9.333}Fe_{1.167}(PO_4)_7$ phase was one of the dominating phases available in all the samples. The ZFHAp-1 sample contained 91 % of $Ca_{9.333}Fe_{1.167}(PO_4)_7$ phase and 2.2% of the zincite (ZnO) phase. The ZFHAp-2 sample consisted of 33 % of the $Ca_{9.333}Fe_{1.167}(PO_4)_7$ phase, 3 % of the $Ca_{28.8}Fe_{3.2}(PO_4)_{21}O_{0.5}$ phase, and 44 % of their mixed-phase along with the 8.3 % of the zincite phase. The ZFHAp-3 contained only 0.8 % of the $Ca_{9.333}Fe_{1.167}(PO_4)_7$ phase, 1.8 % of the $Ca_9Fe(PO_4)_7$ phase, and 84 % of their mixed-phase along with 4.6 % of the zincite phase.

The doping of metal ions into the HAp lattice introduced crystal deforms depending on the concentrations of the dopant ions [342]. In the present study, at the lowest (3 % molar) iron concentration, $Ca_{28.8}Fe_{3.2}(PO_4)_{21}O_{0.5}$ and $Ca_{9.333}Fe_{1.167}(PO_4)_7$ phases were formed in the ZFHAp-2 sample. With the increase in ion molar ratio to 4.5 %, the $Ca_{9.333}Fe_{1.167}(PO_4)_7$ phase was dominated in the ZFHAp-1 sample. However, a further increase in the iron molar ratio to 6% resulted in the formation of $Ca_9Fe(PO_4)_7$ phase and $Ca_{9.333}Fe_{1.167}(PO_4)_7$ phase in the ZFHAp-3 sample. It has been observed that the incorporation of Fe into the HAp lattice incorporates the oxygen to the PO_4 tetrahedral to obtain PO_5 trigonal bipyramids [343].

At the lowest concentration of Fe^{3+} (ZFHAp-2), linear interactions (interstitial coupling) within the ferric-HAp due to Fe-O-Fe planes led to the formation of $Ca_{32-x}Fe_x(PO_4)_{21}O_{0.5}$ phase along with $Ca_{11-x}Fe_x(PO_4)_7$ phase. An increase in the molar concentration of Fe^{3+}, Fe-O-Fe planes diminished

and resulted in ferric-HAp ($Ca_{11-x}Fe_x(PO_4)_7$) rich phase (91%) in the ZFHAp-1 sample. At a further elevated concentration of Fe^{3+} ions, the atomic distribution was shifted from $Ca_{11-x}Fe_x(PO_4)_7$ phase to $Ca_{10-x}Fe_x(PO_4)_7$ phase. Because of the maximum pure phase of $Ca_{9.333}Fe_{1.167}(PO_4)_7$, the ZFHAp-1 sample is expected to provide the highest magnetization values.

On the other hand, no phases corresponding to $(Ca_{10-x}Zn_x)$-$(PO_4)_6(OH)_2$ or $(Ca_{10-x-y}Zn_xFe_y)$-$(PO_4)_6(OH)_2$ were observed in all the samples. However, a separate ZnO phase was present in all the samples leading to the synthesis of the biphasic ferric-HAp-zincite nano-assembly indicating the successful integration of the zinc and iron into the HAp lattice without hampering the HAp phase. The most probable reason for forming a separate phase of ZnO is the available replacement sites for Zn ions in the HAp lattice. It is reported that zinc ions replace only the surficial calcium ions from the HAp lattice [344, 345]. However, due to the high reduction potential of the Fe^{3+} ions than that of Zn^{2+} ions, iron competitively (preferentially) replaced the calcium ions from the HAp lattice, and thus separate zincite phases were formed. The abundance of the zincite phase varied according to the molar concentrations of zinc precursors as ZFHAp-2 > ZFHAp-3 > ZFHAp-1. Therefore, it was expected to attain a higher antibacterial activity of the ZFHAp-2 sample. These observations indicated that the generation of phases in HAp lattice could be governed by the selection of metal ions and their concentrations.

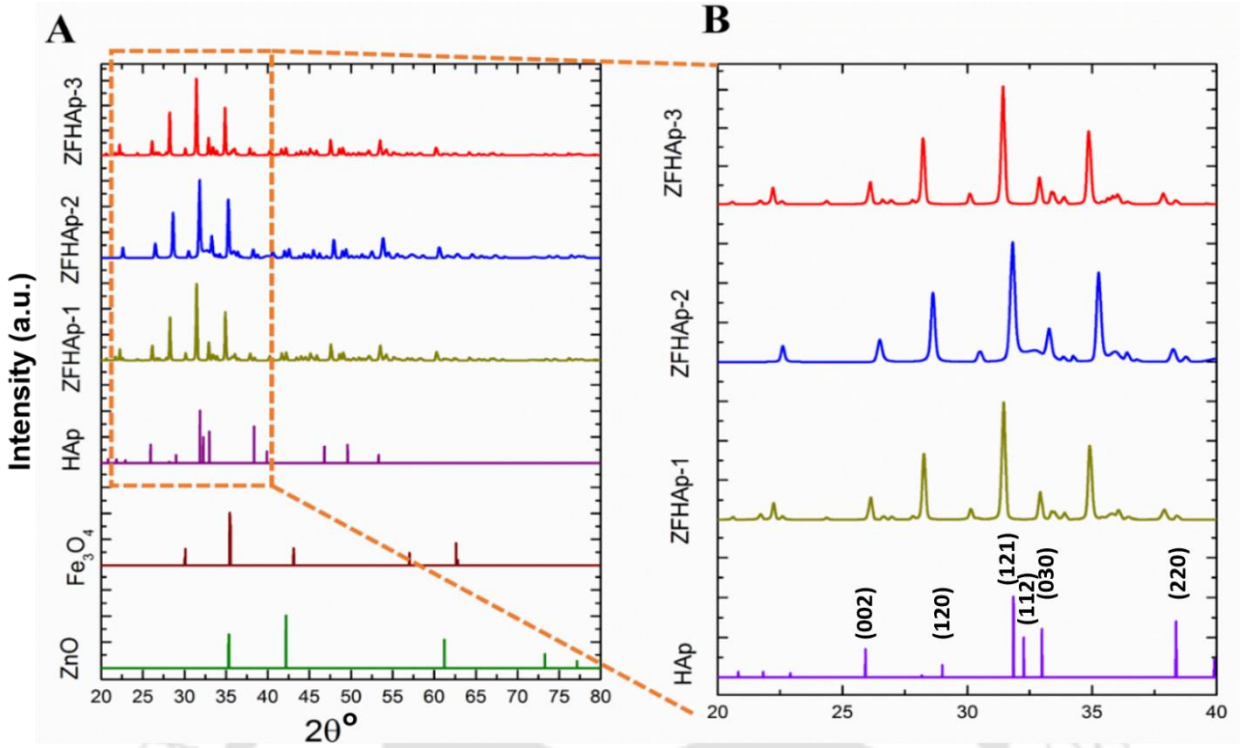

Figure 5.1. A) XRD pattern of various ZFHAp samples with the standard HAp (JCPDS 98-010-3652), ZnO (JCPDS 98-001-5464), and Fe_3O_4 (JCPDS 98-001-7122); **B)** Shift in the peaks of ZFHAp samples

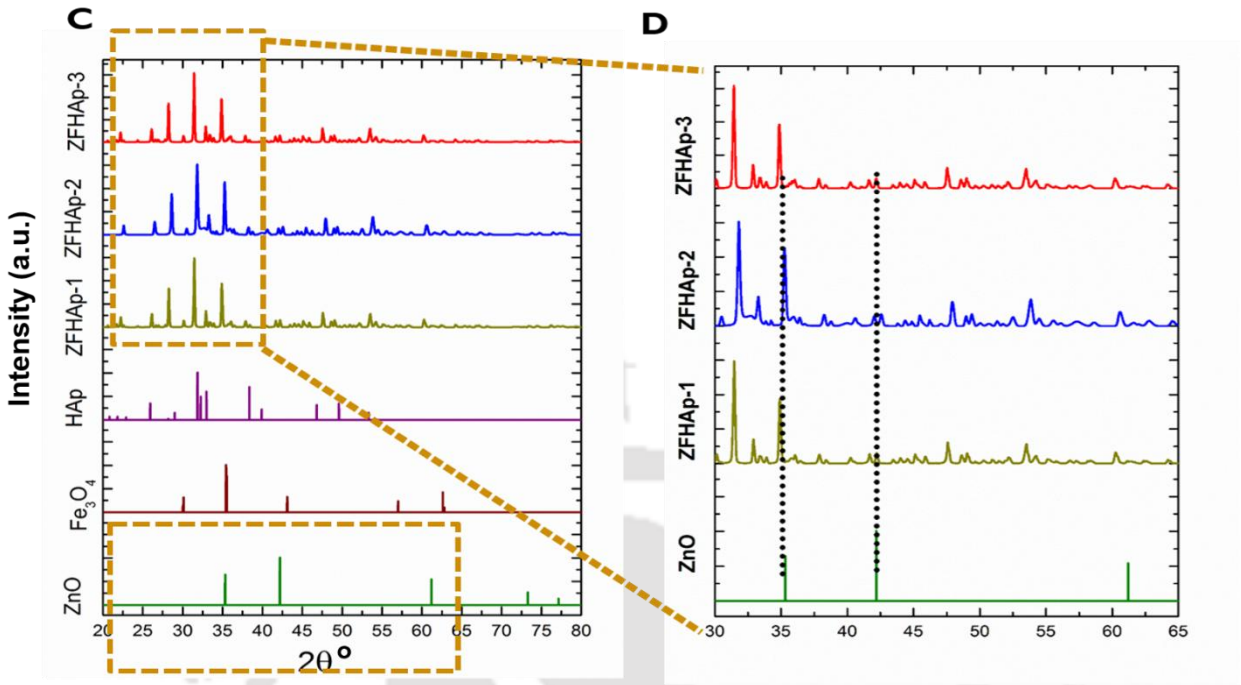

Figure 5.1. C) XRD pattern of various ZFHAp samples with the standard HAp (JCPDS 98-010-3652), ZnO (JCPDS 98-001-5464), and Fe_3O_4 (JCPDS 98-001-7122); **C)** Peaks corresponding to the ZnO (JCPDS 98-001-5464)

To further confirm the structure, the ZFHAp samples were evaluated using the Raman analysis, as shown in Figure 5.2. Three major peaks were observed: a sharp peak at 960 cm^{-1} corresponding to the Raman shift of phosphate group [346], a characteristic vibrational peak of ZnO at 438 cm^{-1} correspondings to E2 (high) [275], and another peak corresponding to Fe-O bond at 580 cm^{-1}. The Raman spectra complemented the XRD data and indicated the successful integration of the Zn^{2+} and Fe^{3+} with hydroxyapatite as the major phase (matrix) of the developed nanomaterials.

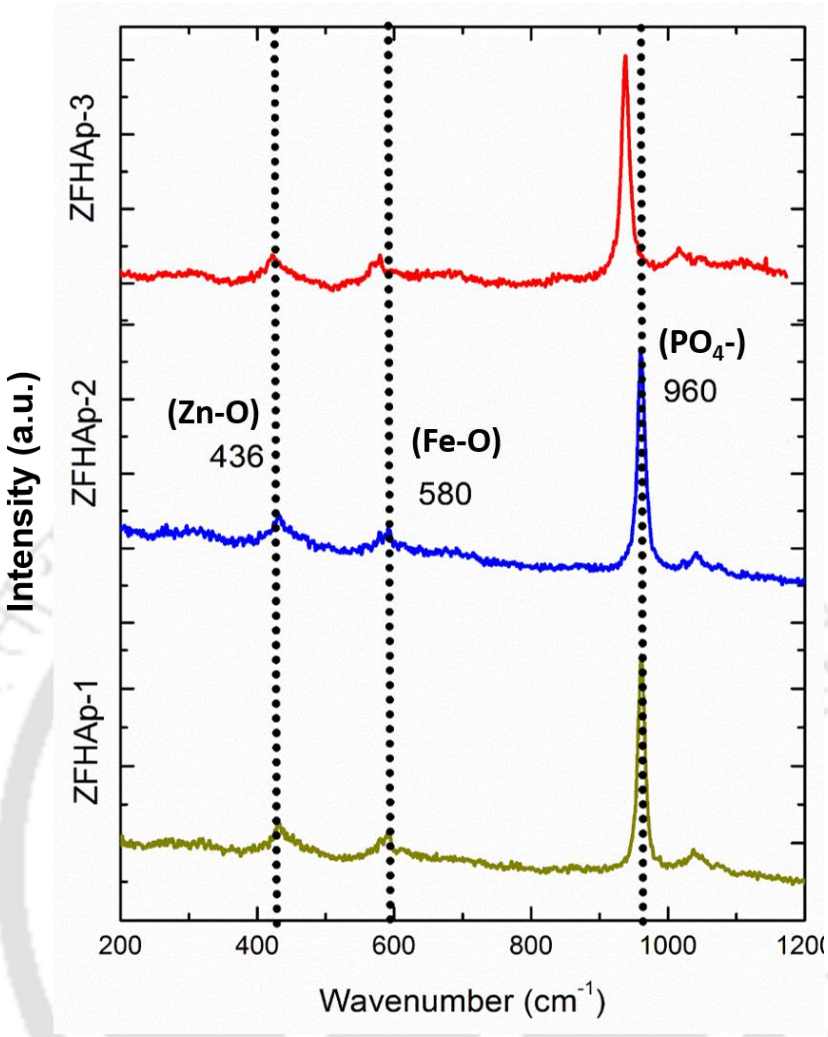

Figure 5.2. Raman Spectra of various ZFHAp samples, showing three major peaks at 980 cm^{-1} of phosphate, 480 cm^{-1} of Zn-O, and 580 cm^{-1} of Fe-O.

For the elemental analysis, the EDX examination was carried out for all the ZFHAp samples using the FESEM instrument. The primary elements in all the samples were Ca, P, O, while minor elements (Zn and Fe) were found in ZFHAp samples (Figure 5.3). The Ca:P ratio of the HAp was 1.63, while the same for ZFHAp samples were slightly lesser due to the formation of new ferric hydroxyapatite phases. The (Ca+Fe):P ratios were found to be 1.43, 1.57, and 1.42 for ZFHAp-1, ZFHAp-2, and ZFHAp-3 samples, respectively. The elemental analysis supported the results obtained from XRD and Raman. The XRD, Raman, and EDX analysis together confirmed the successful synthesis of ZFHAp samples.

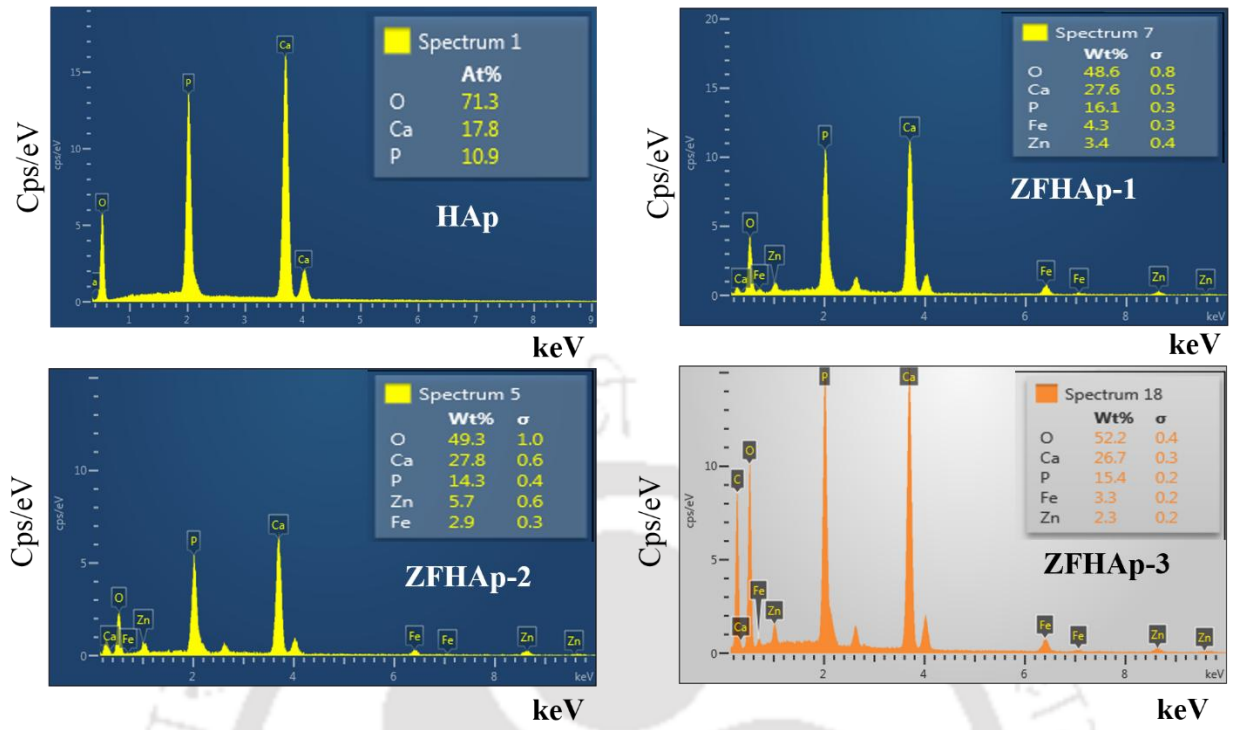

Figure 5.3. EDX analysis of HAp and ZFHAp samples

5.6.2 Morphologies of prepared ZFHAp samples

The biological properties of the biomaterials are dependent on their particle size and morphology [319]. The morphological analysis of ZFHAp samples using FESEM and subsequent image analysis using ImageJ software revealed that the presence of dual morphology in all the ZFHAp samples. The irregular morphology corresponded to HAp and particulate-shaped structures for minor ZnO. The diameter for the irregular morphologies in the HAp and ZFHAp was 58.9 ± 11 nm, 84.4 ± 37 nm, 77.8 ± 10 nm, 56.9 ± 6 nm, respectively (Figure 4A-D). The particulate shaped morphology attained the 56.7 ± 9 nm, 30.9 ± 5 nm, and 22.4 ± 2 nm sizes for ZFHAp-1, ZFHAp-2, and ZFHAP-3 samples, respectively (Figure 5.4B-D). Further, the ZFHAp-2 sample was analyzed using the FETEM. The particle size was confirmed as < 100 nm, with an average size of 96.41 ± 9.9 and 20.71 ± 7.20 nm for rod-shaped and particulate-shaped morphology, respectively (Figure 5.4E). Similarly, the TEM image reflected two distinct *d spacing* of 0.62 nm and 0.21 nm (Figure 5.4F), indicating the high crystallinity and dual planes distances in the biphasic ferric-HAp-ZnO system. This confirmed the dual morphology of the designed nanoassembly.

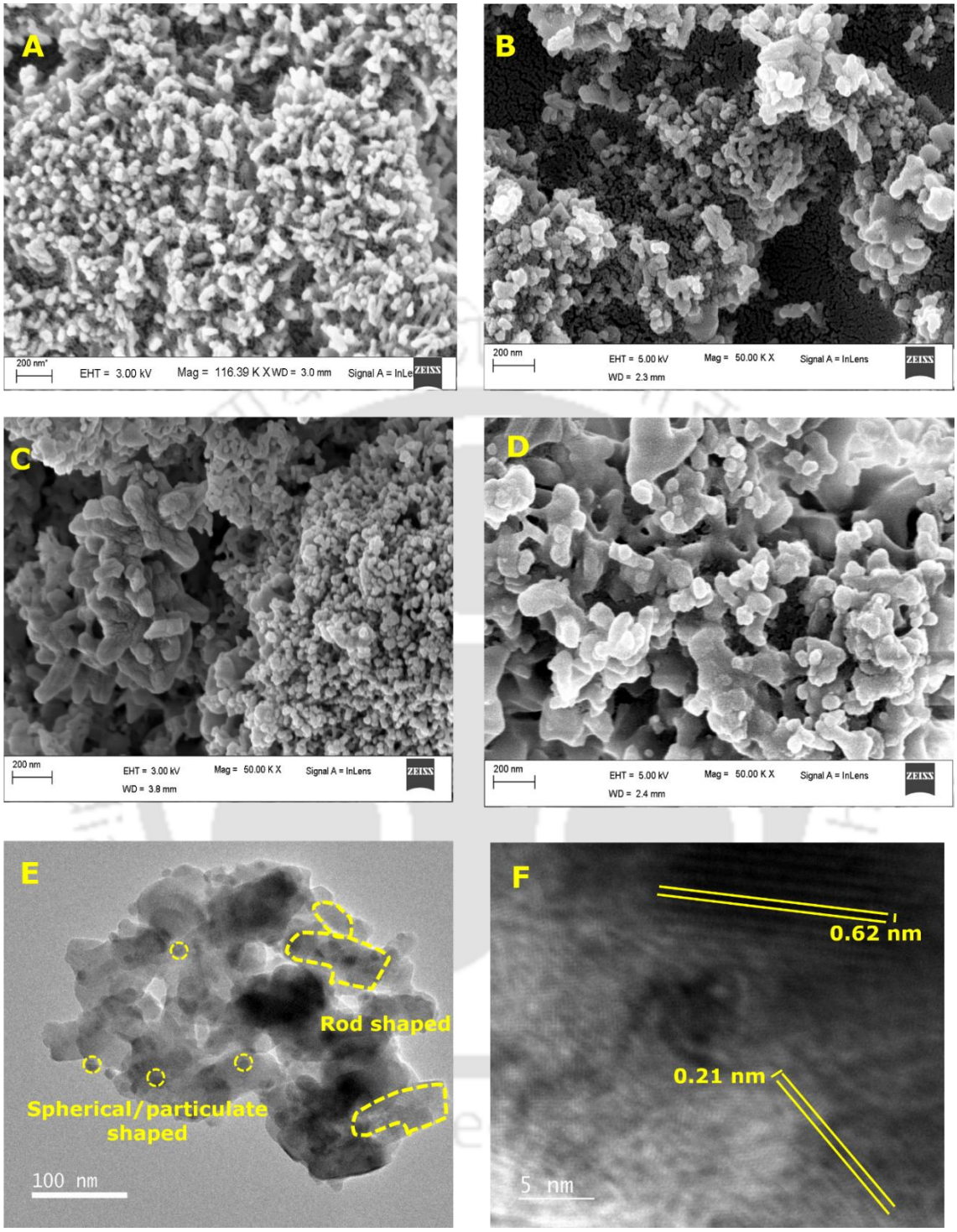

Figure 5.4. FESEM images of ZFHAp samples; **A)** HAp **B)** ZFHAp-1, **C)** ZFHAp-2, **D)** ZFHAp-3; FETEM image **(E)** and lattice fringe pattern **(F)** of ZFHAp-2 sample; indicating the dual morphology, *i.e.*, rod shaped and particulate shaped, and high crystallinity

5.6.3 Magnetic properties and colloidal stability

The integration of Zn and Fe not only provided the dual morphology but was also expected to provide the desired antibacterial as well as the target efficiency. To calculate the target efficiency, the ZFHAp samples were evaluated using VSM. Doping of Fe^{3+} ions incorporated paramagnetic properties to all the ZFHAp samples (Figure 5.5). The pure HAP sample showed diamagnetism behavior [347]. The respective magnetization, retentivity, and coercivity values are listed in Table 5.2. The saturation magnetization values were 0.664, 0.151, and 0.254 emu/gm for ZFHAp-1, ZFHAp-2, and ZFHAp-3 samples, respectively, which are in correlation with the previous reports for targeted drug delivery and other therapeutic applications [10, 348]. As indicated by the XRD data, the highest magnetization values were found to be for the ZFHAp-1 sample containing the purest form of the $Ca_{9.333}Fe_{1.167}(PO_4)_7$ phase, followed by the sample containing the highest Fe^{3+} concentration (ZFHAp-3), or sample containing maximum mixed-phases ($Ca_{9.333}Fe_{1.167}(PO_4)_7$ and $Ca_9Fe(PO_4)_7$ phase). ZFHAp-2 carried the least magnetization values. This corresponded that an increase in the zincite phase decreased the magnetization because of its diamagnetic nature [349]. The colloidal stability of the prepared samples was tested by measuring the zeta potential. All the surfaces carried a negative surface charge, which ranged from -19.9 mV, -20.8 mV, -28.6 mV, and -23.4 mV for HAp, ZFHAp-1, ZFHAp-2, and ZFHAp-3 samples, respectively (Figure 5.5B). The higher values of zeta potential $\geq \pm 20$ mV reflect the greater colloidal stability of the samples [350]. Hence, the obtained values of surface charge indicated the excellent colloidal stability of the prepared ZFHAp samples.

Table 5.2. Magnetic properties of the synthesized ZFHAp samples

S. No	Sample	Magnetization (emu/g)	Coercivity (Oe)	Retentivity (emu/g)
1	HAp	29.41×10^{-3}	106.03	1.75×10^{-3}
2	ZFHAp-1	0.664	0.384	833.28×10^{-6}
3	ZFHAp-2	0.151	105.78	5.29×10^{-3}
4	ZFHAp-3	0.254	198.04	13.35×10^{-3}

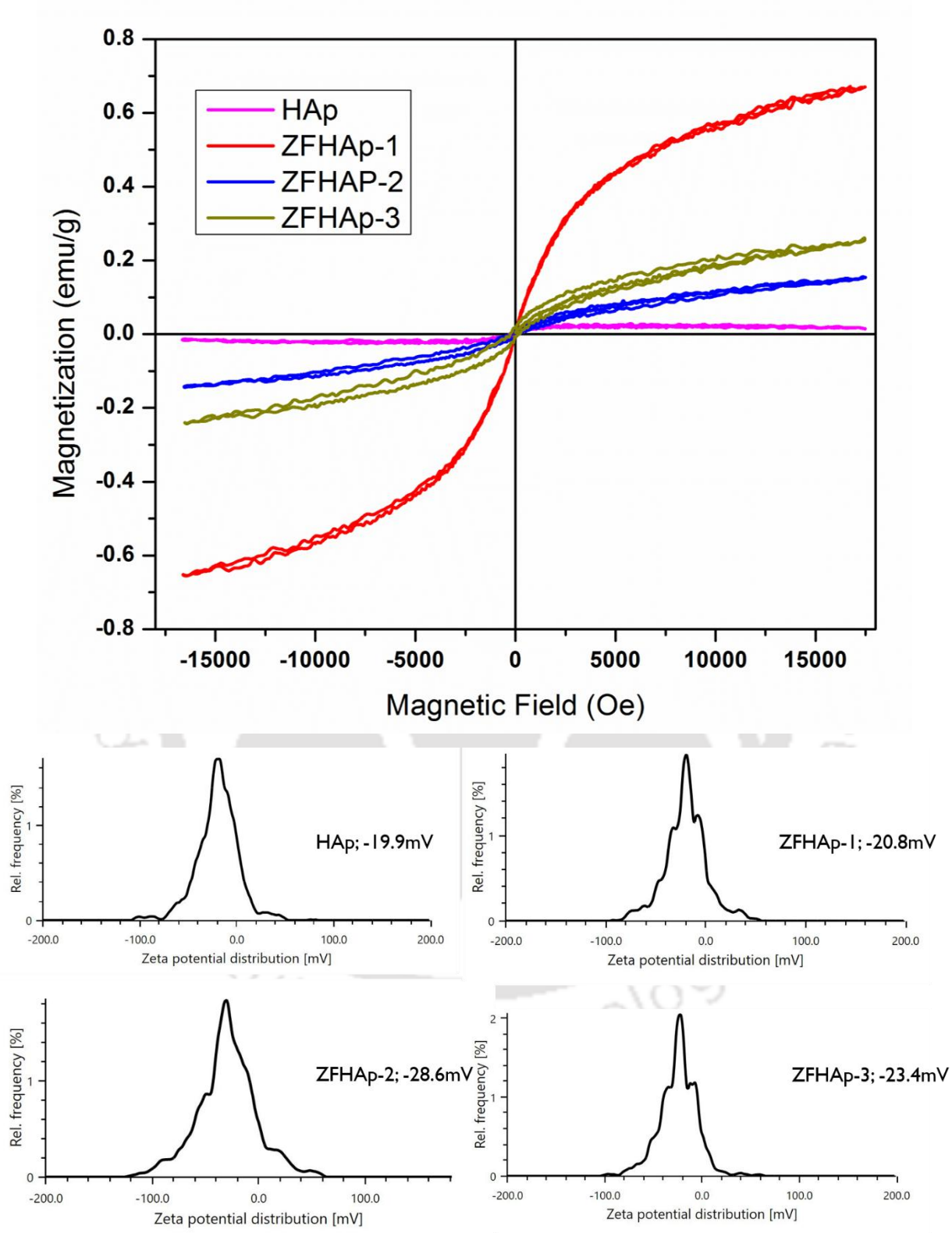

Figure 5.5 A) VSM analysis of HAp and ZFHAp samples **B)** Zeta potential of the ZFHAp samples

5.6.4 Biological activity of ZFHAp samples

After successfully achieving the target efficiency, the biological activities of the ZFHAp samples were evaluated. The detailed discussion is as follows:

5.6.4.1 Antibacterial activity analysis

The antibacterial activity of nanoparticles is usually dependent on their morphology and size [252], which causes a hurdle in the bulk production of the nanoantibiotic due to their high energy input requirements and post-production cost. In addition, most of the nanomaterials are efficient for the photodynamic inactivation of the bacteria or via the generation of ROS [295, 296], which is also a major cause of toxicity to mammalian cells toxicity [29]. Hence, obtaining the desired morphology using simple, non-complex methods with antibacterial action under dark conditions is essential for their commercialization. In this study, ZFHAp samples were synthesized via a simple co-precipitation method, which acquired a dual morphology with sizes < 100 nm. The antibacterial efficacy, as well as the mechanism of action, were investigated. All the samples showed good antibacterial activity against two Gram-positive and two Gram-negative bacteria (Figure 5.6A). The decrease in OD indicated the killing of bacteria. The MIC values were evaluated using equation 1 and the obtained results are listed in Table 5.3. The sample containing the highest amount of ZnO (ZFHAp-2) provided the lowest MIC values. The MIC values were further scrutinized for their effectiveness in terms of ZOI against all the bacterial species via comparing with a traditional antibiotic, kanamycin (Figure 5.6B). The respective ZOI sizes are depicted in Table 5.3. The ZOI sizes of the ZFHAp samples at their respective MIC were found to be comparable with that of kanamycin at 0.5 mg/mL. This indicated that the synthesized ZFHAp NPs were effective at a lower concentration (60-80 μg/mL) and comparable to the kanamycin's antibacterial performances. Interestingly, the antibacterial effectiveness was dependant on the dopant concentration and not on the particle size, as the particle size was found to be the lowest for ZFHAp-3 samples. In contrast, the highest antibacterial activity was observed for the ZFHAp-2 sample.

To evaluate the antibacterial mechanism, the ROS production by the ZFHAp samples was examined. ZFHAp samples showed no ROS generation, as shown in Figure 5.6C. The control samples (Saline, LB Media, and *E.coli* in LB media without ZFHAp samples) showed similar intensities (p values > 0.05) with and without ZFHAp samples, affirming the ROS independent

antibacterial activity of the ZFHAp samples. As HAp lacks in its antibacterial activity, the biphasic ferric-HAp-ZnO system induced the antibacterial activity into the HAp matrix due to the presence of the ZnO phase. Our group has previously reported a ROS-independent antibacterial mechanism of Fe (III) doped ZnO via the release of Zn^{2+} and Fe^{3+} ions [341]. Hence, the release of the Zn^{2+} and Fe^{3+} ions was evaluated under PBS incubation at a pH value of 7.4. As expected, and corresponding to the release pattern of Chapter 4, the Zn^{2+} and Fe^{3+} ions followed linear release kinetics. ZFHAp-2 samples exhibited the highest release of Zn^{2+} ions, while ZFHAp-3 samples showed the highest release of the Fe^{3+} ions (Figure 5.6D). Henceforth, in this study, no ROS production indicated the major antibacterial activity of ZFHAp by the release of Zn^{2+} and Fe^{3+} ions from the HAp matrix.

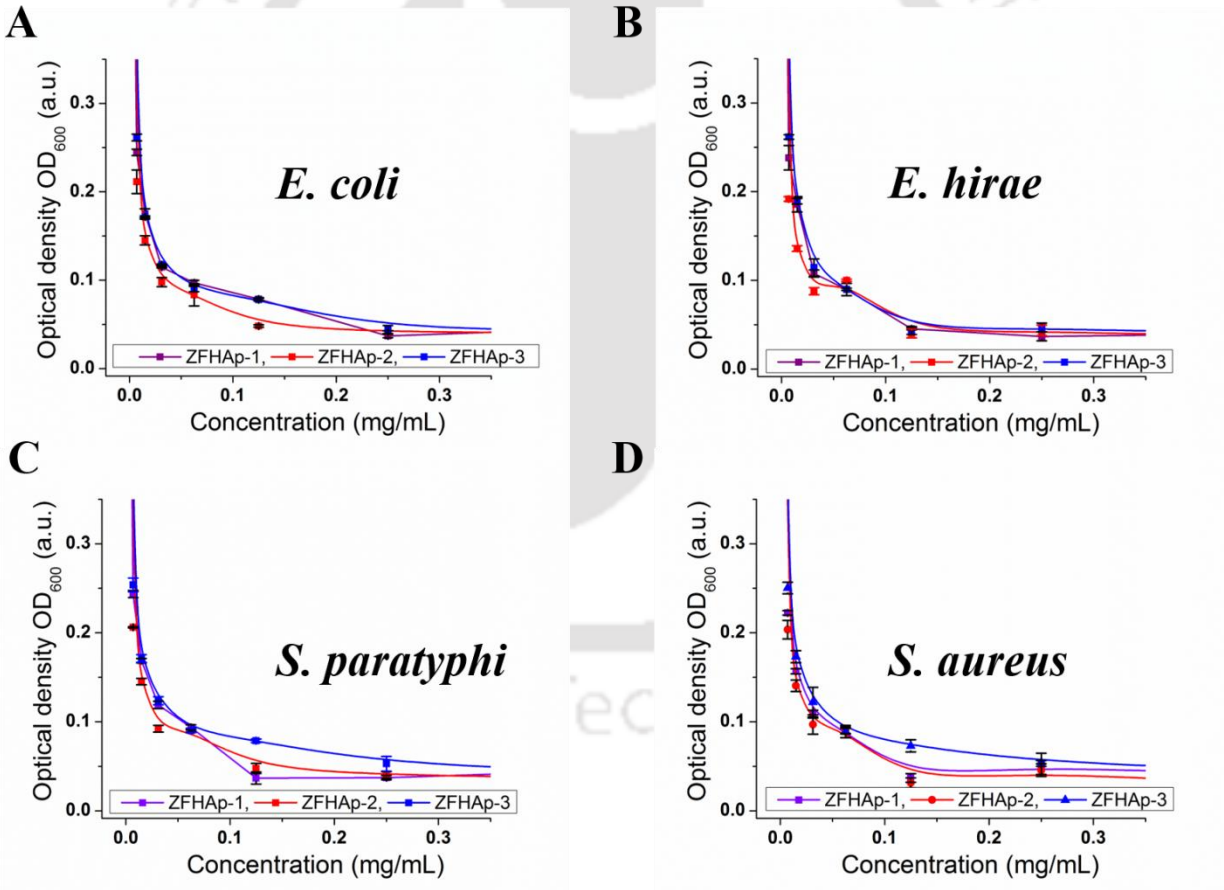

Figure 5.6A. Antibacterial activity of various ZFHAp samples against A) *E.coli*, B) *E. hirae*, C) *S. paratyphi*, and D) *S. aureus*

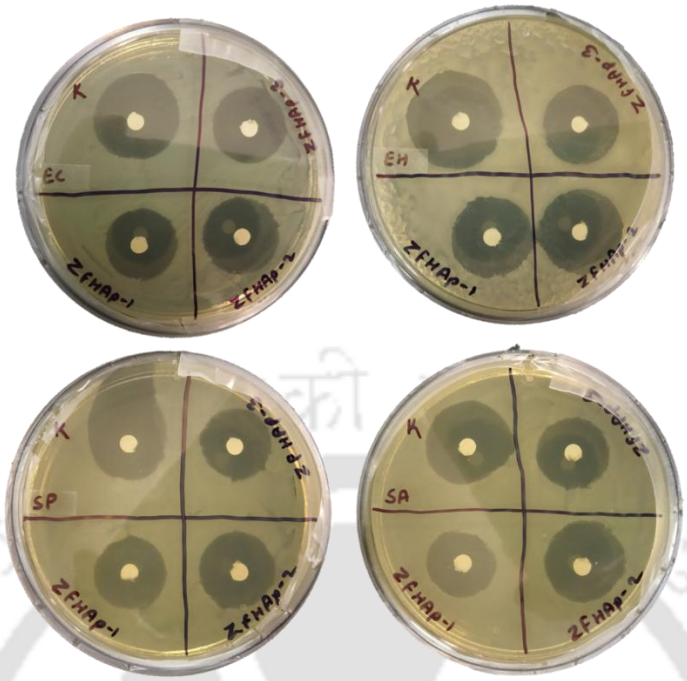

Figure 5.6B: ZOI of various ZFHAp samples against *E. coli*, and *S paratyphi* (Gram-negative) and *E. hirae* and *S. aureus*, (Gram-positive)

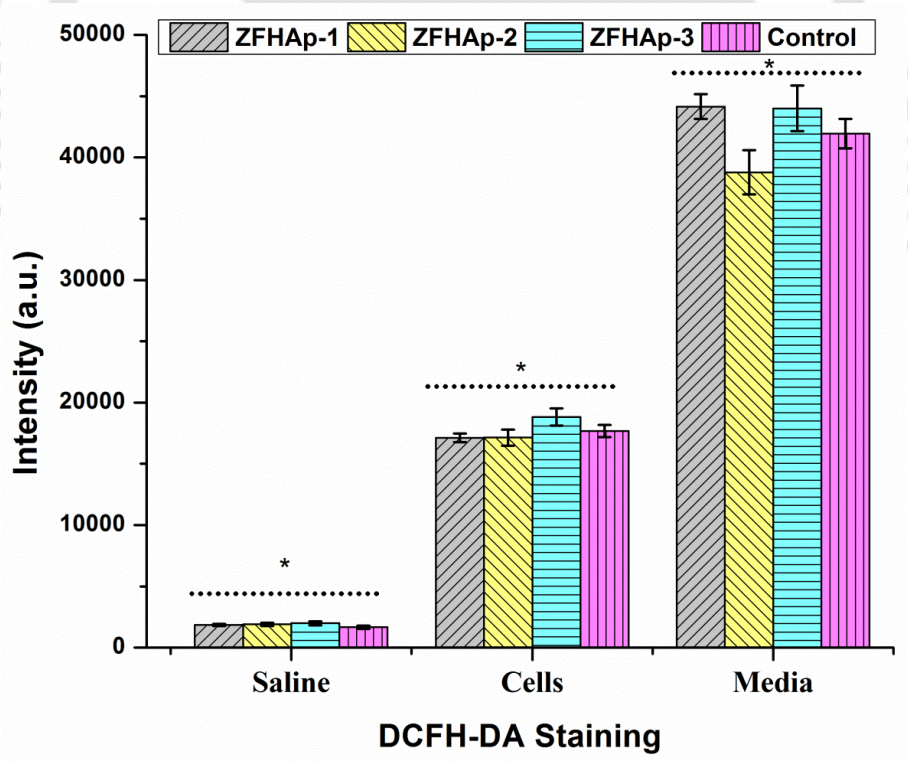

Figure 5.6C: ROS production by ZFHAp samples under incubation with Saline, *E.coli* cells and LB Media. Statistical analysis as compared to control resulted in *p *value* > 0.05 ; n=3.

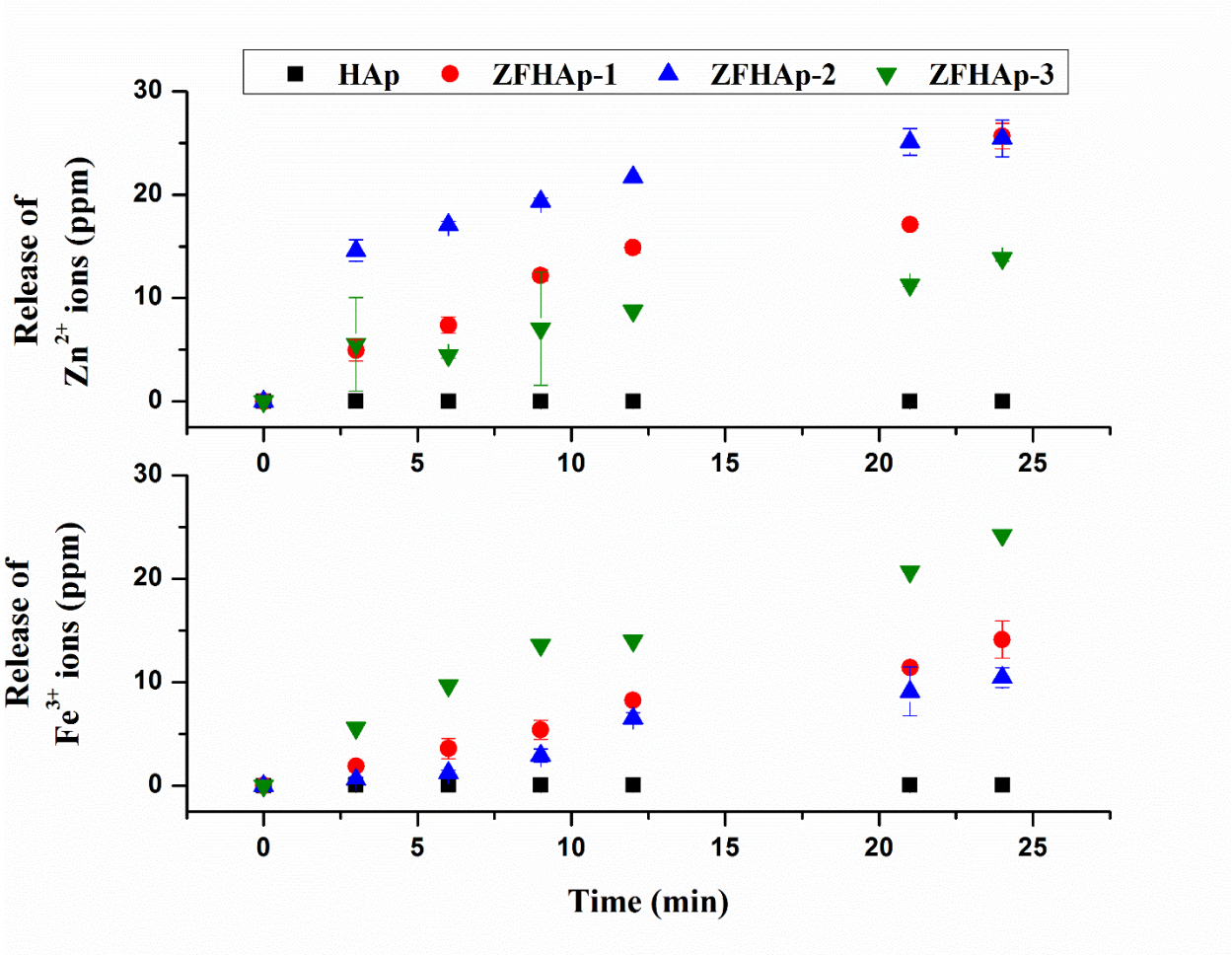

Figure 5.6D. Release of Zn^{2+} and Fe^{3+} ions by ZFHAp samples under PBS incubation at pH 7.4

As a linear release of Zn^{2+} and Fe^{3+} ions was observed, it was expected that the slow release of these two ions might rupture the bacterial cell wall. Hence, to evaluate the rupturing into the bacterial cell wall, the *E.coli* cells were first grown for 6 h and were further treated with the ZFHAp-2 sample for 6 h. After incubation, the cells were first washed, followed by fixing, as discussed in Chapters 3 and 4. The cells were then analyzed by using FESEM imaging. The untreated cells co-cultured for up to 6 h were taken as a positive control. As given in Figure 5.6E(1), the untreated cells reflected the intact cell wall. However, the bacterial cells incubated with ZFHAp-2 samples reflected a shrunk and ruptured cell wall (Figure 5.6E(2)). As discussed in Chapter 3, the slow and steady release of the Zn^{2+} and Fe^{3+} ions was successful in damaging the cell wall of the bacteria; the ZFHAp samples also attained a similar antibacterial mechanism. Hence, the release of Zn^{2+} and Fe^{3+} ions were found to be the main antibacterial mechanism,

avoiding ROS generation. ROS independent antibacterial mechanism indicated the higher cytocompatibility of the ZFHAp samples.

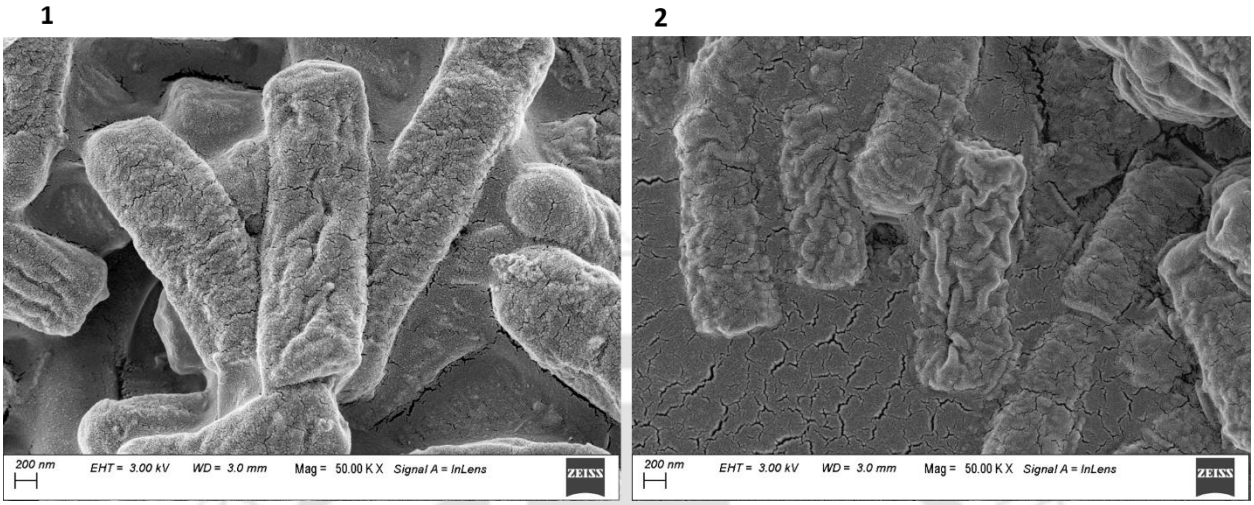

Figure 5.6E. 1) *E.coli* cells untreated, grown up to 6 h, **2)** *E.coli* cells treated with ZFHAp-2 sample up to 6 h

Table 5.3. MIC and ZOI of ZFHAp samples

S. No	Sample	MIC (µg/mL)				ZOI (mm)			
		E.coli	*E.hirae*	*S. aureus*	*S.paratyphi*	*E.coli*	*E.hirae*	*S. aureus*	*S.paratyphi*
1	ZFHAp-1	77.5±0.02	72.2±0.02	71±0.02	72.9±0.01	17.85±1	20.55±2	20.30±1	21.92±1.5
2	ZFHAp-2	66.1±0.01	67.6±0.01	63.3±0.02	66.2±0.01	18.9±1.2	21.96±1.2	22.53±1.1	21.19±1
3	ZFHAp-3	75.9±0.02	73.4±0.02	78.3±0.01	78±0.01.4	18.98±1.4	21.36±1.7	21.09±1.0	20.85±1.3
4	Kanamycin	0.5 mg/mL				23.17±1.2	25.9±1.2	22.±1.3	23.94±1.8

Various recent studies have explored the antibacterial activity of the Zn integrated HAp, but none have focused on exploring or achieving the ROS independent antibacterial mechanism as given in Table 5.4.

Table 5.4: Various metal ions doped HAp, their synthesis methods, and biological performances

S. No	Materials	Methods			Ca/P Ratio: Phase	Antibacterial Activity		Cytotoxicity	Ref.
		Process	Temp. (°C)	Calcination Temp. (°C)		MIC	Mechanism		
1.	Zinc and chromium co-doped calcium HAp	Sol-gel	70-80	800-1000	NA/ HAp and –β-$Ca_3(PO_4)_2$	NA	NA	NA	[351]
2.	Zn- and Mg-doped HAp	Precipitation	90	900	1.9-2.2 for various doping concentrations:	0.5 mg/mL (taken for Zone of inhibition (ZOI): 8-11 mm	NA	NA	[1]
3.	Zn and Co co-doped HAp	Precipitation followed by Spark Plasma Sintering	90-100	NA	NA	17.82±1.81 mm for 0.24 M Co, and 13.11±0.11 mm for 0.24 M Zn	NA	100 µg/mL Cell viability ~85 % at day 6	[11]
4.	Silver-zinc co-doped β-tricalcium phosphate	Spray pyrolysis	RT	1050	(Ca + Ag + Zn)/P ratios: 1.45 to 1.53	99 % antibacterial activity by	NA	NA	[352]

						colony counting			
5.	Ag, Zn or Co doped HAp	Biomimetic approach	37	NA	NA	NA	NA	~85 % cell viability at 0.1 gm HAp	[353]
6.	Ag/Fe co-doped HAp	Co-precipitation method	RT	NA	HAp and maghemite	NA	NA	500 µg/mL toxic conc.	[354]
7.	Strontium/fluoride-codoped HAp	Hydrothermal	160	Lyophilized	1.3-1.9: HAp	18.07-81.56 with increased F and Sr concentration	NA	No toxicity till day 7	[355]
8.	Zinc and strontium co-doped HAp whiskers	Hydrothermal homogeneous precipitation	180	NA	NA: HAp and $CaZn_2(PO_4)_2.2H2O$	NA	NA	NA	[356]
9.	Sr/Fe co-doped HAp	Precipitation	60 for 5 h followed by sonication	NA	NA: HAp	ZOI: *E.coli* (16.6 to 17.5 mm) *S. aureus* (18.5-19.5 mm)	NA	No toxicity as compared to control	[357]

10.	Zn and Fe co-doped HAp	precipitation	65	650	(Ca+Zn+Fe)/P 1.7; HAp	60-80 µg/mL ZOI: *E.coli* (18-19 mm), *E.hirae* (21-22 mm), *S. aureus* (20-23 mm), and *S. paratyphi* (21-22 mm)	By release of ions, no ROS generation	No toxicity as compared to control up to 5 mg/mL	This Study

5.6.4.2 Cytotoxicity and bone cell proliferation analysis

The successful synthesis of ZFHAp and its desirably obtained excellent antibacterial and target efficiency indicated the potential use of this material for bone tissue engineering. However, the cytotoxicity of the nanomaterials is the major concern for material researchers to counteract. On the other hand, HAp based materials are known for their structural similarities with bone [5]. Hence, it is essential to evaluate its effect of incubation with the bone cells for the expected orthopedic applications. In this regard, the synthesized ZFHAp samples were incubated with MG-63 bone cells at various concentrations, as discussed in section 5.5.2 . The maximum concentration for ZFHAp samples was taken as 5 mg/mL, which was about 60 time's higher concentration than the observed MIC values. The cells showed more viability than control samples in the presence of the ZFHAp samples up to 5 mg/mL concentration for six days. Interestingly, the maximum cell viability was found to be for ZFHAp-2 samples (Figure 5.7). At 1 mg/mL concentration (15 times higher concentration than the MIC value), ZFHAp-2 showed the highest cell survival after three days, *i.e.*, 300% survival of cells as compared to the control sample. At a higher concentration of 5 mg/mL, the cell viability was slightly decreased, but still, ZFHAp-2 showed 200% cell survival at day 3. The statistical analysis revealed that the cell growth at day 3 and day 5 was highly significant as compared to control with p value ≤ 0.0001. A decrease in the cell viability at day 6 can be attributed to the high confluency of the cells, leading to less space for the cells to be grown. These results indicated that the ZFHAp samples are highly efficient for bone cell proliferation and did not cause any cytotoxic effect over the bone cells, presumably due to the dual morphology,

nano size, and mineral similarities with bone. It has also been reported that magnetic materials enhance osteoblast activity [358], and the presence of Zn^{2+} and Fe^{3+} ions also promotes cell proliferation [341]. Hence, the designed materials are effectively appropriate for orthopedic as well as other biomedical applications due to their excellent antibacterial activity, target efficiency, and high cell proliferation activity.

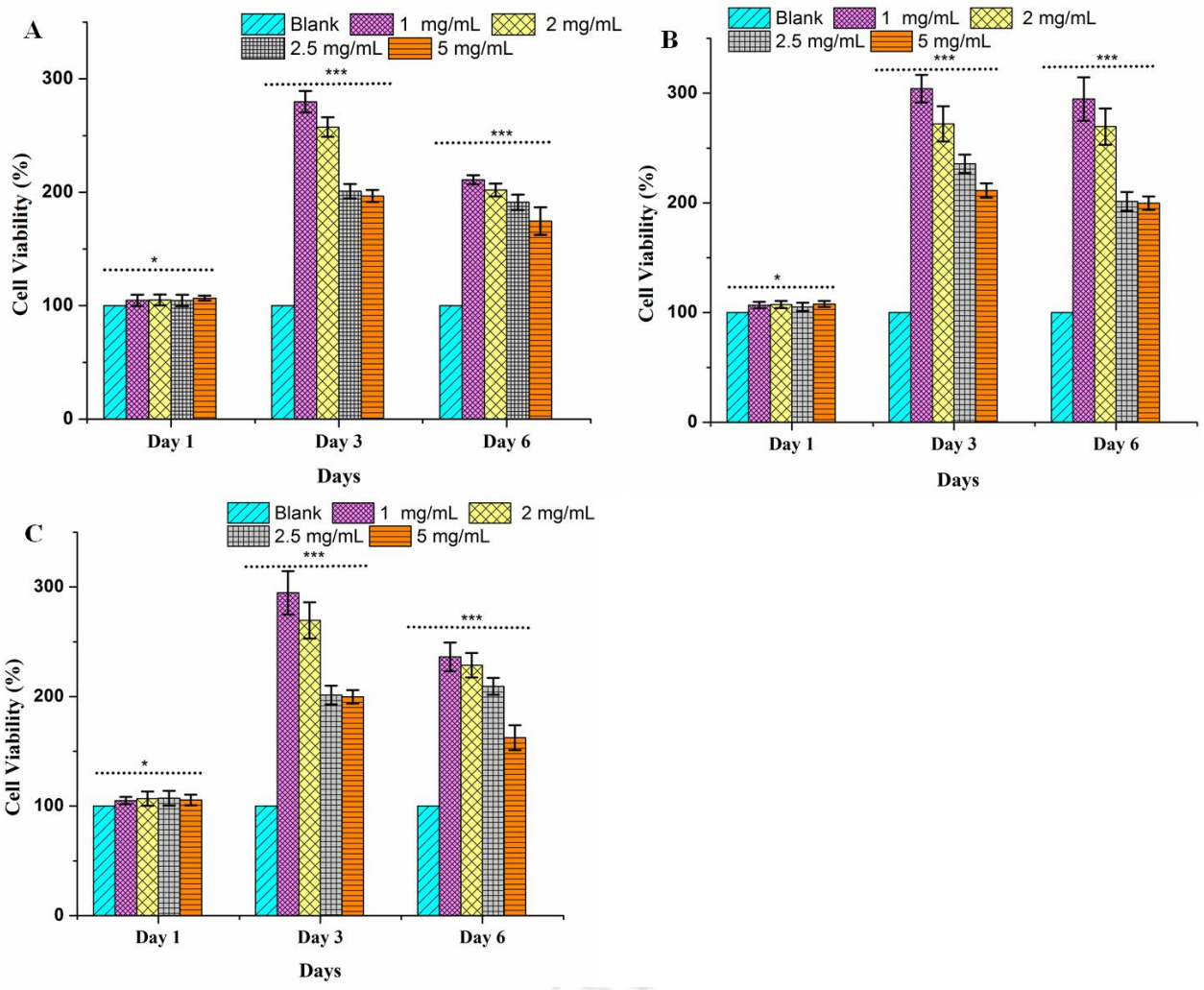

Figure 5.7 Cytocompatibility of ZFHAp NPs against MG-63 cells **(A)** ZFHAp-1, **(B)** ZFHAp-2 and **(C)** ZFHAp-3. Statistical analysis as compared to blank (only cells) *** *p value* ≤ 0.0001 and * *p* value ≥ 0.05; *n*=3.

5.6.4.2.1 Anti-inflammatory assay

The excellent cytocompatibility, as well as the practical applicability analysis of the ZFHAp samples, indicated its potential use for bone treatment. However, the growth of the cells or increase in the number of cells only does not indicate the biocompatibility as well as the cell proliferation ability of the designed material. Hence, to further investigate the ZFHAp samples' biocompatibility, the samples' TNF-α activity was analyzed for up to 21 days. A 1 mg/mL concentration of the samples was incubated with MG-63 cells at an initial 500 cells/well cell seeding density. After 7, 14, and 21 days, the TNF-α activity of the samples was analyzed. As shown in Figure 5.8, the ZFHAp samples exhibited the 735-850 pg/mL, 1181-1273 pg/mL, and 1019-1110 pg/mL of TNF-α protein at Day 7, 14, and 21, respectively (p values ≥ 0.05 for all the samples). However, the release of TNF-α in the presence of the samples was found to be similar to that of MG-63 cells without any incubation. Hence, the release of the TNF-α was not significant, indicating the absence of an inflammatory environment in the presence of the ZFHAp samples [359, 360].

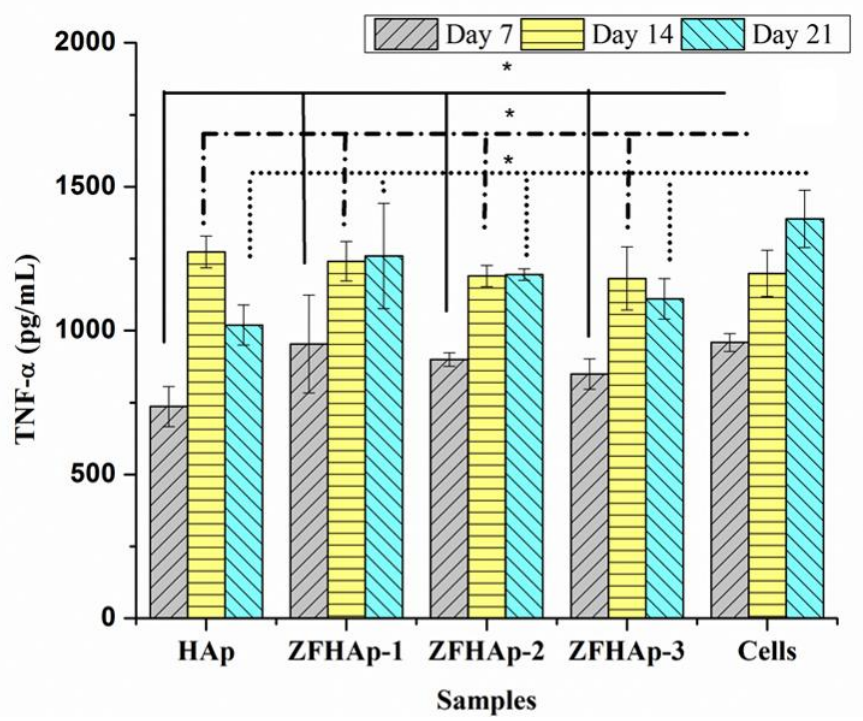

Figure 5.8. TNF-α activity of the ZFHAp samples; MG-63 cells reflected a similar amount of TNF-α release with and without ZFHAp samples; No inflammatory response; * p *value* ≥ 0.05; and ALP activities of ZFHAp samples as compared to HAp ** p *value* ≤ 0.05, *** p *value* ≤ 0.0001; n=2.

5.6.4.2.2 Bone cell proliferation analysis

The practical antibiotic applicability of the ZFHAp samples was evaluated via replacing Pen-strep with ZFHAp nanoantibiotic in the DMEM while incubating the bone cells for their proliferation analysis. The adhered cells on surfaces from media containing Pen-strep antibiotic, ZFHAp-1, ZFHAp-2, and ZFHAp-3 samples are shown in Figure 5.9. These images were analyzed using ImageJ software to calculate the confluency levels. The cells with Pen-strep antibiotic showed 0.75 ± 0.1 circularity index with 22 ± 3 % of the area covered. Correspondingly, the circularity index in the presence of ZFHAp-1, ZFHAp-2, and ZFHAp-3 samples was found to be 0.73 ± 0.1, 0.72 ± 0.1, and 0.73 ± 0.1, respectively. A lesser circularity index reflected better spreading and proliferation of cells. Similarly, the fraction areas covered (%) by the cells in the presence of the ZFHAp-1, ZFHAp-2, and ZFHAp-3 samples were found to be 24 ± 4 %, 26 ± 3 %, and 23 ± 4 %, respectively. These observations agreed to the results obtained during the cell viability analysis using MTT assay. A slight improvement in circularity index and the fraction area covered indicated that ZFHAp samples not only acted as a potential nanoantibiotic but also helped in the proliferation of the bone cells. Among ZFHAp samples, ZFHAp-2 exhibited the least MIC value, highest cell viability, and maximum cell proliferation. Hence, this study designates the ZFHAp as a potential candidate for bone tissue engineering applications.

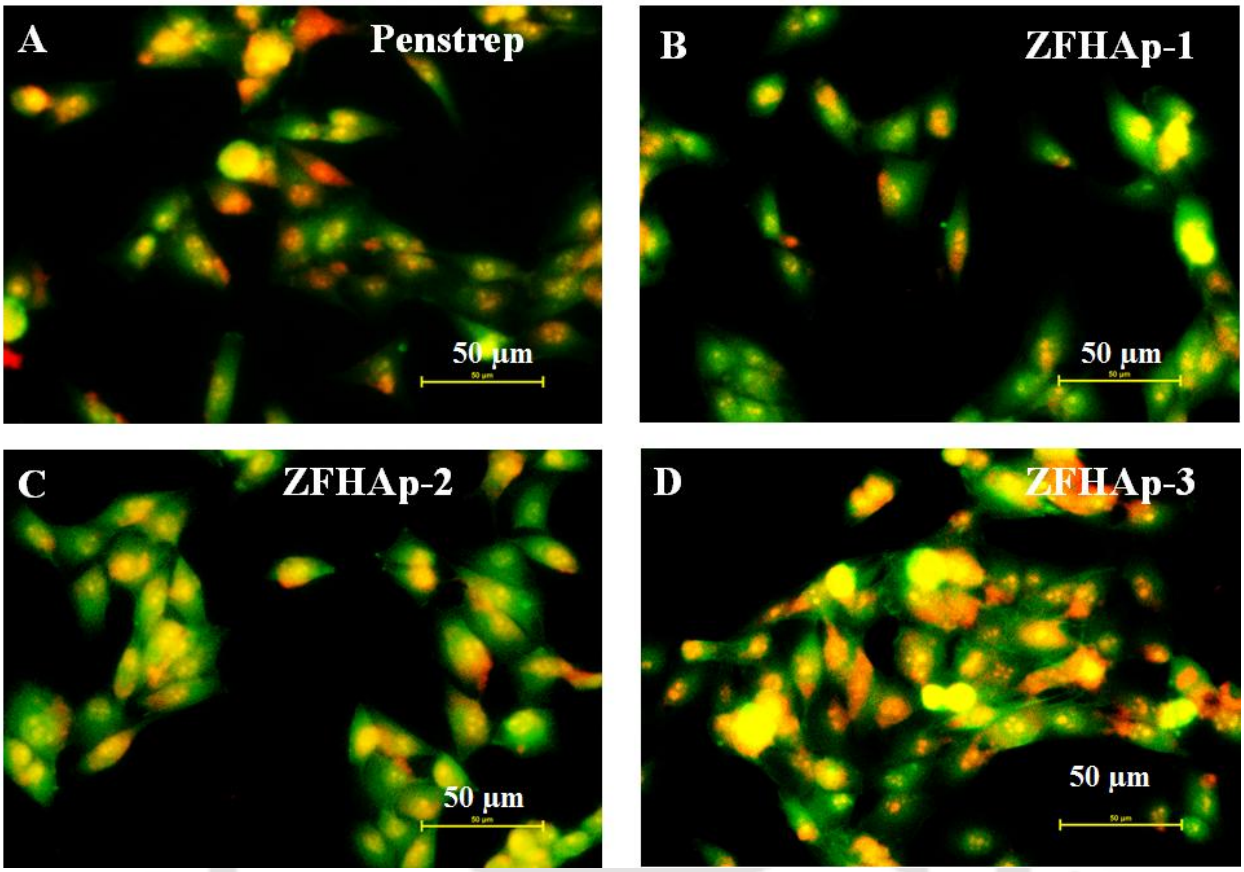

Figure 5.9: MG63 cells grown in DMEM media with Pen-strep as antibiotic and ZFHAp-1, ZFHAp-2, and ZFHAp-3 samples

Further, the ALP activity of the ZFHAp samples was evaluated to examine its bone cell proliferation efficiency. For this purpose, two concentrations, *i.e.*, 1 mg/mL and 0.1 mg/mL were incubated with MG-63 cells, and the ALP activity was examined using the ALP activity kit. As shown in Figure 5.10, the HAp, ZFHAp-1, and ZFHAp-3 samples exhibited the enhanced ALP activity with an increase in time. However, at low concentrations, *i.e.*, 0.1 mg/mL, no significant differences in the samples' ALP activity could be obtained (p value ≤ 0.05). Furthermore, on Day 21, the samples' ALP activity was found to be similar at both concentrations. Conversely, the ZFHAp-2 samples exhibited excellent ALP activity at both low and high concentrations, indicating the highest bone cell proliferation ability (p value ≤ 0.05). The samples containing the highest Zn concentration exhibited maximum ALP activity, *i.e.*, ZFHAp-2, followed by ZFHAp-1 and ZFHAp-3. The results corresponded to the release date of the Zn^{2+} ions. Hence, the presence of

the Zn^{2+} ions not only provided an excellent antibacterial activity to the HAp samples but also provided a higher bone cell proliferation ability.

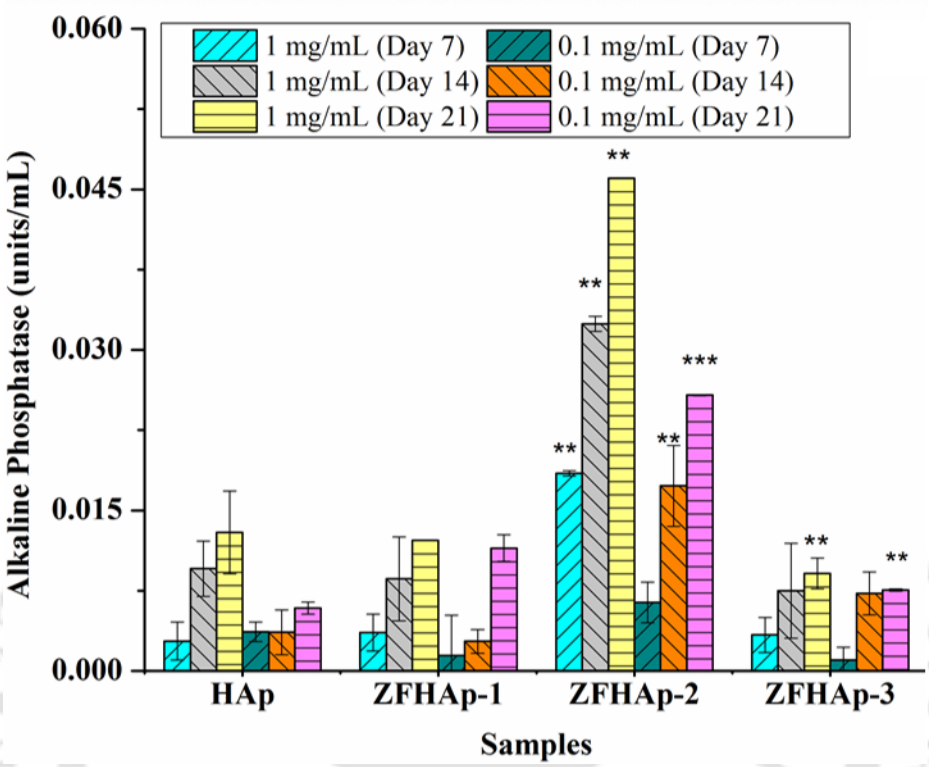

Figure 5.10. ALP activity of the ZFHAp samples; Highest ALP activity in ZFHAp-2 samples (co-related with Zn concentration); * *p value* $\geq$ 0.05; and ALP activities of ZFHAp samples as compared to HAp ** *p value* $\leq$ 0.05, *** *p value* $\leq$ 0.0001; *n*=2.

Hence, the designed materials are effectively appropriate for the orthopedic as well as other biomedical applications due to their excellent antibacterial activity, target efficiency, and high cell proliferation activity.

5.7 Conclusions

This study aimed to incorporate the self-antibacterial activity as well as the target efficiency to the HAp together for orthopedic applications. Hence, the co-integration of the Zn and Fe ions with HAp was investigated under *in-vitro* environments. The co-integration resulted in a biphasic nanoassembly of Ferric-HAp-Zincite via a simple co-precipitation method. The nanoassembly acquired majorly three phases, *i.e.*, $Ca_{9.333}Fe_{1.167}(PO_4)_7$ and zincite phases in all the samples and

the secondary phases of $Ca_9Fe(PO_4)_7$ and $Ca_{28.8}Fe_{3.2}(PO_4)_{21}O_{0.5}$ based on the Fe concentration. All the samples obtained dual morphology with 50-85 nm width of rod-shaped HAp morphology and 30-57 nm particulate shaped morphology of zincite. ZFHAp-2 sample showed a minimum visible MIC value of 66 µg/ml against all the bacteria, and the ZOI was comparable with the traditional kanamycin antibiotic. It enhanced three times higher proliferation of bone cells than that of control at 60 times higher concentration than that of MIC, *i.e.,* 5 mg/mL. The major antibacterial activity of the ZFHAp samples was found to be by the release of the Zn^{2+} and Fe^{3+} ions, causing the rupturing into the bacterial cell wall. Furthermore, the absence of ROS production led to a higher cytocompatibility. As MG-63 cells were grown at a 300 times higher rate than that of control samples, the bone cell proliferation was affirmed. This ability was further confirmed by performing the ALP activity assay. The ALP activity analysis explained the excellent potential of ZFHAp samples for bone tissue engineering. The ALP activity was found to be in correlation with the Zn ions' presence, as the sample containing the highest Zn contained the highest ALP activity. Hence, the presence of the Zn not only incorporated the excellent antibacterial activity but also provided the excellent bone integration ability to the ZFHAp samples. Similarly, the integration of Fe ions provided the target efficiency to the ZFHAp samples and synergistically upgraded the antibacterial activity of the ZFHAp samples. No significant TNF-α release also adds to the ZFHAp samples' biocompatibility, indicating its potential for various biomedical applications.

This study provides an insight into the design of biphasic nanoassembly based on the dopant concentration and opens the access to tune the magnetic as well as antibiotic activity. The study designates the ZFHAp samples as a potential nanomaterial for bone tissue engineering applications. Hence, after achieving the required antibacterial activity, chosen antibacterial mechanism, target efficiency, enhanced bone integration and proliferation ability, and no inflammatory responses, we further analyzed the designed material (ZFHAp-2) for various biomedical applications, including bone tissue engineering via scaffold preparation. The detailed analysis is in the followed chapters.

Chapter 6

In-vitro osteogenic activity analysis via synthesizing scaffold of the designed material

In this chapter, we have described the chitosan-CMC and ZFHAp-2 integrated nanocomposite scaffolds to achieve the inherent antibacterial activity within the scaffold and control the porosity of the scaffold. This chapter focuses on the insight into designing the polymeric scaffolds with self-antibacterial properties along with controlled biochemical behavior. The effects of various amounts of ZFHAp-2 on the biochemical properties (porosity, swelling, and degradation) and antibacterial activity have been investigated. The prepared scaffolds were microporous in structure (25-123 µm), and their biochemical behavior, such as porosity (60-80%), swelling, and enzymatic degradation (21-50%), was dependent on the concentrations of ZFHAp-2. The swelling and degradation of the prepared scaffolds were linearly related. The presence of 5 % ZFHAp-2 in the scaffolds (SCA-5) resulted in a pore size of 92 ± 10 µm and a 50 % degradation time of 42 days. This scaffolds SCA-5 also showed self-antibacterial activities along with excellent cell proliferation ability.

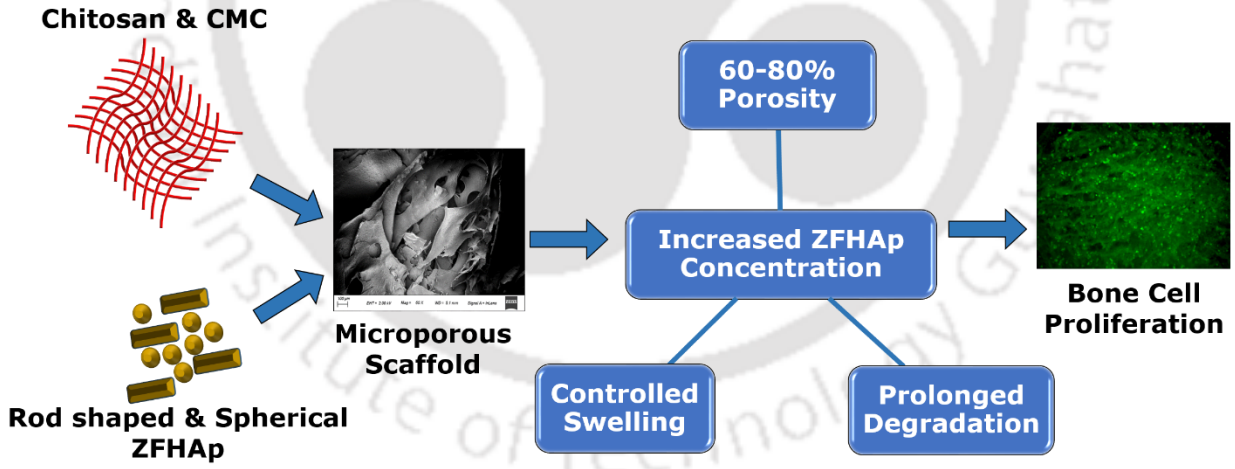

Schematic 6.1. Material concentration based tunability of the biochemical properties of scaffolds (Cellulose; 28, 9207–9226 (2021)

6.1 Introduction

As described in the previous chapter, the ZFHAp-2 samples possessed the minimum MIC values and the biochemical properties compared to others. In addition, ZFHAp-2 samples contained the maximum ALP activity. Hence, to apply the designed material for bone tissue engineering applications, we synthesized the scaffold of Chitosan, CMC, and ZFHAp-2 and evaluated its biochemical properties.

For the appropriate cell attachment and proliferation, 3D scaffolds are the most studied bone tissue engineering systems. The major benefits of using scaffolds include the high specific surface area, porous structure, and the ability to adhere to a large number of cells over it [361]. Chitosan possesses many properties desired for biomedical applications like biodegradability, biocompatibility, bioactivity, and antimicrobial properties [361]. However, the presence of β-1-4-glycosidic linkage makes it more prone to degradation by lysozyme and other body fluids [362], restricting its applicability for controlled cell growth, antibacterial action, and biomolecule delivery. Hence, composite scaffolds were scrutinized to remove these lags.

Cross-linking within polymers has proven to guard the hydrophilicity and water solubility [363]. Carboxymethylcellulose (CMC), an anionic polymer with chemical similarity with chitosan, provides a strong ionic cross-linking to enhance the biochemical feature, *i.e.*, swelling, porosity, and degradation. Further, Chitosan, CMC, and their composites have been integrated with various inorganic materials such as HAp [364-367] to achieve the desired mechanical strength along with biochemical behavior. The swelling and degradation behaviors remain directly dependent on the porous nature of the scaffolds. Hence, the most suitable way to control biochemical behavior is to control the porosity. Yet, the tunability of these behaviors is still under extensive research due to interconnections between porosity, composition, mechanical properties, and bioactivity. The challenge remains to control the biochemical features without compromising the mechanical properties, *i.e.*, strength and biological behavior (bioactivity) and vice-versa. Hence, to control the porosity and its dependant biochemical properties, we varied the concentration of ZFHAp-2 and compared its effect on porosity and other properties compared to the integration of Chitosan and CMC with HAp.

6.1 Materials and Methods

6.1.1 Materials

For the scaffold synthesis, chitosan (CS, Mw = 50–190 kDa and degree of deacetylation = 75–85%, Cat No. 448869) was procured from Sigma, India, and CMC-sodium (RM10844; the degree of substitution of 0.9) was purchased from Himedia, India. Double distilled water (MiliQ, 18 mΩ, Millipore systems) was used throughout the experiments.

6.1.2 Preparation of chitosan-CMC-ZFHAp-2 scaffold

The nanocomposite scaffold of Chitosan, CMC, and ZFHAp-2 was prepared by mixing the Chitosan and CMC at 2 % (w/v) and varying the concentrations of HAp and ZFHAp-2 [361]. Briefly, 2 % (w/v) chitosan solution in acetic acid was mixed with 2 % (w/v) of CMC for three h. After proper mixing various concentrations of designed ZFHAp-2 and HAp nanoparticles (0 %, 1 %, 2 %, 2.5 %, 5 %, 10 % (w/v)) was mixed to the chitosan-CMC mixture until a homogenous mixture was achieved. The mixtures were frozen at -20 °C, and pH neutralized using 1M NaOH prior to freezing drying under vacuum. The prepared scaffolds were stored under vacuum for their characterization and applications. The scaffolds were named as listed in Table 6.1, and the same sample codes are referred throughout the thesis.

Table 6.1. Sample codes of scaffolds with various concentrations of ZFHAp-2

S.No.	Sample code	Chitosan (w/v) %	CMC (w/v) %	ZFHAp-2 (w/v) %	HAp (w/v) %
1	SCA-0	2	2	0	0
2	SCA-1	2	2	1	0
3	SCA-2	2	2	2	0
4	SCA-2.5	2	2	2.5	0
5	SCA-5	2	2	5	0
6	SCA-10	2	2	10	0
7	HSCA-1	2	2	0	1
8	HSCA-2	2	2	0	2
9	HSCA-2.5	2	2	0	2.5
10	HSCA-5	2	2	0	5

11	HSCA-10	2	2	0	10

6.2 Biochemical characterizations of the scaffolds

After successfully analyzing the physical features, the scaffolds were scrutinized for their various biochemical analysis, as discussed below.

6.2.1 Porosity of scaffolds

The porosity of the scaffolds was evaluated using the liquid displacement method as studied previously [368]. In brief, the scaffolds were cut into pieces, and the known weight of scaffolds (W_d) were immersed in hexane under vacuum for the forced entry of hexane into the microporous scaffolds. The scaffolds were quickly transferred into the pre-weighed weighing bottles containing known weight (W_1) and volume (V_1) of hexane and the final weight (W_2) and volume (V_2) were recorded. The porosity of the scaffolds was calculated using the following equation-6.1.

$$\emptyset\% = \frac{W_2 - W_1 - W_d}{\rho(V_2 - V_1)} \tag{6.1}$$

Where ρ is the density of hexane, *i.e.*, (0.655 gcm^{-3}).

6.2.2 Swelling behavior of scaffolds

For various biomedical applications of the scaffolds, along with porosity, the swelling behavior also plays a key role. The bioactivity of a scaffold is majorly dependent on its fluid retention, fluid transfer, and swelling behavior. Along with porosity, swelling behavior governs the scaffolds' degradation behavior, leading to its bone integration ability. To analyze the swelling behavior of the scaffolds, the known weight of scaffolds (W_i) were treated with PBS, pH-7.4, for various time intervals at 37 ºC. At each time interval, the scaffolds were removed and dried using blotting paper. The dried weight (W_f) was measured, and the swelling behavior Q (%) was analyzed using the following equation-6.2.

$$\%\, Swelling\ (Q) = \frac{W_f - W_i}{W_i} \times 100 \tag{6.2}$$

The above Q_t data was fitted a second-order swelling kinetics model [365] using as given in equation 6.3.

$$Q_t = \frac{k_s Q_e^2\, t}{1 + k_s Q_e t} \tag{6.3}$$

Where k_s is the 2nd order rate constant (g $g^{-1}min^{-1}$), the swelling rate constant and Q_e represents the theoretical equilibrium swelling capacity (g g^{-1}).

6.2.3 Enzymatic degradation of scaffolds

The enzymatic degradation studies were carried out using the lysozyme (2 mg mL^{-1}) in PBS solution (pH-7.4). For this purpose, the known weight of scaffolds (M_i) were subjected to the lysozyme-PBS solution under constant stirring (60 rpm) at 37 ºC for the different durations, *i.e.*, 4, 8, 12, 16, and 20 days. The lysozyme-PBS solution was replaced regularly with a fresh solution. After the treatment, the scaffolds were freeze-dried, and the final weight of the scaffolds (M_f) were calculated. The degradation (%) was calculated using the following equation-6.4.

$$Degradation\ \% = \frac{M_f - M_i}{M_i} \times 100 \quad (6.4)$$

In addition, degradation kinetics was also studied. The degradation data were fitted using the first order equation-10 to estimate the degradation rate constant k_d (day^{-1}) and 50 % scaffold degradation (T_{50}).

$$M_t = M_i\,(1 - e^{-k_d t}) \quad (6.5)$$

Similarly, the degradation kinetics was also studied using the Michaelis-Menten equation.

6.3 Biomineralization assay and mechanical strength analysis

The *in-vitro* biomineralization assay was performed to determine the apatite mineralization capabilities of scaffolds for bone tissue engineering applications. Briefly, the synthesized scaffold samples were immersed in SBF solution, which has a concentration and composition similar to human body fluid. HSCA-5, SCA-2.5, and SCA-5 were immersed in the SBF solution for 14 days at 37 °C, and the SBF was replaced every 24 h. The scaffolds were then rinsed gently with ethanol and were washed with Milli Q water thrice, followed by drying at 45 °C overnight to remove any entrapped water molecules. The deposition of the apatite layer after immersion in SBF for 14 days was studied by EDX analysis for their elemental analysis.

The mechanical strength of scaffolds was determined using an Electromechanical Universal Testing Machine (UTM) instrument (Zwick Roell: Z005TN) equipped with a 5kN load cell with a crosshead speed of 1 mm/min.

6.4 Biological activity of scaffolds

After successful synthesis and biochemical characterizations of scaffolds, the prepared scaffolds were subjected to their biological investigations for practical applications. For this purpose, the antibacterial activity, as well as the cell proliferation analyses, were performed.

6.4.1 Antibacterial activity

Many of the implanted biomaterials exhibit bacterial contamination due to surgical procedures, which lead to immunogenic responses and ultimately resulting in the rejection of the implants. Thus it is desirable to impart additional antibacterial characteristics in the biomaterials to prevent such unwanted processes and implant failure. The antibacterial activity was tested against two Gram-negative strains (*E. coli*, MTCC 1610 and *S. paratyphi*, MTCC 735) and two Gram-positive strains (*L. monocytogenes*, (ATCC 19115) and *S. aureus*, MTCC 6538) using ASTM G 21–09 protocol, as reported previously [361]. Briefly, scaffold discs of 15 mm diameter were first washed with 70% alcohol and Milli Q water to remove the adhered bacteria, if any, followed by rinsing with sterilized water. The bacterial culture of all the bacteria (100 µL, 1.0×10^6 CFU mL^{-1}) were seeded on the SCA-0, SCA-2.5, SCA-5, HSCA-2.5, and HSCA-10 scaffolds, and were incubated at 37 °C for 24 h. After the incubation, the scaffolds were washed with 0.87 wt % NaCl solution containing 0.03 wt % Tween 80. The washed solution was diluted suitably and speared over a freshly prepared agar plate. The agar plates were incubated at 37 °C for 24 h. The scaffolds with excellent antibacterial activity (0 % growth) were further investigated for bone cell proliferation.

6.4.2 Bone cell proliferation and cytotoxicity analysis

The bone cell proliferation ability of the scaffolds was studied using an MG-63 cell line procured from NCCS Pune, India. The cells were first grown to their confluency in a T25 flask at 37 °C, 5% CO_2 and 85% humidity under a CO_2 incubator. DMEM supplemented with 10% fetal bovine serum (FBS, Invitrogen) and 1% antibiotic (Pen Strep, Invitrogen) was used for this experiment. The scaffold with no bacterial growth was analyzed for *in-vitro* bone cell proliferation. 1×10^5 cells mL^{-1} of MG-63 were seeded on the scaffolds for five days in DMEM media and incubated at 37 °C and 5 % CO_2. After five days, the scaffolds were washed with sterilized PBS (pH-7.4) multiple times for the removal of un-adhered cells. The scaffolds were then analyzed via two means FESEM analysis as well as fluorescence imaging. In brief, the scaffolds were first treated with Calcein AM

dye (Sigma-India, 4 μM in PBS) for 30 min and directly analyzed using a fluorescent microscope (Zeiss) with an excitation filter of 450-490 nm. For FESEM analysis, after washing with PBS, the cells on the scaffolds were first fixed with 4% paraformaldehyde in PBS for 24 h. Then, the scaffolds were washed multiple times with PBS followed by stepwise dehydration with 30 %, 40 %, 50 %, 60 %, 70 %, 80 %, 90 %, and 100 % concentration gradient of ethanol for 10 minutes each. Finally, the critical point drying was performed by treating the scaffolds with hexamethyldisilazane (HMDS) for 10 min prior to attachment over the carbon tape for FESEM analysis.

Also, the scaffolds were analyzed for their cytotoxicity using an MTT assay similar to that of Chapters 1-3. In brief, the UV sterilized SCA-0, HSCA-2.5, HSCA-5, SCA-2.5, and SCA-5 scaffolds were soaked separately in the serum-free DMEM free media for 24 h at 37 °C. After 24 h, the supernatant was collected and filtered using a 0.22 μm filter. The media was termed as 'conditioned media.' 100 μL of this conditioned media was supplemented to the previously grown MG-63 cells (5000 cells/well in a 24 well plate). The conditioned media was changed every alternate day. The MTT assay was then performed at respective days for the cytotoxicity analysis.

6.5 Results and discussion

6.5.1 Morphology and pore size analysis of the scaffolds

The scaffolds were analyzed to obtain the morphology with respect to the integration of HAp and ZFHAp-2 samples. FESEM analysis was carried out to examine the internal morphology of the scaffolds. All the samples exhibited microporous architecture, as shown in Figures 6.1.1 and 6.1.2, while pore sizes were varied for the different samples. The pore size of the microporous structures plays a critical role in regulating the bio-interfacial aspects (cell infiltration, adhesion, cell signaling, angiogenesis, and nutrient exchange) [361]. A well interconnected macroporous structure was obtained for all the samples, probably due to the cross-linking between amino groups of the chitosan and carboxyl group of CMC and solid-liquid phase separation [369]. Apparently, the aggregation of particles or the formation of clumps was not observed (Figure 6.1.1), which indicated the good dispersion of HAp and ZFHAp-2 throughout the scaffolds. With the increase in HAp and ZFHAp-2 concentrations, the scaffolds were found to be packed more densely, as shown in Figures 6.1.1 and 6.1.2. The pore size of the samples was found to increase with the increase in HAp and ZFHAp-2 concentration as listed in Table 6.2 and 6.3. The pore size of HAp

integrated samples was found to be lesser than that of the ZFHAp-2 integrated scaffolds (Figure 6.1.2). In addition, the ZFHAp-2 integrated scaffolds carried homogenously distributed pores as compared to the HAp integrated scaffolds. The increase in the pore size is attributed to the increased concentration of HAp and ZFHAp-2, as more morphological distortion was supposed to take place due to the dual morphology of the ZFHAp-2 nanoparticles. Covalent bonding between OH groups of HAp and NH_2 groups of chitosan, as well as the coordination bonding, are reported in their composites [366]. Presumably, with an increase in the concentration of ZFHAp-2, these bonds were increased, which interfered with the chitosan (amine group) and CMC (COOH) group interactions. This resulted in increasing the pore size via solid-liquid phase separation [370]. Notably, the pore size of cancellous bone lies 300-600 µm in diameter and cortical bone as 10-50 µm [371]. However, it is reported that the threshold pore size for bone growth remains to be 100 µm [372]. In this study, SCA-2.5, SCA-5, and HSCA-10 resulted in the pore size of 89 ± 8 and 92 ± 10 µm, 78 ± 7 µm, respectively, affixing their suitability for bone tissue engineering.

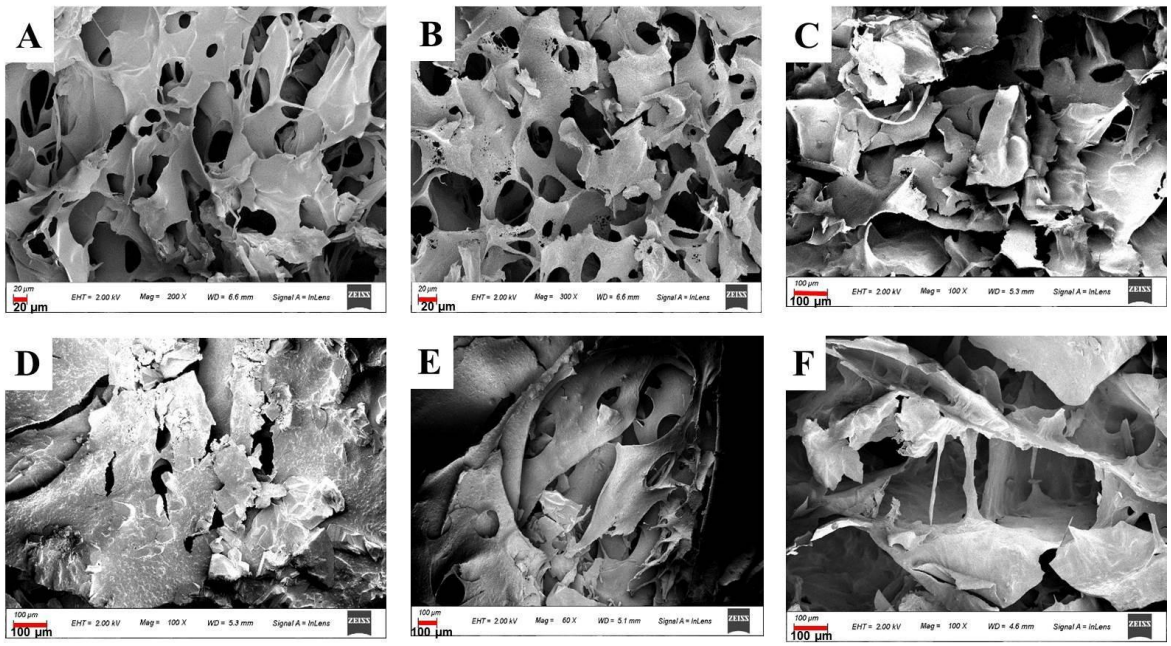

Figure 6.1.1. Morphological analysis of the scaffolds using FESEM; A) SCA-0, B) SCA-1, C) SCA-2, D) SCA-2.5, E) SCA-5.0 and F) SCA-10; Scale bar represents 100 µM

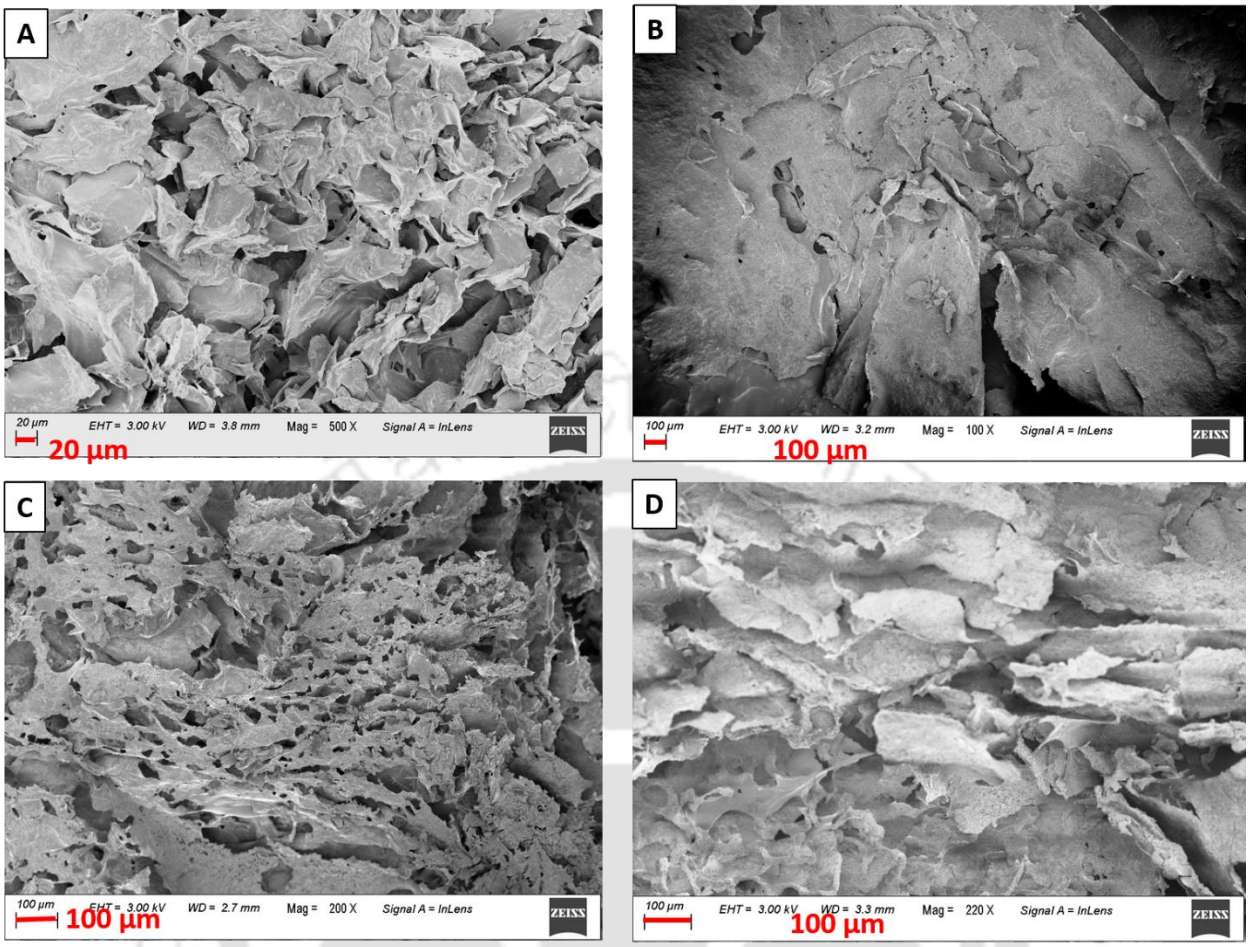

Figure 6.1.2 Morphological analysis of the scaffolds using FESEM; **A)** HSCA-1, **B)** HSCA-2, **C)** HSCA-2.5, **D)** HSCA-10;

6.5.2 Biochemical characterization of scaffolds

The successful synthesis of scaffolds was accessed through its biochemical behavior for biomedical applications. Biological responses to the implant materials depend on various material properties, among which biochemical properties play a significant role. Considering the importance of these properties, the porosity, swelling, and degradation behavior of the scaffolds were analyzed as reported in the following sub-sections.

6.5.2.1 Porosity

The major challenge in designing a scaffold for bone tissue engineering remains its porosity while maintaining its swelling and degradation behavior. Chitosan, due to its cross-linking with CMC,

provides the desired microporous behavior [373]. However, controlling the porosity remains a significant challenge for various biomedical applications, especially in bone tissue engineering. A decrease in the porosity was observed by the systematic increase in the concentration of ZFHAp-2 in the scaffolds' composition. However, no significant differences in the porosity could be observed at the integration of HAp **(**Figure 6.2.2 A**)**. For instance, SCA-0 exhibited 95% porosity, which was significantly reduced to ~ 60 % for all the HSCA samples. However, the porosity was found to be 88 % in SCA-1 (1% addition of ZFHAp-2). Likewise, the porosity further decreased to the range of 68 % - 75 % upon the increase in ZFHAp-2 concentrations. The least porosity of 58 % was observed for the scaffold with the maximum amount of ZFHAp-2 (SCA-10) (Figure 6.2.1 A). A similar pattern, *i.e.*, the decrease in porous morphology, can be seen in Figures 6.1.1 and 6.1.2. Hence, the measured porosity supported the results obtained through the morphological analysis of the scaffolds. The decreased porosity can be ascribed to the high concentration of ZFHAp-2 with dual morphology, *i.e.,* rod-shaped and particulate. The HAp NPs carried single particulate morphology and hence were mixed homogenously with the Chitosan and CMC and did not cause any change at an increase in their concentration. The packing of dual morphology of ZFHAp-2 increases the heterogeneity and hence presumably regulates the density, interconnectivity, and orientation of the designed scaffolds. The osseointegration has been reported to be best observed at 60-80% of porosity, which is similar to the porosity of the cancellous bone [361]. Based on the results, porosities were obtained in this desired range for all HSCA scaffolds and SCA-2, SCA-2.5, and SCA-5 scaffolds. It is to be noted that the porosity can be controlled by varying the concentrations of ZFHAp-2. This provides an advantage of tuneable porosity, which is also expected to alter the scaffolds' swelling behavior.

Table 6.2. Pore size, degradation, and swelling behavior of the ZFHAp-2 integrated scaffolds

S.No.	Scaffold sample	Pore size (µm)	Porosity (%)	Degradation			Swelling		
				k_d (day^{-1})	T_{50} (days)	Michaelis constant	Q_e	$k_s \times 10^3$ ($gg^{-1}min^{-1}$)	R^2
1	SCA-0	25 ± 4	95.44 ± 0.33	0.045	16	7.8	1003	2.24	0.99

2	SCA-1	35 ± 4	87.77 ± 3.0	0.036	19	9.9	949	2.71	0.99
3	SCA-2.5	89 ± 8	75.09 ± 0.6	0.027	26	13.3	738	1.33	0.99
4	SCA-5	92 ± 10	67.74 ± 1.49	0.017	42	28.7	706	0.98	0.99
5	SCA-10	123 ± 28	58.0 ± 2.17	0.013	53	37.8	597	1.53	0.99

Table 6.3. Pore size, degradation, and swelling behavior of the HAp integrated scaffolds

S.No.	Scaffold sample	Pore size (µm)	Porosity (%)	Degradation			Swelling		
				k_d (day^{-1})	T_{50} (days)	Michaelis constant	Q_e	$k_s \times 10^3$ ($gg^{-1}min^{-1}$)	R^2
1	HSCA-1	35 ± 3	62.81 ± 0.59	0.13	6	9.7	1006	1.8	0.99
2	HSCA-2.5	12 ± 3	62.10 ± 3.5	0.14	5	12.2	802	0.9	0.99
3	HSCA-5	22 ± 5	61.33 ± 1.0	0.14	5	12.3	705	0.7	0.99
4	HSCA-10	78 ± 7	61.17 ± 0.58	0.03	23	24.3	565	1.0	0.99

6.5.2.2 Swelling behavior

Similar to the porosity, controlling the swelling behavior is also crucial for maintaining the integrity and fidelity of the scaffolds upon interactions with the biological fluids. However, the swelling of scaffolds is originated from the native properties of the constituent materials, *i.e.*, Chitosan, CMC, HAp, and/or ZFHAp-2. This enables to control the swelling ability at the material selection level. In this study, the swelling behavior was evaluated via immersing the scaffolds into the PBS at 37 °C. It was found that the swelling behavior decreased with an increase in HAp and ZFHAp-2 concentration, as shown in Figures 6.2.1B and 6.2.2B. The obtained experimental data

were fitted to the second-order swelling kinetics model (equation 8). The experimental data fitted well with the second-order kinetics (R^2 = 0.99), while the data did not fit with the first-order kinetics. This indicated that the swelling behavior is affected by the diffusion of the water along with the intermolecular interactions between the constituents of the scaffolds. The fitted kinetic parameters are listed in Tables 6.2 and 6.3, which indicated that the scaffolds' swelling capacity decreased with an increase in the concentration of HAp and ZFHAp-2 due to the reduction of H-bonds between chitosan and CMC [374]. A high decrease in the swelling behavior of the HSCA samples was obtained as compared to the SCA samples, presumably due to the less reduction in the H-bonds owing to the presence of the Zn and Fe in the ZFHAp-2 lattice. Similarly, the rate constant k_s was also found to decrease with the increase in the contents of Hap/ZFHAp-2; however, the k_s values were higher for the ZFHAp-2 based scaffolds. ZFHAp-2 interacted with the Chitosan and CMC with different physical (Van der Waals) and chemical bonds, which resulted in the decreased fluid intake capacity of the scaffolds. The reduced swelling behavior is desirable for the controlled degradation of scaffolds for various biomedical applications, including drug delivery and bone tissue engineering applications. Hence, SCA samples containing ZFHAp-2 NPs were more suitable for these applications than the HSCA samples.

6.5.3 Enzymatic degradation.

Enzymatic degradation is one of the key factors for the performance of scaffolds in biological fluids. Various enzymes such as lysozymes are found abundant in body fluids. The lysozymes' antibacterial activity is reported as the first line of defense against bacterial infection through the rupturing of the β-1-4-glycosidic linkages of peptidoglycan [362]. Chitosan also undergoes catalytic degradation over its β-1-4-glycosidic linkages by the action of lysozyme. Hence, the stability under such body fluids is a significant challenge in designing the implant materials. The degradation of β-1-4- glycosidic linkages in chitosan by lysozyme's action is found to loosen the interactions between Chitosan and CMC, which resulted in collapsing of the scaffold microstructure [361]. The deprotonation under PBS incubation may also weaken the electrostatic interactions between Chitosan/CMC and HAp/ZFHAp-2. However, it has been observed that the scaffolds made up of various polymers containing HAp exhibited negligible degradation. For example, HAp/Polycaprolactone scaffolds degraded only 3.7 % in 10 weeks [375], and no significant degradation was reported in carbon fiber reinforced HAp/polylactide biocomposite

scaffolds even in 12 weeks [376]. Therefore, we performed enzymatic degradation in PBS containing lysozymes. In this study, a higher degradation rate for SCA-0 was obtained as compared to other scaffolds containing HAp and ZFHAp-2 (Figure 6.2.1 and 6.2.2 C, Table 6.2 and 6.3). The degradation was found to be in the range of 21-50 %, depending on the physical and chemical characteristics of the scaffolds. SCA-0 scaffolds resulted in a degradation of 50 %, which was consistent with the previous studies [361]. However, the increase in the HAp and ZFHAp-2 concentration resulted in the augmented form of the coordination bonds between chitosan-HAp, and chitosan-ZFHAp-2 particles, respectively, which prevented and retarded the degradation activity of lysozymes. Thus we observed a faster degradation of scaffolds without (SCA-0) or with less content of HAp and ZFHAp-2 (SCA-1, SCA-2) as compared to SCA-5 and SCA-10. However, the degradation rate of HSCA samples was higher than that of SCA samples, due to the presence of less coordination bonds with Chitosan and CMC as compared to ZFHAp-2.

Table 6.2 lists the fitted data obtained using equation 10. The degradation rate k_d was found to decrease with an increase in the concentration of HAp/ZFHAp-2. T_{50} values were also estimated as $\ln 2/k_d$, which was found to be significantly enhanced with the increase in HAp/ZFHAp-2 concentrations. It has been reported that the bone formation starts at the corner of the scaffolds in the initial 0-10 days, followed by no bone formation for 10-20 days (only changes in scaffolds). Later bone formation occurs along with scaffold degradation up to 90 days and becomes thicker with whole scaffold degradation within 90 to 150 days [377]. The study suggested the role of dense and oriented bone formation at a slower scaffold degradation rate. In this study, the T_{50} degradation for SCA-5 was found to be 42 days (6 weeks; almost double to HSCA), signifying its excellent bone formation ability. The enzymatic degradation was also assessed using the Michaelis-Menten equation. The Michaelis constant was found to be increased with an increase in the sample concentration (Table 6.2 and 6.3). SCA scaffolds possessed higher values of Michaelis constant than that of HSCA samples, indicating their comparatively slower degradation than HSCA scaffolds.

The dual morphology of ZFHAp-2 samples affects the packing and density of Chitosan and CMC. Additionally, the uniformly distributed ZFHAp-2 alters the cross-linking sites and the nature of the bond formations between Chitosan and CMC. Various ionic and van der Waals interactions take place between the three constituents of scaffolds, *i.e.*, Chitosan, HAp/ZFHAp-2, and CMC. For example, the NH_2 groups of Chitosan and OH groups of HAp form bonds, altering the porosity

as well as the degradation rate of the scaffolds. Similarly, the HAp has been reported to form covalent bonds with the CMC [365], altering the swelling and degradation behavior of the scaffolds. In this study, incorporation of ZFHAp-2 is presumed to delay the degradation rate due to synergistic effects of the chemical interactions between the NH_2 groups of chitosan and the carboxyl group of CMC, co-ordination bonds between Ca, Zn, and Fe with Chitosan, and ionic interactions with the carboxyl groups of CMC.

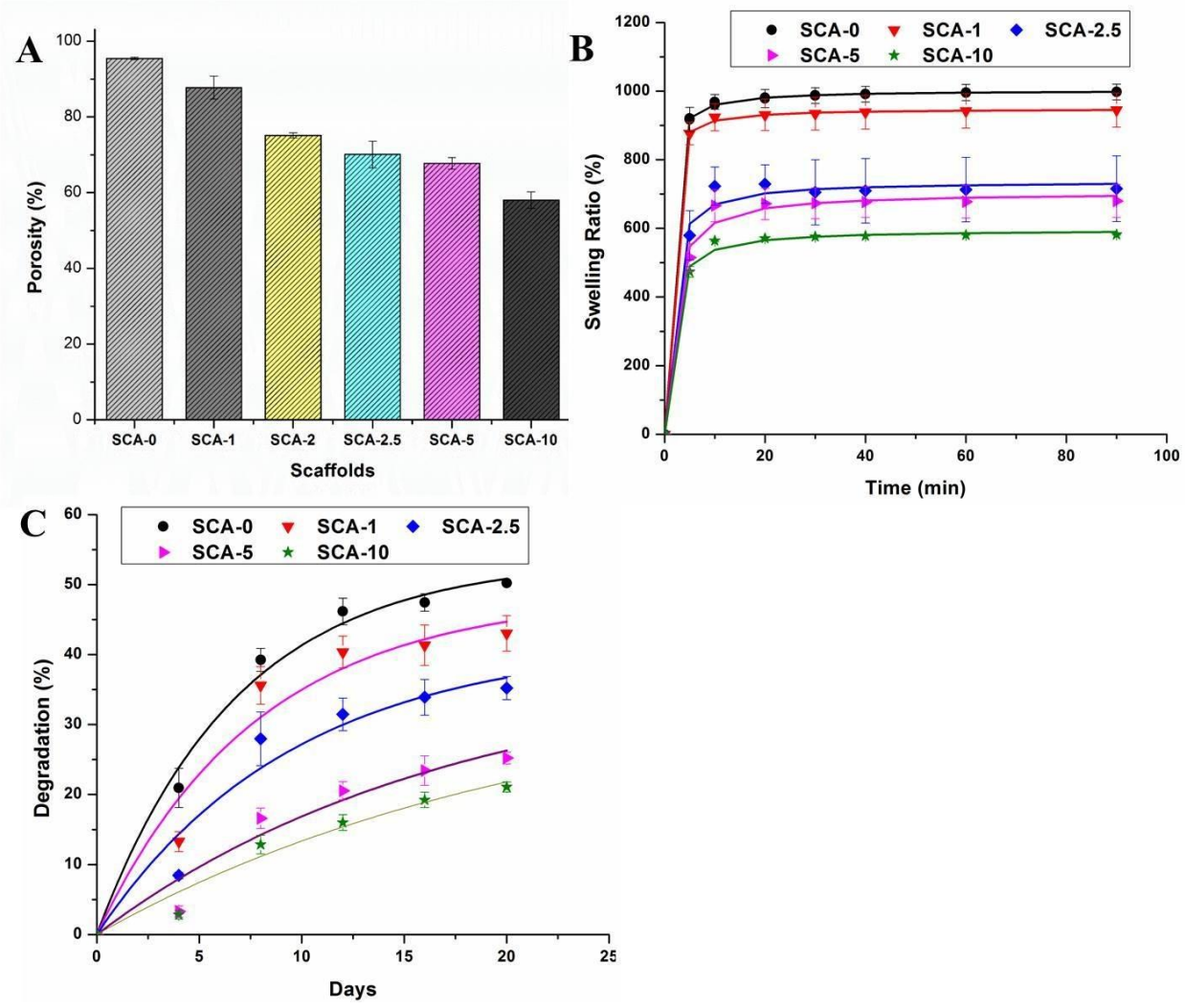

Figure 6.2.1. Biochemical characterizations of the ZFHAp-2 integrated scaffolds; **A)** porosity, **B)** % Swelling, **C)** Degradation studies. Points are the experimental data, while lines refer to the fitted data.

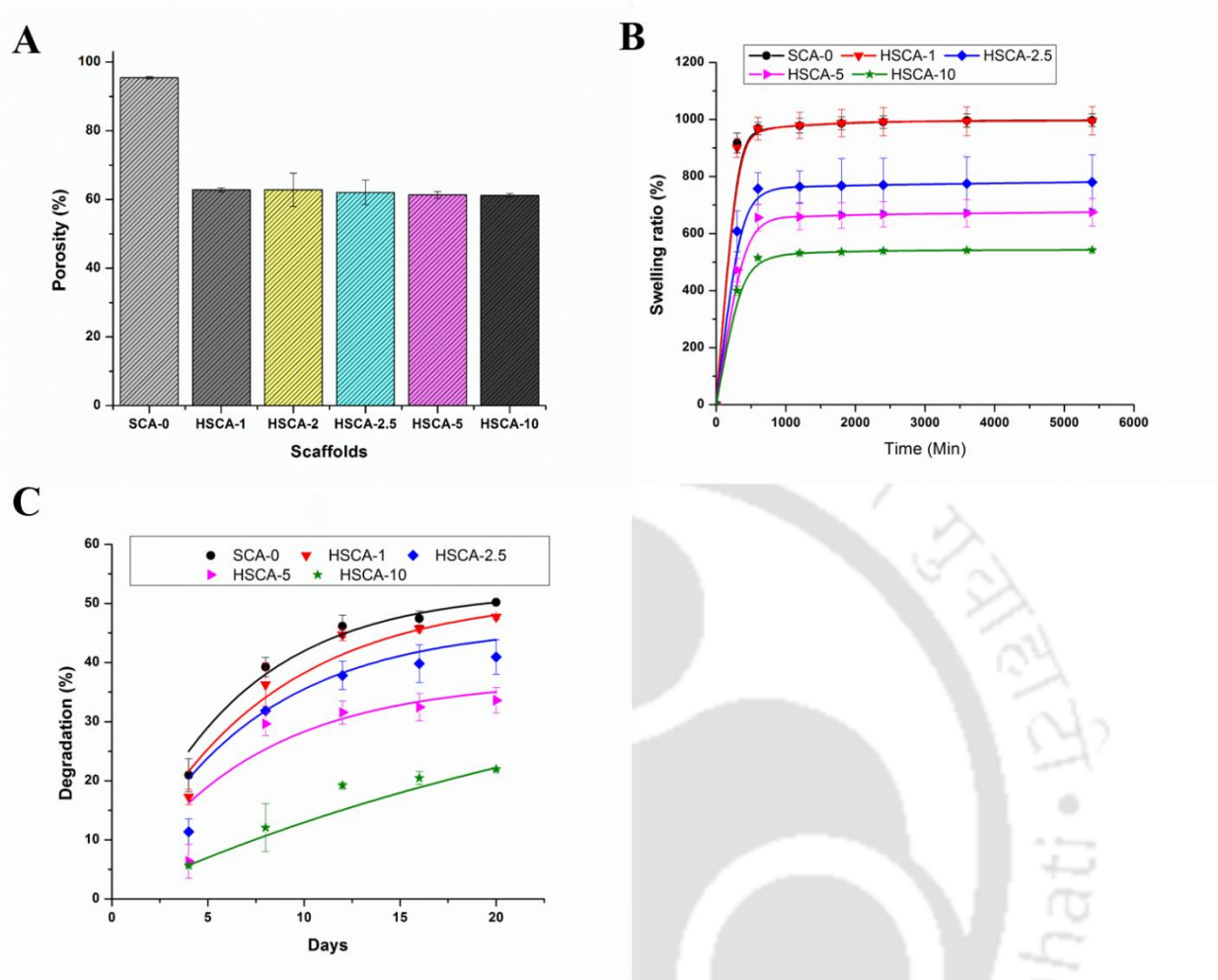

Figure 6.2.2 Biochemical characterizations of the HAp integrated scaffolds; **A)** porosity, **B)** % Swelling, **C)** Degradation studies. Points are the experimental data, while lines refer to the fitted data.

6.6.3 Bio-mineralization and mechanical strength

Biomineralization is a crucial phenomenon required for bone formation. It explains the ability of a scaffold for bone tissue formation by depositing the apatite layer over it. Hence, to analyze the scaffolds' bone formation ability, we examined the bio-mineralization ability of HSCA-5, SCA-2.5, and SCA-5, as given in the material and method section. After 14 days of incubation in SBF, the apatite layer formation was analyzed using the EDX analysis of the scaffolds and was compared with the scaffolds before SBF incubation. As given in Figure 6.3, the deposition of the apatite layer was found with an increase in the Ca and P atomic percentage, the apatite layer in all the samples. HSCA-5 exhibited the atomic percentage of Ca and P as 13.4 and 8.4, respectively,

which was increased to 19.3 and 10.3, respectively, for HSCA-5 after 14 days of incubation under SBF. Similarly, the Ca:P atomic percentage was increased from 1.9:2.4 and 19.3:13.8 to 12.5:5.5 and 20.4:11.1 for SCA-2.5 and SCA-5, respectively. Hence, with an increase in ZFHAp-2 concentration, the scaffolds' biomineralization ability was also found to be increased. This can be attributed to the Chitosan, Ca, P, and Zn/Fe ions within the scaffolds. The presence of the anionic groups such as COO^{-} and OH^{-} in HAp and ZFHAp-2 triggers the apatite's deposition over the scaffolds. Similarly, cationic groups within scaffolds such as NH_2^{+} in HSCA-5, NH_2^{+}, Zn^{2+}, and Fe^{3+} in ZFHAp-2 acted as a nucleation point for the formation of the apatite layer over the deigned scaffolds [378, 379], leading to its high bone cell proliferation ability.

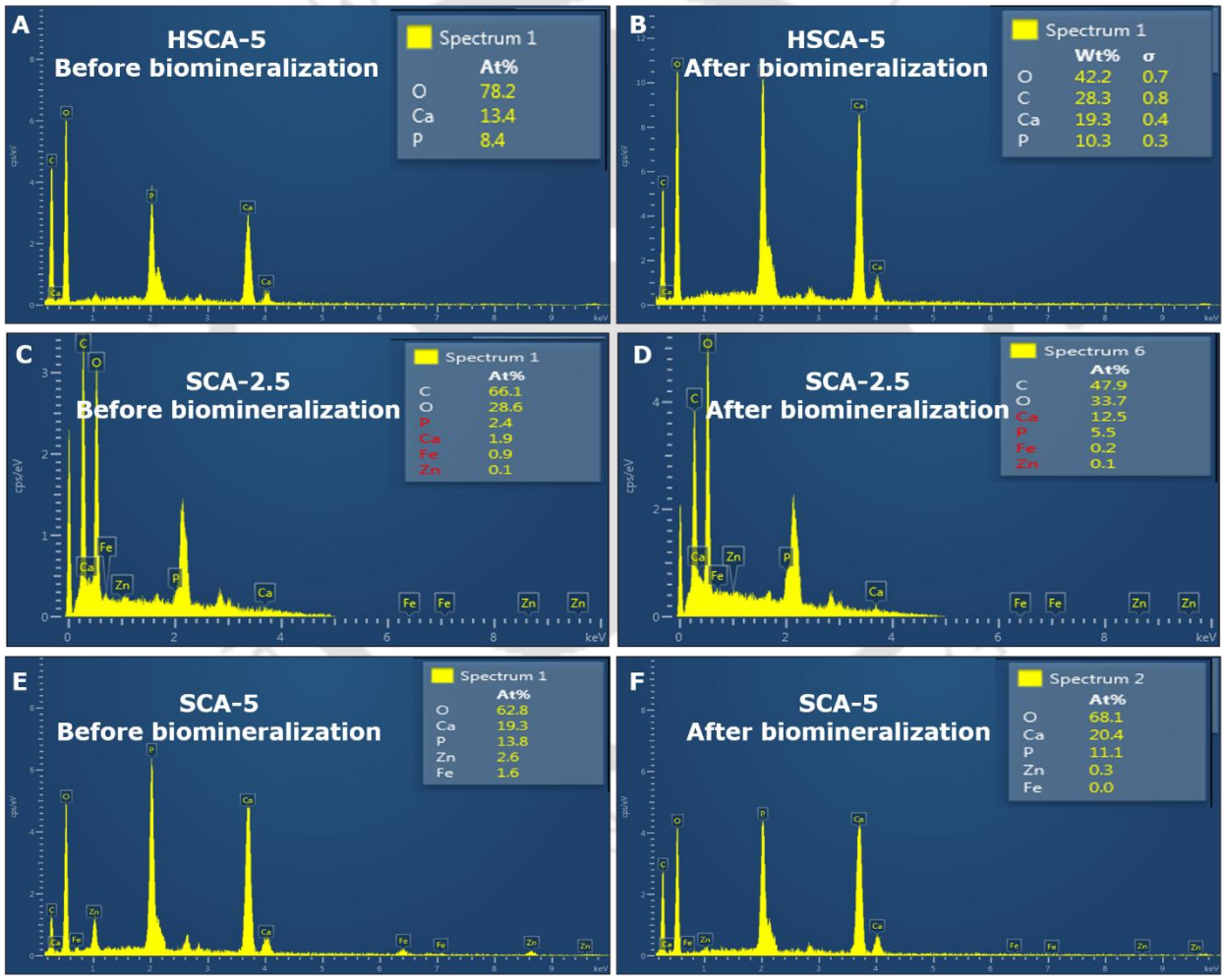

Figure 6.3. Bio-mineralization assay of the HSCA-5, SCA-2.5, and SCA-5 scaffolds

Similarly, the mechanical strength of scaffolds is an essential parameter for the proliferation of the bone cells, as well as the integrity. Hence, we examined the mechanical strength of the HSCA-2.5, HSCA-10, SCA-2.5, and SCA-10 scaffolds as given in the material and methods section. The mechanical strength parameters are given in Table 6.4.

HSCA-10 exhibited the maximum tolerance against the applied force, and the scaffold was not deformed until 0.32 MPa of the force was applied per the 3.14 cm^2 area. HSCA-2.5, ad SCA-2.5 were found to be similar in terms of mechanical strength, suggesting that at low concentrations of the nanocomposite, the presence of metal ions, *i.e.*, Zn and Fe, do not impart any impact on the mechanical strength. However, SCA-10 exhibited the minimum tolerance to the applied force, indicating that at higher concentrations, the dual morphology of the ZFHAp-2 samples caused the maximum distortion, and heterogeneity leading to the poor mechanical strength of the SCA-10 scaffolds. It is to be noted that the scaffolds with minimum degradation rate and swelling behavior exhibited the least mechanical strength, leading to the tunability of the desired properties of the scaffolds based on the concentration of the nanocomposite.

Table 6.4. Mechanical strength analysis of the scaffolds

S.No.	E_{mod} (MPa)	F_{max} (MPa)
HSCA-2.5	0.27	0.25
HSCA-10	0.72	0.33
SCA-2.5	0.17	0.24
SCA-10	0.32	0.16

4.6.3 Antibacterial activity analysis

HAp is considered the most suitable inorganic material for bone tissue engineering because of its physical and chemical properties similar to bone. However, the lack of inherent antibacterial activity remains a significant challenge for biomaterial researchers [19]. For this purpose, we integrated FZO with HAp. The major challenge for this study was to obtain the desired antibacterial activity after the integration of ZFHAp-2 with Chitosan. For this purpose, the antibacterial activity of nanocomposite scaffolds, SCA-0, SCA-2.5, and SCA-5, HSCA-2.5, and HSCA-10 was tested against Gram-negative (*E. coli and S. paratyphi*) and Gram-positive (*S.*

aureus and L. monocytogenes) bacteria. As presumed, SCA-0 did not show any antibacterial activity, and densely packed bacterial colonies (fully covered plates) were observed (Figure 6.3). Similarly, for SCA-2.5, a reduction in the bacterial colony as a visible decrease is seen in Figure 6.3. Although a considerable number was decreased, yet the bacterial colonies were spread all over the agar plate. For SCA-5, no bacterial growth was observed (Figure 6.3), affirming its suitability for antibacterial action. It is to be noted that HAp does not carry antibacterial activity by itself, no antibacterial activity could be obtained for HSCA-2.5 and HSCA-10, and hence the antibacterial activity of the scaffolds can be attributed to the integration of Zn^{2+} and Fe^{3+} ions to the HAp lattice. Chitosan is reported to exhibit antibacterial activity at a higher concentration [380]. In a previous study, we have reported the antibacterial activity of FZO against pathogenic bacteria through the release of Zn^{2+} and Fe^{3+} ions [341]. Hence, the scaffolds' observed antibacterial activity can be attributed to the slow and controlled degradation of the SCA-5, providing the desired bactericidal concentrations of the Zn^{2+} and Fe^{3+} ions.

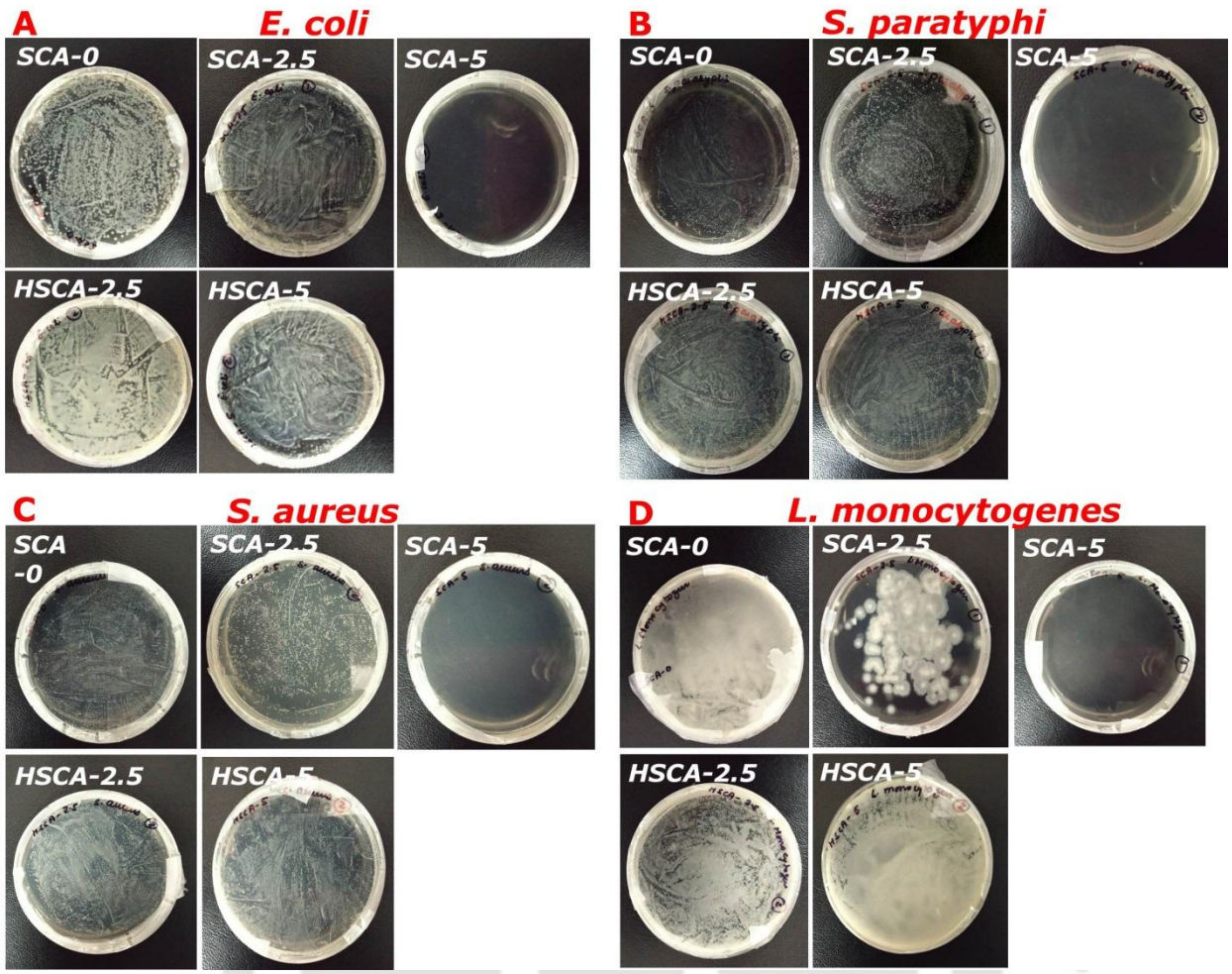

Figure 6.4. Antibacterial activity of scaffolds SCA-0, SCA-2 and SCA-5, HSCA-2.5 and HSCA-10 against *E. coli* **(A),** *S. paratyphi* **(B),** *S.aureus,* **(C),** and *L. monocytogenes* **(D),** respectively; Dense colonies in SCA-0, HSCA-2.5 and HSCA-10 reflecting no antibacterial action; reduction in bacterial colonies by SCA-2.5; and complete inhibition of bacterial growth by SCA-5 scaffolds

6.6.5 Cell proliferation analysis of MG-63 (bone like) cells

The designed scaffolds were analyzed for their bone cell proliferation ability using FESEM and fluorescence microscopy. Human bone-like cells, MG-63, were seeded over the SCA-5 to analyze the bone cell formation ability of the scaffolds. As we identified the best response of the SCA-5 against bacterial cells, the same scaffold sample was further tested for *in-vitro* cell proliferation applications. The FESEM images for the MG-63 cells adhered to the scaffolds for five days were recorded, as shown in Figure 6.5A. The results demonstrated that the MG-63 cells adhered well

and penetrated inside the microporous structure of SCA-5. To analyze the cell proliferation, cells grown for five days on SCA-5 were treated with Calcein-AM dye and monitored using an inverted fluorescent microscope. The bright green spots under the fluorescence microscopy image (Figure 6.5B) represent the dense population of attached and proliferating cells. The interfacial interaction between the scaffold and the cells can be attributed to its bone-like chemical configuration due to the presence of Chitosan and HAp as major constituents and Zn and Fe as trace mineral components. It has been previously reported that the presence of Zn and Fe also promotes better interaction between cells and underlying bone tissue [381]. Additionally, our group previously reported that the MG-63 cells exhibited ~100% viability after days 2, 4, and 6 days; when cultured on the composite scaffolds prepared using chitosan, carboxymethyl cellulose, and silver nanoparticle modified cellulose nanowhiskers [361]. Hence, ZFHAp-2 nanocomposite uniformly distributed within chitosan might have provided a suitable microenvironment for bone cells' growth.

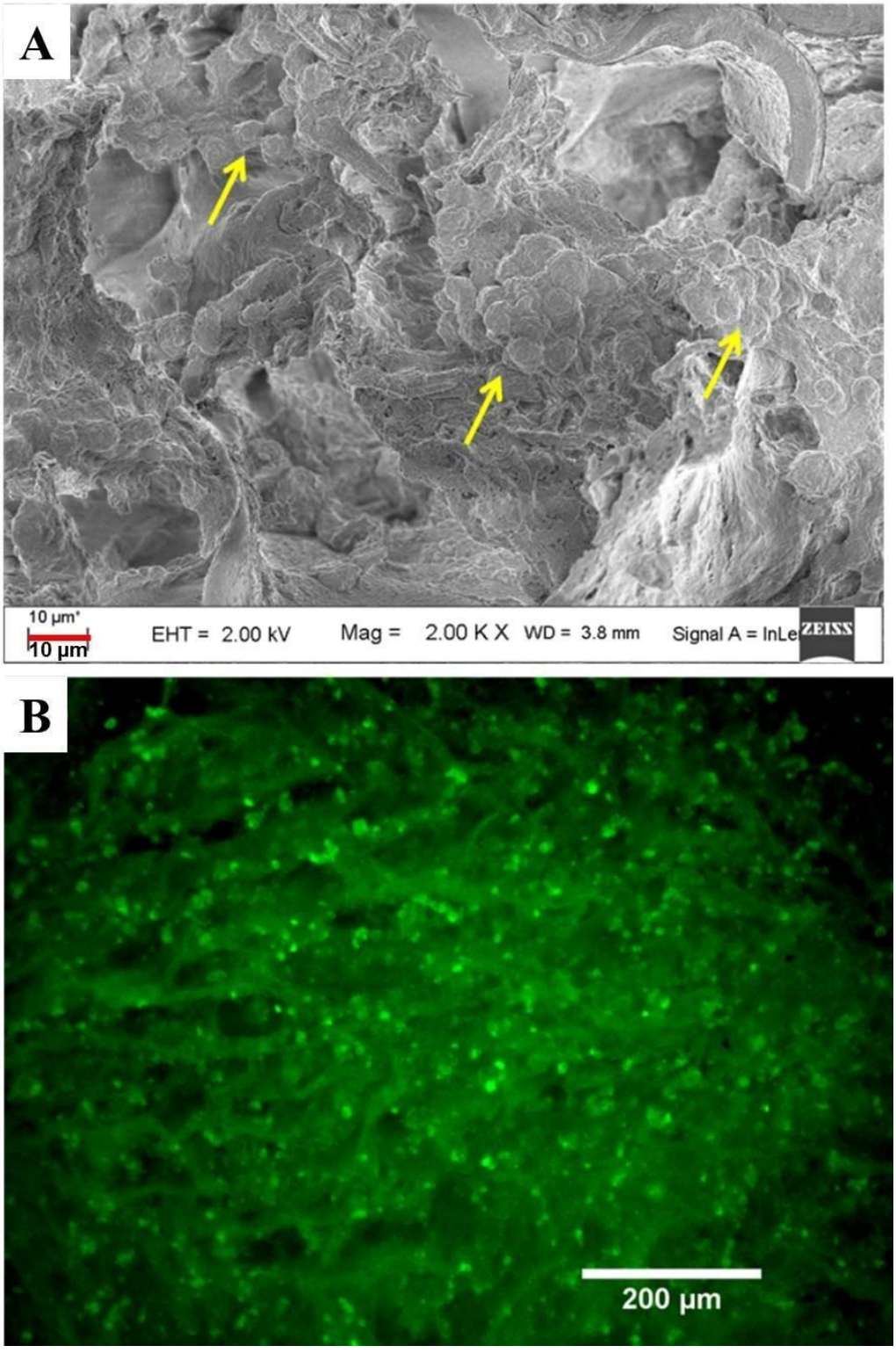

Figure 6.5. The attachment and proliferation of MG-63 cells over SCA-5 scaffold **A)** FESEM image and **B)** Fluorescence image

In addition to the cell proliferation analysis, the HSCA and SCA samples' cytotoxicity analysis was carried out, as described in the materials and method section. To analyze the toxic effect of any degradation by-product or by the scaffolds, the conditioned media was supplemented to the MG-63 cells. The MTT assay analysis revealed no significant decrease in both HSCA and SCA scaffolds (*p value* > 0.05). The cells were found to be ~ 99 % viable as compared to the control cells (Cells grown in DMEM media; Figure 6.6). SCA-0, and HSCA, and SCA scaffolds did not exhibit any cytotoxicity up to 6 days of incubation.

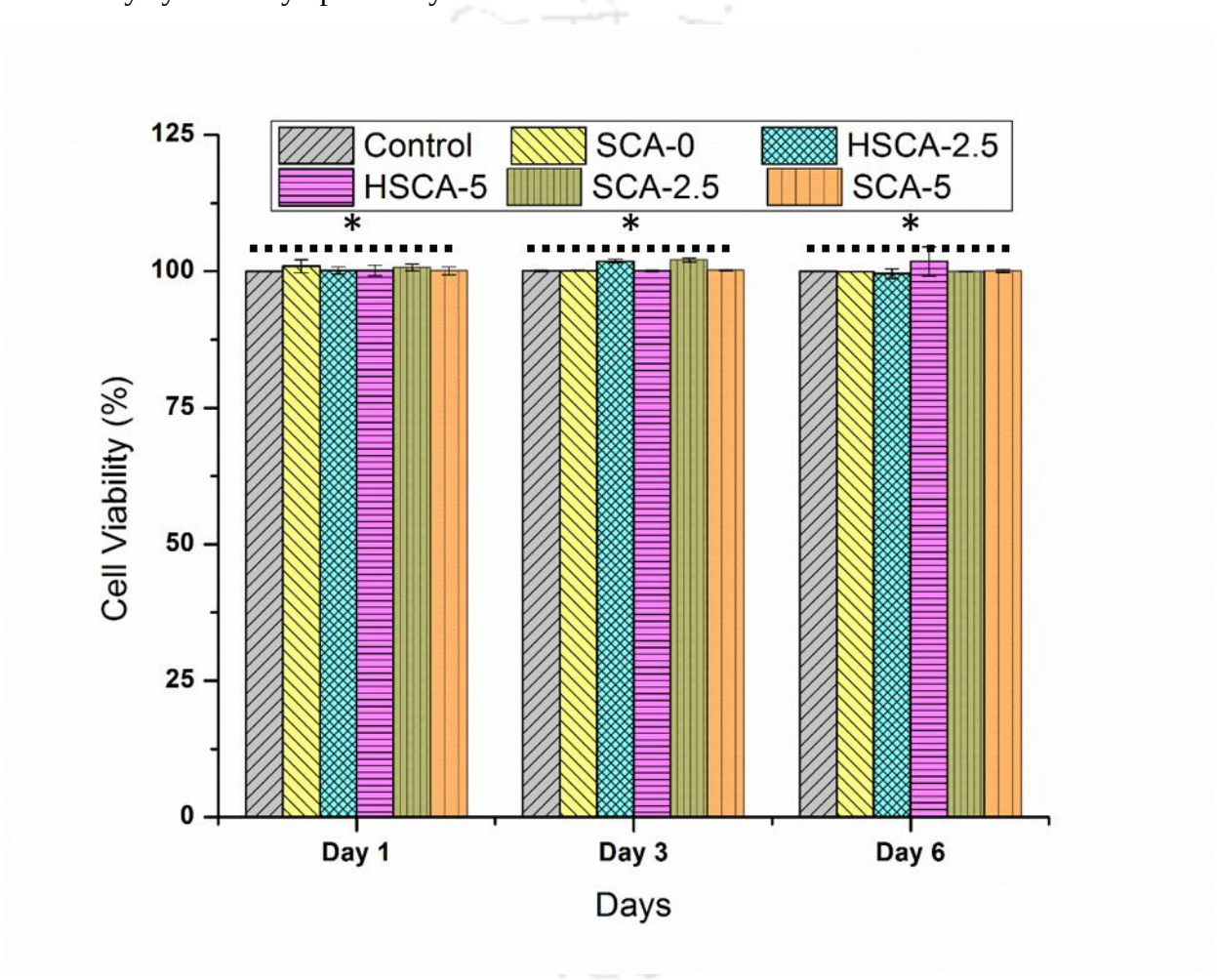

Figure 6.6. Cytotoxicity analysis of the HSCA and SCA scaffolds for 1, 3, and 6 days; No toxicity was reflected by the scaffolds; **p value* > 0.05 ; *n*=3.

Summarily, various physical, chemical, and biological properties of the prepared scaffolds have been tuned by varying the contents of ZFHAp-2. The porosity of the scaffold controls the swelling

behavior as well as the enzymatic degradation of the scaffolds. As shown in Figure 6.7, the scaffolds' porosity was found to be directly correlated with the degradation and the swelling behaviors. Linear correlations between the porosity and enzymatic degradation with an R^2 value of 0.92 and porosity and % swelling with an R^2 value of 0.99 were observed, indicating that the porosity governed the swelling and enzymatic degradation. Hence, it was confirmed that the ZFHAp-2 concentrations directly affected the porosity of the scaffolds, leading to control over its other biochemical behaviors. Hence, along with the controlled swelling and porous behavior, a slower degradation rate was observed (Figure 6.2.1). The presence of ZFHAp-2 also imparted antibacterial properties to the scaffolds (Figure 6.3). The degradation of scaffolds leads to the release of metal ions similar to that of ZFHAp powder samples, and hence the antibacterial mechanism can be attributed to the release of Zn^{2+} and Fe^{3+} ions. The controlled degradation provided an excellent antibacterial activity to the scaffold (~100% cell death) and provided better cell attachment and growth.

Various studies have been performed on chitosan-based scaffolds for the controlled bone tissue engineering and are listed in Table 6.3. A study reported the excellent swelling behavior and the required microporous structure of the scaffolds but with a higher degradation rate, *i.e.,* 50% degradation in 28 days [382]. Few studies utilized HAp as a constituent for the scaffold, yet their degradation was higher (Table 6.3). This can be explained by the bond formation between HAp and Chitosan. However, the antibacterial activities in the Chitosan-HAp based scaffolds were not observed. In this study, the ZFHAp-2 contained three electron donor groups, *i.e.,* Ca, Fe, and Zn, that form the coordination bonds between HAp and Chitosan. With the increase in ZFHAp-2 concentrations, the number of coordinate bonds was increased, and the scaffolds remained unaffected by the enzymatic degradation. Hence, SCA-5 could only show an effective antibacterial action than that of other scaffolds. On the other hand, the integration of Zn and Fe to HAp prior to the scaffold formation provided an excellent antibacterial activity to the scaffolds. The concentration-dependent controlled degradation, excellent antibacterial activity, along with the desired swelling behavior and porosity, enable these scaffolds to be the potential candidates for bone tissue engineering applications. Hence, this study designates the SCA-5 as plausible scaffolds for orthopedic applications.

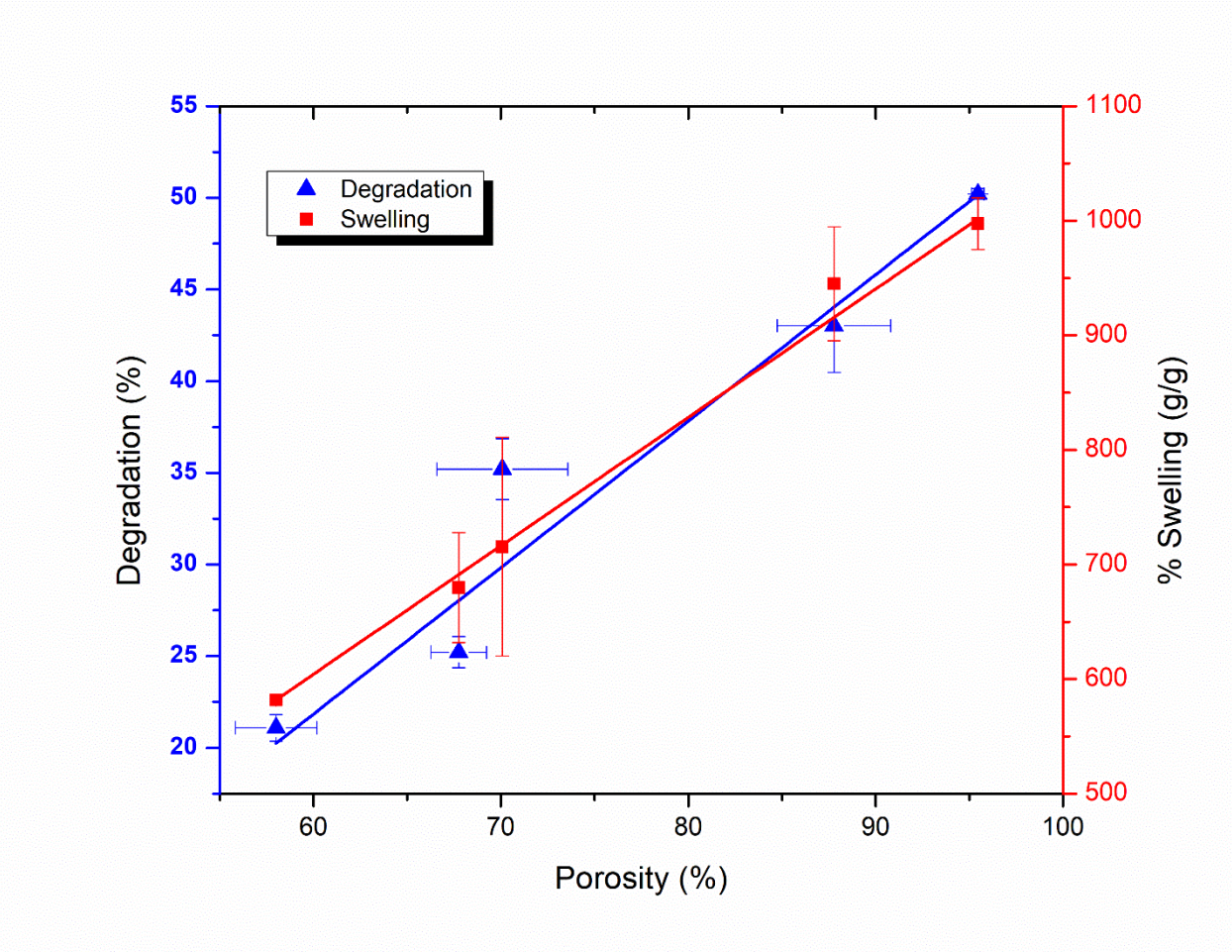

Figure 6.7. Linearly fitted data of correlation between co-relation between Porosity, Degradation and Swelling Behaviour

Table 6.5. Recent advances in chitosan-based scaffolds

S. No.	Scaffolds	Swelling ratio (%)	Porosity (%)	Degradation (%)	Antibacterial Activity	Ref.
1.	nanoHAp/Chitosan/CMC	NA	77.8	30 % (after 30 days)	NA	[383]
2.	nanoHAp/Chitosan/CMC	NA	~72-80	10-12 % (after 56 days)	NA	[384]

3.	Chitosan/HAp	1300-2200	84-91	NA	NA	[385]
4.	Agarose/Chitosan/Graphene oxide	2640-2930	73-79	43-45 % (after 28 days)	NA	[368]
5.	Clinoptilolite-nanoHAp/Chitosan/Gelatin	1200-1800	79-98	28-56 % (after 21 days)	NA	[367]
6.	Chitosan/Silk protein	200-300	77-85	29-50 % (after 28 days)	NA	[386]
7.	Chitosan/CMC/reinforced with multiphasic Calcium Phosphate	600-1500	61-75	NA	NA	[387]
8.	Collagen/Chitosan Poly (ethylene glycol)/nanoHAp	1150-1400	75-84	40-73 %	NA	[382]
9.	Chitosan/CMC/mesoporous wollastonite	1800-2200	NA	~50-80 % (after 14 days)	NA	[388]
10.	Chitosan/Carboxymethyl cellulose/Silver nanoparticles modified Cellulose nanoWhiskers (CCNWs-AgNP)	584-1070	77-96	21-55 % (after 20 days)	100% antibacterial efficiency at 2.5 % and 5 % of CCNWs-AgNP concentration	[361]
11.	Chitosan/HAp	NA	NA	0.5-3 % (after 72 h)	NA	[389]
12.	Chitosan/TCP/HAp	200-800	54-91	13 % (after 28 days)	NA	[390]

13.	Hydroxypropyl chitosan /nano-HAp/Fucoidan	250-2500	61.5–81.2	10-28 % (after 28 days)	NA	[391]
14.	Chitosan	NA	98-99	2.5-14 % (after 14 days)	NA	[392]
15.	Chitosan/CMC/ZFHAp-2	473-997	58-96	21-50 % (after 20 days)	~100 % Antibacterial at 5 % concentration of ZFHAp-2	This Study

NA, Not available; β-TCP, tricalcium phosphate; HAp, hydroxyapatite; CMC, carboxy methyl cellulose

6.7 Conclusions

In this chapter, we successfully prepared the naturally occurring polymer-nanocomposite based hybrid scaffolds with concentration-dependent biochemical behaviors. The Fe and ZnO integrated HAp nanocomposite (ZFHAp-2) showed excellent control over the scaffold's physical and biochemical properties. The dual morphology of ZFHAp-2 and intermolecular interactions altered the packing behavior and thus controlled the porosity, swelling behavior as well as the controlled degradation of the scaffolds. The presence of Zn and Fe ions in the HAp lattice also played a crucial role in controlling the porosity, degradation, and swelling behavior of the scaffolds. The presence of metal ions in the HAp lattice not only altered its morphology but also affected its charge unbalancing, which altered the interaction with Chitosan and CMC to a great extent. The coordination bonding of ZFHAp-2 with Chitosan and CMC resulted in reduced enzymatic degradation, whereas less coordination bond with HAp resulted in rapid degradation as compared to HSCA scaffolds. The swelling behavior and enzymatic degradation were found to be linearly related to the porosity of the scaffolds. The addition of Zn and Fe to the HAp matrix imparted excellent antimicrobial activity to the scaffolds. In addition, synergistically, ZFHAp-2 and Chitosan supported the bone cell proliferation ability of the scaffolds. This study provides an

insight into designing the polymeric scaffolds with self-antibacterial properties along with controlled biochemical behaviors.

Chapter 7

Synthesis and characterization of the antimicrobial peptoids micelles

This chapter explains the synthesis, characterization, and biological evaluation of antimicrobial Peptoids (Ampetoids). As reviewed in Chapter 2, Ampetoids were also scrutinized for their antibacterial activity and cytocompatibility for their potential applications as nanoantibiotics. Ampetoids were designed via sub-monomer synthesis route (solid-phase synthesis) and were characterized via Reverse-Phase High-Pressure Liquid Chromatography (RP-HPLC) and Liquid Chromatography-Mass Spectroscopy (LCMS). The antibacterial activity (MIC calculation) and cytocompatibility analysis of the designed Ampetoids was carried out using the Serial Dilution Method and AlamarBlue assays, respectively. The retention time was found to be increased with an increase in the Nae unit. Similarly, singly, doubly, and triply charged species of the synthesized Ampetoids were present in the LCMS analysis, conforming to a successful synthesis. The addition of the aliphatic chain enhanced the antibacterial activity; however, with an increase in the chain length, the antibacterial activity was found to be decreased. The synthesized Ampetoids were found to be cytostable than being cytotoxic.

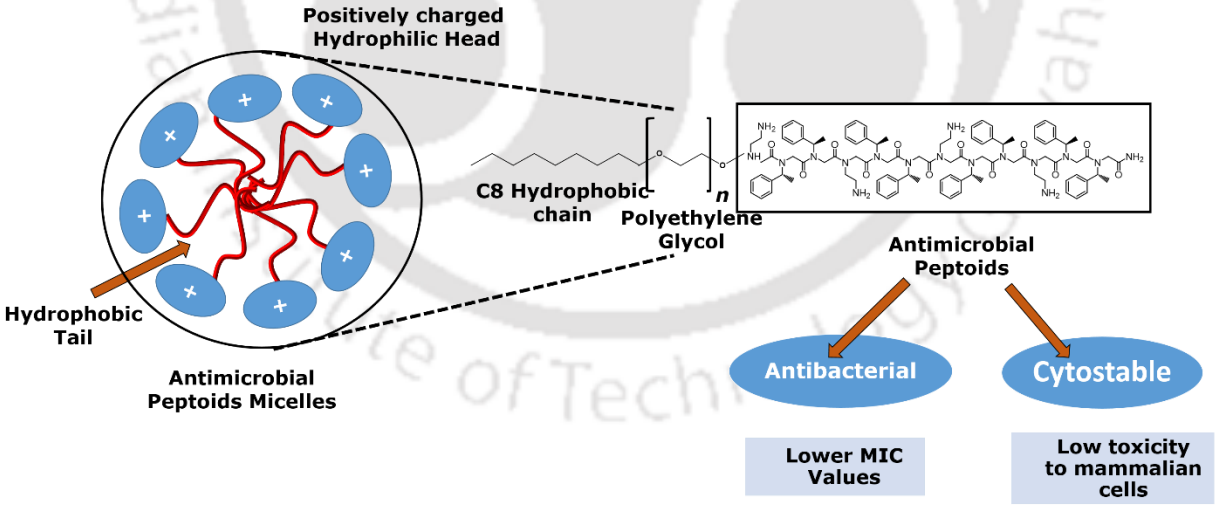

Scheme 7.1. Antimicrobial Peptoid micelles; highly efficient as antibiotic and cytostable

7.1 Introduction

Antimicrobial Peptides (AMPs) are naturally occurring bio-molecules exhibiting excellent antibacterial activity. The AMPs are considered as the intrinsic component of innate immunity against various pathogens [393]. The non-specific interactions between the AMPs and bacterial membrane cause the rupturing into the bacterial cell wall, leading to its broad-spectrum antibacterial activity. Various cationic peptides, majorly derived from the AMPs of the human innate immune system, are under clinical trials. It is believed that the antibiotics, which are produced by the microorganisms, are peptide-based biomolecules. In addition, bacteria can generate resistance against AMPs via passive or inducible mechanisms, known as intrinsic resistance [394]. Furthermore, enzymatic degradation is one of the major issues in the practical applications and commercialization of the AMPs.

In this regard, various bio-mimics of the AMPs are under investigation for their bactericidal activity. For example, Poly-(N-substituted glycine) "Peptoids" are protease-resistant due to the attachment of the functional group at α-nitrogen as compared to the peptides. Functional group attachment at the amide group increases the backbone conformation flexibility while enabling a versatile synthetic route (the "submonomer" method) to install a diverse array of commercially available sidechains (Figure 7.1).

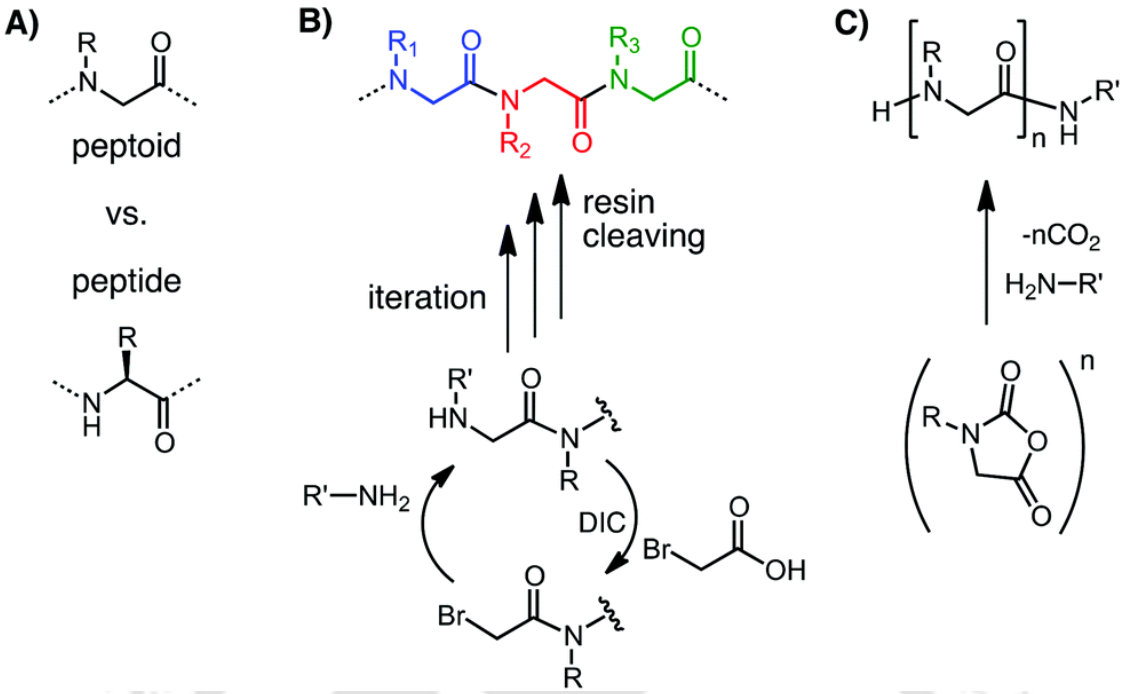

Figure 7.1. Peptoid chemical structure and synthesis. **(A)** A shift in the sidechain connection from the α-carbon to the amide nitrogen, accompanied by loss of main chain chirality and amide hydrogens, differentiates Peptoids from peptides (L-amino acid residue showed). **(B)** Submonomer solid-phase synthesis: residue coupling is split into elongating the chain via acylation with a haloacetic acid and sidechain introduction via displacement with a primary amine submonomer. DIC: N,N′-diisopropyl carbodiimide. **(C)** NCA peptoid polymerization (Adapted with permission from Biomaterials Science 2 (5), 627-633 (2014); [395]

The sub-monomer design of Ampetoids provides an opportunity to tune the sequence and length of the Ampetoids, which alters the antibacterial activity and the cytocompatibility of the Ampetoids. In this chapter, we designed the antimicrobial Peptoids and prepared their micelles by adding the ethylene glycol (EG_2) and eight-carbon aliphatic chain (C8) to enhance their antimicrobial and cytocompatibility. The details are followed in the sequel.

7.2 Materials and Methods

7.3 Materials

All the solvents ((HPLC grade), such as Dimethylformamide (DMF), Dichloromethane (DCM), N-Methyl-2-pyrrolidone (NMP), Trifluoroacetic acid (TFA), N,N-Diisopropylethylamine

(DIEA), Bromoacetic acid (BAA), (2-(1H-benzotriazol-1-yl)-1,1,3,3-tetramethyluronium hexafluorophosphate (HBTU)) and chemicals used were purchased from Sigma-Aldrich UK. Rink amide MBHA resin was bought from Merck, UK. Tert-butyl N-(4-aminobutyl) carbamate (NLys) and (1S)-1-Phenylethylamine (Nspe) monomers were purchased from Apollo Scientific, UK. Fmoc-Amino-3,6 dioxaoctanoic acid was procured from FluroChem, UK. LB Media and MH media for antibacterial analysis was purchased from Merck, UK. AlamarBlue dye for cytocompatibility was purchased from Thermo Scientific.

7.4 Methods

Following methods were used to synthesize and characterize the Ampetoids over various physical and biological means.

7.4.1 Synthesis of antimicrobial Peptoids

Peptoid synthesis was carried out manually using submonomer synthesis on rink amide MBHA resin as reported previously [396-398]. Briefly, MBHA resin was initially swelled in DCM followed by DMF twice. The swelled resin was de-protected twice using 20 % piperidine in DMF for 20 min. Bromoacetylated intermediate was formed on terminal secondary amine groups present on de-protected resin by activating BAA with DIC. Later, bromine was substituted by desired amine submonomers (20x excess, 1M in NMP) (sequence-specific synthesis) through S_N2 displacement. This step was repeated for growing peptoid chain from C to N terminal direction.

For ethylene glycol coupling, 6x excess of Fmoc-amino-3,6 dioxaoctanoic acid and 6x excess of HBTU coupling agent were dissolved in DMF along with 9x excess of DIEA. The reaction mixture was stirred for 2 h at RT and was later recoupled for 4 h to ensure complete coupling. Fatty acids (C8) were coupled using the method reported previously by Dr. Aaron's group [398]. Briefly, 0.5 M solution of fatty acid in DCM and 0.5 M solution of HBTU in DMF was added to the resin, followed by the addition of DIPEA. The reaction was carried out for 2 h at 35°C and was further processed (recoupled) for 4 h. Post synthesis, the peptoid chains were cleaved by treating rink amide resin with a cleavage recipe (TFA:TIPS: H2O/95:2.5:2.5 v/v/v) at RT for 30 min before filtration through cotton wool. To confirm the synthesis, 65 µL of the solution was transferred into a sample vial containing 0.1 % TFA in distilled water (250 µL) and 0.1 % TFA in ACN (250 µL) for analysis via LC-ESI-MS and analytical HPLC.

7.4.2 Characterizations of the synthesized Peptoids

Analytical HPLC measurements were taken across a concentration gradient of mobile phase 95 % water in 5 % ACN to 5 % ACN in 95 % water for 47 min with a flow rate of 1.0 mL min^{-1}. The wavelengths of interest were 214 nm and 220 nm, corresponding to the peptoid backbone. A blank (1:1 solution of 0.1 % TFA in acetonitrile ACN and 0.1 % TFA in MQ) was run along with the samples. Liquid Chromatography-Electrospray Ionisation-Mass Spectrometry (LC-ESI-MS) data were acquired on an Agilent 1200 Series instrument coupled with an Agilent 6130 Mass Spectrometer. The same samples and blanks used in analytical HPLC were used for LC-ESI-MS at a similar sample gradient.

7.4.3 Biological Characterizations

The synthesized Ampetoids were tested for their cytotoxicity against both bacterial and human cells. The detailed procedure is as follows:

7.4.4 Antibacterial activity and determination of MIC values

The antibacterial analysis was performed in the Mueller–Hinton (MH) broth using the serial dilution method (CLSI M07-A10) in 96 well round bottom plates. Briefly, Gram-positive (*Staphylococcus epidermidis,* and Gram-negative *Pseudomonas aeruginosa* (N676) bacteria were incubated with various concentrations of Ampetoids and lipopeptoids ranging from 0-160 µM, at 37 °C for overnight. The OD_{600} values were recorded (Infinite 200 Pro, Tecan), and the MIC value was calculated based on no bacterial growth.

7.4.5 Nano-cytotoxicity analysis for Human cells

The cell viability of the Ampetoids was analyzed using AlamarBlue assay [399, 400]. In brief, Mouse fibroblast cell lines (3T3, NIH, UK) were procured and grown in DMEM at 37 ºC, 5 % CO_2, and 85 % humidity in a CO_2 incubator. The complete medium was prepared by supplementing 10% calf bovine serum, 1% antibiotic (Pen-Strep and Fungizone) into the DMEM.

For the analysis of cell viability, 500 cells per well (24 well plate) in 500 µl of DMEM were incubated for 24 h. After 24 h, the peptoid solution in DMEM (10, 20, 40, 80, 160 µM) was replaced with the previous DMEM. The medium was replaced with fresh Peptoids solution in DMEM at every 2^{nd} day. Cells without Peptoids were considered as a positive control. The viability

of the cells was analyzed for 1, 4^{th,} and 8th days. On desired day, the peptoid-DMEM solution was replaced with 10% Alamar blue in DMEM solution, and the cells were incubated further for 4 h. After 4 h, the AlamarBlue solution was collected, and the optical density (OD) was measured using a spectrophotometer at 570 nm and 600 nm, respectively. The cells were washed with the 1X PBS and were incubated with the respective concentrations of Peptoids for further analysis. The viability was analyzed using the following equation

$$Cell\ viability = \frac{(\varepsilon ox)\lambda 2\ A\lambda 1 - (\varepsilon ox)\lambda 1\ A\lambda 2}{(\varepsilon ox)\lambda 2\ A°\lambda 1 - (\varepsilon ox)\lambda 1\ A°\lambda 2} \quad (7.1)$$

Where, (εox) is molar extinction coefficient of alamarBlue oxidized form (BLUE), A is the absorbance of test wells, A° is the absorbance of positive growth control well, λ1 is 570nm, and λ2 is 600nm wavelengths.

To calculate the cell viability at the MIC values and 10 X MIC values, the obtained cell viability data were further evaluated via double sigmoidal curve fitting, and the cell viability at respective MICs was calculated via the following equation:

$$Cell\ viability = b1\ [1 - \frac{1}{1+e^{-k1(x-xo_1)}}] + b2[1 - \frac{1}{1+e^{-k2(x-xo_2)}}]+C] \quad (7.2)$$

Where b1 and b2 are the differences between the highest and lowest viabilities at individual sigmoidal curves, *k1* and *k2* are the rate constants; x is the known viability at respective peptoid concentration, x_{01} and x_{02} are the peptoid concentrations referring to a drop in the first and 2nd sigmoidal curves respectively, and C is the lowest viability observed.

7.5 Results and discussion

Various Peptoids with sequence formula (Nae-Nspe-Nspe)$_n$ and (Nae-Nspe-Nspe)$_n$-Nae-Nae were synthesized (where n=2,3,4). Post-synthesis ethylene glycol was coupled at the N terminal of the peptoid followed by the addition of fatty acids nonanoic acid (C8), leading to the sequences C8-EG_2-(Nae-Nspe-Nspe)$_4$ and C8-EG_2-(Nae-Nspe-Nspe)$_n$-Nae-Nae. The structure, formulae, and molecular weight for the given sequences are as follows. Same sample codes will be followed throughout the thesis.

Table 7.1. Sample codes, structure, and the molar weight of the respective Peptoids

S.No.	Sequences	Structure	M. Wt
1.	12 mer	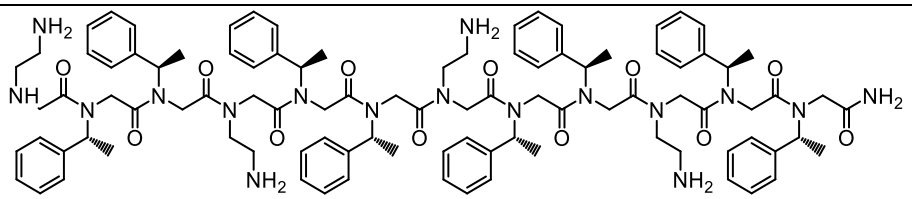	1705.95
2.	9 mer	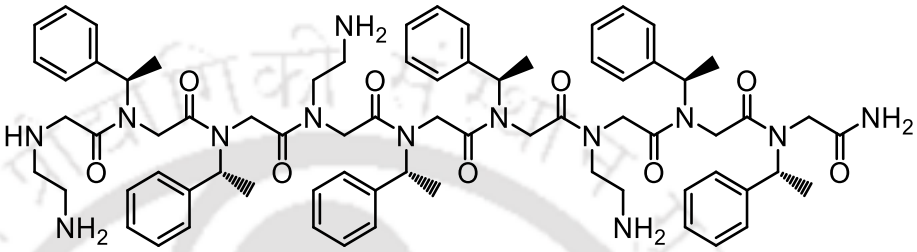	1283.72
3.	6 mer	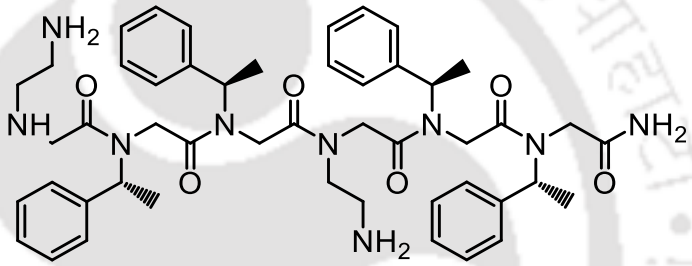	861.49
4.	6+2 mer	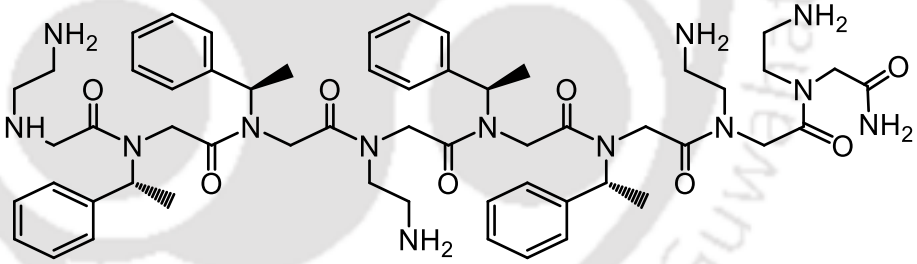	1061.62
5.	9+2 mer	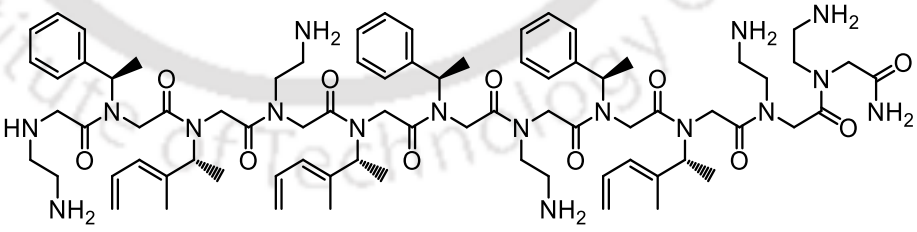	1483.85
6.	12+2 mer	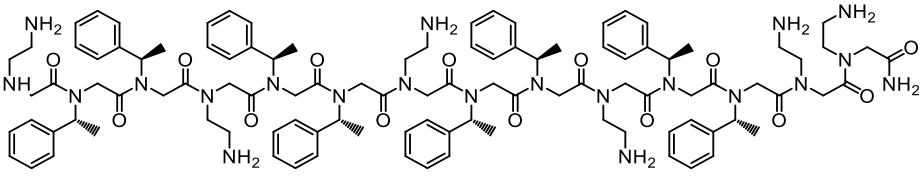	1906.08

7.	C8-EG_2-(12+0)	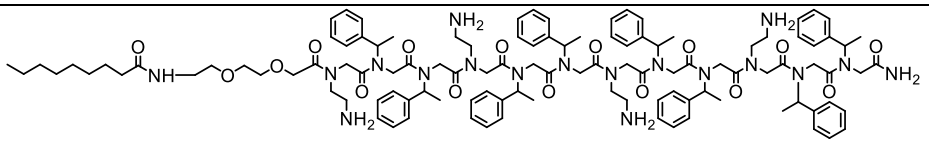	1991.15
8.	C8-EG_2-(6+2)	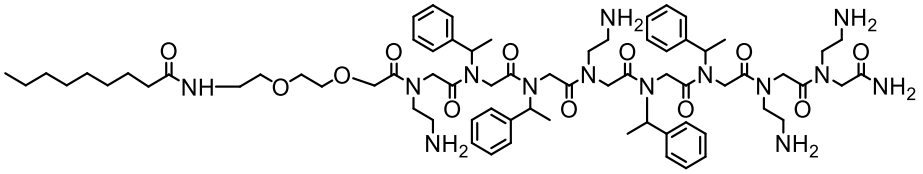	1346.81
9.	C8-EG_2-(9+2)	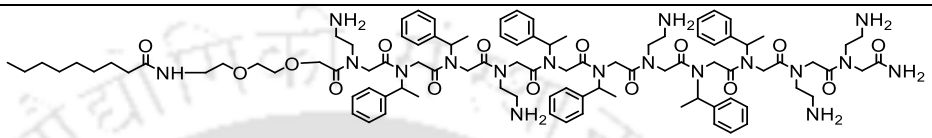	1769.04
10.	C8-EG_2-(12+2)	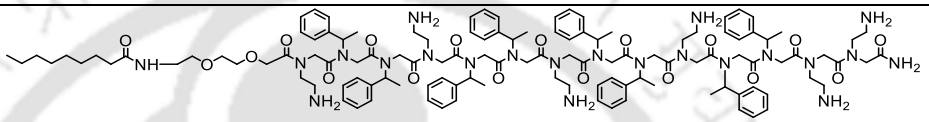	2191.28

The synthesized Peptoids were characterized using HPLC and LCMS. The HPLC curve of the sequences are given below:

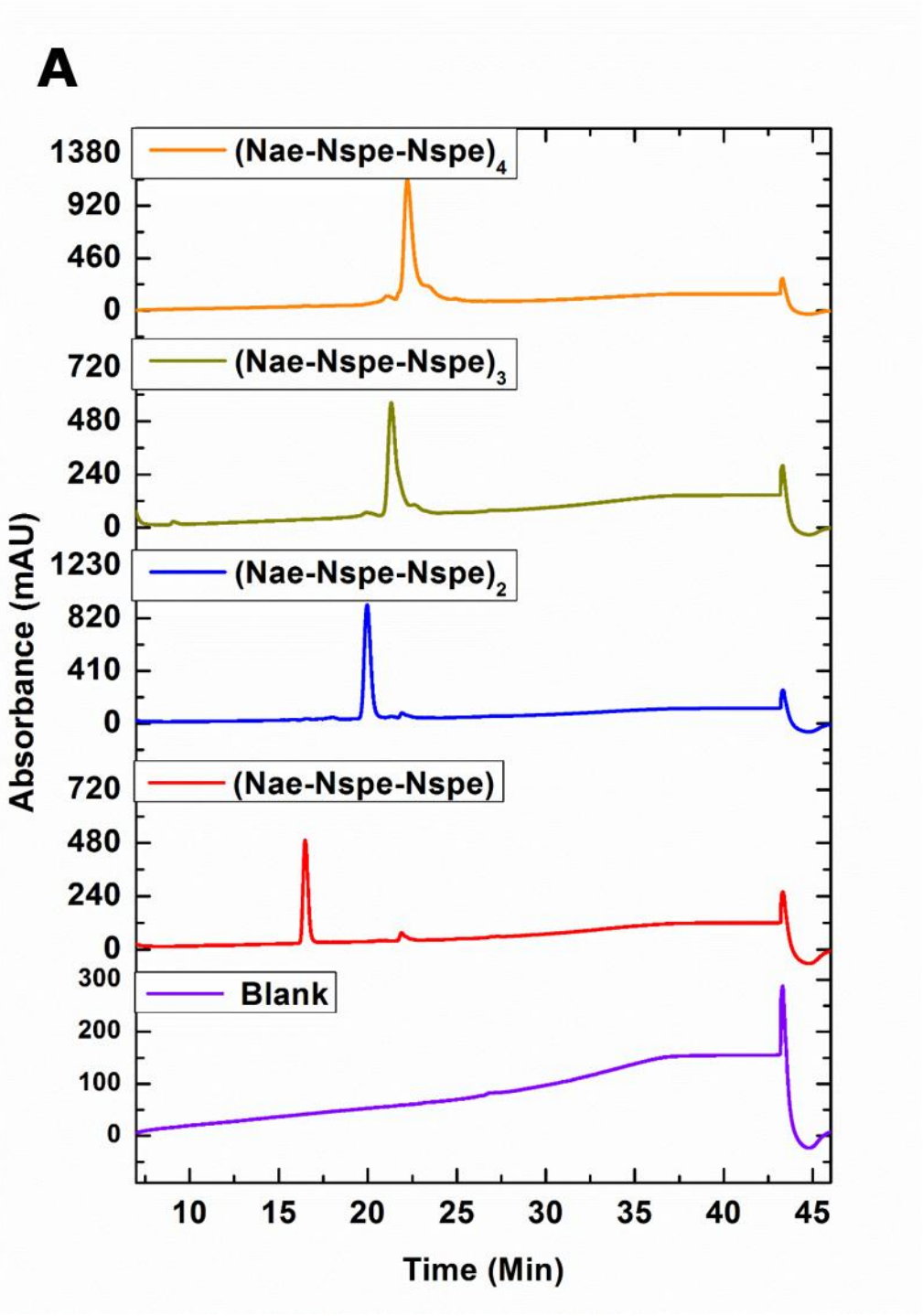

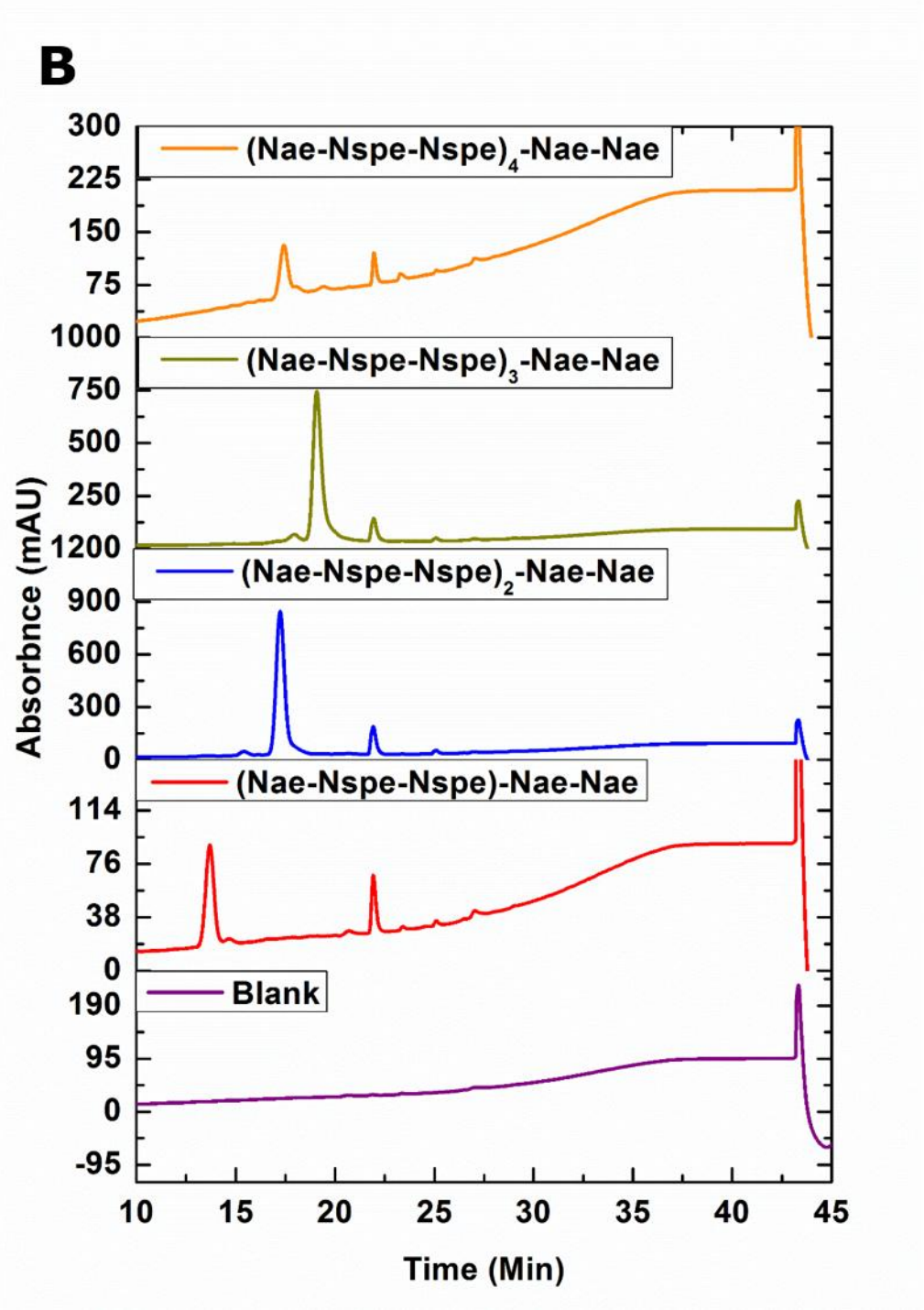

Figure 7.2. HPLC curve of (Nae-Nspe-Nspe)$_n$, **(A)**, and (Nae-Nspe-Nspe)$_n$-Nae-Nae **(B)**, where n=2,3,4

The HPLC curve showed the retention time for 6 mer, 9 mer, and 12 mer was found to be 19.98, 22.21, and 33.28 min, respectively, as shown in Figure 7.2A. With an increase in the

hydrophobicity and chain length [401], the required amount of DCM was intensified, increasing the retention time (with respect to the DCM concentration), indicating the successful synthesis of the sequences. The synthesis of the sequences was confirmed by the LCMS analysis, which showed the peaks at respective masses at 863.5 $[M+H]^+$ for 6 mer, 1284.7 $[M+H]^+$ for 9 mer and 853.5 ($[M+2H]^+/2$), 569.5 ($[M+3H]^+/3$) and 427.5 ($[M+4H]^+/4$) for 12 mer respectively (Figure 7.3A). After successfully synthesizing the $(Nae\text{-}Nspe\text{-}Nspe)_n$, where n=2,3,4 sequences, the chain length was increased by adding two extra Nae units at the N terminal to enhance the hydrophobicity and positive charge of the sequences [401]. The addition of these two Nae units was also expected to enhance the overall positive charge over the sequences leading to its high-expected antimicrobial activity.

The addition of the two Nae units at each sequence decreased the modified sequences' retention time, increasing its hydrophobicity. The decrease in the retention time showed the successful synthesis of the $(Nae\text{-}Nspe\text{-}Nspe)_n$-Nae-Nae sequences (Figure 7.2B). The synthesis was further confirmed by the LCMS analysis. The LCMS data reflected the corresponding peaks of 1064.5 1063 $[M+H]^+$ for 6+2 mer, 1485.7 $[M+H]^+$ for 9+2 mer, and 954.5 ($[M+2H]^+/2$) for 12+2 mer, respectively, confirming the successful synthesis of the desired Peptoids (Figure 7.3B).

A

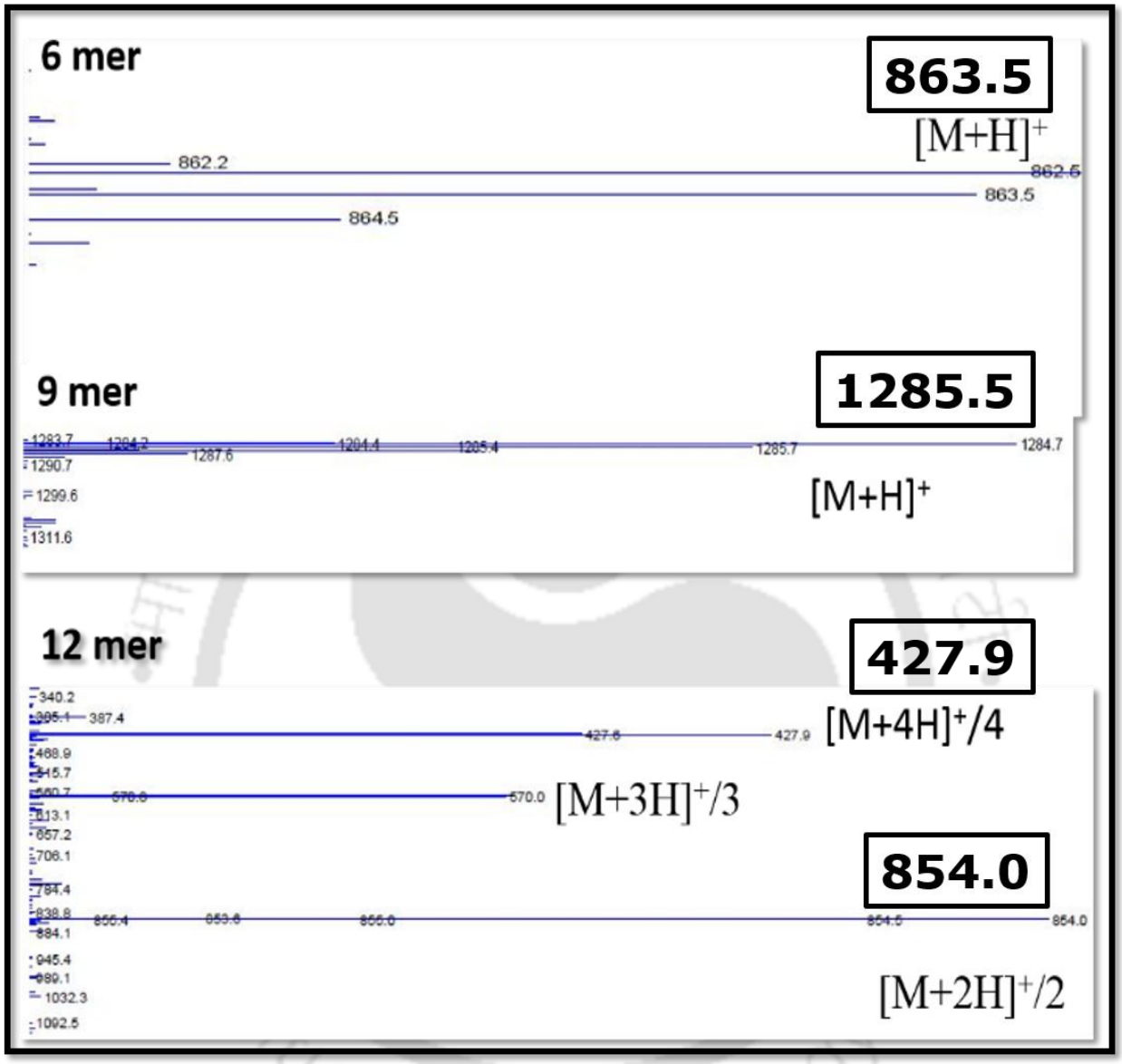
6 mer
863.5
[M+H]+
862.2
862.5
863.5
864.5
9 mer
1285.5
1283.7
1284.2
1287.6
1284.4
1285.4
1285.7
1284.7
1290.7
1299.6
1311.6
[M+H]+
12 mer
427.9
340.2
387.4
427.6
427.9
[M+4H]+/4
468.9
570.0
570.0
[M+3H]+/3
706.1
854.0
856.4
853.6
856.0
854.5
854.0
945.4
1032.3
1092.5
[M+2H]+/2

B

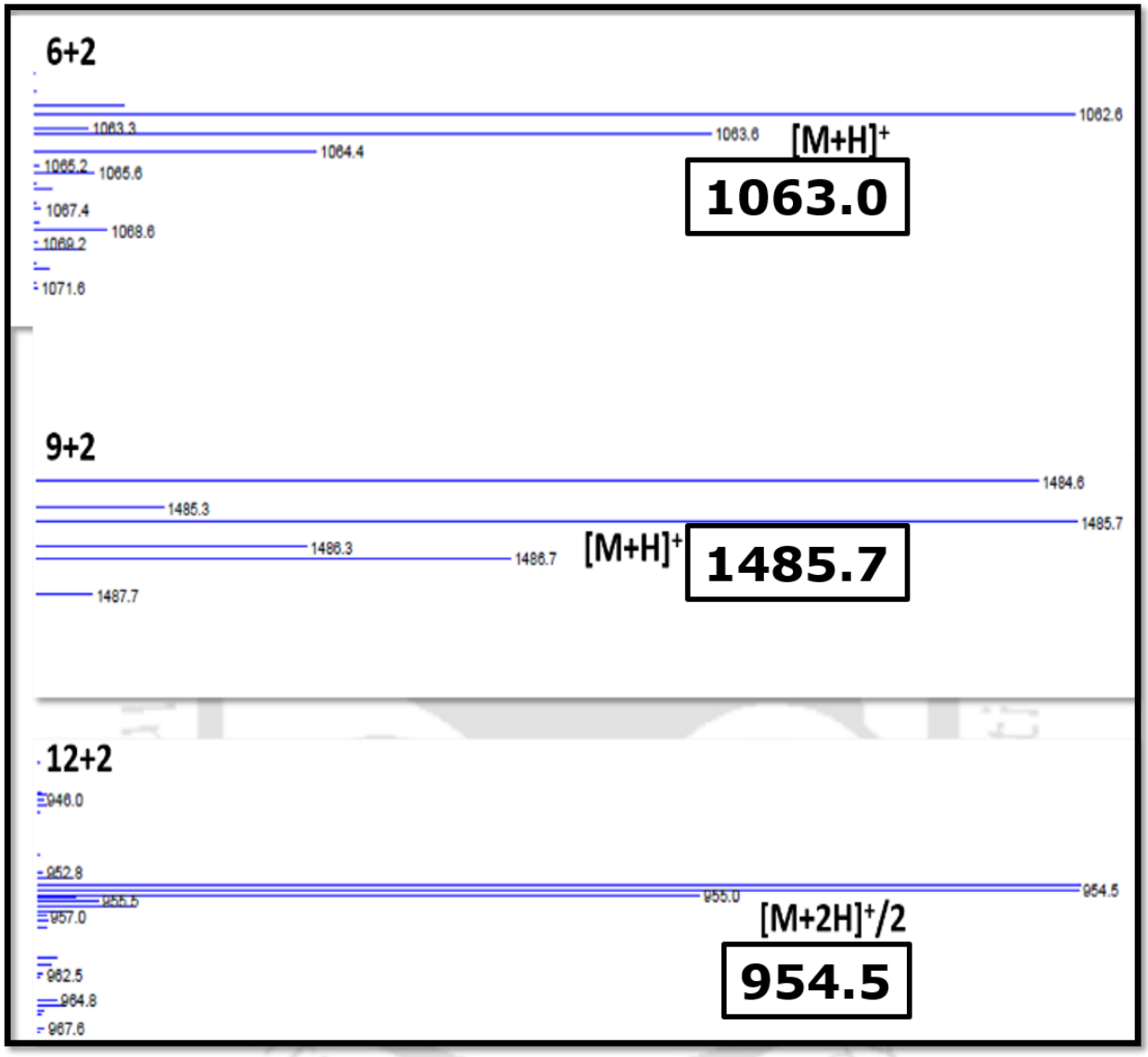

Figure 7.3. LCMS data for (Nae-Nspe-Nspe)n **(A)**, and (Nae-Nspe-Nspe)n-Nae-Nae **(B)**, where n=2,3,4

After successful synthesis of $(Nae\text{-}Nspe\text{-}Nspe)_n$-Nae-Nae sequences, the ethylene glycol coupling and the fatty acid chains were added at the C terminal of the synthesized sequences as per the protocol given in section 7.2.1.

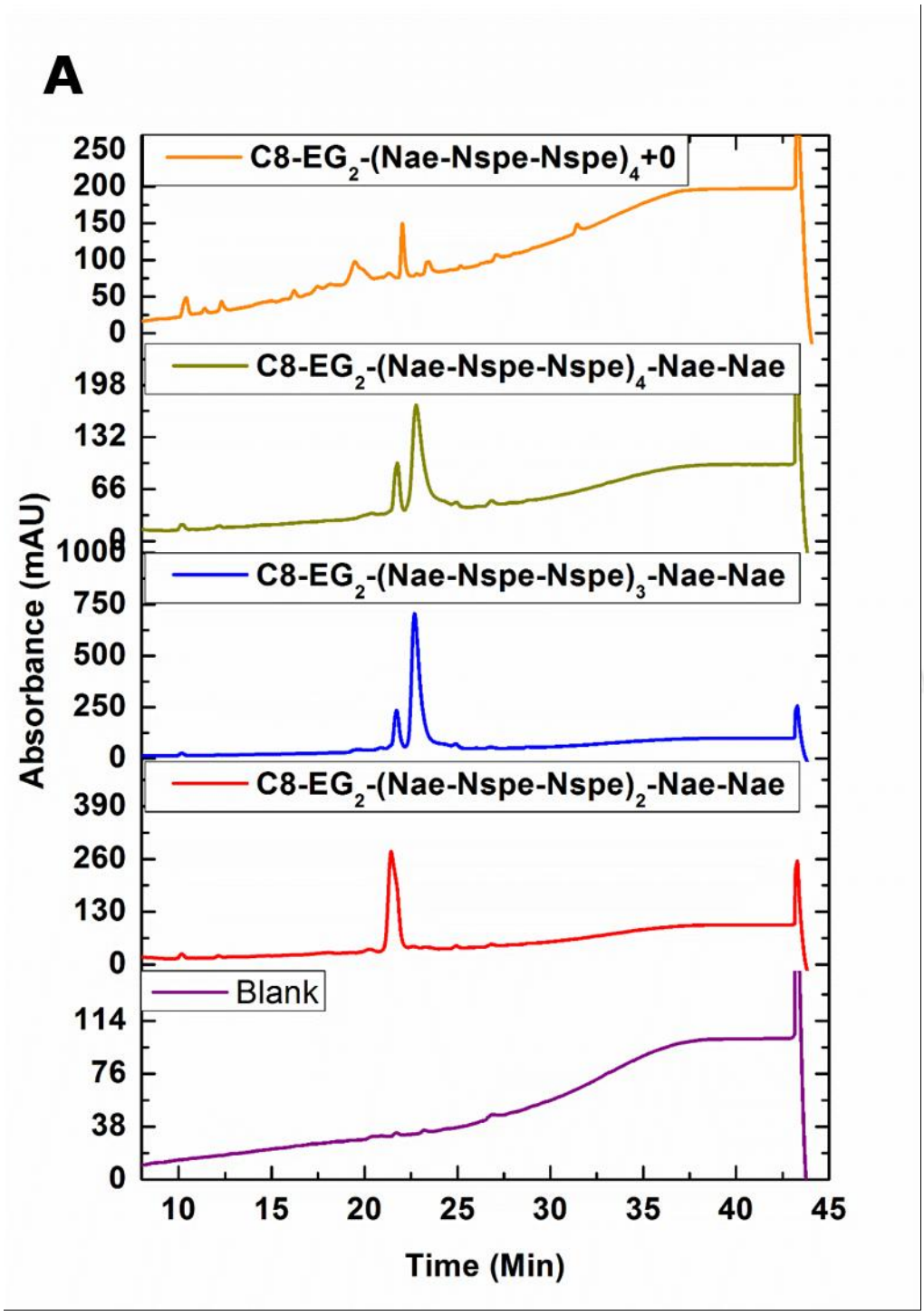
A
C8-EG2-(Nae-Nspe-Nspe)4+0
C8-EG2-(Nae-Nspe-Nspe)4-Nae-Nae
C8-EG2-(Nae-Nspe-Nspe)3-Nae-Nae
C8-EG2-(Nae-Nspe-Nspe)2-Nae-Nae
Blank
Absorbance (mAU)
Time (Min)

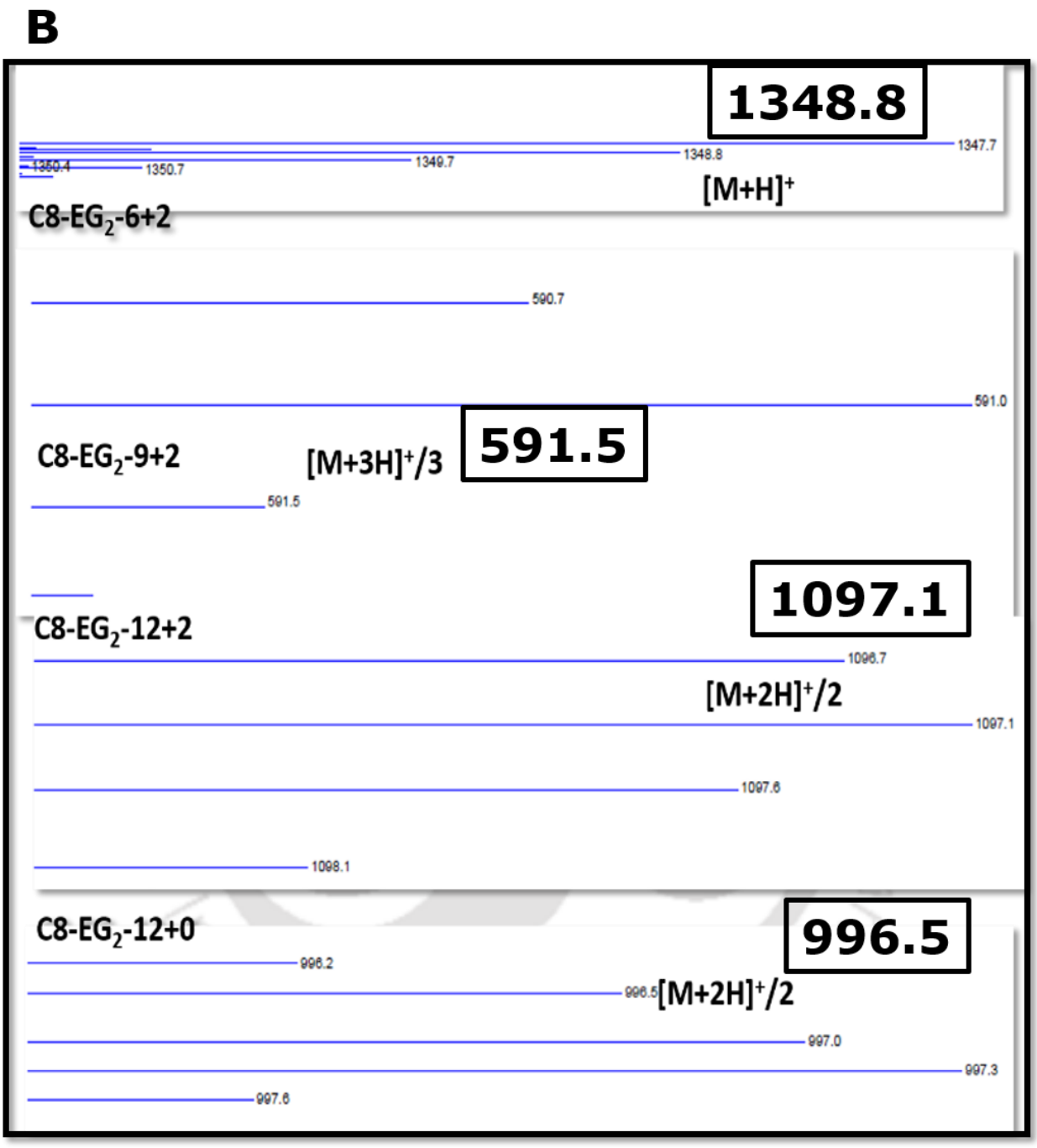

Figure 7.4. HPLC curves **(A)** and LCMS data **(B)** of C8-EG_2-(Nae-Nspe-Nspe)$_n$-Nae-Nae sequences

The ethylene glycol coupling and addition of aliphatic tail slightly enhanced the hydrophobicity and the retention time of the sequences, indicating their successful coupling (Figure 7.4A). The LCMS data as shown in Figure 7.4B further confirmed the successful synthesis with peaks at

1346.8 $[M+H]^+$ for C8-EG_2-6+2, 591.6 ($[M+3H]^+/3$) for C8-EG_2-9+2, 1096.6 ($[M+2H]^+/2$) for C8-EG_2-12+2 and 996.5 ($[M+2H]^+/2$) for C8-EG_2-12+0. The addition of an aliphatic chain along with ethylene glycol adds the capability to fold the antimicrobial sequences and form a micellar structure. These micelles are supposed to possess decent antimicrobial and cytocompatibility properties.

7.5.1 Antibacterial analysis:

In this study, the antibacterial activities (MICs) of differently designed Peptoids were evaluated against both Gram-positive and negative strains (Table 7.3). The peptoid concentration at which no bacterial growth was observed after 24 h of incubation was recorded as MIC.

The antibacterial capability of the designed Peptoids was evaluated for the 12 mer sequence designed. The MIC values were found to be much higher (>50 µM) as compared to the previously designed sequences with NLys $(NLys\text{-}Nspe\text{-}Nspe)_4$ (<15 µM) as compared to sequences with Nae (Figure 7.5). Hence, the bactericidal activity of all the sequences with NLys was analyzed.

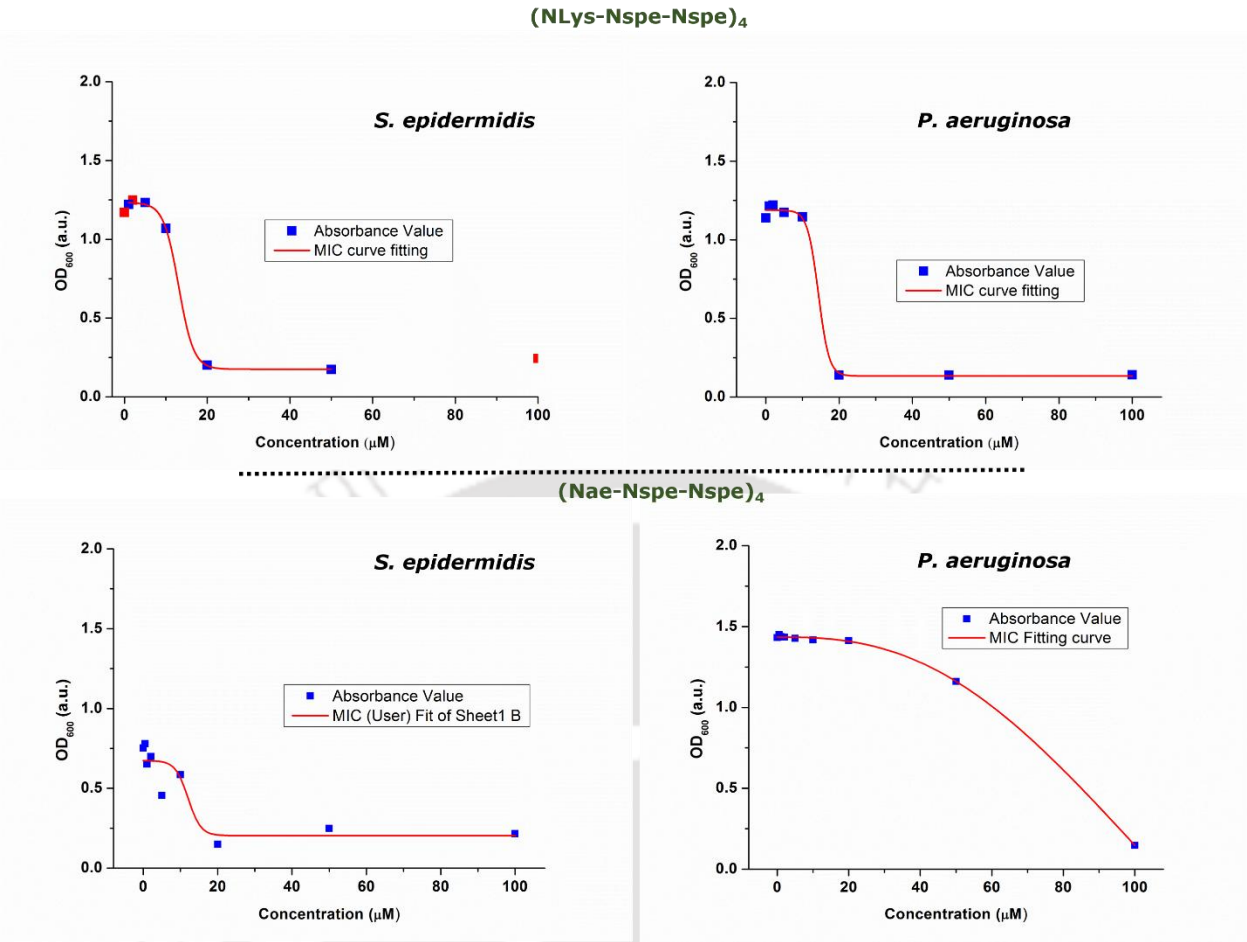

Figure 7.5. Antibacterial activity of (NLys-Nspe-Nspe)$_4$ and (Nae-Nspe-Nspe)$_4$ against *S. epidermidis* and *P. aeruginosa*

Previous members of Dr. Aaron's lab fabricated lipopeptoids library from existing antibacterial peptoid sequences reported by Barron's [186] and Hansen's [189] groups. Various aliphatic chains were added to the base sequences 6-12 mers, and their MICs were calculated. Sequences 9 mer and 12 mer possessed higher antibacterial activity (lower MICs) than that of 6 mer, reflecting that a minimum of three-unit repeats is required for the effective MICs. The addition of the aliphatic chain did not alter the antibacterial activity negatively. The MICs were found to be stable and slightly decreased after the addition of the aliphatic chains to the designed sequences. The MICs were stable after the addition of C8 and C11 chains. However, the addition of C15 chains adversely affected the bactericidal activities of the designed sequences (Table 7.3).

Table 7.2. MIC values of various Peptoids

S. No.	Samples	*S. epidermidis* (MIC, µM)		*P. aeruginosa* N676 (MIC, µM)	
		Value	Stdev	Value	Stdev
8	6 mer	11.1	0.9	*13.5*	*0.74*
9	9 mer	10	0.7	11.9	0.5
10	12 mer	13	0.6	14.29	0.55
11	12 mer with Nae	12.05	2.4	*68.44*	*4.53*
12	15 mer	15.4	3.5	14.5	0.75
13	12 mer-EG_2 (Free N Terminal)	2.31	1.45	17.44	1.6
14	EG_2-12 mer (Free C Terminal)	1.46	0.14	22.9	2.53
15	4K (YZYXKKKK)	3.05	0.99	14.77	1.08
16	5K (YZYXKKKKK)	4.55	0.45	24.73	2.56
17	KYKXK (YKZKYKXK)	7.26	0.71	25.72	4.41
18	C8-EG_2-6+2	11.4	2	12.8	0.34
19	C8-EG_2-9+2	7.6	0.7	15.1	0.59
20	C8-EG_2-12+2	30.5	8	39.7	0.25
21	C8-EG_2-12+0	40	4.6	6.9	0.54
22	C11-EG_2-12+2	9.9	0.31	13.8	0.79
23	C11-EG_2-6+2	8.6	1.7	18.8	0.69
24	C11-EG_2-9+2	9	1.2	15.3	0.42
25	C15-EG_2-12+2	89.9	21	102.9	0.9
26	C15-EG_2-12+0	>100	NA	>100	NA
27	C15-EG_2-4K	>200	NA	>200	NA
28	C15-EG_2-5K	>200	NA	>200	NA
29	C15-EG_2-KYKXK	>200	NA	>200	NA
30	12mer-EG_2-Pentyne	0.94	0.03	14.54	0.56

Where X: N-(butyl)glycyl; K- Lysine; Y: N-(1-naphthalenemethyl)glycyl; Z: N-(4-methylbenzyl)glycyl); NA: Not applicable

7.5.2 Cytotoxicity analysis

The designed sequences were evaluated for their cytocompatibility, as discussed above. The 12 mer sequence with NLys was found to be cytocompatible at its MIC value after Day 1 of incubation. However, a significant drop was observed in the cell concentration on Day 4. Cells were further processed until day 8, and it was observed that the number of cells increased after day 4. The drop in cell concentration might be originated due to the low growth of cells under the influence of the Peptoids. The results obtained indicated that the designed Peptoids are more cytostatic than cytotoxic, as cells were alive and more in number after day 8. The addition of ethylene glycol at C terminal effectively altered the cytotoxicity of Peptoids over the mouse fibroblast until day 8, and cells were found to be more viable at day 8. Similarly, ethylene glycol at N terminal also affected the cell growth, yet the effect wasn't significantly altered as compared to pristine 12 mer (Figure 7.6).

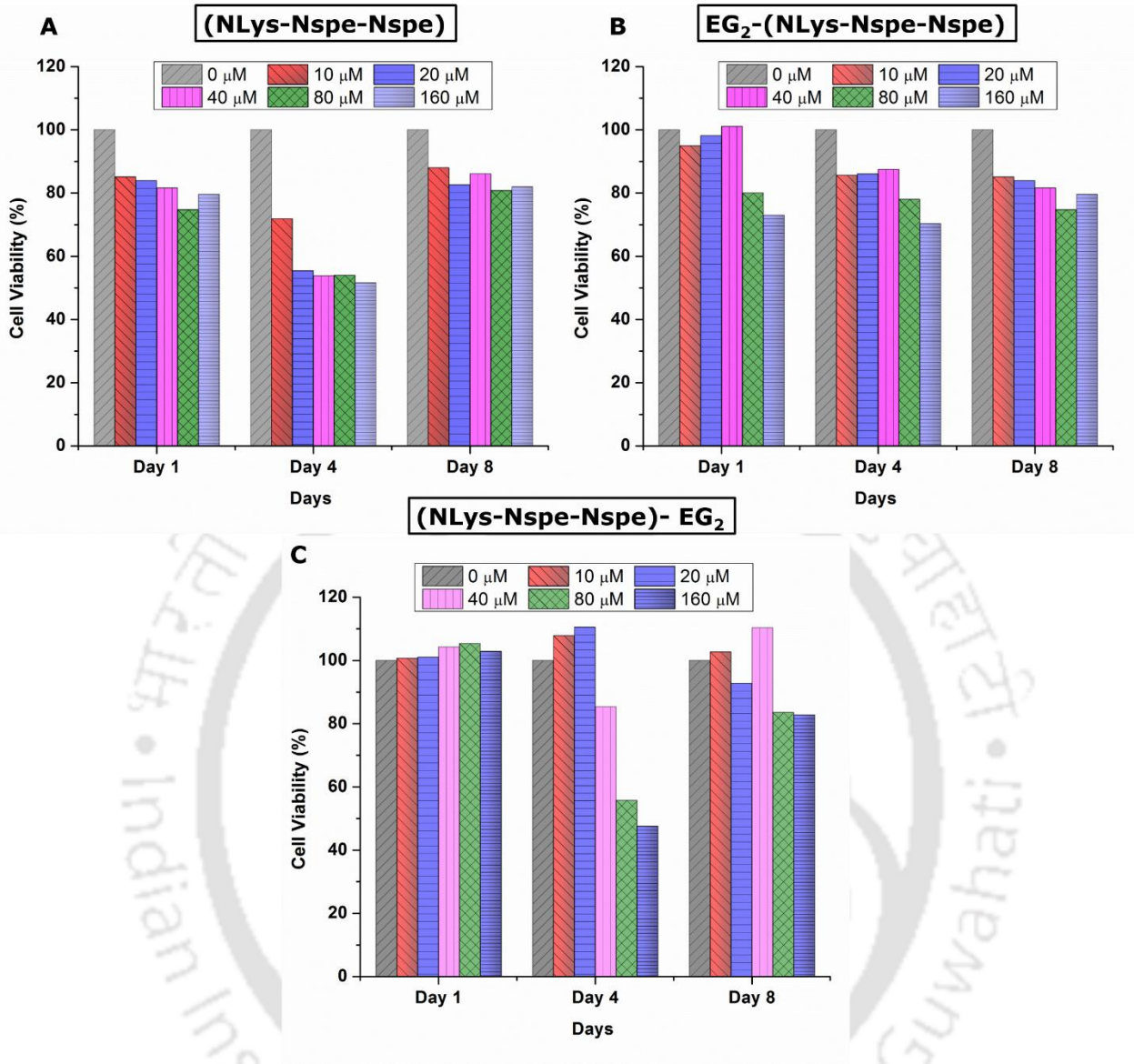

Figure 7.6. Cytocompatibility of the sequences $(NLys\text{-}Nspe\text{-}Nspe)_4$ **(A)**, $(NLys\text{-}Nspe\text{-}Nspe)_4\text{-}EG_2$ **(B)**, and $EG_2\text{-}(NLys\text{-}Nspe\text{-}Nspe)_4$ **(C)**

It was observed that a significant decrease occurred in cell viability under the incubation of C8 modified Peptoids at 1 X MIC concentration after 4 days and at 10 X MIC concentrations after 4 and 8 days. In all the samples, a drop at day 4 and more cell viability at day 8 strongly indicated that the designed sequences are more cytostable than cytotoxic (Figure 7.7).

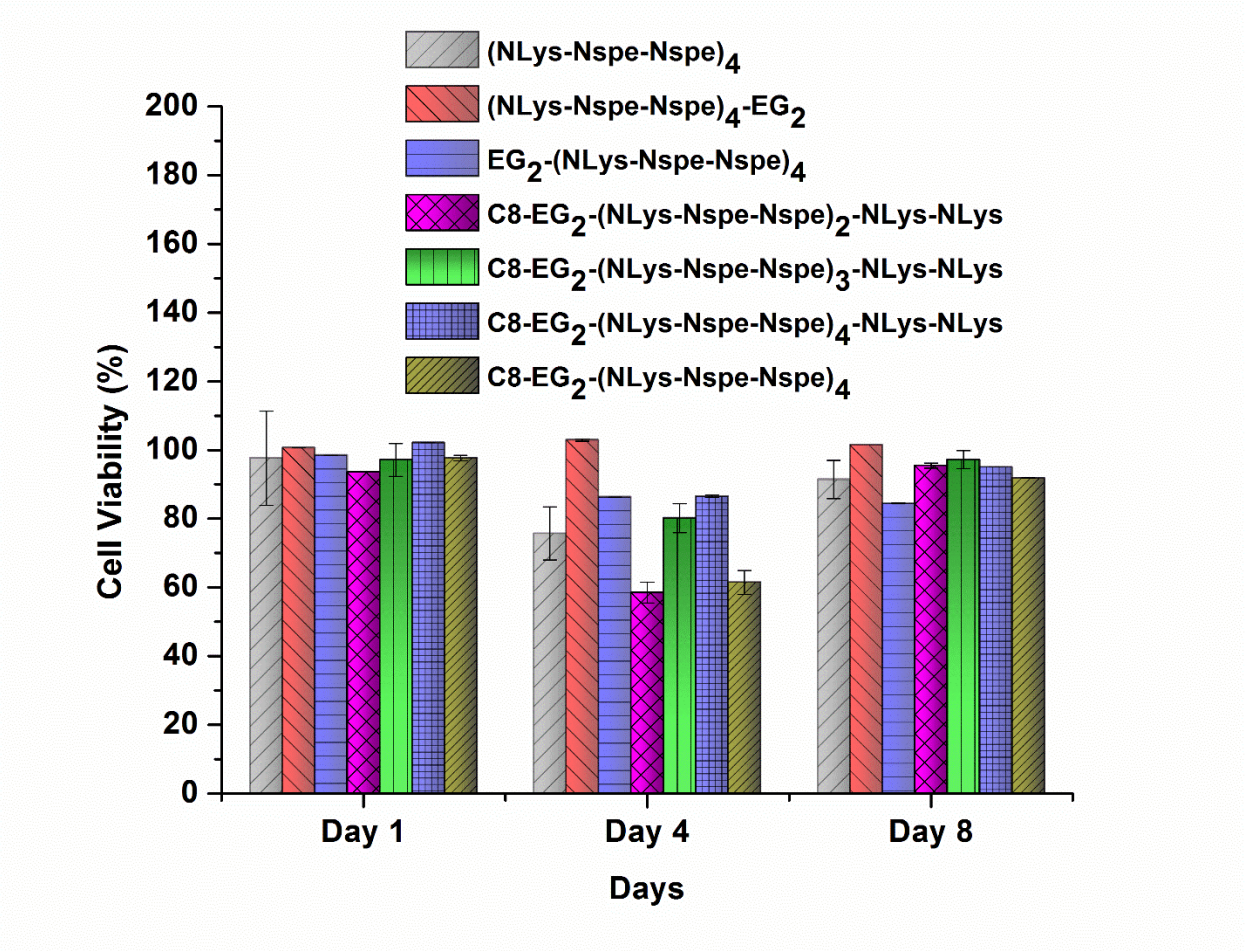

Figure 7.7. Cytotoxicity analysis of the synthesized Peptoids at MIC values

Hence, it can be seen that the synthesized peptoid library with the base sequence $(Nae\text{-}Nspe\text{-}Nspe)_n$ and $(NLys\text{-}Nspe\text{-}Nspe)_n$ were cytostable, and their cytotoxicity can be tuned by altering the structure or adding the functional group at either C or N terminal.

7.6 Conclusion

In this chapter, the antimicrobial Peptoids were synthesized successfully. The 12 mer sequence with Nae did not kill the bacteria effectively; however, the same sequence with NLys was found to be more effective for its antibacterial action. This indicates that the chain length of the functional group also plays a crucial role in its biological responses along with the surface charge. The addition of EG_2 at the free C terminal enhanced the cytocompatibility and reduced the MIC values of 12 mer sequence. However, the addition of aliphatic chains did not alter the bactericidal activity

until C8 and C11, but decreased the bactericidal action at the C15 chain. This indicated the maximum allowed aliphatic chain modification for the peptoid micelles to be effective. Furthermore, the addition of the aliphatic chain indicated the conformation-dependent antibacterial activity as well as the cytocompatibility of the Ampetoids. However, the cytocompatibility of the sequences was decreased with an increase in the chain length. The decreased cytocompatibility at day 4 and a further increase in the cell concentration indicated that the Peptoids are cytostable in nature than cytotoxic. Hence, the designed sequences can be used effectively for a short duration of cell incubation, such as coating over the medical instruments.

Chapter 8

Conclusion and Future work

Calcium hydroxyapatite, the most studied bone-mimetic biomaterial, has shown great potential in bone tissue engineering applications. However, its commercialization and applications are restricted due to lack of self-antibacterial activity, target deficiency, and the generation of other undesired phases such as β-TCP along with the HAp phase. This study aimed to work on the undesirable lags that can help in understanding the microstructure required for the potential biomedical applications of HAp. We planned to improve the crystal lattice of HAp by its integration with self-antibacterial metal ions/metal oxides to generate the antibacterial activity as well as the target efficiency simultaneously, without distorting the HAp phase. For this purpose, various metal ions and their oxides were scrutinized based on their antibacterial activity as well as the mechanism for their possible integration with the HAp lattice.

After a thorough review of the literature, the ZnO NPs were selected to be incorporated with HAp for generating self-antibacterial activity due to their abundance in nature, ease of synthesis, and comprehensive antibacterial mechanisms. Similarly, for incorporating target efficiency, the Fe(III) ions were selected and were expected to incorporate the paramagnetism into the HAp lattice for magnetic target efficiency. Simultaneously, the antimicrobial Peptoids were also studied for their potential antimicrobial applications, and their expected functionalization over ZFHAp coated implants. To reach the goal of generating self-antibacterial HAp, we first synthesized the ZnO NPs via a simple co-precipitation method and evaluated their antibacterial activity. However, the ZnO nanorods were below 100 nm in size and exhibited rod-shaped morphology; their MIC values were higher, *i.e.*, ~340 µg/mL.

Hence, prior to the addition of ZnO into the HAp lattice, the ZnO crystals were modified via doping of trivalent ions. It is well known that the antibacterial activity, as well as the mechanism of ZnO NPs, lies in their size and morphology. To control the size and morphology, various techniques have been designed, which are sophisticated and require more input of raw material and energies. Our idea was to enhance the antibacterial activity by using a simple co-precipitation method. Hence, to govern these two important crystal properties, Al^{3+} and Fe^{3+} were doped into the ZnO lattice separately, and their antibacterial activity, as well as the mechanism, were evaluated. We

observed that the doping of Al^{3+} and Fe^{3+} ions reduced the MIC of ZnO lattice via 10 folds, and the MIC values were found to be 14 µg/mL and 33 µg/mL for AZO and FZO, respectively. The major antibacterial activity via both the designed NPs was found to be due to the release of metal ions, and no ROS production could be obtained. ROS production is not suitable for the cytocompatibility of the NPs for mammalian cells. Hence, obtaining a ROS-independent mechanism added pros to the designed ZnO NPs. However, the MIC values for AZO were lower than that of FZO NPs, yet no rupturing in the bacterial cell wall could be obtained in the presence of AZO, resulting in the complete inactivation of bacteria. Whereas FZO NPs cause complete rupturing into the bacterial cell wall. This was attributed to the kinetics of the release of the toxic Zn^{2+} ions from the AZO and FZO lattice. An exponential release of Zn^{2+} ions from AZO caused the charge imbalance around the bacterial cell wall resulting in the malfunctioning of its permeability. As a result, the ions were internalized and ruptured the genetic material of the bacteria. In the case of FZO, the linear release of the Zn^{2+} ions caused the steady interaction between the bacterial cells and metal ions and caused the rupturing into the bacterial cell wall. FZO samples were paramagnetic in nature; hence, co-doping of Zn and Fe were selected to design the modified HAp lattice. This resulted in the dopant type-based antibacterial action. Further, due to their lower MIC values doping of Zn and Fe was attempted rather than forming a composite of ZnO and HAp, thus providing an opportunity to reduce the generation of multiple phases such as β-TCP.

Following the successful reduction in the MIC of ZnO, the co-integration of Zn and Fe with HAp was tested. The co-integration resulted in a biphasic nanoassembly of Ferric-HAp-Zincite with majorly three phases. $Ca_{9.333}Fe_{1.167}(PO_4)_7$ and zincite phases were present in all the samples and the secondary phases, *e.g.*, $Ca_9Fe(PO_4)_7$ and $Ca_{28.8}Fe_{3.2}(PO_4)_{21}O_{0.5}$ based on the Fe concentration was varied within the samples. A dual morphology (rod-shaped for ferric-HAp and particulate shaped for zincite) with a size less than 100 nm was observed for all the ZFHAp samples. As HAp does not possess antibacterial activity, the major antibacterial activity was related to the co-existing ZnO phase along with the ferric-HAp phase. The MIC values were found to be ~ 66 µg/mL for the sample containing the major zincite phase. ZFHAp-2 samples possessed the least MIC values, as they carried the highest amount of the zincite phase. An obvious increase in MIC values was reported than that of FZO and was found to be highly suitable against both *Gram-positive* and *Gram-negative* bacteria. The linear release of Zn^{2+} ions from the ferric-HAp-zincite nanoassembly

resulted in the rupturing of the bacterial cell wall similar to that of FZO NPs, reflecting its applicability in the treatment of osteomyelitis. The ZFHAp samples possessed paramagnetic behavior suitable for the targeted delivery of the material for biomedical applications. The ZFHAp samples were found to be highly bioactive for bone cells, and 300% more growth in the bone cells than that of control cells (without adding any material) was observed. Moreover, the ALP activity was in co-relation with the Zn ion concentrations, as the sample containing the highest Zn resulted in the highest ALP activity. No significant TNF-α release reflected the high biocompatibility of the ZFHAp samples, signifying its potential for various biomedical applications. Hence, by this work, we were able to remove three of the major lags associated with the HAp, *i.e.*, antibacterial inactivity, target deficiency, and the retaining of the HAp phase at metal ion integrations along with an enhance in its bioactivity.

The designed Ferric-HAp-Zincite nanoassembly was further explored for its potential biomedical applications. A scaffold of Chitosan-CMC and ZFHAp was designed and was evaluated *in-vitro* for their respective biochemical and biological responses. The dual morphology of ZFHAp and intermolecular interactions altered the packing behavior and thus controlled the porosity, swelling behavior as well as the controlled degradation of the scaffolds. The swelling behavior and enzymatic degradation were found to be linearly related to the porosity of the scaffolds. The scaffolds possessed excellent antibacterial activity with around 100 % cytocompatibility, indicating that the designed scaffolds were suitable for bone tissue engineering applications. Hence, the designed ZFHAp samples were prospective for various biomedical applications, *e.g.*, bone tissue engineering, drug delivery, and enhancing the surface responses of metal substrates.

The ZFHAp samples can primarily be used for bone tissue engineering applications. These applications can be performed by using ZFHAp samples as scaffolds, drug delivery vehicles, and as a coating material over the metallic implants, as shown in Scheme 8.1. Hence, ZFHAp samples were utilized in the preparation of scaffolds for bone tissue engineering applications. The antibacterial efficacy of the ZFHAp for surface coating applications can be further enhanced by functionalizing them with organic moieties, including amines, peptides, peptoids, and polyphenols. Hence, the antibacterial activity of peptoids was examined. For this purpose, the antimicrobial Peptoids -based micelles were synthesized, and their structure was examined using RP-HPLC and LCMS. To form the micelles of the Peptoids, coupling with PEG and eight aliphatic carbon chains (C8) were incorporated into them. The C8 chain added sequences showed fewer

MIC values against both *Gram-positive* and *Gram-negative* bacteria, with an excellent cytocompatibility of the fibroblast cells. Peptoid $(NLys\text{-}Nspe\text{-}Nspe)_4$ can be effective to coat over Ferric-HAp-Zincite, as they carry both positively and negatively charged moieties on their surfaces. This interaction can lead to an organic-inorganic hybrid with long-term antibacterial applications, from Ampetoids before degradation and from Ferric-HAp-Zincite after degradation of Ampetoids.

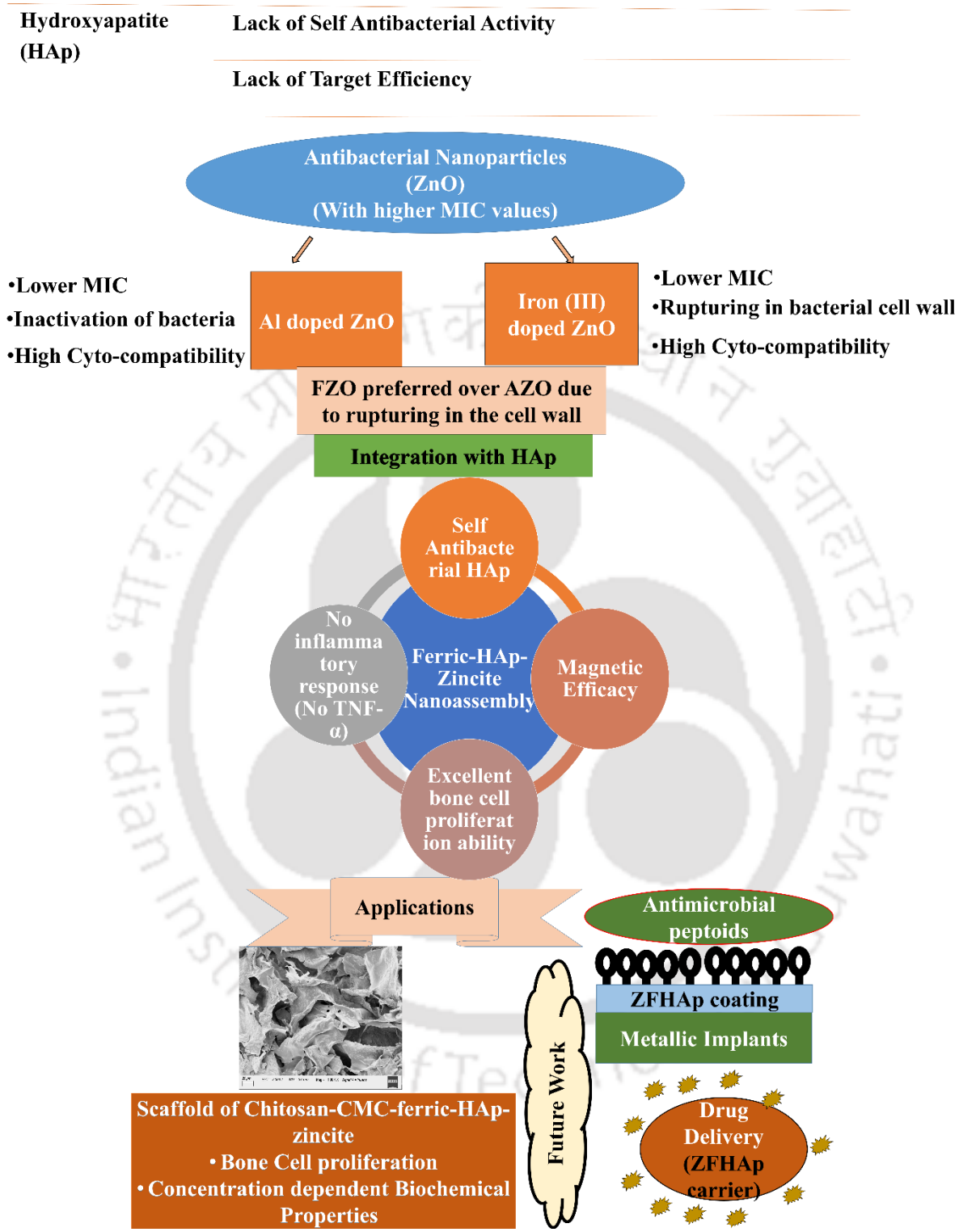

Scheme 8.1: Schematic of the Thesis

8.2 Suggestions for future work

The designed material possessed the desired antibacterial activity and target efficiency without any ROS production and has also shown its potential for various biomedical applications. However, further clinical trials can be performed to evaluate the biological responses under diverse conditions. A few of the suggestions are listed below and are given in scheme 8.1.

8.2.1 Co-relation of impurity level and defect densities with antibacterial activity

We examined the antibacterial activity based on its physical properties, such as particle size, surface area, surface charge, and surface area. Furthermore, the antibacterial activity can be co-related with its antibacterial activity. For example, the impurity level and the defect densities directly affect the antibacterial activity of ZnO NPs via the change in its band-gap. This change in band-gap can control the production of ROS, a major antibacterial mechanism of ZnO. Similarly, with an increase in impurity level, the release of metal ions might be boosted, which should enhance the antibacterial activity of ZnO.

8.2.2 Stem cell differentiation studies

Additionally, the excellent responses of the ferric-HAp-zincite nanoassembly for ALP activity intimate its potential application in stem cell differentiation. Hence, the studies for the differentiation of the Mesenchyme Stem Cells (MSCs) into the bone cells in the presence of ferric-HAp-zincite nanoassembly can be further studied. Furthermore, the molecular biological responses of the ferric-HAp-zincite nanoassembly can also be evaluated under further clinical tests.

8.2.3 Drug delivery, surface coating, and *In-vivo* studies

We executed the *in-vitro* performance of the ferric-HAp-zincite nanoassembly and obtained the required antibacterial activity, target efficacy, enhanced cytocompatibility, bioactivity, and ALP activity. Additionally, various biomedical applications of the designed nano-assembly were scrutinized, and the designed ZFHAp material exhibited great potential for bone tissue engineering applications. Hence, the designed material can also be used as a drug delivery vehicle and a coating material over metallic implants for bone treatment. Correspondingly, the *in-vivo* behavior of the designed material can be evaluated for the given applications. The *in-vivo* tests for all the evaluated

experiments will further aid in the commercial applications of the designed ferric-HAp-zincite nanoassembly.

8.2.4 Integration of Ampetoids and ferric-HAp-zincite nanoassembly

Synthesized antimicrobial Peptoids reflected excellent antibacterial activity and cytocompatibility. The great tunability of the Ampetoids for their antibacterial and cytocompatibility can be explored further for their biological responses. The interaction of metal ions/oxides did not alter the basic HAp phase of the calcium phosphate in the designed ferric-HAp-zincite nanoassembly and possessed the required antibacterial and magnetic target efficacy. A hybrid HAp-Ampetoids organic-inorganic nanosystem can be scrutinized for its latent application as an antimicrobial bone tissue-engineering candidate. Further, ZFHAp coated metallic implants can be functionalized with the synthesized Ampetoids for long-term and enhanced antibacterial activity.

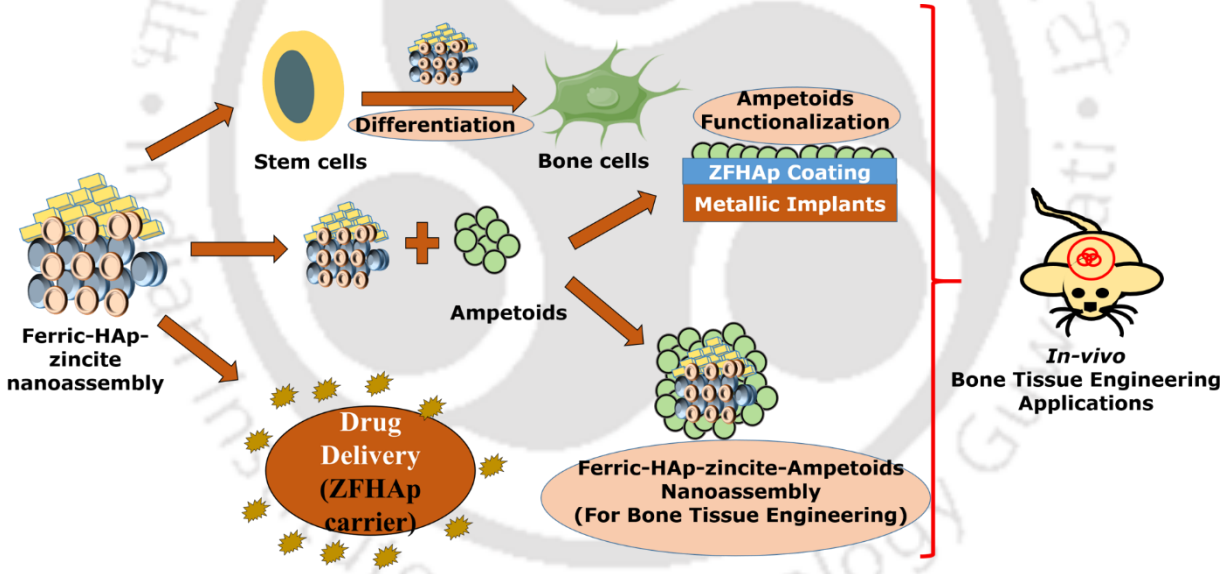

Scheme 8.2. Suggestions for future work for Ferric-HAp-zincite nanoassembly

Appendices

Appendix-3A

Design and characterization of Al-doped ZnO (AZO) nanoassembly

To further confirm the rupturing into the bacterial cell wall, the *E.coli* bacteria were first grown in LB media for 6 h, and the OD_{600} value was set to 0.025. The E.coli bacteria was then sub-cultured in the presence and absence of AZO_{15} NPs overnight. After incubations, the cells were pallet down and were washed with PBS five times. The cells were then fixed using 10% glutaraldehyde and were washed with series of ethyl alcohol concentrations. The cells were finally re-suspended in OPBS and were drop cast over the carbon tape before analysis. As given in Figure 1A-1, the untreated bacteria (control cells) had a distinct morphology, and the treated bacterial cells were found to be shrunk. No rupturing into the bacterial cell wall could be observed; rather, a shrinkage was obtained, affirming that the cells were inactivated by the internalization of the released Zn^{2+} ions from the AZO_{15} nanorods without rupturing the cell wall.

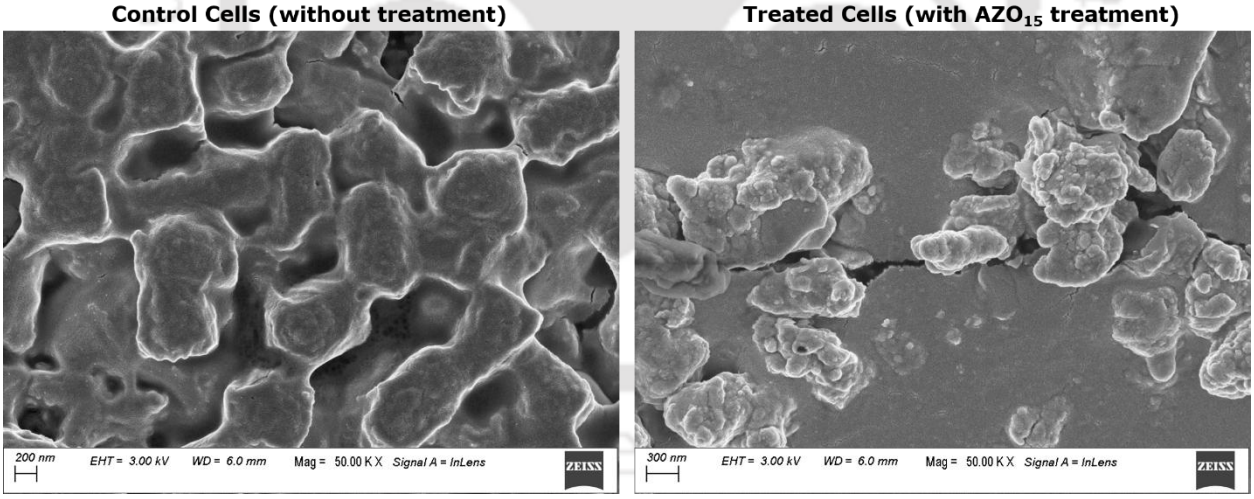

Figure 3A-1. *E. coli* bacteria; before and after treatment with AZO_{15} nanorods

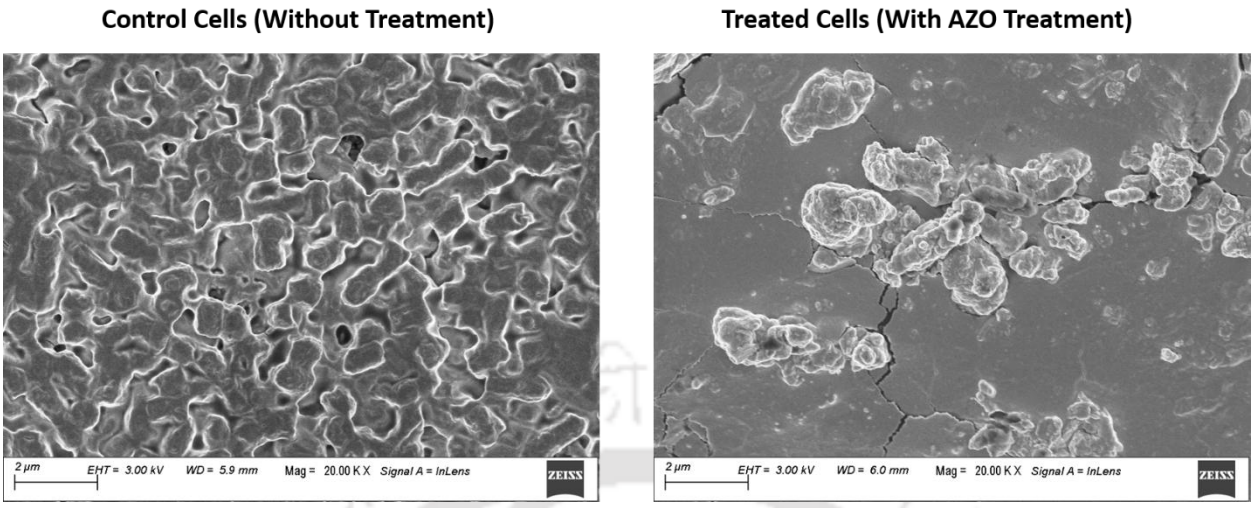

Figure 3A-2. *E. coli* bacteria; before and after treatment with AZO_{15} nanorods at low magnification

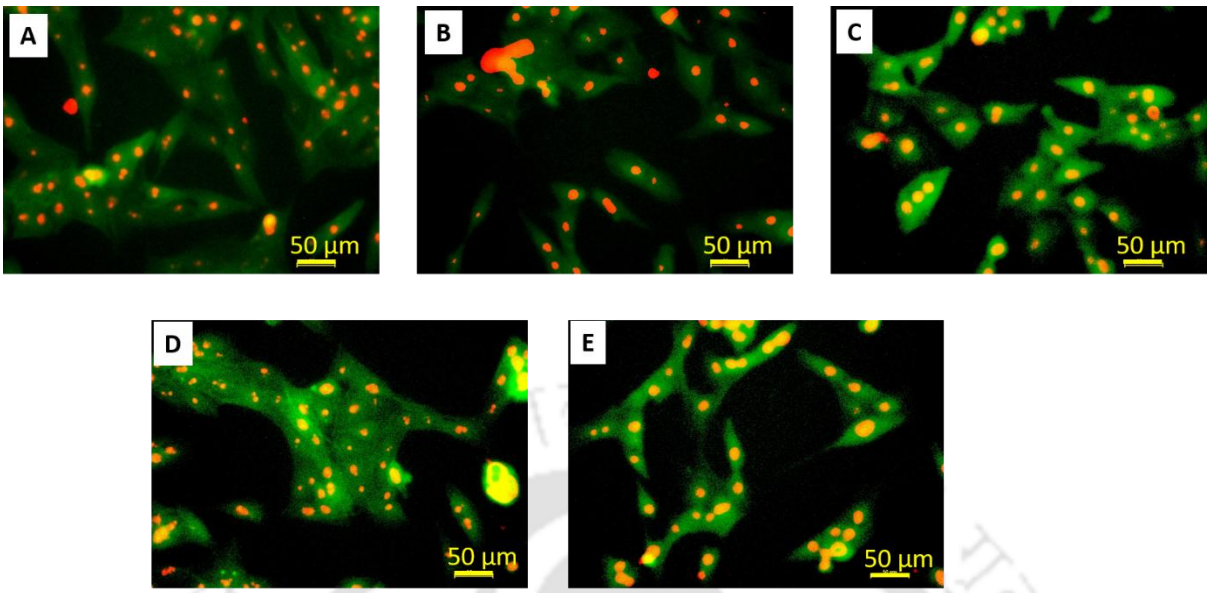

Figure 3A-3. MG63 cells spreading analysis in presence of Penstrap **A)**, and without Penstrap using AZO_5 **B)** , AZO_{10} **C)**, AZO_{15} **D)** and AZO_{20} **E)** samples as nanoantibiotic

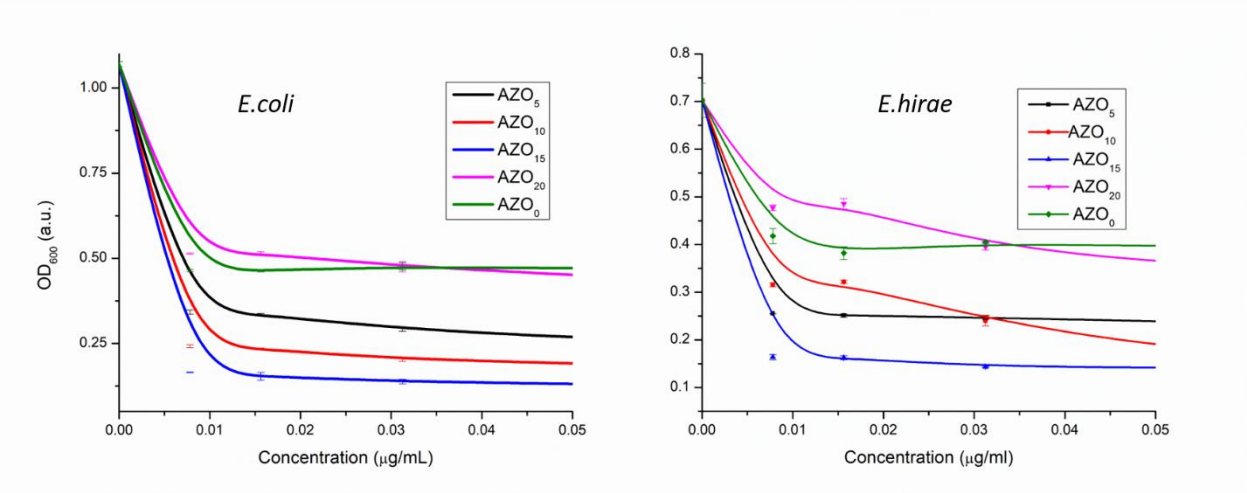

Figure 3A-4. Antibacterial activity of AZO_0, AZO_5, AZO_{10}, AZO_{15} and AZO_{20} samples as against E. coli and E. hirae (At high resolution)

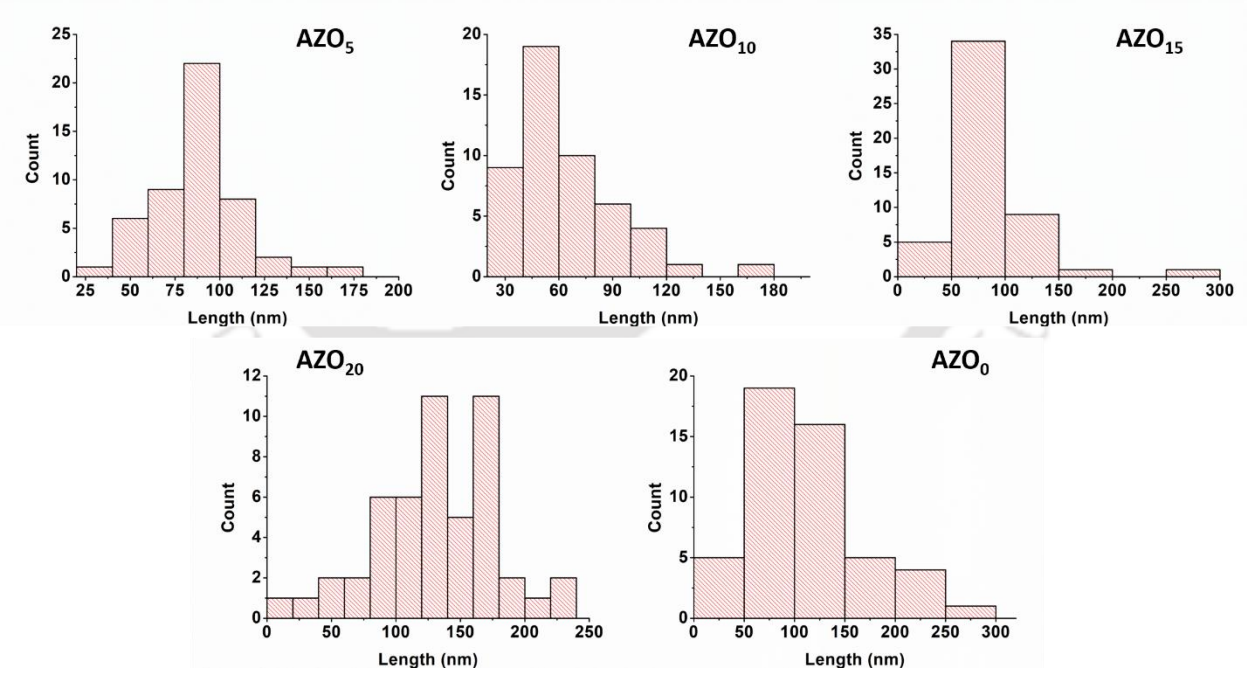

Figure 3A-5. Particle size distribution of AZO_0, AZO_5, AZO_{10}, AZO_{15} and AZO_{20} samples

Appendix-4A

Design and characterization of Fe(III) doped ZnO nanoparticles (NPs) and evaluation of its antibacterial mechanism

For further confirmation of the antibacterial activity, the E.coli cells stained with CFDA, DCFH-DA, and PI were analyzed using a fluorescence microscope. Figure 4A-1 revealed that the CFDA and DCFH-DA did not produce any fluorescence, and only PI staining could be observed. This indicates that the cell wall of the bacteria was ruptured, and no ROS was produced. In a few of the samples, the PI staining was minimal compared to the nucleus staining, indicating the damage in the genetic material of the bacteria. Similarly, to confirm the rupturing of the cell wall, we analyzed the bacterial cells treated with FZO samples using FESEM.

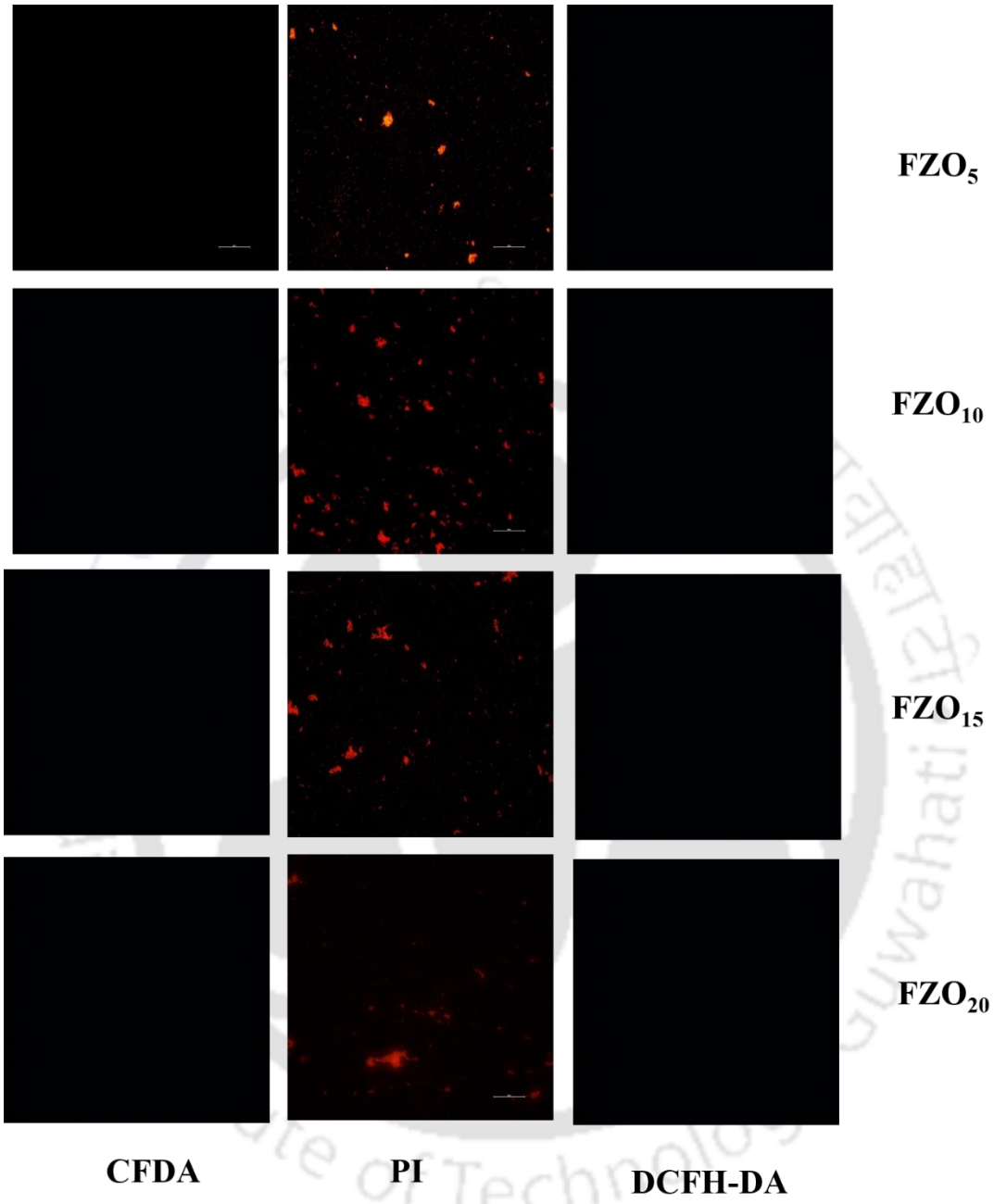

Figure 4A-1. Antibacterial mechanism identification using Fluorescence Microscopy; No green stain in CFDA indicating no live cells, Red stain in PI indicating ruptured cell wall, and No green stain in DCFH-DA, indicting no ROS production

To further confirm the release of the metal ions from the FZO lattice, The release of the metal ions was investigated using AAS. For this purpose, 500 µg/mL of FZO samples were taken in 0.9 saline solution, PBS, and in LB media with cells. 1 mL of this solution was replaced with 1 mL of the fresh solution at every 6 hours. After 6 hours, the bacterial samples were first centrifuged to collect the supernatant, and the pelleted bacteria were further ruptured and diluted in MilliQ water for calculating the intracellular metal ion concentration. The readings were calculated at every 6 hours. All the samples show a linear release of both metal ions, *i.e.*, Zn and Fe. However, FZO_{15} samples indicated a quicker release of Zn and Fe as compared to other samples, leading to its lower MIC values.

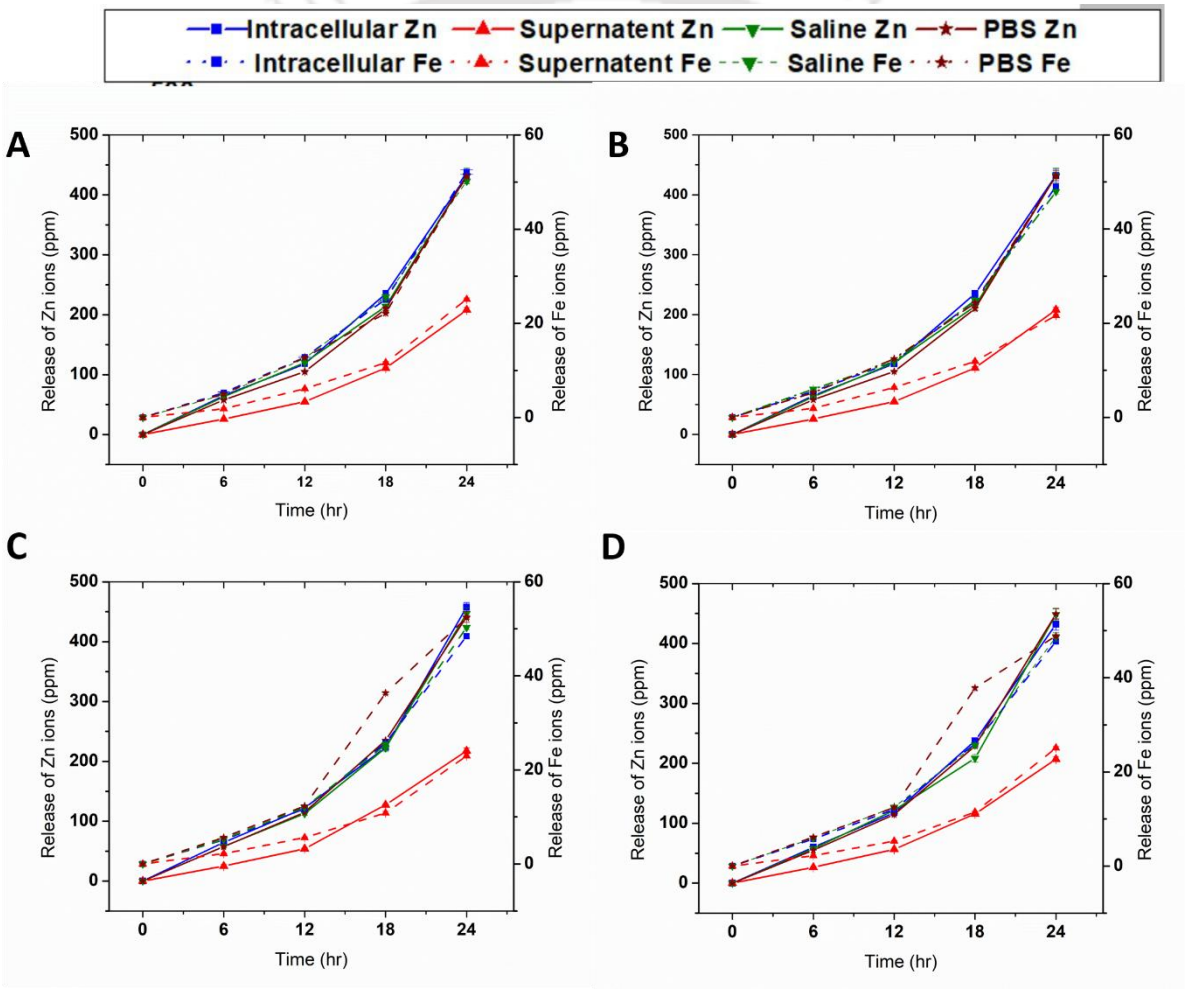

Figure 4A-2. Release of Zn and Fe from FZO samples under various solutions, A) FZO_5, B) FZO_{10}, C) FZO_{15}, D) FZO_{20}

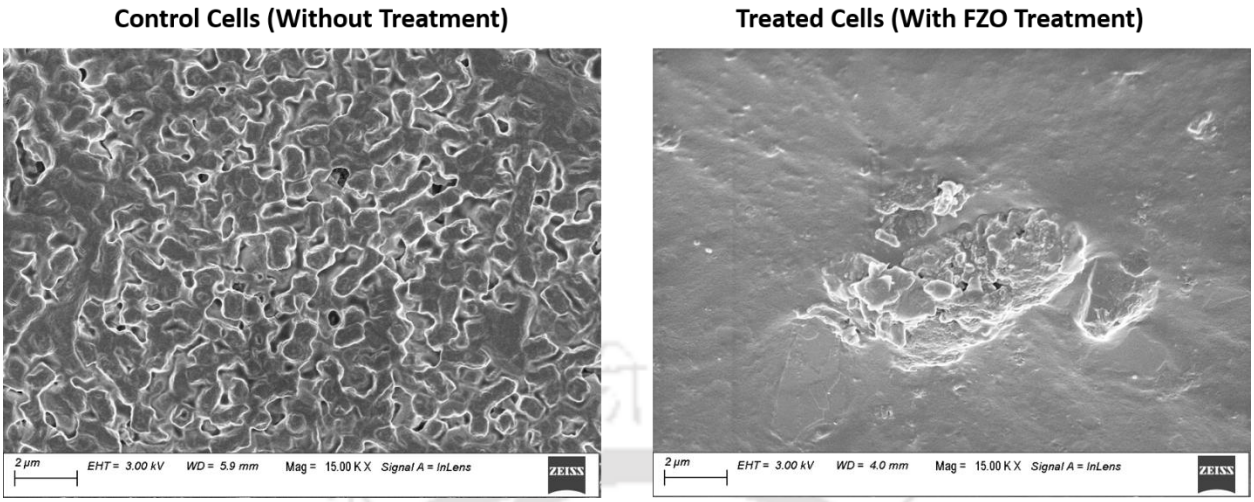

Figure 4A-3. *E. coli* bacteria; before and after treatment with FZO_{15} samples at low magnification

Appendix-5A

Design and characterization of Fe(III) doped ZnO nanoparticles (NPs) and evaluation of its antibacterial mechanism

For further confirmation of the antibacterial mechanism, the cells E.coli cells were treated with ZFHAp-2 samples as given in Appendix 1A. the FESEM image at low resolution is given in Figure 5A-1.

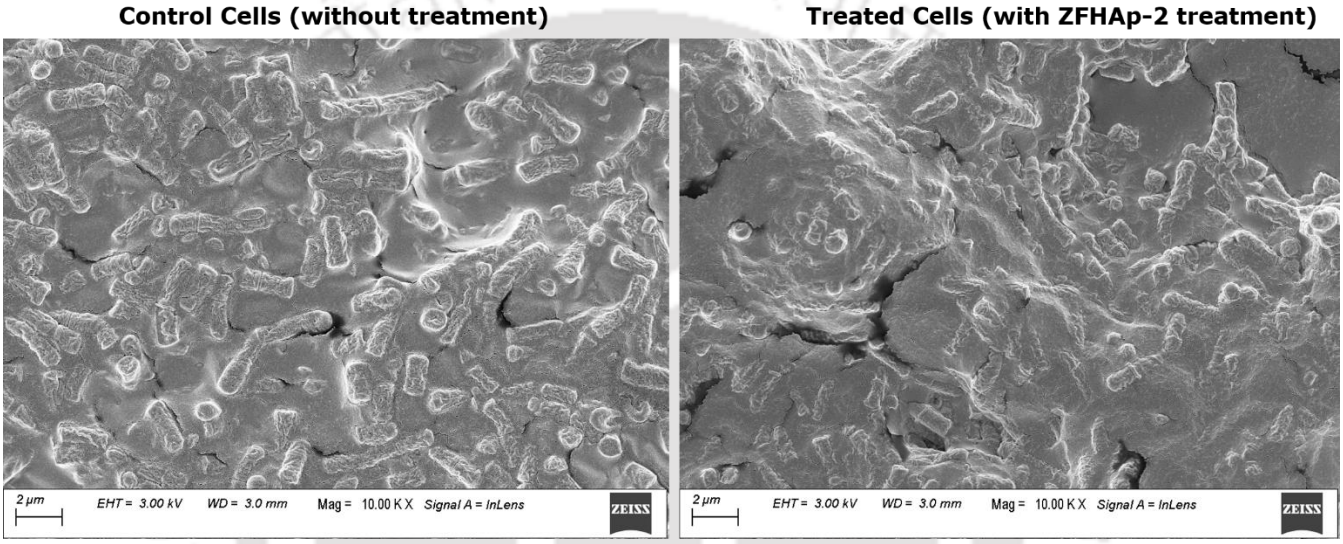

Figure 5A-1. *E. coli* bacteria; before and after treatment with ZFHAp-2 samples at low magnification

References

1. Alioui, H., O. Bouras, and J.-C. Bollinger, *Toward an efficient antibacterial agent: Zn-and Mg-doped hydroxyapatite nanopowders.* Journal of Environmental Science and Health, Part A, 2019. **54**(4): p. 315-327.
2. Mondal, S., et al., *Bioactive, luminescent erbium-doped hydroxyapatite nanocrystals for biomedical applications.* Ceramics International, 2020. **46**(10, Part B): p. 16020-16031.
3. Ryu, T.-K., et al., *Bone-targeted delivery of nanodiamond-based drug carriers conjugated with alendronate for potential osteoporosis treatment.* Journal of Controlled Release, 2016. **232**: p. 152-160.
4. Li, Z., et al., *Effects of fluoridation of porcine hydroxyapatite on osteoblastic activity of human MG63 cells.* Science and Technology of Advanced Materials, 2016. 16: p. 035006
5. Saxena, V., I. Shukla, and L.M. Pandey, *Chapter 8 - Hydroxyapatite: an inorganic ceramic for biomedical applications*, in *Materials for Biomedical Engineering*, A.-M. Holban and A.M. Grumezescu, Editors. 2019, Elsevier. p. 205-249.
6. Maitra, A., *Calcium phosphate nanoparticles: second-generation nonviral vectors in gene therapy.* Expert review of molecular diagnostics, 2005. **5**(6): p. 893-905.
7. Abbasi Aval, N., et al., *Doxorubicin loaded large-pore mesoporous hydroxyapatite coated superparamagnetic Fe3O4 nanoparticles for cancer treatment.* International Journal of Pharmaceutics, 2016. **509**(1): p. 159-167.
8. Ajduković, Z.R., et al., *In Vitro Evaluation of Nanoscale Hydroxyapatite-Based Bone Reconstructive Materials with Antimicrobial Properties.* Journal of Nanoscience and Nanotechnology, 2016. **16**(2): p. 1420-1428.
9. An, L., et al., *Controlled additive-free hydrothermal synthesis and characterization of uniform hydroxyapatite nanobelts.* Ceramics International, 2016. **42**(2): p. 3104-3112.
10. Balakrishnan, S., et al., *Influence of iron doping towards the physicochemical and biological characteristics of hydroxyapatite.* Ceramics International, 2020. 47(4): p. 5061-5070
11. Bhattacharjee, A., et al., *Effect of Zn and Co doping on antibacterial efficacy and cytocompatibility of spark plasma sintered hydroxyapatite.* Journal of the American Ceramic Society, 2020. **103**(8): p. 4090-4100.
12. Zhou, J., et al., *Nano-hydroxyapatite/ZnO coating prepared on a biodegradable Mg–Zn–Ca bulk metallic glass by one-step hydrothermal method in acid situation.* Ceramics International, 2020. **46**(5): p. 6958-6964.
13. Kaygili, O., et al., *Dielectric properties of Fe doped hydroxyapatite prepared by sol–gel method.* Ceramics International, 2014. **40**(7): p. 9395-9402.
14. Kotak, D.J. and P.V. Devarajan, *Bone targeted delivery of salmon calcitonin hydroxyapatite nanoparticles for sublingual osteoporosis therapy (SLOT).* Nanomedicine: Nanotechnology, Biology and Medicine, 2020. **24**: p. 102153.
15. Bhowmick, A., et al., *Organically modified clay supported chitosan/hydroxyapatite-zinc oxide nanocomposites with enhanced mechanical and biological properties for the application in bone tissue engineering.* International journal of biological macromolecules, 2018. **106**: p. 11-19.
16. Ma, N., et al., *Ag–TiO2/HAP/Al2O3 bioceramic composite membrane: Fabrication, characterization and bactericidal activity.* Journal of Membrane Science, 2009. **336**(1-2): p. 109-117.

17. Yang, Y., et al., *Litchi-like Fe 3 O 4@ Fe-MOF capped with HAp gatekeepers for pH-triggered drug release and anticancer effect.* Journal of Materials Chemistry B, 2017. **5**(43): p. 8600-8606.
18. Baskaran, P., A. Udduttula, and V. Uthirapathy, *Development and characterisation of novel Ce-doped hydroxyapatite–Fe3O4 nanocomposites and their in vitro biological evaluations for biomedical applications.* IET Nanobiotechnology, 2017. **12**(2): p. 138-146.
19. Saxena, V., A. Hasan, and L.M. Pandey, *Effect of Zn/ZnO integration with hydroxyapatite: a review.* Materials Technology, 2018. **33**(2): p. 79-92.
20. Šupová, M., *Substituted hydroxyapatites for biomedical applications: A review.* Ceramics International, 2015. **41**(8): p. 9203-9231.
21. Miyaji, F., Y. Kono, and Y. Suyama, *Formation and structure of zinc-substituted calcium hydroxyapatite.* Materials Research Bulletin, 2005. **40**(2): p. 209-220.
22. Hasna, K., et al., *Synthesis of chemically pure, luminescent Eu 3+ doped HAp nanoparticles: a promising fluorescent probe for in vivo imaging applications.* Physical Chemistry Chemical Physics, 2013. **15**(21): p. 8106-8111.
23. Samani, S., et al., *In vitro antibacterial evaluation of sol–gel-derived Zn-, Ag-, and (Zn+ Ag)-doped hydroxyapatite coatings against methicillin-resistant Staphylococcus aureus.* Journal of Biomedical Materials Research Part A, 2013. **101**(1): p. 222-230.
24. Srilakshmi, C. and R. Saraf, *Ag-doped hydroxyapatite as efficient adsorbent for removal of Congo red dye from aqueous solution: Synthesis, kinetic and equilibrium adsorption isotherm analysis.* Microporous and mesoporous materials, 2016. **219**: p. 134-144.
25. Xiu, Z.-m., et al., *Negligible particle-specific antibacterial activity of silver nanoparticles.* Nano letters, 2012. **12**(8): p. 4271-4275.
26. Awwad, A.M., et al., *Green synthesis, characterization of silver sulfide nanoparticles and antibacterial activity evaluation.* Chem. Int, 2020. **6**(1): p. 42-48.
27. Singh, G., et al., *Evaluation of antibacterial activity of ZnO nanoparticles coated sonochemically onto textile fabrics.* Journal of microbiology, biotechnology and food sciences, 2020. **9**(4): p. 106-120.
28. Menazea, A., et al., *Physical characterization and antibacterial activity of PVA/Chitosan matrix doped by selenium nanoparticles prepared via one-pot laser ablation route.* Journal of Materials Research and Technology, 2020. **9**(5): p. 9598-9606.
29. Ghosh, C., et al., *Small molecular antibacterial peptoid mimics: the simpler the better!* Journal of Medicinal Chemistry, 2014. **57**(4): p. 1428-1436.
30. Moghanian, A., et al., *Novel antibacterial Cu/Mg-substituted 58S-bioglass: Synthesis, characterization and investigation of in vitro bioactivity.* International Journal of Applied Glass Science, 2020. **11**(4): p. 685-698.
31. Kadu, K., et al., *Role of surface charges on interaction of rod-shaped magnetic hydroxyapatite nanoparticles with protein.* Colloids and Surfaces B: Biointerfaces, 2019. **177**: p. 362-369.
32. Ramos-Guivar, J.A., M.A. Morales, and F.J. Litterst, *γ-Fe2O3 nanoparticles embedded in nanohydroxyapatite matrix for magnetic hyperthermia and in vitro osteoblast cell studies.* Ceramics International, 2020. 46(8): p. 10658-10666.
33. Bhushan, M., et al., *Antibacterial applications of α-Fe 2 O 3/Co 3 O 4 nanocomposites and study of their structural, optical, magnetic and cytotoxic characteristics.* Applied Nanoscience, 2018. **8**(1-2): p. 137-153.

34. Negut, I., et al., *MAPLE deposition of Nigella sativa functionalized Fe3O4 nanoparticles for antimicrobial coatings.* Applied Surface Science, 2018. **455**: p. 513-521.
35. Raland, R., et al., *Heating efficiency and correlation between the structural and magnetic properties of oleic acid coated MnFe2O4 nanoparticles for magnetic hyperthermia application.* Journal of Physics D: Applied Physics, 2017. **50**(32): p. 325004.
36. Raland, R. and J. Borah, *Efficacy of heat generation in CTAB coated Mn doped ZnFe2O4 nanoparticles for magnetic hyperthermia.* Journal of Physics D: Applied Physics, 2016. **50**(3): p. 035001.
37. Ansar, E.B., et al., *Synthesis and Characterization of Iron Oxide Embedded Hydroxyapatite Bioceramics.* Journal of the American Ceramic Society, 2012. **95**(9): p. 2695-2699.
38. Suetsugu, Y. and T. Tateishi, *Implants and biomaterials (hydroxyapatite).* National Institute of Material Science, Ibaraki, Japan, 2011. 6: p.1-10
39. Li, B., et al., *Impact of pore structure on hydroxyapatite supported nickel catalysts (Ni/HAP) for dry reforming of methane.* Fuel Processing Technology, 2020. **202**: p. 106359.
40. Food, N. *India May Have 60 Million Osteoarthritis Cases by 2025*. 2017 July, 13 2017 [cited 2020 22]; Available from: https://food.ndtv.com/health/india-may-have-60-million-osteoarthritis-cases-by-2025-1231464.
41. Januariyasa, I.K., I.D. Ana, and Y. Yusuf, *Nanofibrous poly (vinyl alcohol)/chitosan contained carbonated hydroxyapatite nanoparticles scaffold for bone tissue engineering.* Materials Science and Engineering: C, 2020. **107**: p. 110347.
42. Chuan, D., et al., *Stereocomplex poly (lactic acid)-based composite nanofiber membranes with highly dispersed hydroxyapatite for potential bone tissue engineering.* Composites Science and Technology, 2020: p. 108107.
43. Prasadh, S., et al. *Bioresorbable Nano-Hydroxyapatite Reinforced Magnesium Alloplastic Bone Substitute for Biomedical Applications: A Study*. in *Nanocomposites VI: Nanoscience and Nanotechnology in Advanced Composites*. Cham: Springer International Publishing, 2019. pp. 71-82
44. Soriano-Souza, C., et al., *Doxycycline containing hydroxyapatite ceramic microspheres as a bone-targeting drug delivery system.* Journal of Biomedical Materials Research Part B: Applied Biomaterials, 2020. **108**(4): p. 1351-1362.
45. Huang, H., et al., *Preparation and characterization of abalone shells derived biological mesoporous hydroxyapatite microspheres for drug delivery.* Materials Science and Engineering: C, 2020: p. 110969.
46. Chen, R., et al., *Mesoporous hollow hydroxyapatite capped with smart polymer for multi-stimuli remotely controlled drug delivery.* Microporous and Mesoporous Materials, 2020. **306**: p. 110447.
47. Segura-Pérez, V., et al., *Hydrotalcite/hydroxyapatite composites with high bacterial activity against clinical bacteria. A new alternative to prevent osteomyelitis diseases.* Microporous and Mesoporous Materials, 2020. **298**: p. 110069.
48. Anugraha, A., et al., *End-capping of amputation stumps with a local antibiotic containing hydroxyapatite bio-composite-A report of 13 cases with chronic lower limb osteomyelitis.* Journal of Orthopaedics, 2020. **17**: p. 124-126.

49. Paterson, T.E., et al., *Electrospun Scaffolds Containing Silver-Doped Hydroxyapatite with Antimicrobial Properties for Applications in Orthopedic and Dental Bone Surgery.* Journal of Functional Biomaterials, 2020. **11**(3): p. 58.
50. Casarrubios, L., et al., *Silicon substituted hydroxyapatite/VEGF scaffolds stimulate bone regeneration in osteoporotic sheep.* Acta Biomaterialia, 2020. **101**: p. 544-553.
51. Zhao, R., et al., *A bioceramic scaffold composed of strontium-doped three-dimensional hydroxyapatite whiskers for enhanced bone regeneration in osteoporotic defects.* Theranostics, 2020. **10**(4): p. 1572.
52. Redey, S., et al., *Osteoclast adhesion and activity on synthetic hydroxyapatite, carbonated hydroxyapatite, and natural calcium carbonate: relationship to surface energies.* Journal of biomedical materials research, 1999. **45**(2): p. 140-147.
53. Kay, M.I., R. Young, and A. Posner, *Crystal structure of hydroxyapatite.* 1964. 204(4963): p. 1050-1052
54. Elliott, J.C., P. Mackie, and R. Young, *Monoclinic hydroxyapatite.* Science, 1973. **180**(4090): p. 1055-1057.
55. Ma, G. and X.Y. Liu, *Hydroxyapatite: hexagonal or monoclinic?* Crystal Growth and Design, 2009. **9**(7): p. 2991-2994.
56. Leventouri, T., *Synthetic and biological hydroxyapatites: crystal structure questions.* Biomaterials, 2006. **27**(18): p. 3339-3342.
57. Xue, B., et al., *Monoclinic Hydroxyapatite Nanoplates Hybrid Composite with Improved Compressive Strength, and Porosity for Bone Defect Repair: Biomimetic Synthesis and Characterization.* Journal of Nanoscience and Nanotechnology, 2016. **16**(3): p. 2254-2263.
58. Lin, K., et al., *Fabrication and Characterization of Hydroxyapatite/Wollastonite Composite Bioceramics with Controllable Properties for Hard Tissue Repair.* Journal of the American Ceramic Society, 2011. **94**(1): p. 99-105.
59. Mardziah, C., et al., *Effect of zinc ions on the structural characteristics of hydroxyapatite bioceramics.* Ceramics International, 2020. 46(9): 13945-13952.
60. Kamonwannasit, S., et al., *Synthesis of copper-silver doped hydroxyapatite via ultrasonic coupled sol-gel techniques: structural and antibacterial studies.* Journal of Sol-Gel Science and Technology, 2020: p. 1-12.
61. Van, H.N., et al., *A novel upconversion emission material based on Er3+-Yb3+-Mo6+ tridoped Hydroxyapatite/Tricalcium phosphate (HA/β-TCP).* Journal of Alloys and Compounds, 2020. **827**: p. 154288.
62. Sathiyavimal, S., et al., *Facile synthesis and characterization of hydroxyapatite from fish bones: Photocatalytic degradation of industrial dyes (crystal violet and Congo red).* Progress in Organic Coatings, 2020. **148**: p. 105890.
63. Behera, R.R., et al., *Mechano-tribological properties and in vitro bioactivity of biphasic calcium phosphate coating on Ti-6Al-4V.* Journal of the Mechanical Behavior of Biomedical Materials, 2018. **86**: p. 143-157.
64. Sricharoen, P., et al., *Ultrasonic-assisted recycling of Nile tilapia fish scale biowaste into low-cost nano-hydroxyapatite: Ultrasonic-assisted adsorption for Hg2+ removal from aqueous solution followed by "turn-off" fluorescent sensor based on Hg2+-graphene quantum dots.* Ultrasonics Sonochemistry, 2020. **63**: p. 104966.
65. Athinarayanan, J., V.S. Periasamy, and A.A. Alshatwi, *Simultaneous fabrication of carbon nanodots and hydroxyapatite nanoparticles from fish scale for biomedical applications.* Materials Science and Engineering: C, 2020. **117**: p. 111313.

66. Mohd Pu'ad, N.A.S., et al., *Nano-size hydroxyapatite extracted from tilapia scale using alkaline heat treatment method.* Materials Today: Proceedings, 2020. **29**: p. 218-222.
67. Saha, S.K., et al. *Effects of synthesis temperature on the chemically precipitated nano-hydroxyapatite*. in *AIP Conference Proceedings*. AIP Publishing LLC.2019. 2121(1): p. 150002
68. El-Meliegy, E., et al., *Improvement of physico-chemical properties of dextran-chitosan composite scaffolds by addition of nano-hydroxyapatite.* Scientific Reports, 2018. **8**(1): p. 1-10.
69. Mondal, S., et al., *Nano-hydroxyapatite bioactive glass composite scaffold with enhanced mechanical and biological performance for tissue engineering application.* Ceramics International, 2018. **44**(13): p. 15735-15746.
70. Lakshmanaperumal, S. and C. Mahendran, *Structural, dielectric, cytocompatibility, and in vitro bioactivity studies of yttrium and strontium co-substituted nano-hydroxyapatite by sol–gel method.* Journal of Sol-Gel Science and Technology, 2018. **88**(2): p. 296-308.
71. Türk, S., et al., *Effect of solution and calcination time on sol-gel synthesis of hydroxyapatite.* Journal of Bionic Engineering, 2019. **16**(2): p. 311-318.
72. Goudarzi, Z., N. Parvin, and F. Sharifianjazi, *Formation of hydroxyapatite on surface of SiO2–P2O5–CaO–SrO–ZnO bioactive glass synthesized through sol-gel route.* Ceramics International, 2019. **45**(15): p. 19323-19330.
73. Lett, J.A., et al., *Tailoring the morphological features of sol–gel synthesized mesoporous hydroxyapatite using fatty acids as an organic modifier.* RSC advances, 2019. **9**(11): p. 6228-6240.
74. Yigit, O., et al., *One-step synthesis of nano-hydroxyapatite/graphene nanosheet hybrid coatings on Ti6Al4V alloys by hydrothermal method and their in-vitro corrosion responses.* Surface and Coatings Technology, 2020: p. 125858.
75. Chen, J., et al., *Regulatory synthesis and characterization of hydroxyapatite nanocrystals by a microwave-assisted hydrothermal method.* Ceramics International, 2020. **46**(2): p. 2185-2193.
76. Nosrati, H., et al., *Effects of hydrothermal pressure on in situ synthesis of 3D graphene-hydroxyapatite nano structured powders.* Ceramics International, 2019. **45**(2): p. 1761-1769.
77. Nosrati, H., et al., *In situ synthesis of three dimensional graphene-hydroxyapatite nano powders via hydrothermal process.* Materials Chemistry and Physics, 2019. **222**: p. 251-255.
78. Nosrati, H., R. Sarraf-Mamoory, and F. Dabir, *Crystallographic study of hydrothermal synthesis of hydroxyapatite nano-rods using Brushite precursors.* Journal of Tissues and Materials, 2019. **2**(3): p. 1-8.
79. Bensalah, H., et al., *Hydrothermal synthesis of nanocrystalline hydroxyapatite from phosphogypsum waste.* Journal of environmental chemical engineering, 2018. **6**(1): p. 1347-1352.
80. Galindo, T.G.P., et al., *Studies on preparation of surfactant-assisted elliptical hydroxyapatite nanoparticles and their protein-interactive ability.* Materials Chemistry and Physics, 2019. **221**: p. 367-376.
81. Padmanabhan, V.P., et al., *Surfactant Assisted Hydroxyapatite Nanoparticles: Drug Loading and In Vitro Leaching Kinetics and Antimicrobial Properties.* Journal of nanoscience and nanotechnology, 2019. **19**(11): p. 7198-7204.

82. Wang, Z., et al., *Synthesis and characterization of hydroxyapatite nano-rods from oyster shell with exogenous surfactants.* Materials Science and Engineering: C, 2019. **105**: p. 110102.
83. Bricha, M., et al., *Investigations on the influence of magnesium ion in the Surfactant Assisted Hydrothermaly Synthesized Nanoscale Hydroxyapatite.* Trends in Biomaterials & Artificial Organs, 2018. **32**(2): p. 1-9.
84. Badran, H., et al., *Lithium-doped hydroxyapatite nano-composites: Synthesis, characterization, gamma attenuation coefficient and dielectric properties.* Radiation Physics and Chemistry, 2017. **130**: p. 85-91.
85. Wang, Y., et al., *In vitro study on the degradation of lithium-doped hydroxyapatite for bone tissue engineering scaffold.* Materials Science and Engineering: C, 2016. **66**: p. 185-192.
86. Ames, B.N., *DNA damage from micronutrient deficiencies is likely to be a major cause of cancer.* Mutation Research/Fundamental and Molecular Mechanisms of Mutagenesis, 2001. **475**(1): p. 7-20.
87. Wang, Y., H. Hao, and S. Zhang, *Lysozyme loading and release from Se doped hydroxyapatite nanoparticles.* Materials Science and Engineering: C, 2016. **61**: p. 545-552.
88. Wang, Y., et al., *In Vitro and in Vivo Mechanism of Bone Tumor Inhibition by Selenium-Doped Bone Mineral Nanoparticles.* ACS nano, 2016. **10**(11): p. 9927-9937.
89. Ali, A.A., H.I. Ahmed, and K. Abu-Elfotuh, *The Potential Effect of Epigallocatechin-3-Gallate alone or in Combination with Vitamin E and Selenium on Alzheimer's Disease Induced by Aluminum in Rats.* of, 2016. **10**: p. 2.
90. Wang, M., et al., *The crystal structure and chemical state of aluminum-doped hydroxyapatite by experimental and first principles calculation studies.* Physical Chemistry Chemical Physics, 2016. **18**(31): p. 21789-21796.
91. Kolekar, T.V., et al., *Nanocrystalline hydroxyapatite doped with aluminium: A potential carrier for biomedical applications.* Ceramics International, 2016. **42**(4): p. 5304-5311.
92. Castkova, K., et al., *Synthesis of Ca, Y-zirconia/hydroxyapatite nanoparticles and composites.* Journal of the European Ceramic Society, 2016. **36**(12): p. 2903-2912.
93. Kaygili, O. and S. Keser, *Zr/Mg, Zr/Sr and Zr/Zn co-doped hydroxyapatites: Synthesis and characterization.* Ceramics International, 2016. **42**(7): p. 9270-9273.
94. Lansdown, A.B., *Silver in health care: antimicrobial effects and safety in use.* Curr Probl Dermatol, 2006. **33**: p. 17-34.
95. Stoica, P., et al., *Antifungal bionanocomposites based on poly (lactic acid) and silver nanoparticles for potential medical devices.* Romanian Biotechnol. Lett, 2015. **20**: p. 10696-10707.
96. Ciobanu, C.S., et al., *Structural and physical properties of antibacterial Ag-doped nano-hydroxyapatite synthesized at 100 C.* Nanoscale Research Letters, 2011. **6**(1): p. 1.
97. Anjaneyulu, U., et al., *Fabrication and characterization of Ag doped hydroxyapatite-polyvinyl alcohol composite nanofibers and its in vitro biological evaluations for bone tissue engineering applications.* Journal of Sol-Gel Science and Technology, 2016: p. 1-12.
98. Huang, Y., et al., *Fabrication of silver-and strontium-doped hydroxyapatite/TiO 2 nanotube bilayer coatings for enhancing bactericidal effect and osteoinductivity.* Ceramics International, 2017. **43**(1): p. 992-1007.
99. Mirzaee, M., M. Vaezi, and Y. Palizdar, *Synthesis and characterization of silver doped hydroxyapatite nanocomposite coatings and evaluation of their antibacterial and*

corrosion resistance properties in simulated body fluid. Materials Science and Engineering: C, 2016. **69**: p. 675-684.
100. Lala, S., et al., *Effect of doping (Mg,Mn,Zn) on the microstructure and mechanical properties of spark plasma sintered hydroxyapatites synthesized by mechanical alloying.* Ceramics International, 2017. **43**(2): p. 2389-2397.
101. Lu, J., et al., *Preparation and preliminary cytocompatibility of magnesium doped apatite cement with degradability for bone regeneration.* Journal of Materials Science: Materials in Medicine, 2011. **22**(3): p. 607-615.
102. Lin, K., et al., *Hollow magnetic hydroxyapatite microspheres with hierarchically mesoporous microstructure for pH-responsive drug delivery.* CrystEngComm, 2013. **15**(15): p. 2999-3008.
103. Tampieri, A., et al., *Intrinsic magnetism and hyperthermia in bioactive Fe-doped hydroxyapatite.* Acta biomaterialia, 2012. **8**(2): p. 843-851.
104. Brender, J.R., et al., *Role of zinc in human islet amyloid polypeptide aggregation.* Journal of the American Chemical Society, 2010. **132**(26): p. 8973-8983.
105. Nowak, G., B. Szewczyk, and A. Pilc, *Zinc and depression. An update.* Pharmacol Rep, 2005. **57**(6): p. 713-8.
106. Saha, N., et al., *Sintering, microstructure, mechanical, and antimicrobial properties of HAp-ZnO biocomposites.* Journal of Biomedical Materials Research Part B: Applied Biomaterials, 2010. **95**(2): p. 430-440.
107. Radulescu, M., et al., *Antimicrobial coatings based on zinc oxide and orange oil for improved bioactive wound dressings and other applications.* Rom J Morphol Embryol, 2016. **57**(1): p. 107-114.
108. Kannan, S., et al., *Synthesis, mechanical and biological characterization of ionic doped carbonated hydroxyapatite/β-tricalcium phosphate mixtures.* Acta Biomaterialia, 2011. **7**(4): p. 1835-1843.
109. Nihmath, A. and M. Ramesan, *Preparation, characterization, thermal, and electrical properties of chlorinated ethylene propylene diene monomer/hydroxyapatite nanocomposites.* Polymer Composites, 2018. 39(6): p. 2093-2100.
110. Rashid, M.U., M.K.H. Bhuiyan, and M.E. Quayum, *Synthesis of silver nano particles (Ag-NPs) and their uses for quantitative analysis of vitamin C tablets.* Dhaka University Journal of Pharmaceutical Sciences, 2013. **12**(1): p. 29-33.
111. Gharibshahian, M., M. Nourbakhsh, and O. Mirzaee, *Evaluation of the superparamagnetic and biological properties of microwave assisted synthesized Zn & Cd doped CoFe 2 O 4 nanoparticles via Pechini sol–gel method.* Journal of Sol-Gel Science and Technology, 2018. **85**(3): p. 684-692.
112. Mohammadi, Z. and M.H. Entezari, *Sono-synthesis approach in uniform loading of ultrafine Ag nanoparticles on reduced graphene oxide nanosheets: An efficient catalyst for the reduction of 4-Nitrophenol.* Ultrasonics sonochemistry, 2018. **44**: p. 1-13.
113. Adhikari, L., et al., *Rapid Microwave-Assisted Synthesis of Silver Nanoparticles in a Halide-Free Deep Eutectic Solvent.* ACS Sustainable Chemistry & Engineering, 2018. **6**(5): p. 5725-5731.
114. Alsammarraie, F.K., et al., *Green synthesis of silver nanoparticles using turmeric extracts and investigation of their antibacterial activities.* Colloids and Surfaces B: Biointerfaces, 2018. **171**: p. 398-405.

115. Shahriary, M., et al., *In situ green synthesis of Ag nanoparticles on herbal tea extract (Stachys lavandulifolia)-modified magnetic iron oxide nanoparticles as antibacterial agent and their 4-nitrophenol catalytic reduction activity.* Materials Science and Engineering: C, 2018. **90**: p. 57-66.
116. Zhang, K.-X., et al., *Synthesis, structural and optical properties of silver nanoparticles uniformly decorated ZnO nanowires.* Chemical Physics Letters, 2018. **698**: p. 147-151.
117. Veisi, H., S. Azizi, and P. Mohammadi, *Green synthesis of the silver nanoparticles mediated by Thymbra spicata extract and its application as a heterogeneous and recyclable nanocatalyst for catalytic reduction of a variety of dyes in water.* Journal of Cleaner Production, 2018. **170**: p. 1536-1543.
118. Shahverdi, A.R., et al., *Synthesis and effect of silver nanoparticles on the antibacterial activity of different antibiotics against Staphylococcus aureus and Escherichia coli.* Nanomedicine: Nanotechnology, Biology and Medicine, 2007. **3**(2): p. 168-171.
119. Wu, Y., et al., *A facile method to prepare size-tunable silver nanoparticles and its antibacterial mechanism.* Advanced Powder Technology, 2018. **29**(2): p. 407-415.
120. Xu, H., et al., *Role of reactive oxygen species in the antibacterial mechanism of silver nanoparticles on Escherichia coli O157: H7.* Biometals, 2012. **25**(1): p. 45-53.
121. Xiu, Z.-m., et al., *Negligible Particle-Specific Antibacterial Activity of Silver Nanoparticles.* Nano Letters, 2012. **12**(8): p. 4271-4275.
122. Su, H.-L., et al., *The disruption of bacterial membrane integrity through ROS generation induced by nanohybrids of silver and clay.* Biomaterials, 2009. **30**(30): p. 5979-5987.
123. Silver, S., *Bacterial silver resistance: molecular biology and uses and misuses of silver compounds.* FEMS Microbiology Reviews, 2003. **27**(2-3): p. 341-353.
124. Panáček, A., et al., *Bacterial resistance to silver nanoparticles and how to overcome it.* Nature Nanotechnology, 2018. **13**(1): p. 65-71.
125. Saxena, V., P. Chandra, and L.M. Pandey, *Design and characterization of novel Al-doped ZnO nanoassembly as an effective nanoantibiotic.* Applied Nanoscience, 2018. 8(8): p. 1925-1941.
126. Khan, M.F., et al., *Sol-gel synthesis of thorn-like ZnO nanoparticles endorsing mechanical stirring effect and their antimicrobial activities: Potential role as nano-antibiotics.* Scientific reports, 2016. **6**: p. 27689.
127. Sharifalhoseini, Z., M.H. Entezari, and M. Shahidi, *Sonication affects the quantity and the morphology of ZnO nanostructures synthesized on the mild steel and changes the corrosion protection of the surface.* Ultrasonics sonochemistry, 2018. **41**: p. 492-502.
128. Chauhan, D.S., et al., *Microwave induced facile synthesis and characterization of ZnO nanoparticles as efficient antibacterial agents.* Materials Discovery, 2018. 11: p. 19-25.
129. Alves, T., et al., *Effect of particle shape and size on the morphology and optical properties of zinc oxide synthesized by the polyol method.* Materials & Design, 2018. **146**: p. 125-133.
130. Steffy, K., et al., *Enhanced antibacterial effects of green synthesized ZnO NPs using Aristolochia indica against Multi-drug resistant bacterial pathogens from Diabetic Foot Ulcer.* Journal of infection and public health, 2018. **11**(4): p. 463-471.
131. Jalal, M., et al., *Anticandidal activity of bioinspired ZnO NPs: effect on growth, cell morphology and key virulence attributes of Candida species.* Artificial cells, nanomedicine, and biotechnology, 2018: p. 1-14.

132. Wang, J., et al., *Zinc oxide nanoparticles induce toxicity in CAL 27 oral cancer cell lines by activating PINK1/Parkin-mediated mitophagy.* International Journal of Nanomedicine, 2018. **13**: p. 3441-3450.
133. Sirelkhatim, A., et al., *Review on zinc oxide nanoparticles: antibacterial activity and toxicity mechanism.* Nano-Micro Letters, 2015. **7**(3): p. 219-242.
134. Khan, M.F., et al., *Sol-gel synthesis of thorn-like ZnO nanoparticles endorsing mechanical stirring effect and their antimicrobial activities: Potential role as nano-antibiotics.* Scientific Reports, 2016. **6**: p. 27689.
135. Xu, M., et al., *Challenge to assess the toxic contribution of metal cation released from nanomaterials for nanotoxicology–the case of ZnO nanoparticles.* Nanoscale, 2013. **5**(11): p. 4763-4769.
136. Singh, A., P. Datta, and L.M. Pandey, *Deciphering the mechanistic insight into the stoichiometric ratio dependent behavior of Cu (II) on BSA fibrillation.* International journal of biological macromolecules, 2017. **97**: p. 662-670.
137. Ngoepe, N., et al., *Biogenic synthesis of ZnO nanoparticles using Monsonia burkeana for use in photocatalytic, antibacterial and anticancer applications.* 2018. **44**(14): p. 16999-17006.
138. Khajuria, A.K., et al., *Biofabrication of Zinc Oxide Nanoparticles from Two Different Zinc Sources and Their Antimicrobial Activity.* 2020: p. 1-17.
139. Mohamed, A.A., et al., *Eco-friendly mycogenic synthesis of ZnO and CuO nanoparticles for in vitro antibacterial, antibiofilm, and antifungal applications.* 2020: p. 1-12.
140. Biswas, A., et al., *Biosynthesis of triangular-shape ZnO nanoparticles using Tecoma stans and its antimicrobial activity.*202. p. 1-24.
141. Aalami, A.H., et al., *Synthesis and Characterization of Green Zinc Oxide Nanoparticles with Antiproliferative Effects through Apoptosis Induction and MicroRNA Modulation in Breast Cancer Cells*. **2020**. p.1-17.
142. Gomathi, R., H.J.I. Suhana, and N.-M. Chemistry, *Green synthesis, characterization and antimicrobial activity of zinc oxide nanoparticles using Artemisia pallens plant extract.* 2020: p. 1-10.
143. Boura-Theodoridou, O., et al., *Performance of ZnO/chitosan nanocomposite films for antimicrobial packaging applications as a function of NaOH treatment and glycerol/PVOH blending.* 2020. **23**: p. 100456.
144. Verma, R., et al., *Antimicrobial potential of Ag-doped ZnO nanostructure synthesized by the green method using Moringa oleifera extract.* 2020: p. 103730.
145. Chauhan, M., et al., *Investigating the efficiency of α-Bismuth zinc oxide heterostructure composite/UV-LED in methylene blue dye removal and evaluation of its antimicrobial activity.* 2020. **180**: p. 108857.
146. Krobthong, S., S.J.J.o.M. Wongrerkdee, Materials, and Minerals, *Incorporation of Fe and Cu for antibacterial performance enhancement of Fe-Cu-ZnO nanocomposites synthesized by a facile chemical precipitation.* Journal of Metals, Materials and Minerals 2020. **30**(3): p. 38-45.
147. Gnanamozhi, P., et al., *Enhanced antibacterial and photocatalytic degradation of reactive red 120 using lead substituted ZnO nanoparticles prepared by ultrasonic-assisted co-precipitation method.* Ceramics International, 2020. 46(11): p. 19593-19599
148. Qamar, M.A., et al., *Highly efficient g-C3N4/Cr-ZnO nanocomposites with superior photocatalytic and antibacterial activity.* 2020. **401**: p. 112776.

149. Costa, S.I., et al., *Synthesis and characterization of Nd (OH) 3-ZnO composites for application in photocatalysis and disinfection.* 2020. **392**: p. 123737.
150. Umavathi, S., et al., *Green Synthesis of Zinc Oxide Nanoparticle Using Justicia procumbense Leaf Extract and Their Application as an Antimicrobial Agent.* 2020. **10**(2): p. 153-164.
151. Ghaffari, S.-B., et al., *A pH-sensitive delivery system based on N-succinyl chitosan-ZnO nanoparticles for improving antibacterial and anticancer activities of curcumin.* 2020. **151**: p. 428-440.
152. Ganesan, V., et al., *Periconium sp.(endophytic fungi) extract mediated sol-gel synthesis of ZnO nanoparticles for antimicrobial and antioxidant applications.* 2020. **105**: p. 104739.
153. Seifunnisha, O. and J.J.J.o.N.-a.E.P. Shanthi, *Aloe Vera Mediated Green Synthesis of ZnO Nanostructure under Sol-gel Method: Effect of Antimicrobial Activity.* Journal of Nano- and Electronic Physics, 2020. **12**(2): p. 02041.
154. Rajivgandhi, G.N., et al., *Substantial effect of Cr doping on the antimicrobial activity of ZnO nanoparticles prepared by ultrasonication process.* **263**: p. 114817.
155. Haque, M.J., et al., *Synthesis of ZnO nanoparticles by two different methods & comparison of their structural, antibacterial, photocatalytic and optical properties.* 2020. **1**(1): p. 010007.
156. Uyen, V.N.L., et al., *Fabrication of Cu_2O-ZnO Nanocomposite by the Sol-gel Technique and its Antibacterial Activity.* 2020. **11**(1): p. 18.
157. Ibrahim, H., et al., *Microstructural, Mechanical and Corrosion Characteristics of Heat-Treated Mg-1.2 Zn-0.5 Ca (wt.%) Alloy for Use as Resorbable Bone Fixation Material.* Journal of the Mechanical Behavior of Biomedical Materials, 2017. 69: p. 203-212.
158. Predoi, D., et al., *Textural, Structural and Biological Evaluation of Hydroxyapatite Doped with Zinc at Low Concentrations.* Materials, 2017. **10**(3): p. 229.
159. Huang, Y., et al., *Corrosion resistance and cytocompatibility studies of zinc-doped fluorohydroxyapatite nanocomposite coatings on titanium implant.* Ceramics International, 2016. **42**(1, Part B): p. 1903-1915.
160. Applerot, G., et al., *Understanding the Antibacterial Mechanism of CuO Nanoparticles: Revealing the Route of Induced Oxidative Stress.* Small, 2012. **8**(21): p. 3326-3337.
161. Jadhav, S.S., et al., *Arrested precipitation assembly of nanosheets Cu 2 ZnCd (S, Se) 3 thin film for solar cell performance: Novel skilful synthesis.* Materials Letters, 2018. **217**: p. 215-218.
162. Islam, I., et al., *Effect of 3d transition metal doping (Co, Ni and Cu) on structural, optical, morphological and dielectric properties of sol–gel assisted auto-combusted Mg 0.95 Mn 0.05 O nanoparticles.* Journal of Materials Science: Materials in Electronics, 2018. **29**(5): p. 3952-3956.
163. Naveenraj, S., et al., *A general microwave synthesis of metal (Ni, Cu, Zn) selenide nanoparticles and their competitive interaction with human serum albumin.* New Journal of Chemistry, 2018. **42**(8): p. 5759-5766.
164. Manoj, D., et al., *Towards green synthesis of monodisperse Cu nanoparticles: An efficient and high sensitive electrochemical nitrite sensor.* Sensors and Actuators B: Chemical, 2018. **266**: p. 873-882.
165. Marković, D., et al., *Antibacterial activity of Cu-based nanoparticles synthesized on the cotton fabrics modified with polycarboxylic acids.* Carbohydrate Polymers, 2018. **200**: p. 173-182.

166. Rosenberg, M., et al., *Rapid in situ assessment of Cu-ion mediated effects and antibacterial efficacy of copper surfaces.* Scientific Reports, 2018. **8**(1): p. 8172.
167. Chatterjee, A.K., R. Chakraborty, and T. Basu, *Mechanism of antibacterial activity of copper nanoparticles.* Nanotechnology, 2014. **25**(13): p. 135101.
168. Liu, H., et al., *Corrosion of antibacterial Cu-bearing 316L stainless steels in the presence of sulfate reducing bacteria.* Corrosion Science, 2018. **132**: p. 46-55.
169. Berg, J., A. Tom-Petersen, and O. Nybroe, *Copper amendment of agricultural soil selects for bacterial antibiotic resistance in the field.* Letters in Applied Microbiology, 2005. **40**(2): p. 146-151.
170. Dupont, C.L., G. Grass, and C. Rensing, *Copper toxicity and the origin of bacterial resistance—new insights and applications.* Metallomics, 2011. **3**(11): p. 1109-1118.
171. Pottier, A., et al., *Synthesis of brookite TiO2 nanoparticlesby thermolysis of TiCl4 in strongly acidic aqueous media.* Journal of Materials Chemistry, 2001. **11**(4): p. 1116-1121.
172. Mosquera, E., et al., *Ultrasonic-Assisted Synthesis and Photocatalytic Activity of TiO2 Nanoparticles for Methyl Orange Degradation under Visible Light.* 2018. p. 1-17.
173. Falk, G., et al., *Microwave-assisted synthesis of TiO2 nanoparticles: photocatalytic activity of powders and thin films.* Journal of Nanoparticle Research, 2018. **20**(2): p. 23.
174. Liu, B., et al., *Low temperature fabrication of V-doped TiO2 nanoparticles, structure and photocatalytic studies.* Journal of Hazardous Materials, 2009. **169**(1): p. 1112-1118.
175. Yadav, H.M., J.-S. Kim, and S.H. Pawar, *Developments in photocatalytic antibacterial activity of nano TiO2: A review.* Korean Journal of Chemical Engineering, 2016. **33**(7): p. 1989-1998.
176. Long, M., et al., *Performance and mechanism of standard nano-TiO2 (P-25) in photocatalytic disinfection of foodborne microorganisms – Salmonella typhimurium and Listeria monocytogenes.* Food Control, 2014. **39**: p. 68-74.
177. Ma, S., et al., *Superior Antibacterial Activity of Fe3O4-TiO2 Nanosheets under Solar Light.* ACS Applied Materials & Interfaces, 2015. **7**(39): p. 21875-21883.
178. Zhang, Q., et al., *Dermal exposure to nano-TiO2 induced cardiovascular toxicity through oxidative stress, inflammation and apoptosis.* The Journal of toxicological sciences, 2019. **44**(1): p. 35-45.
179. Brzicova, T., et al., *Nano-TiO2 stability in medium and size as important factors of toxicity in macrophage-like cells.* Toxicology in Vitro, 2019. **54**: p. 178-188.
180. Andreoli, C., et al., *Critical issues in genotoxicity assessment of TiO2 nanoparticles by human peripheral blood mononuclear cells.* Journal of Applied Toxicology, 2018. **38**(12): p. 1471-1482.
181. Knight, A.S., et al., *Sequence programmable peptoid polymers for diverse materials applications.* Advanced Materials, 2015. **27**(38): p. 5665-5691.
182. Lau, K.H.A., *Peptoids for biomaterials science.* Biomaterials Science, 2014. **2**(5): p. 627-633.
183. Prakash, A., et al., *Peptoid backbone flexibilility dictates its interaction with water and surfaces: a molecular dynamics investigation.* Biomacromolecules, 2018. **19**(3): p. 1006-1015.
184. Gangloff, N., et al., *Peptoids and Polypeptoids at the Frontier of Supra- and Macromolecular Engineering.* Chemical Reviews, 2016. **116**(4): p. 1753-1802.
185. Song, Y.M., et al., *Cell Selectivity and Mechanism of Action of Antimicrobial Model Peptides Containing Peptoid Residues.* Biochemistry, 2005. **44**(36): p. 12094-12106.

186. Chongsiriwatana, N.P., et al., *Peptoids that mimic the structure, function, and mechanism of helical antimicrobial peptides.* Proceedings of the National Academy of Sciences, 2008. **105**(8): p. 2794-2799.
187. Bicker, K.L. and S.L. Cobb, *Recent advances in the development of anti-infective peptoids.* Chemical Communications, 2020. **56**(76): p. 11158-11168.
188. Molchanova, N., et al., *Antimicrobial activity of α-peptide/β-peptoid lysine-based peptidomimetics against colistin-resistant Pseudomonas aeruginosa isolated from cystic fibrosis patients.* Frontiers in Microbiology, 2019. **10**: p. 275.
189. Ryge, T.S. and P.R. Hansen, *Novel lysine-peptoid hybrids with antibacterial properties.* Journal of peptide science: an official publication of the European Peptide Society, 2005. **11**(11): p. 727-734.
190. Uchida, M., et al., *Soft X-ray tomography of phenotypic switching and the cellular response to antifungal peptoids in Candida albicans.* Proceedings of the National Academy of Sciences, 2009. **106**(46): p. 19375-19380.
191. Corson, A.E., et al., *Discovery and characterization of a peptoid with antifungal activity against Cryptococcus neoformans.* ACS medicinal chemistry letters, 2016. **7**(12): p. 1139-1144.
192. Eggimann, G.A., et al., *Investigating the Anti-leishmanial Effects of Linear Peptoids.* ChemMedChem, 2015. **10**(2): p. 233-237.
193. Vedel, L., et al., *Antiplasmodial and Prehemolytic Activities of α-Peptide–β-Peptoid Chimeras.* ChemBioChem, 2007. **8**(15): p. 1781-1784.
194. Carvalho, O., et al., *HAp-functionalized zirconia surfaces via hybrid laser process for dental applications.* Optics & Laser Technology, 2018. **106**: p. 157-167.
195. Reis, D.P., et al., *Remineralizing potential of dental composites containing silanized silica-hydroxyapatite (Si-HAp) nanoporous particles charged with sodium fluoride (NaF).* Journal of Dentistry, 2019. **90**: p. 103211.
196. Mondal, S., et al., *Rare earth element doped hydroxyapatite luminescent bioceramics contrast agent for enhanced biomedical imaging and therapeutic applications.* Ceramics International, 2020. 46(18): p. 29249-29260.
197. Predoi, D., S.L. Iconaru, and M.V. Predoi, *Fabrication of Silver-and Zinc-Doped Hydroxyapatite Coatings for Enhancing Antimicrobial Effect.* Coatings, 2020. **10**(9): p. 905.
198. Prodan, A.M., et al., *Silver-Doped Hydroxyapatite Thin Layers Obtained by Sol-Gel Spin Coating Procedure.* Coatings, 2020. **10**(1): p. 14.
199. Hendi, A.A. and F. Yakuphanoglu, *Dielectric and ferroelectric properties of the graphene doped hydroxyapatite ceramics.* Journal of Molecular Structure, 2020. **1207**: p. 127734.
200. Wang, Q., et al., *Magnetic lanthanum-doped hydroxyapatite/chitosan scaffolds with endogenous stem cell-recruiting and immunomodulatory properties for bone regeneration.* Journal of Materials Chemistry B, 2020. 8(24): p. 5280-5292.
201. Padmanabhan, V.P., et al., *Facile fabrication of phase transformed cerium (IV) doped hydroxyapatite for biomedical applications – A health care approach.* Ceramics International, 2020. **46**(2): p. 2510-2522.
202. Kamonwannasit, S., et al., *Synthesis of copper-silver doped hydroxyapatite via ultrasonic coupled sol-gel techniques: structural and antibacterial studies.* Journal of Sol-Gel Science and Technology, 2020. 96(2): p. 452-463.

203. Zhou, R., et al., *Hyaluronan-directed fabrication of co-doped hydroxyapatite as a dual-modal probe for tumor-specific bioimaging.* Journal of Materials Chemistry B, 2020. **8**(10): p. 2107-2114.
204. Zakhireh, S., et al., *Osteogenesis Promotion of Selenium-Doped Hydroxyapatite for Application as Bone Scaffold.* Biological Trace Element Research, 2020. 199(5): p. 1802-1811.
205. Ciobanu, S.C., et al., *Physico-Chemical Properties and In Vitro Antifungal Evaluation of Samarium Doped Hydroxyapatite Coatings.* Coatings, 2020. **10**(9): p. 827.
206. Singh, R.P., et al., *Encapsulation of vancomycin in copper doped hydroxyapatite mesoporous nanoparticles of different morphologies.* Journal of Drug Delivery Science and Technology, 2020. **55**: p. 101441.
207. Barbanente, A., et al., *Platinum-loaded, selenium-doped hydroxyapatite nanoparticles selectively reduce proliferation of prostate and breast cancer cells co-cultured in the presence of stem cells.* Journal of Materials Chemistry B, 2020. **8**(14): p. 2792-2804.
208. Kolesnikov, I.E., et al., *Structural and luminescence properties of Ce3+-doped hydroxyapatite nanocrystalline powders.* Optical Materials, 2020. **99**: p. 109550.
209. Saranya, S. and M.P. Rani, *In Vitro Studies of Ce-Doped Hydroxyapatite Synthesized by Sol–Gel Method for Biomedical Applications.* Journal of Pharmaceutical Innovation, 2020. 16(3): p. 493-503.
210. Ribeiro, T.P., F.J. Monteiro, and M.S. Laranjeira, *Duality of iron (III) doped nano hydroxyapatite in triple negative breast cancer monitoring and as a drug-free therapeutic agent.* Ceramics International, 2020. **46**(10, Part B): p. 16590-16597.
211. Indra, A., et al., *Enhancing the physical and mechanical properties of pellet-shaped hydroxyapatite by controlling micron-and nano-sized powder ratios.* Ceramics International, 2020. 46(10): p. 15882-15888.
212. Ran, J., et al., *Comparisons among Mg, Zn, Sr, and Si doped nano-hydroxyapatite/chitosan composites for load-bearing bone tissue engineering applications.* Materials Chemistry Frontiers, 2017. **1**(5): p. 900-910.
213. Karunakaran, G., et al., *Mesoporous Mg-doped hydroxyapatite nanorods prepared from bio-waste blue mussel shells for implant applications.* Ceramics International, 2020. 46(18): p. 28514-28527.
214. Abutalib, M. and I. Yahia, *Novel and facile microwave-assisted synthesis of Mo-doped hydroxyapatite nanorods: Characterization, gamma absorption coefficient, and bioactivity.* Materials Science and Engineering: C, 2017. **78**: p. 1093-1100.
215. Garbo, C., et al., *Advanced Mg, Zn, Sr, Si Multi-Substituted Hydroxyapatites for Bone Regeneration.* International Journal of Nanomedicine, 2020. **15**: p. 1037.
216. De Luca, A., et al., *Improvement of osteogenic differentiation of human mesenchymal stem cells on composite poly l-lactic acid/nano-hydroxyapatite scaffolds for bone defect repair.* Journal of bioscience and bioengineering, 2020. **129**(2): p. 250-257.
217. Ma, L., et al., *A novel photothermally controlled multifunctional scaffold for clinical treatment of osteosarcoma and tissue regeneration.* Materials Today, 2020. 36: p. 48-62.
218. Mobika, J., et al., *Substantial effect of silk fibroin reinforcement on properties of hydroxyapatite/silk fibroin nanocomposite for bone tissue engineering application.* Journal of Molecular Structure, 2020. **1206**: p. 127739.
219. Luz, E.P.C.G., et al., *In vitro degradability and bioactivity of oxidized bacterial cellulose-hydroxyapatite composites.* Carbohydrate Polymers, 2020: p. 116174.

220. Kandasamy, S., V. Narayanan, and S. Sumathi, *Zinc and manganese substituted hydroxyapatite/CMC/PVP electrospun composite for bone repair applications.* International journal of biological macromolecules, 2020. **145**: p. 1018-1030.
221. Gan, S., et al., *Nano-hydroxyapatite enhanced double network hydrogels with excellent mechanical properties for potential application in cartilage repair.* Carbohydrate Polymers, 2020. **229**: p. 115523.
222. Pereira, M., et al., *Amino hydroxyapatite/chitosan hybrids reticulated with glutaraldehyde at different pH values and their use for diclofenac removal.* Carbohydrate Polymers, 2020. **236**: p. 116036.
223. Saxena, V., et al., *Edible oil nanoemulsion: An organic nanoantibiotic as a potential biomolecule delivery vehicle.* International Journal of Polymeric Materials and Polymeric Biomaterials, 2018. **67**(7): p. 410-419.
224. Yang, X., et al., *Rhein-PEG-nHA conjugate as a bone targeted drug delivery vehicle for enhanced cancer chemo-radiotherapy.* Nanomedicine: Nanotechnology, Biology and Medicine, 2020: p. 102196.
225. Dewhurst, R.M., et al., *Development of natural-based bone cement for a controlled doxorubicin-drug release.* Frontiers in Bioengineering and Biotechnology, 2020. **8**: p. 754.
226. Zha, L., et al., *Preparation, characterization and preliminary pharmacokinetic study of pH-sensitive Hydroxyapatite/Zein nano-drug delivery system for doxorubicin hydrochloride.* Journal of Pharmacy and Pharmacology, 2020. **72**(4): p. 496-506.
227. Hasan, A., V. Saxena, and L.M. Pandey, *Surface Functionalization of Ti6Al4V via Self-assembled Monolayers for Improved Protein Adsorption and Fibroblast Adhesion.* Langmuir, 2018. 34(11): p. 3494-3506.
228. Behera, R.R., et al., *Laser cladding with HA and functionally graded TiO2-HA precursors on Ti–6Al–4V alloy for enhancing bioactivity and cyto-compatibility.* Surface and Coatings Technology, 2018. **352**: p. 420-436.
229. Behera, R., et al., *Deposition of biphasic calcium phosphate film on laser surface textured Ti–6Al–4V and its effect on different biological properties for orthopedic applications.* Journal of Alloys and Compounds, 2020: p. 155683.
230. Behera, R., et al., *Effect of TiO2 addition on adhesion and biological behavior of BCP-TiO2 composite films deposited by magnetron sputtering.* Materials Science and Engineering: C, 2020: p. 111033.
231. Wang, X.-s., et al., *A highly integrated precision nanomedicine strategy to target esophageal squamous cell cancer molecularly and physically.* Nanomedicine: Nanotechnology, Biology and Medicine, 2018. **14**(7): p. 2103-2114.
232. Khan, M.I., et al., *Induction of ROS, mitochondrial damage and autophagy in lung epithelial cancer cells by iron oxide nanoparticles.* Biomaterials, 2012. **33**(5): p. 1477-1488.
233. Fu, P.P., et al., *Mechanisms of nanotoxicity: generation of reactive oxygen species.* Journal of food and drug analysis, 2014. **22**(1): p. 64-75.
234. Rebleanu, D., et al., *The impact of photocatalytic Ag/TiO2 and Ag/N-TiO2 nanoparticles on human keratinocytes and epithelial lung cells.* Toxicology, 2019. 416: p. 30-43.
235. Yazdanbakhsh, A.R., et al., *Responses of flocculated activated sludge to bimetallic Ag-Fe nanoparticles toxicity: Performance, activity enzymatic, and bacterial community shift.* Journal of Hazardous Materials, 2019. **366**: p. 114-123.

236. Davaeifar, S., et al., *Synthesizing, characterizing, and toxicity evaluating of Phycocyanin-ZnO nanorod composites: A back to nature approaches.* Colloids and Surfaces B: Biointerfaces, 2019. **175**: p. 221-230.
237. Das, B.K., et al., *Altered electrical properties with controlled copper doping in ZnO nanoparticles infers their cytotoxicity in macrophages by ROS induction and apoptosis.* Chemico-Biological Interactions, 2019. **297**: p. 141-154.
238. Líbalová, H., et al., *Toxicity of surface-modified copper oxide nanoparticles in a mouse macrophage cell line: Interplay of particles, surface coating and particle dissolution.* Chemosphere, 2018. **196**: p. 482-493.
239. Katsumiti, A., et al., *Cytotoxicity and cellular mechanisms of toxicity of CuO NPs in mussel cells in vitro and comparative sensitivity with human cells.* Toxicology in Vitro, 2018. **48**: p. 146-158.
240. Gao, X., et al., *Distinct effects of soluble and bound exopolymeric substances on algal bioaccumulation and toxicity of anatase and rutile TiO2 nanoparticles.* Environmental Science: Nano, 2018. **5**(3): p. 720-729.
241. Su, H., et al., *In vitro evaluation of the toxicity and underlying molecular mechanisms of Janus Fe3O4-TiO2 nanoparticles in human liver cells.* Environmental Toxicology, 2018. **33**(10): p. 1078-1088.
242. Tiwari, S., R.S. Yadav, and B.K. Kuanr, *Hemolysis and Cytotoxicity Studies of Surface Functionalized and Bare Core–Shell Fe3O4 Nanoparticles.* Advanced Science Letters, 2018. **24**(2): p. 907-912.
243. Zhang, X., et al., *Toxic effects of CuO, ZnO and TiO2 nanoparticles in environmental concentration on the nitrogen removal, microbial activity and community of Anammox process.* Chemical Engineering Journal, 2018. **332**: p. 42-48.
244. Mo, Y., Y. Zhang, and Q. Zhang, *Evaluation of Pulmonary Toxicity of Nanoparticles by Bronchoalveolar Lavage*, in *Nanotoxicity*. 2019, Springer. p. 313-322.
245. Wysokińska, E., et al., *Toxicity Mechanism of Low Doses of NaGdF4: Yb3+, Er3+ Upconverting Nanoparticles in Activated Macrophage Cell Lines.* Biomolecules, 2019. **9**(1): p. 14.
246. He, T., et al., *Influence of bovine serum albumin pre-incubation on toxicity and ER stress-apoptosis gene expression in THP-1 macrophages exposed to ZnO nanoparticles AU - Liang, Hongying.* Toxicology Mechanisms and Methods, 2018. **28**(8): p. 587-598.
247. Moghimi, S.M., et al., *Material properties in complement activation.* Advanced Drug Delivery Reviews, 2011. **63**(12): p. 1000-1007.
248. Kah, J.C.Y., *Non-specific adsorption of complement proteins affects complement activation pathways of gold nanomaterials AU - Quach, Quang Huy.* Nanotoxicology, 2017. **11**(3): p. 382-394.
249. Xie, Y., et al., *Antibacterial activity and mechanism of action of zinc oxide nanoparticles against Campylobacter jejuni.* Applied and environmental microbiology, 2011. **77**(7): p. 2325-2331.
250. Sanoop, P.K., et al., *Synthesis of yttrium doped nanocrystalline ZnO and its photocatalytic activity in methylene blue degradation.* Arabian Journal of Chemistry, 2016. **9**: p. S1618-S1626.
251. Raghupathi, K.R., R.T. Koodali, and A.C. Manna, *Size-dependent bacterial growth inhibition and mechanism of antibacterial activity of zinc oxide nanoparticles.* Langmuir, 2011. **27**(7): p. 4020-4028.

252. Sharma, R.K., M. Agarwal, and K. Balani, *Effect of ZnO morphology on affecting bactericidal property of ultra high molecular weight polyethylene biocomposite.* Materials Science and Engineering: C, 2016. **62**: p. 843-851.
253. Zhang, L., et al., *Investigation into the antibacterial behaviour of suspensions of ZnO nanoparticles (ZnO nanofluids).* Journal of Nanoparticle Research, 2007. **9**(3): p. 479-489.
254. Rekha, K., et al., *Structural, optical, photocatalytic and antibacterial activity of zinc oxide and manganese doped zinc oxide nanoparticles.* Physica B: Condensed Matter, 2010. **405**(15): p. 3180-3185.
255. Sharma, N., et al., *Antibacterial study of silver doped zinc oxide nanoparticles against Staphylococcus aureus and Bacillus subtilis.* Drug Invention Today, 2013. **5**(1): p. 50-54.
256. Mahalingam, R., V. Ambikapathy, and A. Panneerselvam, *Studies on antifungal activities of some medicinal plants against Ceratocystis paradoxa causing pineapple disease.* World J. Sci. Technol, 2011. **1**: p. 10-13.
257. Wang, F., et al., *Simultaneous phase and size control of upconversion nanocrystals through lanthanide doping.* Nature, 2010. **463**(7284): p. 1061-1065.
258. Nikam, A., B. Prasad, and A. Kulkarni, *Wet chemical synthesis of metal oxide nanoparticles: a review.* CrystEngComm, 2018. **20**(35): p. 5091-5107.
259. Mishra, P.K., et al., *Zinc oxide nanoparticles: a promising nanomaterial for biomedical applications.* Drug Discovery Today, 2017. **22**(12): p. 1825-1834.
260. Khan, J., et al., *Zno/NiO coated multi-walled carbon nanotubes for textile dyes degradation.* Arabian Journal of Chemistry, 2017. 11(6): p. 880-896.
261. Zhang, W.-Q., et al., *Controlled Synthesis and Biocompatibility of Water-Soluble ZnO Nanorods/Au Nanocomposites with Tunable UV and Visible Emission Intensity.* The Journal of Physical Chemistry C, 2008. **112**(50): p. 19872-19877.
262. Hasan, A., et al., *Fabrication and characterization of chitosan, polyvinylpyrrolidone, and cellulose nanowhiskers nanocomposite films for wound healing drug delivery application.* Journal of Biomedical Materials Research Part A, 2017. **105**(9): p. 2391-2404.
263. Saxena, V., et al., *Edible oil nanoemulsion: An organic nanoantibiotic as a potential biomolecule delivery vehicle.* International Journal of Polymeric Materials and Polymeric Biomaterials, 2018. 67(7): p. 410-419.
264. Fernández, D., C. García-Gómez, and M. Babín, *In vitro evaluation of cellular responses induced by ZnO nanoparticles, zinc ions and bulk ZnO in fish cells.* Science of the Total Environment, 2013. **452**: p. 262-274.
265. Wang, X., et al., *A study on the antibacterial activity of one-dimensional ZnO nanowire arrays: effects of the orientation and plane surface.* Chemical Communications, 2007(42): p. 4419-4421.
266. Zhang, Q., et al., *Structure–Property Correlations of Reactive Oxygen Species-Responsive and Hydrogen Peroxide-Eliminating Materials with Anti-Oxidant and Anti-Inflammatory Activities.* Chemistry of Materials, 2017. **29**(19): p. 8221-8238.
267. Thinh Pham Nguyen, H., et al., *Characterization and photocatalytic activity of new photocatalysts based on Ag, F-modified ZnO nanoparticles prepared by thermal shock method.* Arabian Journal of Chemistry, 2018. 13(1): p. 1837-1847.
268. Le, T.K., et al., *Enhanced photocatalytic activity of ZnO nanoparticles by surface modification with KF using thermal shock method.* Arabian Journal of Chemistry, 2017. 13(1): p. 1032-1039.

269. Sengupta, D., B. Mondal, and K. Mukherjee, *Genesis of flake-like morphology and dye-sensitized solar cell performance of Al-doped ZnO particles: a study.* Journal of Nanoparticle Research, 2017. **19**(3): p. 100.
270. Sandeep, K.M., S. Bhat, and S.M. Dharmaprakash, *Nonlinear absorption properties of ZnO and Al doped ZnO thin films under continuous and pulsed modes of operations.* Optics & Laser Technology, 2018. **102**: p. 147-152.
271. Fan, Z., et al., *An environmentally friendly and efficient route for the reduction of graphene oxide by aluminum powder.* Carbon, 2010. **48**(5): p. 1686-1689.
272. Mei, X. and J. Ouyang, *Ultrasonication-assisted ultrafast reduction of graphene oxide by zinc powder at room temperature.* Carbon, 2011. **49**(15): p. 5389-5397.
273. Shamsuzzaman, et al., *Biological synthesis of ZnO nanoparticles using C. albicans and studying their catalytic performance in the synthesis of steroidal pyrazolines.* Arabian Journal of Chemistry, 2017. **10**: p. S1530-S1536.
274. Al-Ruqeishi, M.S. and T. Mohiuddin, *Growth of Single-sided ZnO nanocombs/ML graphene Heterostructures.* Arabian Journal of Chemistry, 2019. 12(8): p. 2774-2781.
275. Hansen, M., et al., *Spatially distinct Raman scattering characteristics of individual ZnO nanorods under controlled polarization: intense end scattering from forbidden modes.* Nanoscale, 2017. 9(24): p. 8470-8480.
276. Chouchene, B., et al., *Porous Al-doped ZnO rods with selective adsorption properties.* Applied Surface Science, 2017. **409**: p. 102-110.
277. Wang, C. and L.L. Shaw, *On synthesis of Fe2SiO4/SiO2 and Fe2O3/SiO2 composites through sol–gel and solid-state reactions.* Journal of sol-gel science and technology, 2014. **72**(3): p. 602-614.
278. Sahni, K., et al., *On the synthesis of lithium boron nitride (Li3BN2).* Ceramics International, 2018. **44**(7): p. 7734-7740.
279. Suchea, M., et al., *Comparative study of zinc oxide and aluminum doped zinc oxide transparent thin films grown by direct current magnetron sputtering.* Thin Solid Films, 2007. **515**(16): p. 6562-6566.
280. Berney, M., et al., *Specific growth rate determines the sensitivity of Escherichia coli to thermal, UVA, and solar disinfection.* Applied and environmental microbiology, 2006. **72**(4): p. 2586-2593.
281. Garvey, M., B. Moriceau, and U. Passow, *Applicability of the FDA assay to determine the viability of marine phytoplankton under different environmental conditions.* Marine Ecology Progress Series, 2007. **352**: p. 17-26.
282. Zotta, T., et al., *A comparison of fluorescent stains for the assessment of viability and metabolic activity of lactic acid bacteria.* World Journal of Microbiology and Biotechnology, 2012. **28**(3): p. 919-927.
283. Costa, P. and J.M.S. Lobo, *Modeling and comparison of dissolution profiles.* European journal of pharmaceutical sciences, 2001. **13**(2): p. 123-133.
284. Jantrasee, S., P. Moontragoon, and S. Pinitsoontorn, *Thermoelectric properties of Al-doped ZnO: experiment and simulation.* Journal of Semiconductors, 2016. **37**(9): p. 092002.
285. Cai, K.F., et al., *Preparation and thermoelectric properties of Al-doped ZnO ceramics.* Materials Science and Engineering: B, 2003. **104**(1): p. 45-48.
286. Choi, H.-J., et al., *Resistance against water and acid water (pH= 4.0) via Al-doped ZnO thin films for environmentally friendly glass panels.* Journal of Alloys and Compounds, 2017. **719**: p. 271-280.

287. Joe, A., et al., *Antibacterial mechanism of ZnO nanoparticles under dark conditions.* Journal of Industrial and Engineering Chemistry, 2017. **45**: p. 430-439.
288. Li, M., L. Zhu, and D. Lin, *Toxicity of ZnO nanoparticles to Escherichia coli: mechanism and the influence of medium components.* Environmental science & technology, 2011. **45**(5): p. 1977-1983.
289. Brayner, R., et al., *Toxicological impact studies based on Escherichia coli bacteria in ultrafine ZnO nanoparticles colloidal medium.* Nano Letters, 2006. **6**(4): p. 866-870.
290. Agarwal, H., et al., *Mechanistic study on antibacterial action of zinc oxide nanoparticles synthesized using green route.* Chemico-biological interactions, 2018. 286: p. 60-70.
291. Maruthupandy, M., et al., *Biologically synthesized zinc oxide nanoparticles as nanoantibiotics against ESBLs producing gram negative bacteria.* Microbial pathogenesis, 2018. 121: p. 224-231.
292. Saxena, V., P. Chandra, and L.M. Pandey, *Design and characterization of novel Al-doped ZnO nanoassembly as an effective nanoantibiotic.* Applied Nanoscience, 2018. **8**(8): p. 1925-1941.
293. Xiong, D., et al., *Effects of nano-scale TiO2, ZnO and their bulk counterparts on zebrafish: acute toxicity, oxidative stress and oxidative damage.* Science of the Total environment, 2011. **409**(8): p. 1444-1452.
294. Zhang, W., et al., *Photogeneration of reactive oxygen species on uncoated silver, gold, nickel, and silicon nanoparticles and their antibacterial effects.* Langmuir, 2013. **29**(15): p. 4647-4651.
295. Parthasarathy, A., et al., *Conjugated polyelectrolytes with imidazolium solubilizing groups. Properties and application to photodynamic inactivation of bacteria.* ACS applied materials & interfaces, 2015. **7**(51): p. 28027-28034.
296. Wang, Y., et al., *Understanding the dark and light-enhanced bactericidal action of cationic conjugated polyelectrolytes and oligomers.* Langmuir, 2013. **29**(2): p. 781-792.
297. Gudkov, S.V., et al., *Unmodified hydrated C60 fullerene molecules exhibit antioxidant properties, prevent damage to DNA and proteins induced by reactive oxygen species and protect mice against injuries caused by radiation-induced oxidative stress.* Nanomedicine: Nanotechnology, Biology and Medicine, 2019. **15**(1): p. 37-46.
298. Yaghini, E., et al., *In vivo biodistribution and toxicology studies of cadmium-free indium-based quantum dot nanoparticles in a rat model.* Nanomedicine: Nanotechnology, Biology and Medicine, 2018. **14**(8): p. 2644-2655.
299. Srivastav, A.K., et al., *Sub-acute oral exposure of zinc oxide nanoparticles causes alteration in iron homeostasis through acute phase response: A protective effect by surface modification.* Journal of Trace Elements in Medicine and Biology, 2019. **52**: p. 270-287.
300. Steffy, K., et al., *Potential bactericidal activity of S. nux-vomica–ZnO nanocomposite against multidrug-resistant bacterial pathogens and wound-healing properties.* Journal of Trace Elements in Medicine and Biology, 2018. **50**: p. 229-239.
301. Shahid, S., et al., *Size-dependent Bacterial Growth Inhibition and Antibacterial Activity of Ag-doped ZnO Nanoparticles under Different Atmospheric Conditions.* Indian Journal of Pharmaceutical Sciences, 2018. **80**(1): p. 173-180.
302. Bomila, R., et al., *Enhanced photocatalytic degradation of methylene blue dye, opto-magnetic and antibacterial behaviour of pure and La-doped ZnO nanoparticles.* Journal of Superconductivity and Novel Magnetism, 2018. **31**(3): p. 855-864.

303. Bhushan, M., et al., *Facile synthesis of Fe/Zn oxide nanocomposites and study of their structural, magnetic, thermal, antibacterial and cytotoxic properties.* Materials Chemistry and Physics, 2018. **209**: p. 233-248.
304. Poller, W.C., et al., *Very small superparamagnetic iron oxide nanoparticles: Long-term fate and metabolic processing in atherosclerotic mice.* Nanomedicine: Nanotechnology, Biology and Medicine, 2018. **14**(8): p. 2575-2586.
305. Aakansha and S. Ravi, *Structural, magnetic and dielectric properties of Cr substituted yttrium iron garnets.* Journal of the American Ceramic Society, 2018. **101**(11): p. 5046-5060.
306. Aakansha, B. Deka, and S. Ravi, *Magnetic and Dielectric Properties of Y3−xSmxFe5O12 (x = 0.0 to 3.0).* Journal of Superconductivity and Novel Magnetism, 2018. **31**(7): p. 2121-2129.
307. Hébert, C., *Films minces nanocomposites ZnxFe1-xO1+ δ: phases wurtzite, sel gemme et spinelle*. 2017, Thesis Paris 6.
308. Barbier, A., et al., *Dislocation network driven structural relaxation in hematite thin films.* Materials Science and Engineering: B, 2007. **144**(1): p. 19-22.
309. Perrière, J., et al., *On the relevance of large scale pulsed-laser deposition: Evidence of structural heterogeneities in ZnO thin films.* Journal of Applied Physics, 2014. **116**(12): p. 123502.
310. Justh, N., et al., *Photocatalytic hollow TiO2 and ZnO nanospheres prepared by atomic layer deposition.* Scientific Reports, 2017. **7**(1): p. 4337.
311. He, L., et al., *Effects of calcination temperature and heating rate on the photocatalytic properties of ZnO prepared by pyrolysis.* Journal of Colloid and Interface Science, 2018. **509**: p. 448-456.
312. Polsongkram, D., et al., *Effect of synthesis conditions on the growth of ZnO nanorods via hydrothermal method.* Physica B: Condensed Matter, 2008. **403**(19): p. 3713-3717.
313. Sienkiewicz, M., et al., *The ability of selected plant essential oils to enhance the action of recommended antibiotics against pathogenic wound bacteria.* Burns, 2017. **43**(2): p. 310-317.
314. Orou, S.F.C., et al., *Antibacterial activity by ZnO nanorods and ZnO nanodisks: A model used to illustrate "Nanotoxicity Threshold".* Journal of industrial and engineering chemistry, 2018. **62**: p. 333-340.
315. Oquendo-Cruz, A. and O. Perales-Pérez, *Synthesis, Characterization and Bactericide Properties of Pure and Li Doped ZnO Nanoparticles for Alternative Water Disinfection Methods.* Journal of Electronic Materials, 2018. **47**(10): p. 6260-6265.
316. Wang, S., et al., *Antibacterial activity and mechanism of Ag/ZnO nanocomposite against anaerobic oral pathogen Streptococcus mutans.* Journal of Materials Science: Materials in Medicine, 2017. **28**(1): p. 23.
317. Liu, J., et al., *Photo-enhanced antibacterial activity of ZnO/graphene quantum dot nanocomposites.* Nanoscale, 2018. **10**(1): p. 158-166.
318. Hassanpour, M., et al., *Synthesis, characterization and antibacterial activities of Ni/ZnO nanocomposites using bis(salicylaldehyde) complex precursor*. Journal of Alloys and Compounds, 2019. **788**: p. 383-390.
319. Lallo da Silva, B., et al., *Increased antibacterial activity of ZnO nanoparticles: Influence of size and surface modification.* Colloids and Surfaces B: Biointerfaces, 2019. **177**: p. 440-447.

320. Phuruangrat, A., et al., *Microwave-assisted synthesis, photocatalysis and antibacterial activity of Ag nanoparticles supported on ZnO flowers.* Journal of Physics and Chemistry of Solids, 2019. **126**: p. 170-177.
321. Wong, K.-A., S.-M. Lam, and J.-C. Sin, *Wet chemically synthesized ZnO structures for photodegradation of pre-treated palm oil mill effluent and antibacterial activity.* Ceramics International, 2019. **45**(2, Part A): p. 1868-1880.
322. Chakraborty, R., et al., *Synthesis, characterization and cytocompatibility assessment of hydroxyapatite-polypyrrole composite coating synthesized through pulsed reverse electrochemical deposition.* Materials Science and Engineering: C, 2019. **94**: p. 597-607.
323. Jiang, L., et al., *Effect of bamboo fiber on the degradation behavior and in vitro cytocompatibility of the nano-hydroxyapatite/poly(lactide-co-glycolide) (n-HA/PLGA) composite.* Cellulose, 2019. **26**(2): p. 1099-1110.
324. Das, B.K., et al., *Altered electrical properties with controlled copper doping in ZnO nanoparticles infers their cytotoxicity in macrophages by ROS induction and apoptosis.* Chemico-biological interactions, 2019. **297**: p. 141-154.
325. Song, W., et al., *Role of the dissolved zinc ion and reactive oxygen species in cytotoxicity of ZnO nanoparticles.* Toxicology Letters, 2010. **199**(3): p. 389-397.
326. Visnapuu, M., et al., *UVA-induced antimicrobial activity of ZnO/Ag nanocomposite covered surfaces.* Colloids and Surfaces B: Biointerfaces, 2018. **169**: p. 222-232.
327. Titma, T., et al., *Toxicity of antimony, copper, cobalt, manganese, titanium and zinc oxide nanoparticles for the alveolar and intestinal epithelial barrier cells in vitro.* Cytotechnology, 2016. **68**(6): p. 2363-2377.
328. Muna, M., et al., *Combined Effects of Test Media and Dietary Algae on the Toxicity of CuO and ZnO Nanoparticles to Freshwater Microcrustaceans Daphnia magna and Heterocypris incongruens: Food for Thought.* Nanomaterials, 2018. **9**(1): p. 23.
329. He, W., et al., *Production of Reactive Oxygen Species and Electrons from Photoexcited ZnO and ZnS Nanoparticles: A Comparative Study for Unraveling their Distinct Photocatalytic Activities.* The Journal of Physical Chemistry C, 2016. **120**(6): p. 3187-3195.
330. Xia, T., et al., *Comparison of the Mechanism of Toxicity of Zinc Oxide and Cerium Oxide Nanoparticles Based on Dissolution and Oxidative Stress Properties.* ACS Nano, 2008. **2**(10): p. 2121-2134.
331. Hameed, A.S.H., et al., *In vitro antibacterial activity of ZnO and Nd doped ZnO nanoparticles against ESBL producing Escherichia coli and Klebsiella pneumoniae.* Scientific Reports, 2016. **6**: p. 24312.
332. Wiesmann, N., et al., *Zinc overload mediated by zinc oxide nanoparticles as innovative anti-tumor agent.* Journal of Trace Elements in Medicine and Biology, 2019. **51**: p. 226-234.
333. Wang, D., et al., *Antibiofilm peptides against biofilms on titanium and hydroxyapatite surfaces.* Bioactive Materials, 2018. **3**(4): p. 418-425.
334. Jerri Al-Bakhsh, B.A., et al., *In-vitro bioactivity evaluation and physical properties of an epoxy-based dental sealer reinforced with synthesized fluorine-substituted hydroxyapatite, hydroxyapatite and bioactive glass nanofillers.* Bioactive Materials, 2019. **4**: p. 322-333.
335. Gnaneshwar, P.V., et al., *Ramification of zinc oxide doped hydroxyapatite biocomposites for the mineralization of osteoblasts.* Materials Science and Engineering: C, 2019. **96**: p. 337-346.

336. Gomes, S., J.-M. Nedelec, and G. Renaudin, *On the effect of temperature on the insertion of zinc into hydroxyapatite.* Acta Biomaterialia, 2012. **8**(3): p. 1180-1189.
337. Begam, H., et al., *MG63 osteoblast cell response on Zn doped hydroxyapatite (HAp) with various surface features.* Ceramics International, 2017. **43**(4): p. 3752-3760.
338. Mardziah, C.M., et al., *Effect of zinc ions on the structural characteristics of hydroxyapatite bioceramics.* Ceramics International, 2020. **46**(9): p. 13945-13952.
339. Ofudje, E.A., et al., *Synthesis and characterization of Zn-Doped hydroxyapatite: scaffold application, antibacterial and bioactivity studies.* Heliyon, 2019. **5**(5): p. e01716.
340. Jeong, J., et al., *Bioactive calcium phosphate materials and applications in bone regeneration.* Biomaterials Research, 2019. **23**(1): p. 4.
341. Saxena, V. and L.M. Pandey, *Bimetallic assembly of Fe(III) doped ZnO as an effective nanoantibiotic and its ROS independent antibacterial mechanism.* Journal of Trace Elements in Medicine and Biology, 2020. **57**: p. 126416.
342. Basu, S. and B. Basu, *Unravelling doped biphasic calcium phosphate: synthesis to application.* ACS Applied Bio Materials, 2019. **2**(12): p. 5263-5297.
343. Low, H.R., et al., *The Crystal Chemistry of Ferric Oxyhydroxyapatite.* Inorganic Chemistry, 2008. **47**(24): p. 11774-11782.
344. Hu, W., et al., *Fine structure study on low concentration zinc substituted hydroxyapatite nanoparticles.* Materials Science and Engineering: C, 2012. **32**(8): p. 2404-2410.
345. Tang, Y., et al., *Zinc incorporation into hydroxylapatite.* Biomaterials, 2009. **30**(15): p. 2864-2872.
346. Cuscó, R., et al., *Differentiation between hydroxyapatite and β-tricalcium phosphate by means of μ-Raman spectroscopy.* Journal of the European Ceramic Society, 1998. **18**(9): p. 1301-1305.
347. Balakrishnan, S., et al., *Influence of iron doping towards the physicochemical and biological characteristics of hydroxyapatite.* Ceramics International, 2020. 47(4): p. 5061-5070.
348. Sneha, M. and N.M. Sundaram, *Preparation and characterization of an iron oxide-hydroxyapatite nanocomposite for potential bone cancer therapy.* International journal of nanomedicine, 2015. **10 Suppl 1**(Suppl 1): p. 99-106.
349. Xu, Q., S. Zhou, and H. Schmidt, *Magnetic properties of ZnO nanopowders.* Journal of Alloys and Compounds, 2009. **487**(1-2): p. 665-667.
350. Fopase, R., et al., *Yttrium iron garnet for hyperthermia applications: Synthesis, characterization and in-vitro analysis.* Materials Science and Engineering: C, 2020. **116**: p. 111163.
351. Tautkus, S., et al., *Zinc and chromium co-doped calcium hydroxyapatite: Sol-gel synthesis, characterization, behaviour in simulated body fluid and phase transformations.* Journal of Solid State Chemistry, 2020. **284**: p. 121202.
352. Chou, Y.-J., H.S. Ningsih, and S.-J. Shih, *Preparation, characterization and investigation of antibacterial silver-zinc co-doped β-tricalcium phosphate by spray pyrolysis.* Ceramics International, 2020. **46**(10, Part B): p. 16708-16715.
353. Türk, S., et al., *Biomimetic synthesis of Ag, Zn or Co doped HA and coating of Ag, Zn or Co doped HA/fMWCNT composite on functionalized Ti.* Materials Science and Engineering: C, 2019. **99**: p. 986-998.

354. Veerla, S.C., et al., *Controlled nanoparticle synthesis of Ag/Fe co-doped hydroxyapatite system for cancer cell treatment.* Materials Science and Engineering: C, 2019. **98**: p. 311-323.
355. Wang, Q., et al., *Experimental and simulation studies of strontium/fluoride-codoped hydroxyapatite nanoparticles with osteogenic and antibacterial activities.* Colloids and Surfaces B: Biointerfaces, 2019. **182**: p. 110359.
356. Zhang, D., et al., *Preparation and characteristics of zinc and strontium co-doped hydroxyapatite whiskers.* IOP Conference Series: Earth and Environmental Science, 2019. **233**: p. 022007.
357. Ullah, I., et al., *Impact of structural features of Sr/Fe co-doped HAp on the osteoblast proliferation and osteogenic differentiation for its application as a bone substitute.* Materials Science and Engineering: C, 2020. **110**: p. 110633.
358. Pasandideh, Z., et al., *The effects of Fe3+ and Co2+ substitution in Ca10-x-yFexCoy(PO4)6(OH)2 hydroxyapatite nanoparticles: Magnetic, antibacterial, and improved drug release behavior.* Ceramics International, 2020. **46**(10, Part B): p. 16104-16118.
359. Hagiu, A., et al., *Dose-dependent green tea effect on decrease of inflammation in human oral gingival epithelial keratinocytes: in vitro study.* Clinical oral investigations, 2020. **24**(7): p. 2375-2383.
360. Fusaro, L., et al., *Polylysine Enriched Matrices: A Promising Approach for Vascular Grafts.* Frontiers in Bioengineering and Biotechnology, 2020. **8**(281): p.1-13.
361. Hasan, A., et al., *Nano-biocomposite scaffolds of chitosan, carboxymethyl cellulose and silver nanoparticle modified cellulose nanowhiskers for bone tissue engineering applications.* International Journal of Biological Macromolecules, 2018. **111**: p. 923-934.
362. Benbow, N.L., et al., *Lysozyme uptake into pharmaceutical grade fucoidan/chitosan polyelectrolyte multilayers under physiological conditions.* Journal of Colloid and Interface Science, 2020. **565**: p. 555-566.
363. Schoolaert, E., et al., *Nanofibers with a tunable wettability by electrospinning and physical crosslinking of poly(2-n-propyl-2-oxazoline).* Materials & Design, 2020. **192**: p. 108747.
364. Pasqui, D., et al., *Carboxymethyl cellulose—hydroxyapatite hybrid hydrogel as a composite material for bone tissue engineering applications.* Journal of Biomedical Materials Research Part A, 2014. **102**(5): p. 1568-1579.
365. Grande, C.J., et al., *Nanocomposites of bacterial cellulose/hydroxyapatite for biomedical applications.* Acta Biomaterialia, 2009. **5**(5): p. 1605-1615.
366. Venkatesan, J., et al., *Chitosan–amylopectin/hydroxyapatite and chitosan–chondroitin sulphate/hydroxyapatite composite scaffolds for bone tissue engineering.* International Journal of Biological Macromolecules, 2012. **51**(5): p. 1033-1042.
367. Sadeghinia, A., et al., *Design and fabrication of clinoptilolite–nanohydroxyapatite/chitosan–gelatin composite scaffold and evaluation of its effects on bone tissue engineering.* Journal of Biomedical Materials Research Part A, 2020. **108**(2): p. 221-233.
368. Sivashankari, P.R. and M. Prabaharan, *Three-dimensional porous scaffolds based on agarose/chitosan/graphene oxide composite for tissue engineering.* International Journal of Biological Macromolecules, 2020. **146**: p. 222-231.
369. Cao, B., et al., *Porous Scaffolds Based on Cross-Linking of Poly(L-glutamic acid).* Macromolecular Bioscience, 2011. **11**(3): p. 427-434.

370. Ghalia, M.A. and Y. Dahman, *Chapter 6 - Advanced nanobiomaterials in tissue engineering: Synthesis, properties, and applications*, in *Nanobiomaterials in Soft Tissue Engineering*, A.M. Grumezescu, Editor. 2016, William Andrew Publishing. p. 141-172.
371. Lee, S., et al., *Potential bone replacement materials prepared by two methods.* MRS Online Proceedings Library Archive, 2012. p. **1418**.
372. Itälä, A.I., et al., *Pore diameter of more than 100 μm is not requisite for bone ingrowth in rabbits.* Journal of Biomedical Materials Research, 2001. **58**(6): p. 679-683.
373. Mittal, H., et al., *Recent progress in the structural modification of chitosan for applications in diversified biomedical fields.* European Polymer Journal, 2018. **109**: p. 402-434.
374. Berger, J., et al., *Structure and interactions in covalently and ionically crosslinked chitosan hydrogels for biomedical applications.* European Journal of Pharmaceutics and Biopharmaceutics, 2004. **57**(1): p. 19-34.
375. Wang, Y., L. Liu, and S. Guo, *Characterization of biodegradable and cytocompatible nano-hydroxyapatite/polycaprolactone porous scaffolds in degradation in vitro.* Polymer Degradation and Stability, 2010. **95**(2): p. 207-213.
376. Shen, L., et al., *Preparation and mechanical properties of carbon fiber reinforced hydroxyapatite/polylactide biocomposites.* Journal of Materials Science: Materials in Medicine, 2009. **20**(11): p. 2259-2265.
377. Adachi, T., et al., *Framework for optimal design of porous scaffold microstructure by computational simulation of bone regeneration.* Biomaterials, 2006. **27**(21): p. 3964-3972.
378. Türk, S., et al., *3D porous collagen/functionalized multiwalled carbon nanotube/chitosan/hydroxyapatite composite scaffolds for bone tissue engineering.* Materials Science and Engineering: C, 2018. **92**: p. 757-768.
379. Hu, J.-X., et al., *Biomineralization-inspired synthesis of chitosan/hydroxyapatite biocomposites based on a novel bilayer rate-controlling model.* Colloids and Surfaces B: Biointerfaces, 2015. **136**: p. 457-464.
380. Fei Liu, X., et al., *Antibacterial action of chitosan and carboxymethylated chitosan.* Journal of Applied Polymer Science, 2001. **79**(7): p. 1324-1335.
381. Saxena, V., I. Shukla, and L.M. Pandey, *Hydroxyapatite: an inorganic ceramic for biomedical applications*, in *Materials for Biomedical Engineering*. 2019, Elsevier. p. 205-249.
382. Kozlowska, J., N. Stachowiak, and A. Sionkowska, *Preparation and characterization of collagen/chitosan poly (ethylene glycol)/nanohydroxyapatite composite scaffolds.* Polymers for Advanced Technologies, 2019. **30**(3): p. 799-803.
383. Liuyun, J., L. Yubao, and X. Chengdong, *Preparation and biological properties of a novel composite scaffold of nano-hydroxyapatite/chitosan/carboxymethyl cellulose for bone tissue engineering.* Journal of Biomedical Science, 2009. **16**(1): p. 65.
384. Jiang, L., et al., *Preparation and properties of nano-hydroxyapatite/chitosan/carboxymethyl cellulose composite scaffold.* Carbohydrate Polymers, 2008. **74**(3): p. 680-684.
385. Rogina, A., et al., *In situ hydroxyapatite content affects the cell differentiation on porous chitosan/hydroxyapatite scaffolds.* Annals of biomedical engineering, 2016. **44**(4): p. 1107-1119.
386. Wang, F., et al., *Enhanced physical and biological properties of chitosan scaffold by silk proteins cross-linking.* Carbohydrate Polymers, 2020. **229**: p. 115529.

387. Matinfar, M., A.S. Mesgar, and Z. Mohammadi, *Evaluation of physicochemical, mechanical and biological properties of chitosan/carboxymethyl cellulose reinforced with multiphasic calcium phosphate whisker-like fibers for bone tissue engineering.* Materials Science and Engineering: C, 2019. **100**: p. 341-353.
388. Sainitya, R., et al., *Scaffolds containing chitosan/carboxymethyl cellulose/mesoporous wollastonite for bone tissue engineering.* International Journal of Biological Macromolecules, 2015. **80**: p. 481-488.
389. Pu, X.-m., K. Wei, and Q.-q. Zhang, *In situ forming chitosan/hydroxyapatite rods reinforced via genipin crosslinking.* Materials Letters, 2013. **94**: p. 169-171.
390. Shavandi, A., et al., *Development and characterization of hydroxyapatite/β-TCP/chitosan composites for tissue engineering applications.* Materials Science and Engineering: C, 2015. **56**: p. 481-493.
391. Lu, H.-T., et al., *Development of genipin-crosslinked and fucoidan-adsorbed nano-hydroxyapatite/hydroxypropyl chitosan composite scaffolds for bone tissue engineering.* International Journal of Biological Macromolecules, 2019. **128**: p. 973-984.
392. Kruppke, B., et al., *In Situ Crosslinking of Highly Porous Chitosan Scaffolds for Bone Regeneration: Production Parameters and In Vitro Characterization.* Macromolecular Materials and Engineering, 2017. **302**(10): p. 1700147.
393. Hancock, R.E. and H.-G. Sahl, *Antimicrobial and host-defense peptides as new anti-infective therapeutic strategies.* Nature biotechnology, 2006. **24**(12): p. 1551-1557.
394. Andersson, D.I., D. Hughes, and J.Z. Kubicek-Sutherland, *Mechanisms and consequences of bacterial resistance to antimicrobial peptides.* Drug Resistance Updates, 2016. **26**: p. 43-57.
395. AaronáLau, K.H., *Peptoids for biomaterials science.* Biomaterials science, 2014. **2**(5): p. 627-633.
396. Zuckermann, R.N., et al., *Efficient method for the preparation of peptoids [oligo (N-substituted glycines)] by submonomer solid-phase synthesis.* Journal of the American Chemical Society, 1992. **114**(26): p. 10646-10647.
397. Lau, K.H.A., et al., *Molecular Design of Antifouling Polymer Brushes Using Sequence-Specific Peptoids.* Advanced materials interfaces, 2015. **2**(1): p. 1400225.
398. Lau, K.H.A., et al., *Self-assembly of ultra-small micelles from amphiphilic lipopeptoids.* Chemical Communications, 2017. **53**(13): p. 2178-2181.
399. O'brien, J., et al., *Investigation of the Alamar Blue (resazurin) fluorescent dye for the assessment of mammalian cell cytotoxicity.* European journal of biochemistry, 2000. **267**(17): p. 5421-5426.
400. Hu, Y. and S. Aksoy, *An antimicrobial peptide with trypanocidal activity characterized from Glossina morsitans morsitans.* Insect biochemistry and molecular biology, 2005. **35**(2): p. 105-115.
401. Hasan, A., et al., *Chain-End Modifications and Sequence Arrangements of Antimicrobial Peptoids for Mediating Activity and Nano-Assembly.* 2020. **8**(416).

Research outputs:

Manuscript Published

1. **Varun Saxena**, Abshar Hasan, Lalit M. Pandey, **Antibacterial nano-biocomposite scaffolds of Chitosan, Carboxymethyl Cellulose and Zn & Fe integrated Hydroxyapatite (Chitosan-CMC-FZO@HAp) for bone tissue engineering**. Cellulose; (28), 9207–9226; 2021
2. **Varun Saxena**, Lalit M. Pandey, **Design and characterization of biphasic ferric hydroxyapatite-zincite nanoassembly for bone tissue engineering**. Ceramic International; 47 (20); 28274-28287; 2021
3. **Varun Saxena**, Lalit M. Pandey, **Bimetallic assembly of Fe(III) doped ZnO as an effective nanoantibiotic and its ROS independent antibacterial mechanism,** Journal of Trace Elements in Medicine and Biology; (57); 126416; 2020
4. **Varun Saxena**, Lalit M. Pandey, T.S. Srivastan, **Nano hydroxyapatite (nano-HAp): a potential bioceramic for biomedical applications.** Current Nanotechnology; (http://doi.org/10.2174/2405461506666210412154837)
5. **Varun Saxena**, Lalit M. Pandey**, Nanomaterial-based hydrogels for coronary interventions: a mini review,** Mini Invasive Surgery; (4); 62; 2020
6. **Varun Saxena**, Swati Sharma, Lalit M. Pandey. **Fe(III) doped ZnO nano-assembly as a potential heterogeneous nano-catalyst for the production of biodiesel,** Materials Letters; (237), 232-235; 2019
7. **Varun Saxena**, Pranjal Chandra, & Lalit M. Pandey. **Design and characterization of novel Al-doped ZnO nanoassembly as an effective nanoantibiotic**. Applied Nanoscience; (8), 1925-1941; 2018
8. **Varun Saxena**, Lalit M Pandey, **Synthesis, characterization and antibacterial activity of aluminum doped zinc oxide,** Materials Today: Proceedings; (18) 3; 1388-1400; 2019
9. **Varun Saxena,** Abshar Hasan, & Lalit M. Pandey. **Effect of Zn/ZnO integration with Hydroxyapatite: A Review.** Materials Technology, (33); 79-92; 2018
10. **Varun Saxena**, Abshar Hasan, Swati Sharma & Lalit M. Pandey. **Edible oil nanoemulsion: An organic nanoantibiotic as a potential biomolecule delivery vehicle.** International Journal of Polymeric Materials and Polymeric Biomaterials; (67); 410-419; 2017

11. Abshar Hasan, **Varun Saxena**, Valeria Castelletto, Georgina Zimbitas, Jani Seitsonen, Janne Ruokolainen, Lalit M Pandey, Jan Sefcik, Ian W Hamley, King Hang Aaron Lau; **Chain-end modifications and sequence arrangements of antimicrobial peptoids for mediating activity and nano-assembly**; Frontiers in Chemistry, (8); 416; 2020

12. Nilkamal Mahanta, **Varun Saxena,** Lalit M. Pandey, Priyanka Batra, U. S. Dixit, **Performance study of a sterilization box using a combination of heat and ultraviolet light irradiation**; Environmetal Research, (198), 111309; 2021

13. Aquib Jawed, **Varun Saxena,** Lalit M. Pandey. **Recent developments on the applications of emerging nanomaterials for the removal of heavy metals.** Journal of Water Process Engineering; (33), 101009; 2020

14. Rushikesh Fopase, **Varun Saxena**, Papori Seal, JP Borah, Lalit M Pandey; **Yttrium iron garnet for hyperthermia applications: Synthesis, characterization and in-vitro analysis,** Materials Science and Engineering: C; (116); 111163; 2020

15. Sunayan Deka, **Varun Saxena**, Abshar Hasan, Pranjal Chandra, Lalit M. Pandey. **Synthesis, characterization and *in-vitro* analysis of α-Fe_2O_3-$GdFeO_3$ biphasic materials as therapeutic agent for magnetic hyperthermia applications**. Materials Science and Engineering C; (92); 932-941; 2018

16. Swati Sharma, **Varun Saxena**, Anupriya Baranwal, Pranjal Chandra, Lalit M. Pandey. **Engineered nanoporous materials mediated heterogeneous catalysts and their implications in biodiesel production.** Materials Science for Energy Technologies. 1(1), 11-21; 2018

17. Abhishek Roy, **Varun Saxena** & Lalit M. Pandey. **3D printing of cardio-vasculatures: A Review**. Materials Technology; 33 (6), 433-442; 2018

18. Abshar Hasan, **Varun Saxena**, & Lalit M. Pandey. **Surface functionalization of Ti6Al4V via self-assembled monolayers for improved biocompatibility in tissue engineering applications**; Langmuir; 34(11); 3494-3506; 2018

19. Abshar Hasan, Gyan Waibhaw, **Varun Saxena** & Lalit M. Pandey. **Nano-biocomposite scaffolds of chitosan, carboxymethyl cellulose and silver nanoparticle modified cellulose nanowhiskers for bone tissue engineering applications.** International journal of biological macromolecules; (111), 923-934; 2018

20. Swati Sharma, Sakshi Tiwari, Abshar Hasan, **Varun Saxena** & Lalit M. Pandey. **Recent advances in conventional and contemporary methods for remediation of heavy metal contaminated soils**. 3 Biotech; 8 (4), 216; 2018
21. Apurba Das, Emon Barua, Suman Kumar Mushahary, Aman Bhardwaj**, Varun Saxena,** Lalit Pandey, Ashish Deoghare, Pamu Dobbidi. **A comparative study of Microstructural, Biological, and Mechanical properties in 20H-80B and 20H-80S composite scaffolds.** Material Letters; (304), 130668; 2021

Book Chapters published

1. **Varun Saxena**, I Shukla, Lalit M. Pandey. **Hydroxyapatite: an inorganic ceramic for biomedical applications.** Materials for Biomedical Engineering Nanobiomaterials in Tissue Engineering, 2019, Pages 205-249.
2. **Varun Saxena**, Martyn Merrilees, K. H. Aaron Lau, **Antifouling Peptoid Biointerfaces;** Biointerface Engineering: Prospects in Medical Diagnostics and Drug Delivery, 2020, Pages 55-73.
3. **Varun Saxena**, Lalit M. Pandey, **Synthesis and sintering of biomimetic hydroxyapatite nanoparticles for biomedical applications;** Encyclopedia of Materials; Elsevier's Accepted (https://doi.org/10.1016/B978-0-12-820352-1.00136-X)
4. Vivek Singh, **Varun Saxena**, Lalit M. Pandey, **Fiber Reinforced Nano Composites; Mechanical and Biological Prospects for Biomedical Application**. Fiber-Reinforced Polymers ISBN: 978-1-53619-049-6; Pages 343-378.
5. Aquib jawed, Rahul Verma, **Varun Saxena**, Lalit M. Pandey. **Photocatalytic metal nanoparticles: a green approach for degradation of dyes**; Photocatalytic Degradation of Dyes Current Trends and Future Perspectives. (ISBN: 978-0-12-823876-9) Pages 251-274.

Conferences and Seminars

1. International conference on Nanotechnology: Ideas, innovations and initiatives-2017, IIT Roorkee, India. Varun Saxena, Lalit M. Pandey Oral presentation on "Synthesis characterization and antibacterial activity of Al doped zinc oxide", Dec-06 to Dec 08, 2017.

2. International conference on BioMaterials, BioEngineering, and BioTheranostics-2018, VIT Vellore, India; Varun Saxena, Lalit M. Pandey, Poster presentation on "Antibacterial mechanism of Fe(III) doped ZnO nanoantibiotic under dark conditions", 24th-28th July, 2018
3. Extended Rheology Characterization, Sept. 18th, 2017, by Anton Paar at IIT Guwahati, India
4. ZE5 (Flow cytometer) and Droplet digital PCR-QX-200, Oct. 30 to, by Bio-Rad at IIT Guwahati, India; Nov. 3rd 2017.
5. International Biomaterial Symposium, University of Lancaster, United Kingdom; Varun Saxena, and Lalit M. Pandey, Synthesis, characterization and antibacterial activity of Zinc and Iron co-doped hydroxyapatite nanoparticles, February 2019.
6. International conference, University of Strathclyde, United Kingdom, RSC; Varun Saxena, and Lalit M. Pandey, Synthesis, characterization and antibacterial activity of Zinc and Iron co-doped hydroxyapatite nanoparticles, March 2019.
7. International conference "Peptide Synthesis and Purification" Heriot Watt university, Edinburgh, UK; Varun Saxena, Lalit M. Pandey, K. H. Aaron Lau, Solid phase synthesis of Sequence Specific "Peptoids". Anuary 2020.
8. Workshop cum Symposium on Bioinspired Nanomaterials for Environmental Applications, Centre for the Environment, Indian Institute of Technology Guwahati, Assam; Varun Saxena, Aquib Jawed, Lalit M. Pandey, Application of bimetallic Al-doped ZnO nano-assembly for heavy metal removal and decontamination of wastewater; February 12-13, 2020.
9. 6th International conference on Nanoscience and Nanotechnology (ICONN-2021); SRM University (Digital); Varun Saxena, Lalit M. Pandey, Synthesis, characterization and antibacterial activity of zinc and iron co-integrated hydroxyapatite nanoparticles; February 01-03, 2021.

Awards

Received prestigious Commonwealth Split-site Fellowship-2019 for one year (January 2019 to January 2020) to work at Dr. King Hang Aaron Lau's lab, Dept. of Pure and Applied Chemistry at University of Strathclyde, UK.